AD-A121 450 HIGH-INTENSITY SOUND IN AIR SATURATED FIBROUS BULK POROUS MATERIALS(U) TEXAS UNIV AT AUSTIN APPLIED RESEARCH LABS H L KUNTZ 03 SEP 82 ARL-TR-82-54 1/3

UNCLASSIFIED N00014-75-C-0847 F/G 11/6 NL

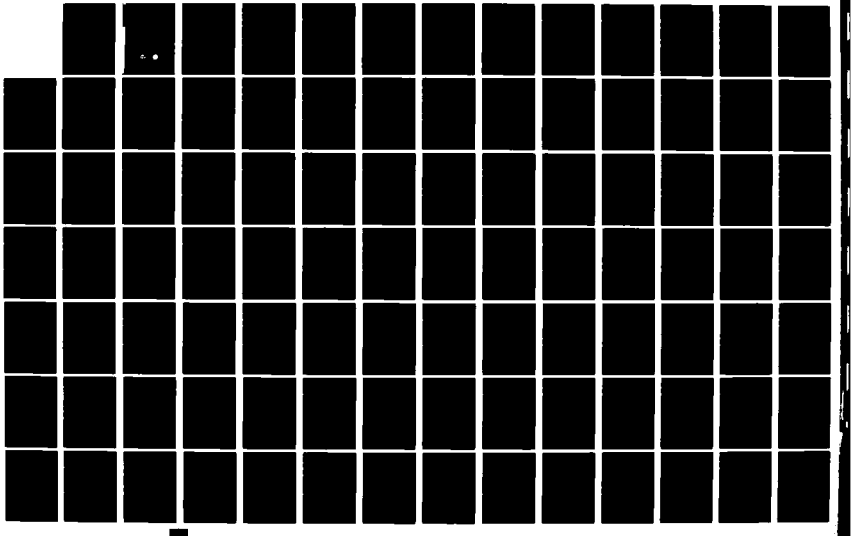

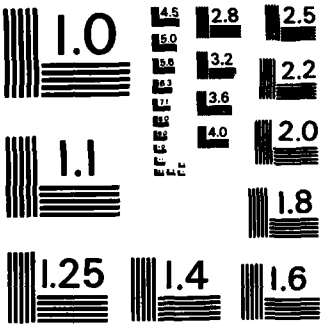

MICROCOPY RESOLUTION TEST CHART
NATIONAL BUREAU OF STANDARDS - 1963 - A

ARL-TR-82-54

Copy No.____

HIGH-INTENSITY SOUND IN AIR SATURATED FIBROUS BULK POROUS MATERIALS

Final NASA Contractor Report 167979 for NSG 3198

Herbert L. Kuntz, II

APPLIED RESEARCH LABORATORIES
THE UNIVERSITY OF TEXAS AT AUSTIN
POST OFFICE BOX 8029, AUSTIN, TEXAS 78712-8029
AND
DEPARTMENT OF MECHANICAL ENGINEERING
THE UNIVERSITY OF TEXAS AT AUSTIN
AUSTIN, TEXAS 78712

3 September 1982

Final Report

1 September 1978 - 31 August 1981

APPROVED FOR PUBLIC RELEASE;
DISTRIBUTION UNLIMITED.

Prepared for:

FLUID MECHANICS AND ACOUSTICS DIVISION
NASA LEWIS RESEARCH CENTER
21000 BROOKPARK ROAD
CLEVELAND, OHIO 44135

UNCLASSIFIED

SECURITY CLASSIFICATION OF THIS PAGE (When Data Entered)

REPORT DOCUMENTATION PAGE		READ INSTRUCTIONS BEFORE COMPLETING FORM
1. REPORT NUMBER	2. GOVT ACCESSION NO. AD-A121 450	3. RECIPIENT'S CATALOG NUMBER CR 167979
4. TITLE (and Subtitle) HIGH-INTENSITY SOUND IN AIR SATURATED, FIBROUS BULK POROUS MATERIALS		5. TYPE OF REPORT & PERIOD COVERED final report 1 Sep 78 - 31 Aug 81
		6. PERFORMING ORG. REPORT NUMBER ARL-TR-82-54
7. AUTHOR(s) Herbert L. Kuntz, II		8. CONTRACT OR GRANT NUMBER(s) NSG 3198 N00014-75-C-0817
9. PERFORMING ORGANIZATION NAME AND ADDRESS Department of Mechanical Engineering and Applied Research Laboratories The University of Texas at Austin P. O. Box 8029, Austin, TX 78712-8029		10. PROGRAM ELEMENT, PROJECT, TASK AREA & WORK UNIT NUMBERS
11. CONTROLLING OFFICE NAME AND ADDRESS Fluid Mechanics and Acoustics Division NASA Lewis Research Center, 21000 Brookpark Rd. Cleveland, OH 44135		12. REPORT DATE 3 September 1982
		13. NUMBER OF PAGES 228
14. MONITORING AGENCY NAME & ADDRESS(if different from Controlling Office)		15. SECURITY CLASS. (of this report) UNCLASSIFIED
		15a. DECLASSIFICATION/DOWNGRADING SCHEDULE

16. DISTRIBUTION STATEMENT (of this Report)

Unlimited

17. DISTRIBUTION STATEMENT (of the abstract entered in Block 20, if different from Report)

18. SUPPLEMENTARY NOTES

19. KEY WORDS (Continue on reverse side if necessary and identify by block number)

intense sound, bulk porous materials, excess attenuation, saturation, acoustic impedance, nonlinear propagation, sound attenuation, absorption, nonlinear acoustics, experiments, data, reflection

20. ABSTRACT (Continue on reverse side if necessary and identify by block number)

An investigation of the interaction of high-intensity sound with bulk porous materials is reported. The work is mainly experimental but some theoretical results are obtained. Previous studies of high-intensity sound in porous materials have been limited to porous sheets. Most tests in the present study were done on Kevlar® 29, a fibrous plastic material, for the porosity range between 0.985 and 0.809. The nonlinear behavior of the materials was first described by dc flow resistivity tests. Then acoustic

DD FORM 1 JAN 73 1473 EDITION OF 1 NOV 65 IS OBSOLETE

UNCLASSIFIED

SECURITY CLASSIFICATION OF THIS PAGE (When Data Entered)

propagation and reflection were measured. Small signal (100 dB re/20 μPa spectrum level), broadband (frequency range from 0.1 to 10 kHz) measurements of phase speed and attenuation were carried out. High-intensity tests (120-172 dB) were made with 1, 2, and 3 kHz tone bursts to measure harmonic generation and extra attenuation of the fundamental. Small signal (100 dB), standing wave tests were used to measure impedance between 0.1 and 3.5 kHz. High level tests (120-165 dB) with single cycle tone bursts at 1 to 4 kHz show that impedance increases with intensity. A theoretical analysis is presented for high-porosity, rigid-frame, isothermal materials (the isothermal assumption is justified by a separate analysis of heat transfer effects). One-dimensional equations of motion are derived and solved by perturbation. The measured data is not, however, well explained by the perturbation results. The experiments show that there is excess attenuation of the fundamental component and in some cases a close approach to saturation. A separate theoretical model is developed to explain the excess attenuation. This model yields predictions that are in good agreement with the measurements. Impedance and attenuation at high intensities are modeled by substituting the nonlinear flow resistivity relation into the linear impedance expressions. The model is useful in predicting the effects of a porous material on sinusoidal signals.

FOREWORD

This report is an adaptation of the Ph.D. dissertation by Herbert L. Kuntz, "High-Intensity Sound in Air Saturated, Fibrous Bulk Porous Materials." Dr. Kuntz was enrolled in the Department of Mechanical Engineering and received his degree in August 1982.

Most of the research was carried out at Applied Research Laboratories. Some of the early measurements were made in the Electroacoustics Research Laboratory, Department of Electrical Engineering. The author also carried out experiments at National Aeronautics and Space Administration (NASA) Lewis Research Center during the period June-July 1980.

Primary support for the work came from the NASA Lewis Research Center, under Grant NSG 3198. Additional support came from the Office of Naval Research (ONR) under Contract N00014-75-C-0867. Technical monitors were E. J. Rice for NASA and L. E. Hargrove for ONR.

David T. Blackstock

N. Duke Perreira

Supervisors

ACKNOWLEDGEMENTS

Many people have assisted in the course of this research. The author attempts to acknowledge most of these people here. Most of all the author thanks his supervisors Drs. D. T. Blackstock and N. D. Perreira for their invaluable interest, help, and time.

The author thanks Mr. J. M. Estes for his help in many areas of the experimental research. Without his knowledgeable assistance in making measurement devices, taking data, computer programming, and general help, this project would have been much more limited in its scope.

For their helpful discussions over the course of this work, the author thanks Drs. E. L. Hixson, R. L. Panton, C. H. Yew and B. G. Lucas and Messrs. J. A. TenCate, R. D. Essert, D. A. Nelson, and M. F. Hamilton.

For their expert typing of this manuscript through many drafts, their patience, and their help in many aspects of this project the author thanks Miss R. G. Mundine, Miss D. E. Morgan, and Mrs. B. S. Becker. Gratitude is also expressed to the many others on the staff of the Applied Research Laboratories, The University of Texas at Austin, where this research was conducted, for their valuable assistance in the many facets of this research and for use of the facilities.

The main support for this research came from NASA Lewis Research Center Grant NSG 3198. In 1980 the author spent two months at NASA Lewis doing experiments for this project. For their help and interest in the research, the author thanks Drs. E. J. Rice and K. J. Baumeister. The help of the NASA Lewis Research Center staff during the visit is appreciated.

Additional support came from the Office of Naval Research Contract N00014-75-C-0867 and the use of these additional funds is appreciated.

Several manufacturers of porous materials contributed materials for use in this study: H. L. Blachford, Inc., Globe-Albany Industrial Fabrics, Johns-Manville Fiberglass, and Scott Paper Company. The author is very thankful for their contributions.

September 1982 Herbert L. Kuntz, II

TABLE OF CONTENTS

LIST OF FIGURES

LIST OF TABLES

LIST OF SYMBOLS

Symbol	
a	Fiber radius
a_n	Normal specific acoustic absorption coefficient
b_o	Isothermal speed of sound, $b_o = \sqrt{\gamma P_o/\rho_o}$
b	Arbitrary amplitude of harmonic component (Eq. II-29)
c	Speed of sound
c_{PH}	Phase speed of sound
c_o	Adiabatic speed of sound, $c_o = \sqrt{\gamma p_o/\rho_o}$
d	Diameter of fiber in a porous material
e	Internal energy/unit mass, or 2.71828...
f	Frequency of oscillation
g	Empirical constant (Eq. I-12)
$h(P)$	Arbitrary function of porosity (Eq. I-14)
j	$\sqrt{-1}$
k	Acoustic wavenumber, $k = \omega/c$
ℓ	Integer, index
p	Acoustic pressure, $p = P - P_o$
p_o	Peak acoustic pressure
p_1	Fundamental component peak acoustic pressure (Eq. II-77)
q	Heat flux/unit area
r	Radius

Symbol	
$\mathcal{R}(z)$	Resistive part of impedance (for Eq. I-28 only), $\mathcal{R}(z) = \mathrm{Re}(z) - \rho_o c_o$
s	Entropy/unit volume
t	Time
u	Particle velocity
u_o	Peak particle velocity
x	Coordinate variable
$\bar{x}$	Shock formation distance, $\bar{x} = 1/\beta' \epsilon k$
A	Area
A_1	Dimensionless attenuation, $A_1 = \beta_1 b_o/\omega$
B	First order equation unknown
B_1	Dimensionless phase, $B_1 = \beta_1 b_o/\omega$
C_p	Specific heat at a constant pressure
C_v	Specific heat at a constant volume
D	Unknown (Eq. A-3)
D_n, D_p	Variables (Eqs. I-18a and I-18b)
E	Internal energy/unit volume
F	Generalized Drag Force/unit volume
F_1	Dimensionless drag force, $F_1 = F/\rho_o \omega$
G	Gol'dberg number, $G = \beta' \epsilon k/\alpha$
G	Gol'dberg number for a porous material, $G = \frac{p_o}{\alpha T}$
Im(•)	Imaginary part of a complex number
$J_n(\cdot)$	Bessel function of the first kind

Symbol	
K	Heat transfer parameter, (Eq. I-19)
$K_n(\cdot)$	Modified Bessel function of the second kind
L	Length of sample
$\mathcal{L}$	Operator (Eq. II-56)
$M_n(\cdot)$	Magnitude of the Kelvin functions of the first kind, $M_n(\cdot) = \sqrt{\text{ber}_n^2(\cdot) + \text{bei}_n^2(\cdot)}$
$N_n(\cdot)$	Magnitude of the Kelvin functions of the second kind, $N_n(\cdot) = \sqrt{\text{ker}_n^2(\cdot) + \text{kei}_n^2(\cdot)}$
P	Porosity, $P = V_{fluid}/V$
P	Total pressure
P_i	Incident acoustic pressure
P_o	Ambient pressure
P_r	Reflected acoustic pressure
Pr	Prandtl number, $Pr = \mu C_p/\kappa$
Q	Heat flux/unit volume
Q_ℓ	Coefficients (Eq. II-58)
R	Reflection coefficient (Eq. I-28)
$\mathcal{R}$	Gas constant, $\mathcal{R} = C_p - C_v$
$\text{Re}(\cdot)$	The real part of a complex number
Re	Acoustic Reynolds number, $\text{Re} = \rho_o \omega d^2/\mu$
R_{dc}	DC flow resistance
R_ℓ	Coefficients, $R_\ell = -Q_\ell$
R_m	Modified Reynolds number (Eq. I-27)

Symbol	
S	Fiber spacing
$\mathcal{S}$	Surface area/unit volume (Eq. I-27)
T	Total temperature
T_n	Fitting constant (Eq. I-19)
T_o	Ambient temperature
U	Dimensionless particle velocity, $U = u/c$
V	Volume
V_n	Empirical parameter (Eq. I-17)
V_p	Empirical parameter (Eq. I-17)
W	Work done
$\mathcal{W}$	Normal specific acoustic impedance (dimensional)
$\mathcal{W}_R$	Real part of the impedance
$\mathcal{W}_I$	Imaginary part of the impedance
Z_N	Nonlinear approximation to the acoustic impedance
Z_1	First order normal specific acoustic impedance (dimensionless)
Z_t	Temporal impedance operator (Eq. I-30)
α	Attenuation, nepers/meter
$\bar{\alpha}$	Attenuation, dB/meter
α_T	Thermal diffusivity
β	Wave number, radians/meter
β'	Nonlinearity parameter $\beta' = (\gamma + 1)/2$
γ	Ratio of specific heats, $\gamma = C_p/C_v$
δ	Denotes a small change

Symbol	
ε	Dimensionless particle velocity, $\varepsilon = u_o/c_o$
η	Nonlinear flow resistivity coefficient (Eq. II-13)
η_1	Dimensionless nonlinear flow resistivity coefficient, $\eta_1 = \eta b_o/\rho_o\omega$
$\theta(r)$	Radial temperature
κ	Thermal conductivity
λ	Wavelength, $\lambda = c/f$
μ	Dynamic viscosity
ν	Kinematic viscosity, $\nu = \mu/\rho$
ξ	Heat conduction parameter, $\xi = \sqrt{\omega/\alpha_T}$
π	3.14159...
ρ	Total density
ρ_o	Ambient density
$\delta\rho$	Acoustic density
σ	Small signal flow resistivity parameter, (Eq. I-12)
σ_H	Small signal flow resistivity parameter, (Eq. I-17)
σ_ℓ	ℓ^{TH} order flow resistivity parameter, $\ell = 1,2,3,4$
σ^*	Shock formation parameter, $\sigma^* = \beta'\varepsilon kx$
τ	Dimensionless time, $\tau = \omega t$
ϕ	Phase difference between two harmonic components
$\phi_n(\cdot)$	Phase angle of the Kelvin functions of the second kind $\phi_n(\cdot) = \arctan[\mathrm{kei}_n(\cdot)/\mathrm{ker}_n(\cdot)]$
χ	Dimensionless distance, $\chi = x\omega/c$

Symbol	
$\psi_n(\cdot)$	Phase angle of the Kelvin functions of the first kind $\psi_n(\cdot) = \arctan[\text{bei}_n(\cdot)/\text{ber}_n(\cdot)]$
ω	Angular frequency, $\omega = 2\pi f$
∂	Partial derivative
Γ	Dimensional complex propagation coefficient, $\Gamma = (\beta - j\alpha)$
Γ_ℓ	Dimensionless complex propagation coefficient, $\Gamma_\ell = \frac{c}{\omega}(\beta_\ell - j\alpha_\ell)$, $\ell = 1,2,3,4$
Γ_ℓ^*	Complex conjugate of Γ_ℓ
Δ	Dimensionless density, $\Delta = \rho/\rho_o$, or differential change
$<$	Less than
$>$	Greater than
Λ	General, thermal driving function
Λ_o	Magnitude of the sinusoidal thermal driving function, $\Lambda = \Lambda_o e^{j\omega t}$
Π	Dimensionless acoustic pressure, $\Pi = p/\rho_o c^2$
T	Nonlinearity coefficient (Eq. II-77)
∞	Infinity
$\text{ber}_n(\cdot)$	Real part of the Kelvin function of the first kind
$\text{bei}_n(\cdot)$	Imaginary part of the Kelvin function of the first kind
$\text{ker}_n(\cdot)$	Real part of the Kelvin function of the second kind
$\text{kei}_n(\cdot)$	Imaginary part of the Kelvin function of the second kind

CHAPTER I

INTRODUCTION AND BACKGROUND

A. Introduction

The topic of high-intensity sound propagation has been mostly limited to sound waves in fluids and solids (see Beyer [10]*). Very little has been done in the study of high-intensity sound propagation in bulk porous materials. Studies of intense sound interaction with perforated sheets, thin sheets of porous materials, and Helmholtz resonators have been done (for example, see Refs. 37, 48, 55, 86).

Recently the use of porous materials in jet engine inlets has increased. At high intensities it has been observed that the impedance of a porous material changes with sound level, i.e., the material behaves nonlinearly. An understanding of sound reflection from and propagation in bulk porous materials has therefore become necessary. In this study many experiments have been performed on air saturated, fibrous, and expanded plastic porous materials. The materials have porosities in the range $0.809 \leq P \leq 0.985$, where P is the porosity (the volume of air per total volume). The emphasis of this study is on the experimental results and explanation of these results.

In this investigation a theoretical model for intense sound propagation in very porous, rigid, air saturated, fibrous bulk ma-

*References are listed alphabetically by author and referred to by number at the end of this dissertation.

terials is developed. A separate empirical model is proposed to describe finite amplitude losses (inexplicable losses in linear theory) in the porous material. Modeling of the reflection of high intensity sound waves from the surface of porous materials was also carried out. The reflection process is very complicated; both resistive and reactive components can depend upon the particle velocity amplitude of the incoming wave. Experimental data obtained from measurements on a variety of bulk porous materials are used to test the validity and limits of the theoretical models.

After this introductory section, some background theory is presented in the remainder of this chapter. First, a brief discussion of the theories on low intensity sound propagation in porous materials is used to put the theory of Chapter II in perspective. Second, a brief summary of high-intensity sound propagation in ordinary fluids is presented. Third, past work on the reflection of high-intensity sound from surfaces and thin sheets is described.

In Chapter II a high-intensity sound theory is presented. The one-dimensional mass, momentum, and internal energy equations for a nonlinearly behaving bulk porous material are derived. The resulting equations are solved by perturbation. A single boundary condition is used. The input signal is assumed to be a sinusoid which is distorted by a second harmonic component. A mathematical approximation to model the high-intensity impedance of semi-infinite materials is also presented. An empirical model is adapted from the nonlinear acoustics of fluids to help describe the excess attenuation and approach to

saturation* of an intense sine wave in a porous material. The various theoretical results from Chapter II are compared to data in Chapter IV.

In Chapter III the devices and methods used in the experiments are described. The devices are used to determine the porosity, material structure, flow resistivity, acoustic impedance, and acoustic propagation parameters (attenuation and phase speed). Data are presented in Chapter IV.

In Chapter IV the experimentally determined data are compared to the theoretical results derived in Chapter II. The results of the porosity and dc flow resistivity measurements are presented and then used in the theory to predict the acoustical properties of the various materials. In the linear region the propagation parameter test results agreed with theoretical predictions in some cases and disagreed in other cases. The perturbation theory was found to be a poor predictor of the data at high intensities, porosities, and nonlinearities. As the porosity was reduced the agreement between measurements and predictions was better at higher intensities. The excess attenuation model predicts the excess attenuation of the fundamental over a large range of sound intensities, material nonlinearities, and porosities. Results of small-signal impedance measurements on finite and effectively semi-infinite

---

*Saturation occurs when the finite amplitude losses become so large that, no matter how much energy enters a porous material, only a specific amount of acoustic energy (saturation level) will arrive at some location within the material. The saturation level depends upon the distance the wave travels, nonlinearity, and small-signal attenuation [81].

materials are presented and, in most cases, agree with theoretical predictions. Results of high-intensity impedance measurements for effectively semi-infinite materials are presented and compared to the mathematical approximation presented in Chapter II. The advantages and problems of each model are discussed.

In Chapter V the investigation of acoustic waves in porous materials is summarized, conclusions are discussed, and proposals for future work are presented. The appendices include a theoretical analysis of heat transfer in fibrous porous materials, assembly drawings of some of the devices discussed in Chapter III, and computer programs.

B. Linear Theory

A review of the various theories of low-intensity propagation in and impedance of porous materials is presented in this section. The following discussion is intended to help orient the reader with respect to the vast literature on porous materials and the present study. The intent is not to cover all the literature but to give a general view. High intensity effects are postponed to Section C of this chapter. The linear theories are arranged in four categories based on the model used. After discussion, each theory is related to the present analysis. The four categories are the scattering model, the capillary tube-fiber motion models, the rigid frame model, and the lumped element model.

1. Scattering Model

Sound wave scattering from the fibers of the porous material is an approach that has been employed with varying success. The approach has the advantage that no empirical constants have to be determined from measured data. One minor drawback is that the theory is developed only for very porous fibrous materials.

In 1910 Sewell [72] applied this method to fibrous materials containing a viscous gas. At that time there were no experimental results for comparisons. In 1970 Kozhin [42-44] reworked Sewell's theory, but made no comparison with available experiments. These theories yield predicted attenuations that greatly exceed the attenuations measured in this study.

In 1970 Attenborough and Walker [3] published a scattering theory for fibrous materials. They show accurate prediction of the absorption coefficient at frequencies above 500 Hz, accurate prediction of the phase speed, and predicted attenuation exceeding measured attenuation at all frequencies. The predicted acoustic impedance is high. The theory includes both rigid and flexible porous materials. A more detailed discussion is given in Ref. 77.

In 1976 Mechel [53,54] derived a long and complicated scattering theory in which he includes the scattering of viscosity, thermal, and density waves. He concluded that the theory was not as good a predictor as some of the empirically related theories, such as Delany and Bazley's [25] analysis of Zwikker and Kosten's model [88] (discussed later in this section).

Scattering theory cannot be used to predict all the acoustical properties of a fibrous porous material, but in many cases the theory is adequate. In the present study, which is of high-intensity sound, this theory is not applicable because of the assumption that particle displacement is small in the porous material. It would be very difficult to generalize scattering theory to make it apply to high-intensity waves.

2. Capillary Tube-Fiber Motion Models

Two types of models are discussed in this section. They are, in most cases, intertwined with each other to such a degree that they cannot be separated. Most of these models include material motion in the acoustical analysis. The major difference between the models is the manner in which the viscous and thermal properties of the material are determined. In one case, the capillary tube model, the viscous and

thermal properties are defined by calculating the acoustical effects of a large number of adjacent capillary tubes. In the other case, the flow resistance model, the dc flow resistance of the material is used to determine the viscous properties. In both cases, one or more empirical factors must be included to match the theory to data. The following review is presented as historically as possible.

The first attempt at theoretical analysis of the acoustical properties of bulk porous materials was done by Rayleigh in 1883 [66]. He expanded his work in the second volume of his book [67]. Rayleigh assumed that the porous material could be modeled as an array of packed capillary tubes with the sound traveling axially along the tubes. Porous material structures are actually much different from a simple model of packed capillary tubes. He based his work on Kirchhoff's [41] theory of viscosity and heat conduction effects on sound waves traveling in circular tubes made of perfectly rigid and heat conducting walls. Many others [6,8,11,25,73,74,88] have used Rayleigh's approach as a basis for analysis and have used complicated schemes to predict experimental data. Some of these theories are discussed here.

Adaptation of Rayleigh's theory (see, for example, Zwikker and Kosten [88], Beranek [6,8], and Bies [11]) requires that an empirical parameter called the structure factor be determined. The definition of the structure factor depends on the author. The most common definition of the structure factor is that it is a correction for the tortuosity the sound wave encounters as it travels in the material [6,8,11,88]. Another definition of the structure factor is that it is a correction for the effective acoustic air density caused by motion of the frame

[11,88]. Although the theories discussed in this section can be tied, in special cases, to the theory used in the present study, the structure factor is not used here.

Zwikker and Kosten [88] have presented the most comprehensive study of the acoustics of porous materials. They used Rayleigh's basic theory [67] as a starting place and introduced the structure factor and frame motion. In turn, their theory has become the starting point for the rest of the theories discussed in this sub-section.

Beranek [8] started with the equations that Zwikker and Kosten [88] derived in their analysis. Except for the structure factor, Beranek's analysis reduces to the rigid material model described in the next sub-section. Beranek measured the propagation parameters and impedance and, through his analysis, presented results illustrating the volume coefficient of elasticity of air in the porous material (heat transfer effects) and the effects of having the sample vibrate in its holder. A theoretical analysis of heat transfer effects is discussed in Appendix A of this study. Beranek's measured data show a much smaller transition region between the two heat transfer states than was determined here or by others [11,34,88]. In determining the sample vibrations in its holder, Beranek addressed a problem important to avoid in the experiments. If the sample holder holds the sample too tightly, or too loosely, the sample will tend to resonate at low frequencies and cause the experimental results to be erroneous relative to results determined from properly held materials. The resonance problem was considered in the present study and the experimental results indicate that the problem was avoided. Beranek also discussed coupling of acoustic

and solid waves, but concluded that, at higher frequencies, the material becomes decoupled from the acoustic waves.

Delany and Bazley [25] carried out an extensive empirical study of the acoustical properties of fibrous porous materials. They normalized their data to the dimensional parameter f/σ,* where f is the frequency in Hertz and σ is the flow resistivity in MKS Rayls/meter. The empirical relations they determined are useful over the specified range of $0.01 \leq f/\sigma \leq 1.0$. The relations are used to calculate the attenuation, phase speed, and impedance. Although not directly applicable to the present study, the equations are useful in checking measurements made at low intensities.

Bies [11] reviewed some of the above theories. He also discussed measurement of flow resistance and porosity. Bies gave an approximate relation for the structure factor. The discussion was not limited to fibrous materials. He presented data on cloths, fibrous materials, and fiberboard materials.

Most of the above theories account for fiber motion (other than sample resonance). Lambert's [49] analysis of Zwikker and Kosten's theory [88] indicates that above 130 Hz the air and frame of Kevlar® 29 aramid (du Pont de Nemours Company) are "decoupled".† Because $f \geq 100$ Hz in the present study, we are not concerned with frame motion. Support

---

*All the symbols are listed together at the beginning of this dissertation.

†Kevlar®29 is a plastic fibrous material that is used extensively in the present study.

for Lambert's conclusion is given in Chapter IV. Lambert also determined that the decoupling frequency for Scottfoam (Scott Paper Company) was at 85 Hz. Scottfoam is a fully reticulated,* expanded polyurethane foam and is similar to the Scottfelt (Scott Paper Company) used in the present study. Although Lambert used the material density $\rho_s = 600$ kg/m^3 when, in actuality, the density of Scottfoam is $\rho_s = 1153 \pm 32$ kg/m^3 [89], the error leads to an error of only 4 Hz in the decoupling frequency. We conclude from Lambert's analysis that the rigid frame model is appropriate for use in this study.

3. Rigid Frame Model

In this section the low-intensity theory that is used as a basis and reference for the analysis in Chapter II is presented. This theory is based on the assumptions that (1) the dc flow resistivity can be used directly in the momentum equation and (2) the material structure is rigid. The first to use these assumptions were Kühl and Meyer [45]. By using the flow resistivity σ, their paper (1932) represents a simplification of Rayleigh's more complicated treatment. Other authors [23, 30,32,33,68] have used or rediscovered Kühl and Meyer's approach as a starting place and expanded on it.

Kühl and Meyer used equations equivalent to the linearized continuity equation

$$\delta\rho_{,t} + \frac{\rho_o u_{,x}}{P} = 0 \quad , \tag{I-1}$$

*In the process of making a foamed plastic, thin plastic membrances form between the air cells of the foamed plastic. In a fully reticulated foam the membranes have all been removed.

the linearized momentum equation

$$\frac{\rho_o u_{,t}}{P} + p_{,x} + \frac{\sigma u}{P} = 0 \quad , \tag{I-2}$$

and the equation of state $P=c^2\rho$ to solve for the impedance, attenuation, and phase speed, where u is the acoustic particle velocity in the x direction, p is the acoustic pressure, $\delta\rho$ is the acoustic density, ρ_o is the ambient density, c is the sound speed, P is the porosity, x is the distance, t is the time, and the comma denotes differentiation of the dependent variables with respect to x or t (the independent variables). In their theoretical analysis Kühl and Meyer assumed the compressibility of air in a porous material to be variable. They assumed the adiabatic sound speed $c_o=\sqrt{\gamma P_o/\rho_o}$, where $\gamma=C_P/C_v$ is the ratio of specific heats. They reasoned that the compressibility, and thus the density, of the air could be determined by experiment. In their calculations they used the standard compressibility of air $\rho_o c_o^2$. In Appendix A we assume a constant density ρ_o. We show that, because of heat transfer effects, the speed of sound is a function of both porosity and frequency. Because the relation derived in Appendix A is frequency dependent, we use the isothermal sound speed $b_o = \sqrt{P_o/\rho_o}$.

The above equations may also be combined to obtain a wave equation [23]

$$u_{,xx} - \frac{u_{,tt}}{b_o^2} + \frac{\sigma u_{,t}}{b_o^2 \rho_o} = 0 \quad . \tag{I-3}$$

The use of P as a divisor of u depends upon whether the reference u is in the material or in the open air (no material). Here, as P decreases the particle velocity in the material increases. The importance of using u/P as the effective particle velocity is discussed in Chapter II. Note that although Eq. I-3 seems to be independent of P, the flow resistivity σ is actually a function of P.

To solve Eq. I-3, one can assume that a time harmonic wave

$$u=e^{j(\omega t-\Gamma x)} \quad ,$$

where $\Gamma=\beta-j\alpha$, $\omega=2\pi f$, and $j=\sqrt{-1}$, propagates in a porous material. The wave encounters the attenuation

$$\alpha = \frac{\omega}{\sqrt{2}b_o}\sqrt{-1+\sqrt{1+\left(\frac{\sigma}{\omega\rho_o}\right)^2}} \qquad \text{(I-4)}$$

and the wave number

$$\beta = \frac{\omega}{\sqrt{2}b_o}\sqrt{1+\sqrt{1+\left(\frac{\sigma}{\omega\rho_o}\right)^2}} \quad . \qquad \text{(I-5)}$$

The phase speed $c_{PH}=\omega/\beta$ is

$$c_{PH} = \frac{\sqrt{2}\ b_o}{\sqrt{1+\sqrt{1+\left(\frac{\sigma}{\omega\rho_o}\right)^2}}} \quad . \qquad \text{(I-6)}$$

Plots of attenuation and of phase speed versus frequency for several commonly found resistivity values are shown in Figs. I-1 and I-2,

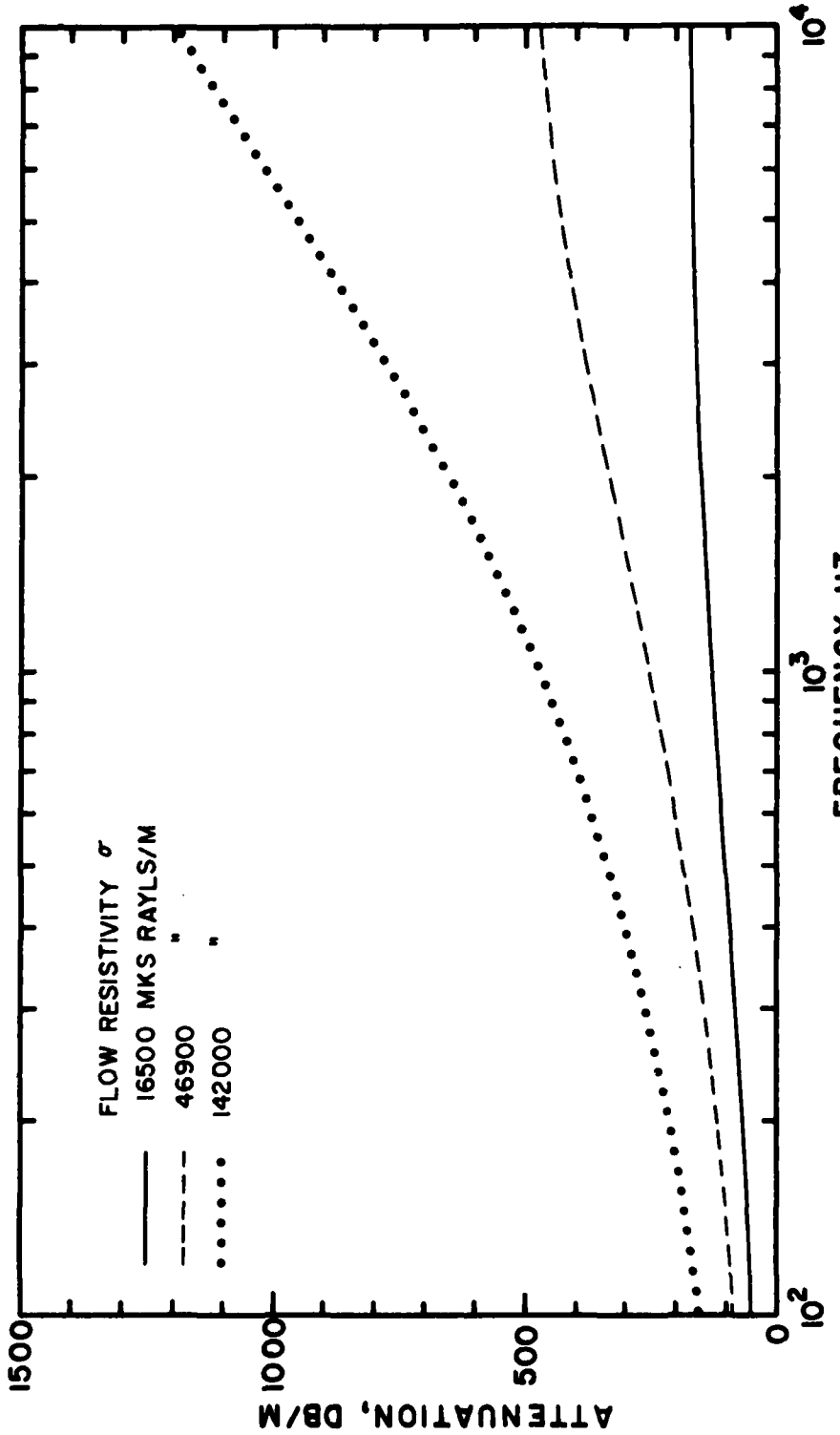

FIGURE I-1
ATTENUATION VERSUS FREQUENCY FOR THREE FLOW RESISTIVITIES OF A POROUS MATERIAL.

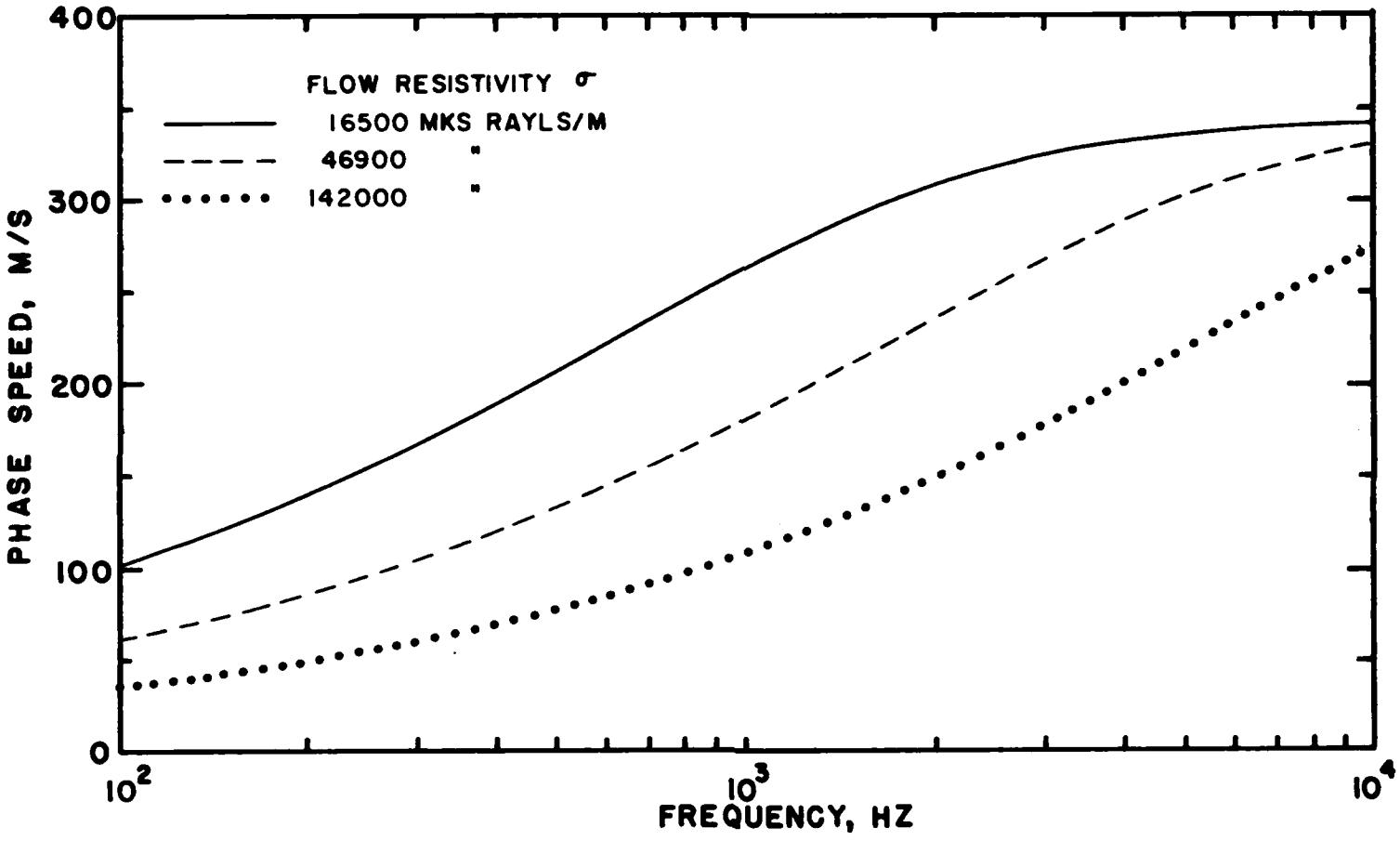

FIGURE I-2
PHASE SPEED VERSUS FREQUENCY FOR THREE FLOW RESISTIVITIES OF A POROUS MATERIAL.

respectively. Both the attenuation and phase speed can change dramatically over a relatively small frequency range. These changes are important in the propagation of intense sound in porous materials. In porous materials intense sounds do not behave in the same manner as in open air, which has a low, uniformly varying attenuation ($\alpha \propto \omega^2$) and only minor (usually negligible) dispersion.

Kühl and Meyer showed that the specific acoustic impedance internal to an essentially semi-infinite ($\alpha L >> 1$, where L is the sample length) porous material is

$$W = W_R + jW_I \tag{I-7}$$

where the resistive part is

$$W_R = \frac{\rho_o b_o}{\sqrt{2}P} \sqrt{1 + \sqrt{1 + \left(\frac{\sigma}{\omega \rho_o}\right)^2}} \tag{I-8}$$

and the reactive part is

$$W_I = -\frac{\rho_o b_o}{\sqrt{2}P} \sqrt{-1 + \sqrt{1 + \left(\frac{\sigma}{\omega \rho_o}\right)^2}} \; . \tag{I-9}$$

We see that Eqs. I-4 and I-5 are of equivalent forms to Eqs. I-9 and I-8, respectively. We conclude that, for the small signal case, measuring the impedance when $\alpha L >> 1$ is equivalent to measuring α and β. This comparison proves to be a good check on both the theory and data.

The real and imaginary parts of the impedance are plotted versus frequency for three flow resistivities in Fig. I-3.

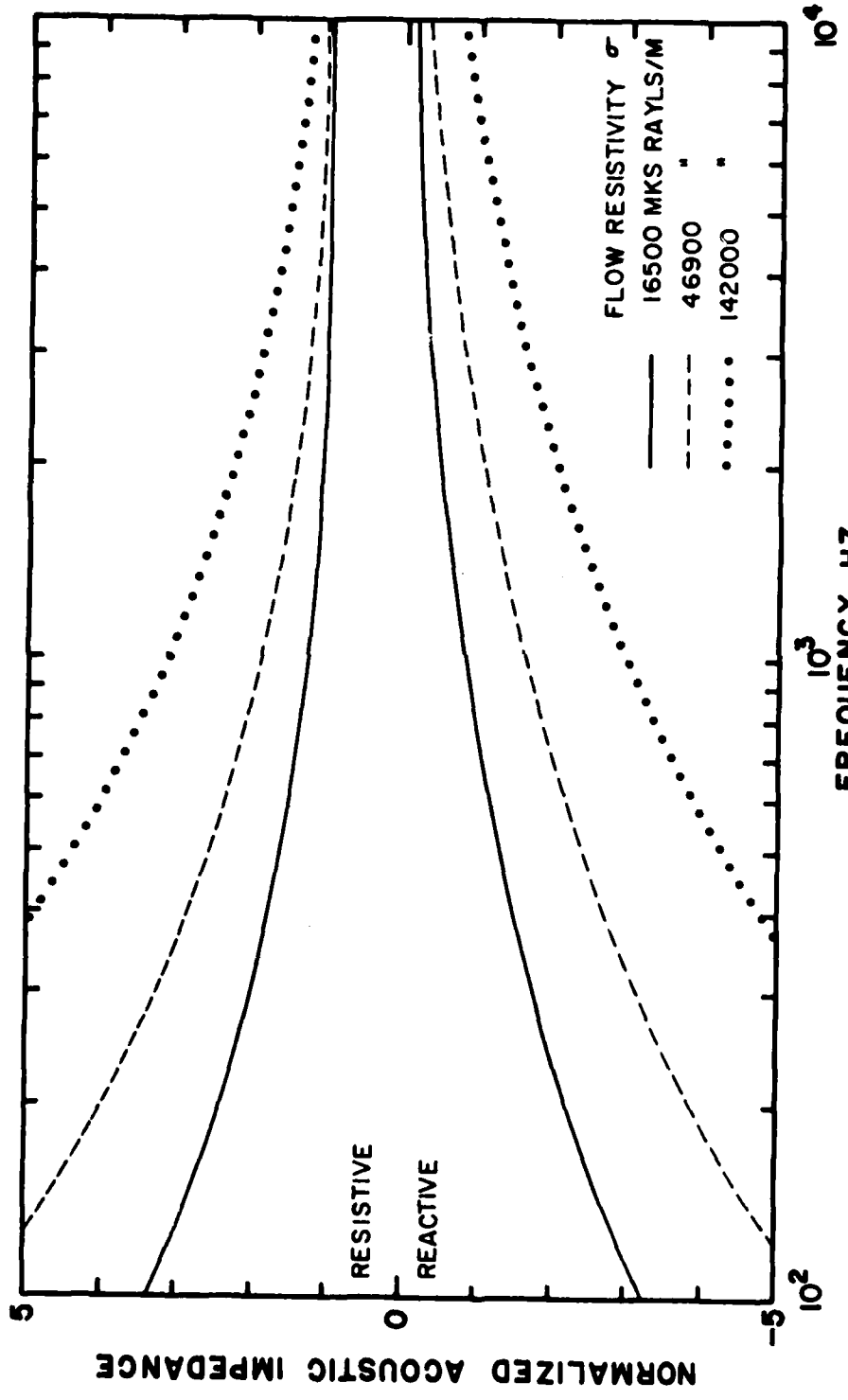

FIGURE I-3
ACOUSTIC IMPEDANCE VERSUS FREQUENCY FOR THREE FLOW RESISTIVITIES OF A POROUS MATERIAL.

The general propagation parameter Γ and impedance W equations are related to each other by [49,88]

$$W(L) = (W_R + jW_I) \coth(\alpha + j\beta)L \quad . \tag{I-10}$$

Equation I-10 is for finite length ($\alpha L < 1$) materials mounted on a hard surface. Equation I-10 is appropriate for most low-intensity impedance measurements and is used in the analysis presented in Chapter IV.

When a sound wave traveling in air encounters a porous material some of the energy of the incident wave is reflected from the material surface and some is transmitted into the material. The impedance difference between the air $\rho_o c_o$ and the material $W(L)$ causes the separation of the incident wave into two parts. The ratio of the transmitted (absorbed) energy to the incident energy is the absorption coefficient.

$$a_n = 1 - \left| \frac{W(L) - \rho_o c_o}{W(L) + \rho_o c_o} \right|^2 \tag{I-11}$$

As the transmitted wave travels in the material it is attenuated (Eq. I-4) by the action of viscous effects. In the present study the term absorption is used to describe a reflection/transmission process, whereas, the term attenuation is used to describe the decay of a traveling sound wave. Absorption coefficients ($\alpha L >> 1$) are plotted versus frequency for three flow resistivities in Fig. I-4.

In Figs. I-1 through I-4 we find that the value of the flow resistivity affects the acoustical properties of porous materials. Thus, the importance of determining flow resistivity cannot be overstated. The

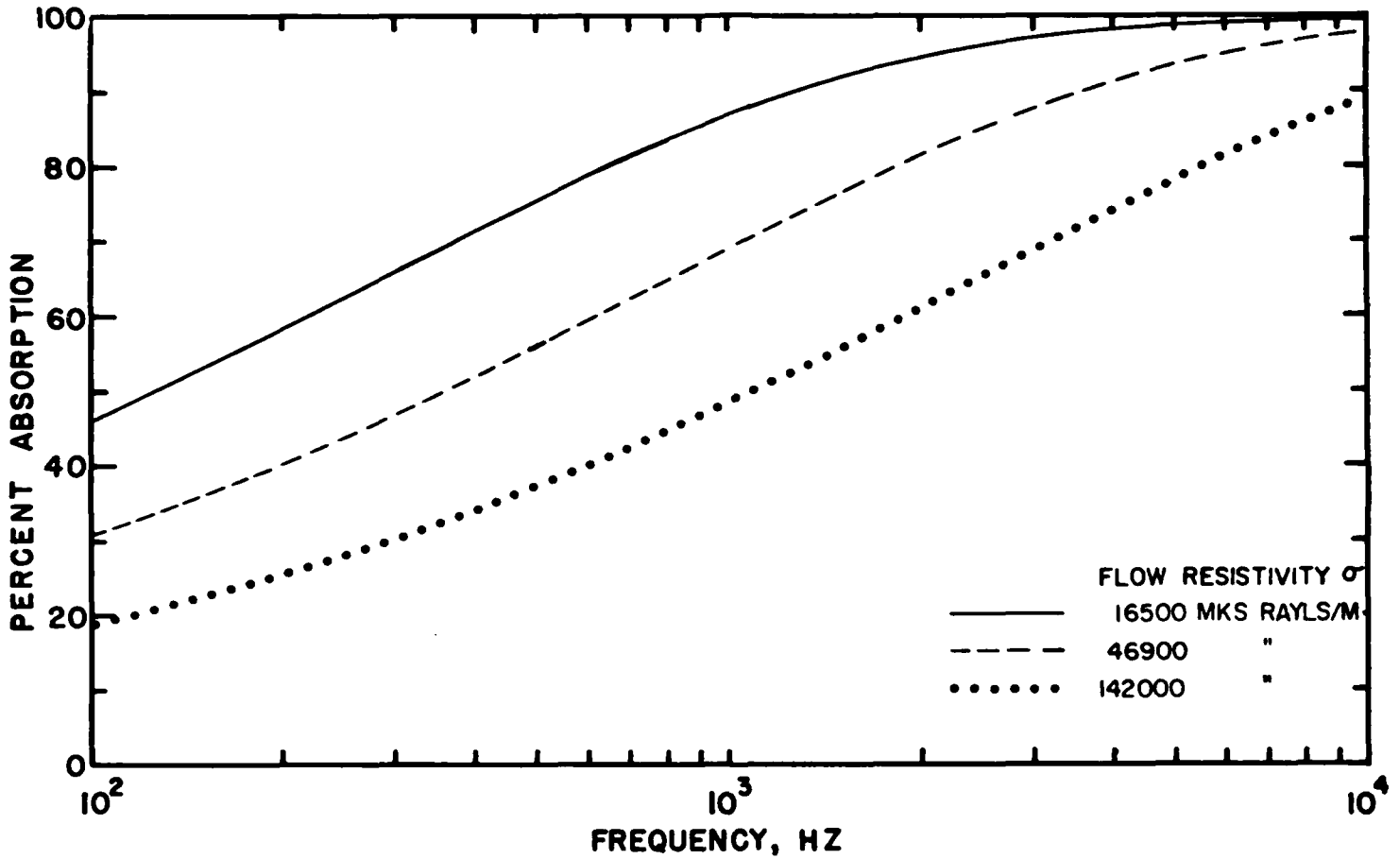

FIGURE I-4
ABSORPTION COEFFICIENT VERSUS FREQUENCY FOR THREE FLOW RESISTIVITIES OF A POROUS MATERIAL.

flow resistivity σ depends on the material structure. Flow resistivity may be determined either through acoustical testing or through dc (steady state) flow resistance testing. Both methods are used in the present study. At this time, there are no theoretical relations that can be used to predict σ. Several empirical relations [24,33,34,60,78] have been formulated to predict the flow resistivity of fibrous materials. Only two relations [33,34] will be discussed in the present study.

By using hydrodynamic analysis, Hersh and Walker [35] determined a relation between viscosity, porosity, fiber diameter d, and flow resistivity inside a fibrous porous material with flow perpendicular to the fibers,

$$\sigma = \frac{\mu \left[1+g\sqrt{\frac{\pi}{4(1-P)}} \right]}{d^2 g \left[\frac{\pi}{4(1-P)} \right]^{3/2}} \quad , \tag{I-12}$$

where g is an empirical constant. Equation I-12 is used in Chapter IV to calculate the dc flow resistivity for unmeasured values of σ. Hersh and Walker determined g=0.059 for batted Kevlar 29. They compared data and theory at low frequencies.

For their data-theory comparisons Hersh and Walker derived a low frequency approximation to Eq. I-3 by ignoring the $u_{,tt}$ term. For a sinusoidal wave they found that the attenuation α and wave number β were equal to

$$\alpha=\beta=\sqrt{\frac{\omega\sigma}{2b_o^2\rho_o}} \quad . \tag{I-13}$$

For porosities in the range of $0.9<P<0.97$, the low frequency approximation is valid for $f<2$ kHz. For a full frequency range prediction the constant g must be redefined.

Hersh and Walker [33] showed that σ is related to d, μ, and P by

$$\sigma = \frac{\mu}{d^2} h(P) \quad , \tag{I-14}$$

where h(P) is a structurally dependent function of P. For their specific case the relationship is given by Eq. I-12. In dimensionless quantities Eq. I-14 is

$$\sigma_1 = \frac{\mu}{\rho_o \omega d^2} h(P) = h(P)/Re \quad , \tag{I-15}$$

where Re is an acoustic Reynolds number [5,33]. The value of the acoustic Reynolds number is important in our analysis. When $Re>>1$ the acoustic boundary layer is small relative to the fiber size, viscous effects are unimportant, and Eq. I-12 is not valid. When $Re<<1$ the boundary layer is large, viscous effects are important, and Eq. I-12 is valid. For the materials and frequency range used in the present study, $10^{-3} \leq Re \leq 23$. Most of the experiments were done such that $Re<1$.

Flow resistance data for many different porous materials have been presented in several studies. Nichols [60] dealt solely with the linear flow resistance of fibrous porous materials. He also determined an empirical relation for fibrous materials. Brown and Bolt [19] presented data on both linearly and nonlinearly behaving materials and were the first to plot flow resistance data versus particle velocity on a log-log plot. Plotting the data in this manner illustrates the relative

nonlinearity of the dc flow resistivity (see Chapter IV). Bies and Hansen [12] present linear flow resistance data for many porous materials.

Only viscous effects are considered in the above theory. The frequency dependent effects of heat transfer on the compressibility of the gas in the porous material are ignored. Heat transfer effects cause the compressibility of the air to be neither adiabatic nor isothermal and, for comparison with data and for simplicity in the calculations, the limiting values of the adiabatic and isothermal sound speeds are each used in the low-intensity sound calculations. In the high-intensity sound calculations, because of increased heat conduction, only the isothermal sound speed is used. The theory that has been summarized up to this point will be used as a basis for comparison between the first order theory developed in Chapter II and the small signal experiment results presented in Chapter IV.

In 1980 Hersh and Walker [33] extended their 1979 theory [34] to include heat transfer effects. They used results of experiments on dc flow through fiber bundles to determine relations to fit equations for heat transfer and viscosity effects. They obtained a one-dimensional wave equation that combines both heat transfer and viscosity effects. There are three empirical constants to fit to the data; one constant deals with heat transfer and two constants deal with viscosity. The values of the viscosity constants depend on whether the sound travels perpendicularly or axially with respect to the fiber orientation. The wave equation is

$$P_{,xx} - j\gamma\left(\frac{\omega}{c_o}\right)^2\left[\frac{\frac{K}{\rho_o\omega} + j}{\frac{K}{\rho_o\omega} + j\gamma}\right]\left(\frac{\sigma_H}{\rho_o\omega}+j\right)P = 0 \quad , \tag{I-16}$$

where K is a heat transfer parameter and σ_H is a viscous drag parameter; both parameters are functions of the porosity, fiber size, and their respective fitted constants. The viscous drag parameter presented by Hersh and Walker [34] is

$$\sigma_H = -\frac{4\mu(1-P)}{d^2}\left[V_n D_n + V_p D_p\right], \tag{I-17}$$

where

$$D_n \approx 16\sqrt{1-P}\left[1 + 14.75(1-P)^3\right] , \tag{I-18a}$$

$$D_p \approx 3.94(1-P)^{0.413}\left[1 + 27(1-P)^3\right] , \tag{I-18b}$$

where V_n and V_p are the empirical constants and the subscripts denote flow parallel (p) to the fibers and flow normal (n) to the fibers. Hersh and Walker fit Eq. I-18a to dc flow resistance data taken on many different materials by Davies [24]. Davies found very little scatter of measured data from his own theoretical predictions. Hersh and Walker fit Eq. I-18b to dc flow resistance data taken on a variety of compact bundles of parallel fibers by Sullivan [78]. Sullivan also found little deviation of measured data from his own theoretical predictions. Even though Davies and Sullivan found little scattering in their data, the data fitting constants V_n and V_p in Eq. I-17 should be determined for each material to be used. It appears that, since there are two constants,

the equation may be used for a material made of randomly oriented fibers [34]. As shown by Hersh and Walker and in Chapter IV, the definition of σ_H can be used to define the flow resistivity without including heat transfer effects.

The heat transfer parameter presented by Hersh and Walker is

$$K = \frac{21.6\gamma\mu(1 - P)^{3/2}[1 + 3.94(1 - P)^3]}{Prd^2PT_n} , \qquad (I\text{-}19)$$

where $Pr=\mu C_p/\kappa$ is the Prandtl number, κ is the thermal conductivity of the medium, and T_n is an empirical constant. The basis for this equation was taken from work done by Masliyah [55] on dc energy and momentum transfer from cylinders oriented normally to the fluid flow. The heat transfer effects on the sound speed in Eq. I-19 are similar to those determined in Appendix A.

The material Hersh and Walker used in their tests is Kevlar 29. As noted earlier, this material is used in many of the experiments in the present study. In addition, other materials are used in the present study and the test results are discussed in Chapter IV.

4. Lumped Element Model

The last linear theory to be considered here was published by Zarek in 1978 [82]. He considered sound absorption by flexible polyurethane foams. He considered materials with and without an impermeable membrane facing. He approached the theory from a lumped parameter model for the gas and material and used the results to determine a Lagrangian that includes Rayleigh dissipation. He then applied Hamilton's

principle and determined equations of motion for the coupled air-material system. He stated that the parameters only include the small scale effects of the porous medium; all nonlinearities of the air and material are ignored. His theoretical predictions agree well with his experimental results. Zarek also compared his theoretical predictions to some of Beranek's [7] data and found fairly good agreement between the two. Zarek's theory is not useful in the present study because he considered material motion and he ignored all nonlinearities.

The theories discussed in this section all pertain to the acoustical properties of the porous materials at low intensities. Many of the theories include frame motion of the material, but Lambert's analysis shows that, for the present study, the frame motion is negligible. Neglecting the frame motion greatly simplifies the analysis. In Chapter II we use the conservation equations and show which assumptions lead to the rigid frame theory.

C. Nonlinear Theory

This section contains a presentation of two topics. The first topic is a brief review of how an intense sound propagates in a fluid and how absorption and dispersion affect shock formation and attenuation. The second topic is a brief presentation of the theoretical and experimental studies of intense sound reflected from thin porous sheets.

1. Intense Sound in a Fluid

The propagation of an intense sound in a fluid is fairly well understood. The brief theoretical treatment presented here is based on extensive work by others and is presented as background to the nonlinear theory used in Chapter II.

For any point on the waveform the propagation speed will vary as [10]

$$\left.\frac{dx}{dt}\right|_{u=\text{const}} = c + u \quad . \tag{I-20}$$

Equation I-20 adds the effect of convection u to the sound speed

$$c = \sqrt{\left.\frac{dP}{d\rho}\right|_s} \quad , \tag{I-21}$$

where P is the total pressure, s is the entropy, and ρ is the total density. The pressure-density relation is nonlinear, c depends on temperature, and for a simple wave

$$c = c_o + \frac{\gamma-1}{2}u \quad . \tag{I-22}$$

The propagation speed becomes

$$\left.\frac{dx}{dt}\right|_{u=const} = c_o + \beta' u \quad , \tag{I-23}$$

where $\beta'=(\gamma+1)/2$ is the nonlinearity parameter of air. In the small signal case, where $u << c_o$,

$$\left.\frac{dx}{dt}\right|_{u=const} = c_o \quad .$$

In an isothermal situation, such as in a porous material, $\gamma=1$ and $\beta'=1$ and the nonlinearity of the air is reduced. In a porous material the nonlinear effects are more complicated than suggested here.

Since the propagation speed varies with location on the waveform the wave peaks will travel the fastest and the wave troughs the slowest. The thermal and convective effects are cumulative, the waveform distorts as it travels, and, when u is large enough, the compressional phases steepen and form shocks. Distortion of the wave is accomplished by the generation of higher frequency harmonic components. All fluids dissipate energy, the high frequency components are attenuated at a faster rate than the fundamental component, and, thus, dissipation limits the distortion of the waveform. By shifting energy to the higher harmonic components, the fundamental loses energy more rapidly than at low intensities. The increased loss is called excess attenuation and we find that the excess attenuation increases with source intensity. Above a certain source level we find that, no matter how much we increase the

energy input, the excess attenuation limits the measured level to a constant. We call this constant level the saturation level [4,57,76,81]. The farther a measurement point is from the source the lower the saturation level is at that location. Before the dissipative effects are discussed, the progressive distortion of the wave is discussed.

In studying shock formation and dissipation in a lossless fluid, the Fubini solution [16]

$$\frac{u}{u_o} = \sum \frac{2}{n\sigma^*} J_n(n\sigma^*) \sin n(\omega t - kx) \qquad \text{(I-24)}$$

applies to the region before shocks are formed ($\sigma^*<1$) when the boundary condition at x=0 is

$$u(0,t) = u_o \sin \omega t \quad , \qquad \text{(I-25)}$$

where u_o is the initial particle velocity amplitude, $J_n(\cdot)$ is the n^{th} order Bessel function, $\sigma^*=x/\bar{x}$, $\bar{x}=1/\beta'\epsilon k$ is the shock formation distance, $\epsilon=u_o/c_o$, $k=\omega/c_o$, and n denotes the n^{th} harmonic.

In the region ($\sigma^*>3$) where shocks are well formed and have begun to decay, the Fay solution [16]

$$\frac{u}{u_o} = \sum \frac{2/G}{\sinh[n(1+\sigma^*)/G]} \sin n(\omega t - kx) \qquad \text{(I-26)}$$

is applicable, where $G=\beta'\epsilon k/\alpha$, which is sometimes called the Gol'dberg number [10]. In the limit, as $G\to\infty$, Eq. I-26 represents a sawtooth wave. In this limit the ordinary dissipation is small relative to the rate at which energy is pumped into the higher harmonic components and dissipated in the shocks. Blackstock [16] devised a scheme to combine the two

solutions, Eqs. I-21 and I-23 ($G=\infty$), into a third solution such that the whole region from the boundary to infinity may be explored.

Since $G\neq\infty$, a perfect sawtooth wave never forms. The Gol'dberg number indicates the relative importance between distortion and ordinary dissipation. For a very strong wave, such that $\beta'\varepsilon k>>\alpha$, the shock forms quickly, approximating a sawtooth, and takes some distance to dissipate. For weak waves or large viscous dissipation, such that $\beta'\varepsilon k<<\alpha$, a shock wave will not form.

In 1977 Bjørnø [14] compared dissipation effects to nonlinearity effects by using both the Gol'dberg number and the Keck and Beyer [40] perturbation solution of a nonlinear wave equation to study intense sound propagation in a viscous fluid saturated, rigid sediment. Bjørnø experimentally determined the parameter of acoustic nonlinearity in fluid-saturated sediments by using Beyer's analysis [9]. Bjørnø showed in his analysis that the amplitude of the second harmonic component could not exceed 1.3% of the fundamental components because the attenuation effects are much larger than the nonlinearity effects. Bjørnø indicated that, for most high-amplitude sounds, the sound goes directly from finite-amplitude distortion into the "old age" (the waveform is nearly sinusoidal) propagation region. He noted that a shock wave propagating in a sediment decays rapidly and he concluded that the nonlinear effects are negligible in viscous fluid saturated sediments.

Determining the nonlinear behavior of a material is important. If the material behaves very nonlinearly, relative to attenuation, then harmonics are generated very rapidly. In the present study the dc flow

resistivity characteristics are used to define both the viscous dissipation and nonlinear properties of the material. Carman [21] stated that for dc gas flow through porous materials the transition to nonlinear behavior is related to the onset of turbulence and the modified Reynolds number

$$R_m = \frac{u}{\nu S} \quad , \tag{I-27}$$

where ν is the kinematic viscosity and $S=4(1-P)/d$ is the surface area/unit volume. Carman stated that when $R_m \geq 1$ the flow resistivity behaves nonlinearly, i.e., the flow resistivity depends on the particle velocity. Later in this study we find that the manner in which the nonlinearity is caused, i.e., turbulence, may be important to how an intense sinusoid loses energy. We find that the complexities of excess attenuation of a sinusoid are not as easily defined in a porous material as in an open fluid. In addition, how the nonlinearity is defined and used becomes extremely important to how well the effects of nonlinearity are predicted.

Blackstock [17] presented a perturbation solution for a Burgers equation governing the propagation of sound in an absorbing, dispersive fluid. He showed that the dispersive characteristic affects the level of the generated second harmonic component. This effect has importance in a porous material. Equation I-7 shows that porous materials are very dispersive. The harmonic components of intense sounds generated in a porous material may be greatly affected by the dispersion because energy added to the components will be added out of phase with the energy already present.

Zorumski [84] presented conservation equations for thin sheets of porous materials with nonlinear dc flow resistance. He used these equations to determine the scattering of sound from porous elliptic cylinders. He did not attempt to solve the conservation equations for the propagation of intense sound in a bulk porous material. His results are described in the next section.

In this section a very brief review on intense sound propagation through lossless and dissipative fluids has been presented. These ideas are useful in the analysis and comparisons made in Chapter IV.

2. Reflection of Intense Sound

For all practical purposes, a sound propagating in a porous material must first enter the material from an adjacent medium. A wave incident on the surface of a bulk material is reflected from as well as transmitted into the material. In order for us to understand the losses associated with the transition from one medium to another, we must determine the impedance of the material. Most materials are acoustically finite ($\alpha L<1$) and, as shown in Eq. I-10, the impedance, the propagation parameters, and the material termination impedance (at $x=L$) all influence the measured impedance. At high intensities the analysis becomes difficult because both the impedance and propagation parameters depend on intensity. We have just seen that as an intense wave propagates, energy is transferred to the higher harmonic components. The harmonic components interact with each other and superposition is no longer valid. When an intense wave is used to measure reflection (or absorption) properties of a porous material, the sound level, instead of just frequency, must

also be specified. Since superposition is not valid, the incident and reflected waves may influence each other. For short interaction regions this influence may be small. For large interaction regions, such as in long pulse trains or standing waves, the mutual influence must be accounted for.

This section contains a review of past studies of the reflection of intense sound from different surfaces and the determination of the impedance of sheets of porous materials. Both theoretical and experimental studies are examined.

In 1960 Blackstock [15] showed that intense sounds reflected from surfaces do not always follow the commonly used small signal laws. Blackstock considered a pressure release surface, an infinite impedance surface (a hard wall), and a thin resistive sheet. Regardless of intensity, reflections from a pressure release surface are accompanied by a doubling of the particle velocity at the interface. In addition, Blackstock found that at a hard wall the variational sound speed c is the variable that doubles throughout the intensity range. The pressure doubling law for reflection from a hard wall is only an approximation. However, at a sound pressure level of 174 dB re/20 μPa the deviation from pressure doubling is only 6%. Above 174 dB pressure amplification at the wall increases and a more exact relation must be used.

In the case that most interests us here, the thin resistive sheet, Blackstock found a relation for the pressure reflection coefficient

$$\frac{P_r}{P_i} = R = \frac{1 + \frac{r(z)}{\rho_o c_o} + \frac{\gamma+1}{4\gamma}\left[1-\gamma\left(1+\frac{r(z)}{\rho_o c_o}\right)^2\right]\varepsilon\sin\omega\phi}{1+\frac{r(z)}{2\rho_o c_o}+\frac{\gamma+1}{8\gamma}\left[1-\gamma\left(1+\frac{r(z)}{\rho_o c_o}\right)^2\right]\varepsilon\sin\omega\phi} - 1 \quad , \qquad \text{(I-28)}$$

where P_r is the reflected pressure, P_i is the incident pressure, $r(z)=Re(z)-\rho_o c_o$, z is the specific normal acoustic impedance, $Im(z)=0$, $\varepsilon=u_o/c_o$ is the acoustic Mach number of the initial wave, and ϕ is a specific location on the wave that is followed through the course of travel of the wave.

Unfortunately, porous materials do not meet the condition that $Im(z)=0$. However, the case of purely resistive porous materials is instructive. From the analysis results the acoustical characteristics of the real material may be inferred. Equation I-28 may be used to follow only one point on the waveform at a time. If the first peak of the sine wave (compression) is followed as it leaves the piston, $\sin\omega\phi=1.0$. In terms of the real part of the acoustic impedance, the absorption coefficient is

$$a_n = 1 - |R|^2 = 1 - \left| 1 - \frac{\frac{2Re(z)}{\rho_o c_o} + \frac{\gamma+1}{2\gamma}\left[1-\gamma\left(\frac{Re(z)}{\rho_o c_o}\right)^2\right]\varepsilon}{1+\frac{Re(z)}{\rho_o c_o}+\frac{\gamma+1}{4\gamma}\left[1-\gamma\left(\frac{Re(z)}{\rho_o c_o}\right)^2\right]\varepsilon} \right|^2 . \qquad \text{(I-29)}$$

Equation I-29 can be used to calculate the absorption coefficient that the peak of an initially sinusoidal wave encounters.

If the minimum of the sine wave (rarefaction) is followed as it leaves the piston, $\sin\omega\phi=-1.0$ and the signs of the two ε terms in Eq. I-29 become negative. This change of sign indicates that the phase of the wave is important to reflection from purely resistive porous materials. This statement of phase dependence should hold for any porous material. For example, when $Re(z)/\rho_o c_o=3.0$ and $\varepsilon=0.02$ (160 dB re/20 μPa) $a_n=0.763$ for $\sin\phi=1.0$ and $a_n=0.738$ for $\sin\phi=-1.0$. The difference increases with increases in $Re(z)$ and ε.

In the above analysis $Re(z)$ is arbitrary and may be a function of the particle velocity. If the impedance is a function of the particle velocity and $Im(z)\neq 0$, then a_n changes more dramatically than indicated by Eq. I-29, because both $Re(z)$ and $Im(z)$ affect the value of a_n.

Zorumski and Parrot [83,86] and Zorumski [84,85] are the only researchers to present a combined theoretical-experimental analysis of thin nonlinearly behaving porous materials. The most general presentation is in Ref. 86. The mathematical and computational details are in Refs. 84 and 85, respectively. We summarize their general theory, experiments, and results below.

In this theory Zorumski and Parrot present generalized, functional relations for the conservation of mass and momentum. They assume the material is thin enough that $\lambda >> L$, where λ is the wavelength, and that the velocity differential across the sample is negligible. They also assume negligible compressibility in the material. Thus, the conservation of mass equation does not enter into their analysis. Their analysis is based on use of the momentum equation. They assume that the

particle velocity dependent dc flow resistance can be used to describe the acoustic flow resistivity $R[V(t)]$, where $V(t)$ is the acoustic particle velocity. In addition, they assume the acoustic reactance $X[V(t)]$ is a function of particle velocity. From their version of the momentum equation they obtain a temporal impedance operator Z_t such that

$$Z_t V(t) = \left\{ R[V(t)] + X[V(t)] \frac{\partial}{\partial t} \right\} V(t) \quad . \tag{I-30}$$

The temporal impedance operator is evaluated from their experimental data. They claim the theory can be used to evaluate the impedance encountered by any distorted waveform. Their analysis is done for distorted sinusoids. As discussed below, if there is no nonlinear interaction between the harmonic components nor between the incident and reflected waves, then their claim appears to be valid.

We now discuss Zorumski and Parrot's [83,86] experimental investigation. They used a standing wave tube with a microphone flush mounted with the surface of the rigid termination of the tube. They placed the material at one-fourth wavelength from the rigid termination. A second microphone was placed outside the material surface that was away from the termination. Tests were done at 0.5, 1.0, 1.25, 2.0, and 4.0 kHz and at sound levels from 120 to 160 dB. They noted, that, because of the material and second microphone placement, all even harmonic components of the fundamental were ignored in the experiment and, thus, in the theory. Ignoring the even harmonic components might lead to problems because the components may interact with the waves everywhere

except for in the material. As seen in Eq. I-24 harmonic component generation from a sinusoid starts by generating all harmonics, and, mainly, the second harmonic. If all the even harmonics are ignored, then much of the energy lost by the fundamental is being ignored and measurement error is being introduced.

Zorumski and Parrot presented several interesting results. First, they showed that the acoustic flow resistivity is independent of frequency and closely approximates the dc flow resistance at all particle velocities. Second, they showed the acoustic reactance to be a function of both frequency and particle velocity. The theoretical-experimental results are found to be consistent and in fairly good agreement over large frequency and sound level ranges.

The above analyses presented by Blackstock and Zorumski and Parrot show that the analytical and experimental determination of nonlinear porous material impedance is extremely complex. This complexity has led many researchers to experimentally determine the impedance and absorption of various materials. Shock tube experiment results [27,35, 79] will not be discussed.

In 1970 Powell and Van Houten [64] used band-limited tone bursts at frequencies between 500 Hz and 10 kHz to study the absorption properties of porous material covered resonators. They measured the incident and reflected peak pressures at a single microphone position and discussed design considerations for the test procedures. The evaluation of their results is difficult because the exact length and diameter of their wave tube, or tubes, was not specified. It appears that the tube

length could have been greater than the shock formation distance at high frequencies and sound levels. They discuss design criteria for the optimum tube lengths and diameters, but do not state how, or if, the criteria were implemented. They analyze the waveform and spectral content of what appears to be their input waveform to the acoustic driver. They never indicate what the incident and reflected acoustic waveforms look like. They did not indicate whether they saw shock formation or if the acoustic waveform was distorted by the reflecting surface. The tube length is important because at high intensity, if the tube length is too long, then the measured absorption coefficient would be incorrect. Measurement of the absorption coefficient depends on the attenuation of the traveling wave being constant with sound level change. A wave traveling in a tube longer than the shock formation distance $\bar{x}$ experiences different attenuations. The attenuation depends on where the wave is with respect to $\bar{x}$. Before the wave reaches $\bar{x}$, the shock is forming and the attenuation of the fundamental component is greater than tube wall attenuation. After $\bar{x}$, the attenuation increases and then, when $x>4\bar{x}$, asymptotically approaches tube wall attenuation [16]. Some nonlinear attenuation effects can be accounted for in the calibration measurements, but, as indicated above, the error can grow rapidly and a short tube is necessary.

In 1973 Melling [55] experimentally and theoretically determined the impedance of perforated plates and perforated plate resonators at low and high intensities. He showed how both the real and imaginary parts of the impedance change with the intensity. He designed a high

intensity standing wave impedance tube which has a frequency range of 300 to 3250 Hz and upper sound pressure limits of 144 to 159 dB [56]. The system is large and also requires large transducers to generate the required steady state sound levels. Melling's program is well thought out and could be useful for evaluating bulk porous absorber characteristics. Unfortunately, the cost of building a system of this type is large and this type system was not used in the present study.

In 1980 Nakamura et al. [58] described the absorption of a small-signal, plane N wave by finite length porous materials. They showed that the individual Fourier components of the N wave interact individually with the porous material. If the material is long enough, one can determine W_R and W_I and, if it is short enough ($\alpha L<1$), one can determine α and β.

In a later paper Nakamura et al. [59] described the reflection of a plane N wave from the end of an open pipe. They showed, as in their earlier paper, that the low level impedance is predicted by low level N wave tests, but the high intensity N wave reflections are drastically modified as the amplitude increases. They stated that their results show the total reflected energy between zero and 10 kHz to be approximately invariant with respect to the N wave amplitude. In this latter paper, they used a much different system in the measurement of impedance. The large amplitude N wave does not propagate in a linear fashion and the frequency components interact. They used an algorithm similar to the algorithm developed by Pestorius [62] to mathematically propagate the measured incident wave to the pipe termination. They

modified Pestorius' algorithm to mathematically propagate the measured reflected wave backward from the microphone to the pipe termination. After they mathematically propagated both waves to the end of the pipe, they subtracted the Fourier transform of the reflected waveform from the Fourier transform of the incident waveform. They used the results of this subtraction to calculate the pressure reflection coefficient and the energy reflection coefficient of the open pipe. This method works because the reflected wave is inverted with respect to the incident wave and much of the high frequency energy of the incident wave is lost out the end of the pipe so that no shock exists in the reflected wave. In fact, by the time the reflected wave reaches the microphone, the wave does not develop a shock.

If a porous material was placed in the system of Nakamura et al. [59], the reflected wave would (usually) not invert. A shock could reform in the reflected wave and the above method could not be used. Once a shock has formed in a wave the process cannot be mathematically reversed to obtain the original waveform because information has been irretrievably lost in the shock formation process. The method devised by Nakamura et al. is limited because it may not be useful above certain sound levels and requires a computer for the calculations. For these reasons a more useful method was sought.

In 1981 Kuntz et al. [47] described a simple impedance measurement method. This method is described in detail in Chapter III of this study and experimental data is presented in Chapter IV.

In this section several test methods and theoretical descriptions that show the change of impedance with intensity have been discussed. The advantages and disadvantages of the different methods have been discussed and serve as background information for the measurement methods described in Chapter III.

D. Summary

Several diverse topics have been considered in this chapter. In spite of their diversity, the topics are the basis for understanding the theory and results that follow in the remainder of this study. Many theories have been developed to explain low-intensity sound propagation in porous materials. In this study, because of the complexity of the nonlinear acoustics analysis, only the simplest approach is used, that of using the dc flow resistivity to define the viscous effects in a rigid porous material [30,32,33,45,68]. The more complicated approaches that include heat transfer and material motion [8,11,34,49,67, 88] could, conceivably, be used, but the mathematical complications are prohibitive. In most cases, the simple approach is seen to result in adequate prediction of the acoustical properties.

From the nonlinear acoustic theory for fluids we have shown that, because of the high dissipation in a porous material, shock waves will probably not be formed in an intense sound wave. Perturbation of the conservation equations is used in Chapter II to describe the propagation of intense waves in bulk porous materials.

Propagation of a wave in the material is not the only aspect of sound interaction to be considered. The wave must enter the material and, consequently, a wave incident on the surface of a bulk porous material is reflected from as well as transmitted into the material. The mathematical prediction of the impedance that an incident, high-intensity sound wave encounters at the surface of a bulk porous material is not a trivial task. In fact, the task has never been accomplished. In this

study only a simple mathematical approximation to the impedance will be made.

Because superposition is invalid for intense sound, the measurement of the impedance of a bulk porous material exposed to an intense sound is also not trivial. Many measurement methods have been developed to measure the impedance of both bulk and sheet materials. These methods all show that the acoustic impedance and absorption coefficient of a porous material depend on the amplitude and frequency content of the incident sound wave. Another measurement method is presented and used here because it appears to circumvent some of the prolems that the other methods do not address.

II. THEORY AND MODELING

In Chapter I various theories for sound propagation in acoustic materials were described. The rationale for modeling porous materials as rigid materials was presented as a reasonable assumption.

In Sections A through C of this chapter the mass, momentum, and energy conservation equations are derived for porous materials. The model is limited to rigid, isotropic, nonlinear, air saturated, bulk porous materials.

In Section D perturbation is used to determine approximate solutions to the conservation equations. These solutions are used in an attempt to predict the manner in which intense sound propagates through a porous material. Because the measured boundary conditions are not ideal, an approximate boundary condition is considered. The boundary radiates both the first and second harmonic components into the material. The two components can be set to arbitrary amplitudes and relative phase. A second-order approximation is determined. In Chapter IV the solution is compared to the data.

In addition to sound propagation in the porous material, the characteristic impedance of the material is important. In Chapter I we found this problem to be extremely complicated at high intensities. In Section E an approximation to the impedance relations is made to determine a useful intensity dependent impedance relation. The results only apply to sinusoidal waves normally incident on the surface of a semi-infinite porous material.

In Section F the approximation of Section E is extended to illustrate nonlinear propagation of the fundamental component. In addition, another model is proposed to illustrate the effects of saturation and excess attenuation on the fundamental component.

In Section G a short summary of the chapter is presented. In Chapter IV the various models are compared to the data.

A. Continuity Equation Derivation

The physical concept of how a fluid flows through a porous material is necessary for us to understand how the flow is distorted and impeded by the material. The continuity equation derivation is presented in simple physical arguments so that we may take certain assumptions for granted in future derivations.

A simplified cross section drawing of a bulk porous material control volume is shown in Fig. II-1. The structure is made of many parallel fibers. The control volume is fixed to the rigid structure. If no structure is present, the particle velocity is represented by u. When the fluid enters the porous material the velocity is increased by a factor of the porosity P. The porosity is the volume of the air in the control volume relative to the total volume (including fibers) of the control volume. We assume the material to be homogeneous and the porosity constant in each derivation.

For the derivations we need to know the relation between porosity and the cross sectional area a fluid encounters in a material. In Fig. II-1 a single "cell" has been drawn such that the four sides each bisect two fibers. Thus, a quarter of each fiber is enclosed by the cell. Assume each cell to be of length L along the fibers. The porosity of the cell is

$$P = 1 - \frac{\pi d^2}{4DHL} \quad , \tag{II-1}$$

where D and H are defined in Fig. II-1.

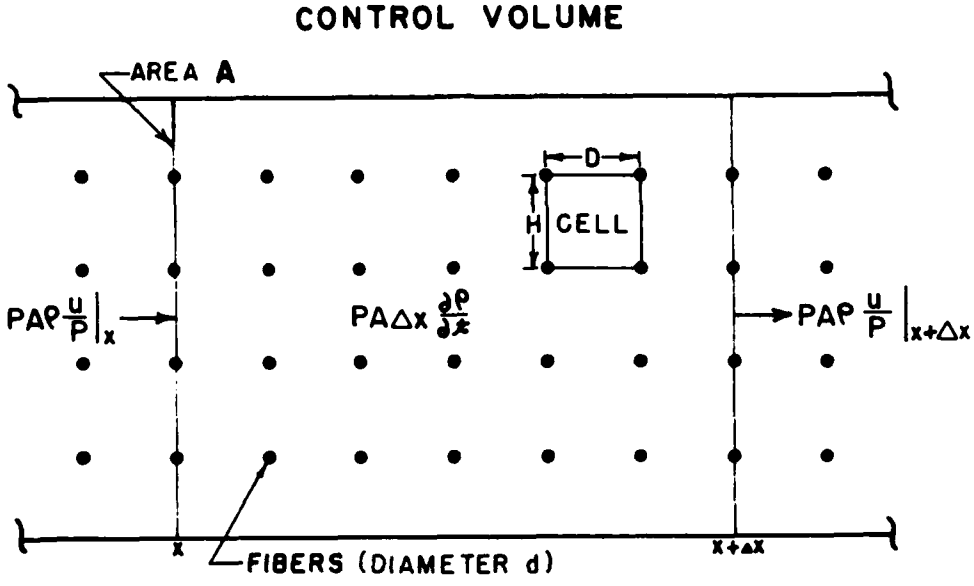

RELATIVE TO THE CONTROL VOLUME THE FIBERS ARE STATIONARY.

FIGURE II-1
STATIONARY CONTROL VOLUME USED IN THE DETERMINATION OF THE CONSERVATION OF MASS RELATION FOR POROUS MATERIALS.

A gas flowing through the material will not have a constant speed. Thus, the average open area encountered by the gas flow may not be evaluated at any point in the medium. The open area, as a function of x, is integrated along the length D of the cell. In doing the integration we find the same relation for the area as for the porosity, Eq. II-1. We define the average open area to be

$$A_p = PA \quad , \tag{II-2}$$

where A is the cross sectional area of the control volume.

A physical statement of the continuity equation is that

the mass flux across the control volume surface	=	the time rate of change of mass in the control volume.

For the one-dimensional system shown in Fig. II-1, the continuity equation is

$$\rho \frac{u}{P} PA\Big|_x - \rho \frac{u}{P} PA\Big|_{x+\Delta x} = \frac{\partial \rho}{\partial t} PA\Delta x \quad , \tag{II-3}$$

where ρ is the total density, x is the position, Δx is the control volume length, and t is the time. A differential form of Eq. II-3 is found by dividing Eq. II-3 by $PA\Delta x$ and taking the limit as Δx goes to zero. Since both A and P are constant, the continuity equation becomes

$$\frac{1}{P} \frac{\partial (\rho u)}{\partial x} + \frac{\partial \rho}{\partial t} = 0 \quad . \tag{II-4}$$

Equation II-4 is used to describe one-dimensional mass flow in a porous material and is one of the three conservation equations used in Section D. Except for the porosity term P, Eq. II-4 is the usual continuity equation for fluids. In all future derivations u and P are combined as u/P because a change in porosity only modifies the particle velocity in Eq. II-4.

B. Momentum Equation Derivation

In the following momentum equation derivation a one-dimensional model is assumed. As discussed in Section II-A, the porosity is included with the particle velocity.

The forces on the control volume fluid are illustrated in Fig. II-2. The conservation of momentum states that

the time rate of change of momentum inside the control volume	=	the sum of external forces in the x-direction (pressure and drag)	+	x-momentum inflow through the two end surfaces .

For the one-dimensional system shown in Fig. II-2, the momentum equation is

$$\frac{A}{P}\frac{\partial \rho u}{\partial t}\Delta x = PA\Big|_x - PA\Big|_{x+\Delta x} - FA\Delta x + \rho\frac{u^2}{P^2}A\Big|_x - \rho\frac{u^2}{P^2}A\Big|_{x+\Delta x}, \qquad \text{(II-5)}$$

where P is the total pressure and F is the drag force/unit volume. Dividing Eq. II-5 by $A\Delta x$ and taking the limit as $\Delta x \to 0$ yields

$$\frac{1}{P}(\rho u)_{,t} = -P_{,x} - \frac{1}{P^2}(\rho u^2)_{,x} - F \quad . \qquad \text{(II-6)}$$

Rewrite Eq. II-6 as

$$\frac{1}{P}\left[\underline{\rho_{,t}u} + \rho u_{,t}\right] = -P_{,x} - \frac{1}{P^2}\left[\underline{\rho_{,x}u^2} + \underline{\rho u u_{,x}} + \rho u u_{,x}\right] - F \quad , \qquad \text{(II-7)}$$

where, from Eq. II-4, the underlined terms equal zero. The x-direction momentum equation becomes

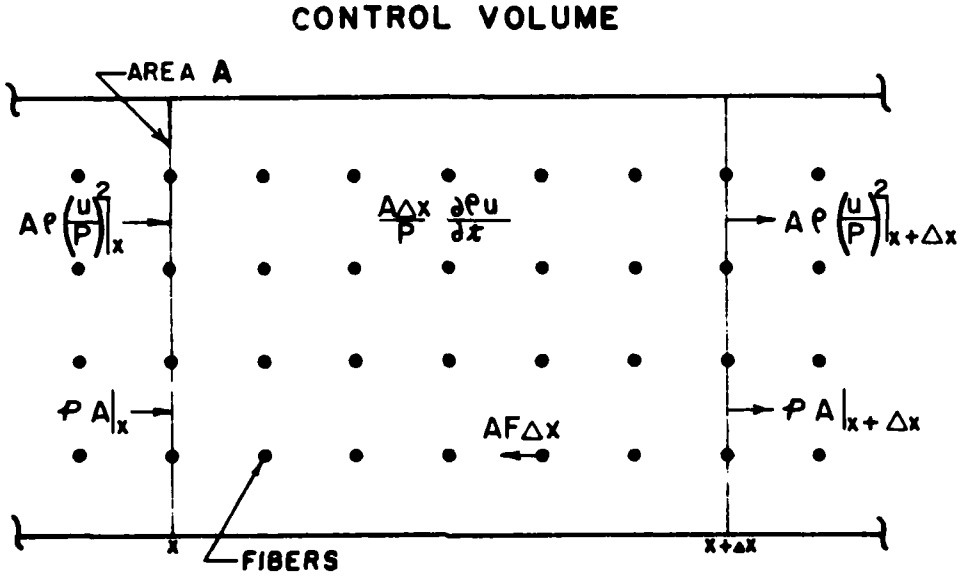

RELATIVE TO THE CONTROL VOLUME THE FIBERS ARE STATIONARY.

FIGURE II-2
STATIONARY CONTROL VOLUME USED IN THE DETERMINATION OF THE CONSERVATION OF MOMENTUM RELATION FOR POROUS MATERIALS.

$$\frac{\rho u_{,t}}{P} + \frac{\rho uu_{,x}}{P^2} + P_{,x} = -F \quad . \tag{II-8}$$

Except for the P and F terms, Eq. II-8 is the momentum equation for inviscid flow in an open fluid.

The drag term F in Eq. II-8 must be evaluated. Fulks et al. [29] give a derivation of their three-dimensional term which is equivalent to F. A different approach is used here. By using the following analysis F can be defined experimentally.

Both the drag and the dc flow resistivity are used to define dissipation in a porous material. Whereas we have not defined F, we can measure the flow resistivity and mathematically relate the two variables. The dc flow resistivity in a porous material is determined by first forcing a gas through the material at various, known particle velocities. The pressure drop ΔP is measured at each particle velocity u/P. Once these measurements are obtained the dc flow resistivity is calculated by using [2]

$$\frac{PR_{dc}}{L} = \frac{P\Delta P}{uL} \quad , \tag{II-9}$$

where L is the sample length. The dc flow resistance R_{dc} is a function of particle velocity and is fit to the first order equation [12,19,21,55,88]

$$\frac{PR_{dc}}{L} = \sigma + \eta \frac{u}{P} \quad , \tag{II-10}$$

where the coefficients σ and η are fit to the dc flow resistivity data.

The drag term F is defined by noting that if the flow is steady (dc), then the first and second terms of Eq. II-8 equal zero [86]. The momentum equation becomes

$$P_{,x} = -F \quad . \tag{II-11}$$

Divide Eq. II-11 by the particle velocity inside the porous material u/P to determine the dc flow resistivity inside the material

$$-\frac{PR_{dc}}{L} = P\frac{P_{,x}}{u} = -\frac{PF}{u} \quad , \tag{II-12}$$

and

$$F = \left(\sigma + \eta\frac{u}{P}\right)\frac{u}{P} \quad . \tag{II-13}$$

Both Hersh and Walker [33,34] and Zorumski and Parrott [86] have shown the flow resistivity to be independent of the frequency. Thus, the coefficients σ and η are independent of any time derivatives.

C. Energy Equation Derivation

In this section the internal energy equation for the fluid in the porous material is derived for use as the third conservation equation in the perturbation analysis. As discussed in Section II-A, the porosity is included with the particle velocity.

The energy transfer in the control volume fluid is illustrated in Fig. II-3. The conservation of energy states that

the time rate of change of energy inside the control volume	=	net flux of energy across the control volume surfaces	+	work/unit time done by surface forces on the fluid	+	heat added to the fluid.

For the one-dimensional system shown in Fig. II-3 the energy equation is

$$A\Delta x \frac{\partial \rho (e+u^2/2P^2)}{\partial t} = \frac{\rho(e+u^2/2P^2)uA}{P}\bigg|_x - \frac{\rho(e+u^2/2P^2)uA}{P}\bigg|_{x+\Delta x} \tag{II-14}$$

$$+ \frac{PuA}{P}\bigg|_x - \frac{PuA}{P}\bigg|_{x+\Delta x} + qA\bigg|_x - qA\bigg|_{x+\Delta x} ,$$

where e is the internal energy/unit mass and q is the heat flux/unit area. Dividing Eq. II-14 by $A\Delta x$ and taking the limit as $\Delta x \to 0$, yields

$$(e+u^2/2P^2)_{,t} = -\frac{[\rho(e+u^2/2P^2)\ u]}{P}_{,x} - \frac{(Pu)}{P}_{,x} - q_{,x} \tag{II-15}$$

Equation II-15 is rewritten as

$$\left(e+\frac{u^2}{2P^2}\right)[\rho_{,t} + (\rho u)_{,x}] + \frac{De}{Dt} + \frac{u}{P}\left(\frac{\rho}{P}\frac{Du}{Dt} + P_{,x}\right) + \frac{Pu_{,x}}{P} + q_{,x} = 0 \tag{II-16}$$

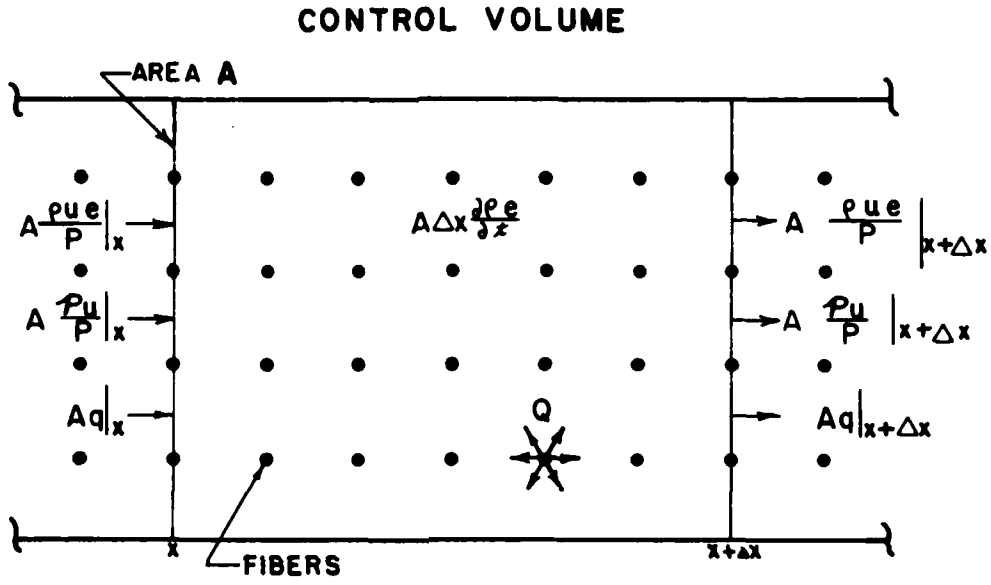

RELATIVE TO THE CONTROL VOLUME THE FIBERS ARE STATIONARY.

FIGURE II-3
STATIONARY CONTROL VOLUME USED IN THE DETERMINATION OF THE CONSERVATION OF ENERGY RELATION FOR POROUS MATERIAL.

where the total derivative is

$$\frac{D}{Dt} = \frac{\partial}{\partial t} + \frac{u}{P}\frac{\partial}{\partial x} \quad . \tag{II-17}$$

The terms in the square brackets of Eq. II-16 equal Eq. II-4, the continuity equation. The terms in the curly brackets of Eq. II-16 equal-F in Eq. II-8, the momentum equation. The energy equation becomes

$$\rho\frac{De}{Dt} = - q_{x,x} + F\frac{u}{P} - \frac{Pu_{,x}}{P} \tag{II-18}$$

The fluid in the porous material is assumed to be an ideal gas, which has the properties

$$P = R\rho T \tag{II-19}$$

and

$$de = C_v dT \tag{II-20}$$

where $R=(\gamma-1)C_v$, $\gamma=C_p/C_v$, T is the temperature, and C_p and C_v are the specific heats. By using Eqs. II-19 and II-20, Eq. II-18 is rewritten as

$$\frac{D}{Dt}\left(\frac{P}{\rho}\right) + \frac{(\gamma-1)Pu_{,x}}{\rho P} = \frac{(\gamma-1)}{\rho}\left(-q_{x,x} + F\frac{u}{P}\right) \quad . \tag{II-21}$$

We may rewrite the continuity equation (Eq. II-4) as

$$\frac{1}{\rho}\frac{D\rho}{Dt} + \frac{u_{,x}}{P} = 0 \quad . \tag{II-22}$$

Equation II-22 is used in Eq. II-21 to eliminate the density variable such that

$$\frac{DP}{Dt} + \frac{\gamma P u_{,x}}{P} = (\gamma - 1)(-q_{x,x} + F\frac{u}{P}) \quad . \tag{II-23}$$

This form of the energy equation is simplified by noting that the heat flux q_x is negligible. There are three reasons for ignoring the heat flux term q_x in Eq. II-23. First, in open air q_x is usually ignored between 20 Hz and 20 kHz, because the relatively long wavelengths and short oscillation times are not conducive to heat transfer. Second, in a porous material the wavelength is much longer than the fiber spacing and the heat cannot flow along the direction of propagation without encountering many fibers in a wavelength. The analysis presented in Appendix A shows that heat transfer effects are localized around the fibers of the porous material, thus further reducing $q_{x,x}$. Finally, in a porous material it can also be assumed that $Fu/P >> q_{x,x}$ and Eq. II-23 is rewritten as

$$\frac{DP}{Dt} + \frac{\gamma P u_{,x}}{P} = (\gamma - 1)\frac{u}{P}F \quad . \tag{II-24}$$

If the heat transfer rate from the fibers to the air is large enough, the compressions of the air are almost isothermal, $\gamma \approx 1$, and

$$\frac{D\rho}{Dt} + \frac{\rho u_{,x}}{P} = 0 \quad . \tag{II-25}$$

Equation II-25 is the internal energy equation used in the perturbation analysis that is presented in the next section. For

high intensity sound the rate of heat transfer increases because of convection and mixing in the air (see Appendix A) and we assume $\gamma \approx 1$ for calculation of the acoustic terms of the perturbation analysis. Equation II-25 leads to the relation $b_o = \sqrt{P_o/\rho_o}$.

D. Perturbation Analysis

In the last three sections the conservation equations were derived. In this section perturbation analysis is used to solve dimensionless forms of the conservation equations for a single boundary condition. The boundary condition is a second harmonic distorted sine wave. Both components are of arbitrary phase and amplitude. The boundary condition is used in an attempt to approximate the measured signals which are described in Chapter IV.

1. Perturbation of Conservation Equations

In terms of the total derivative, the three conservation equations derived in Sections A, B, and C are

$$\frac{1}{\rho}\frac{D\rho}{Dt} + \frac{u_{,x}}{P} = 0 \quad , \tag{II-26}$$

$$\frac{\rho Du}{PDt} + P_{,x} = -\sigma\frac{u}{P} - \eta\left(\frac{u}{P}\right)^2 = -F \quad , \tag{II-27}$$

and

$$\frac{DP}{Dt} + \frac{\gamma P u_{,x}}{P} = (\gamma-1)\frac{u}{P}F \quad . \tag{II-28}$$

We remind the reader here that, in a porous material, we will assume isothermal conditions ($\gamma = 1$). For generality and because $\gamma = 1$ is not exactly true, we use $\gamma \neq 1$ to compute the perturbed wave equations and, in solution of these equations, set $\gamma = 1$.

The measurement results, presented in Chapter IV, show that the initial waveform is not a pure sinusoid. The microphone is located some distance from the source (See Chapter III) and the intense sound distorts as it travels to the microphone. At high intensities, if the

level of the second harmonic component is large, it can affect the propagation of the fundamental component [81]. Excess attenuation of the fundamental component may occur [16,80], but this is a third-order effect for an initial sinusoid and can be a second order effect for a second harmonic distorted sinusoid. Because of the mathematical complexities an unsuccessful attempt was made to derive a third-order solution of an initially sinusoidal wave.

The second harmonic distorted sinusoid boundary condition is used in an attempt to describe the propagation of intense sound in a porous material. The boundary condition is used to introduce both the first and second harmonics at the boundary

$$p(0,t) = p'(\sin \omega t + b \sin 2\omega t) \qquad \text{(II-29)}$$

and, since we only consider outward traveling waves, $p(\infty,t) = 0$, where p' is the fundamental component amplitude and b is the harmonic component relative amplitude. Because of more higher harmonics present at the boundary, Eq. II-29 does not accurately describe the conditions at the first microphone. This inaccurate description appears to be a source of problems in the Chapter IV data-theory comparisons.

The first step in the analysis is to make the equation dimensionless. This is done by using the following substitutions:

$$\Delta = \frac{\rho}{\rho_o}, \quad U = \frac{u}{c}, \quad \Pi = \frac{P}{\rho_o c^2}$$

$$\chi = \frac{x\omega}{c}, \quad \tau = \omega t, \text{ and } \varepsilon = \frac{u_o}{c} \quad . \qquad \text{(II-30)}$$

where we defined the sound speed c as neither adiabatic c_o nor isothermal b_o. In the solution of the equations we let $c \to b_o$. The dimensionless equations are

$$\Delta_{,\tau} + \frac{U\Delta_{,X}}{P} + \frac{\Delta U_{,X}}{P} = 0 \quad , \tag{II-31}$$

$$\frac{\Delta U_{,\tau}}{P} + \frac{U\Delta U_{,X}}{P^2} + \Pi_{,X} = -\frac{\sigma_1 U}{P} - \frac{\eta_1 U^2}{P^2} = -F_1 \quad , \tag{II-32}$$

and

$$\Pi_{,\tau} + \frac{U\Pi_{,X}}{P} + \frac{\gamma\Pi U_{,X}}{P} = (\gamma-1)\frac{U}{P}F_1 \quad , \tag{II-33}$$

where $\sigma_1 = \sigma/\rho_o\omega$, $\eta_1 = \eta c/\rho_o\omega$, and $F_1 = F/\rho_o\omega$. The dimensionless boundary conditions are

$$\Pi(0,\tau) = \varepsilon(\sin\tau + b\sin 2\tau) = \varepsilon \mathrm{Im}(e^{j\tau} + be^{j2\tau}) \tag{II-34}$$

and $\Pi(\infty,\tau) = 0$.

The solution to these nonlinear equations for a wave traveling in the material can be found through perturbation. Each of the three dependent variables are expanded in a power series in ε as follows [15]

$$\begin{aligned} \Pi &= \Pi_o + \varepsilon\Pi_1 + \varepsilon^2\Pi_2 + \varepsilon^3\Pi_3 + \ldots \quad , \\ U &= U_o + \varepsilon U_1 + \varepsilon^2 U_2 + \varepsilon^3 U_3 + \ldots \quad , \end{aligned} \tag{II-35}$$

and

$$\Delta = \Delta_o + \varepsilon\Delta_1 + \varepsilon^2\Delta_2 + \varepsilon^3\Delta_3 + \ldots \quad ,$$

where $\Pi_o = p_o/c^2\rho_o = 1/\gamma$, $U_o = 0$, and $\Delta_o = 1$. These expansions are substituted into both the conservation equations and the boundary conditions. The terms multiplied by like powers of ε^n are then combined to give the n^{th} order equations.

The first-order conservation equations are

$$\Delta_{1,\tau} + \frac{U_{1,\chi}}{P} = 0 \quad , \tag{II-36}$$

$$\frac{U_{1,\tau}}{P} + \Pi_{1,\chi} + \frac{\sigma_1 U_1}{P} = 0 \quad , \tag{II-37}$$

and

$$\Pi_{1,\tau} + \frac{U_{1,\chi}}{P} = 0. \tag{II-38}$$

These equations are the small signal conservation equations for a rigid porous material. Combining Eqs. II-37 and II-38, to eliminate U_1, yields the wave equation

$$\Pi_{1,\tau\tau} - \Pi_{1,\chi\chi} + \sigma_1 \Pi_{1,\tau} = 0 \quad , \tag{II-39}$$

which has been solved by others [23,30,32,33,45,68] and is discussed in Chapter I. The boundary conditions are

$$\Pi_1(0,\tau) = \sin\tau + b \sin 2\tau \text{ and } \Pi_1(\infty,\tau) = 0 \quad . \tag{II-40}$$

The second-order conservation equations are

$$\Delta_{2,\tau} + \frac{U_{2,\chi}}{P} = -\frac{1}{P}(\Delta_1 U_1)_{,\chi} \quad , \tag{II-41}$$

$$\frac{U_{2,\tau}}{P} + \Pi_{2,\chi} + \frac{\sigma_1 U_2}{P} = -\frac{\Delta_1 U_{1,\tau}}{P} - \frac{U_1 U_{1,\chi}}{P^2} - \frac{\eta_1 U_1^2}{P^2} \quad , \tag{II-42}$$

and

$$\Pi_{2,\tau} + \frac{U_{2,\chi}}{P} = -\frac{U_1\Pi_{1,\chi}}{P} - \frac{\gamma\Pi_1 U_{1,\chi}}{P} + \frac{\sigma_1 U_1^2(\gamma-1)}{P^2} \quad . \tag{II-43}$$

Combination of Eqs. II-42 and II-43 to eliminate the U_2 terms yields the second-order wave equation

$$\begin{aligned}\Pi_{2,\tau\tau} - \Pi_{2,\chi\chi} + \sigma_1\Pi_{2,\tau} = -\frac{1}{P}\Big[&(U_1\Pi_{1,\chi})_{,\tau} + \sigma_1 U_1\Pi_{1,\chi} \\ &+ \gamma(U_{1,\chi}\Pi_1)_{,\tau} + \gamma\sigma_1 U_{1,\chi}\Pi_1 + (\Pi_1 U_{1,\tau})_{,\chi}\Big] \\ -\frac{1}{P^2}\Big[&(\sigma_1 U_{1,\tau}^2 + \sigma_1^2 U_1^2)(\gamma-1) + (U_1 U_{1,\chi})_{,\chi} + \eta_1 U_{1,\chi}^2\Big] \quad .\end{aligned} \tag{II-44}$$

The second-order boundary conditions at $x = 0$ and ∞ equal zero. The first order solutions are used in the second order equations and then the second order solutions are found.

2. First-Order Solution

In small signal, first-order, wave propagation, each harmonic component travels independently, i.e., superposition holds. As in Chapter I we can assume a pure sinusoid

$$\Pi_1(\chi,\tau) = Be^{j(\tau-\Gamma_1\chi)} \quad , \tag{II-45}$$

where $\Gamma_1 = (\beta_1 - j\alpha_1)\, b_o/\omega$. Substitution of Eq. II-45 into Eq. II-39 yields the dispersion relation

$$\Gamma_1 = \sqrt{1 - j\sigma_1} \quad , \tag{II-46}$$

or, in dimensional form,

$$(\beta_1 - j\alpha_1)^2 - \frac{\omega^2}{b_o^2} + j\frac{\sigma_1\omega^2}{b_o^2} = 0 \quad , \tag{II-47}$$

where we have set $c = b_o$. Equation II-47 can be written in terms of the attenuation

$$\alpha_1 = \frac{\omega}{\sqrt{2}b_o} \sqrt{-1 + \sqrt{1 + \sigma_1^2}} \tag{II-48}$$

and the phase

$$\beta_1 = \frac{\omega}{\sqrt{2}\, b_o} \sqrt{1 + \sqrt{1 + \sigma_1^2}} \quad . \tag{II-49}$$

As noted in Chapter I, the phase speed $c_{1PH} = \omega/\beta_1$ is

$$c_{1PH} = \frac{\omega}{\beta_1} = \frac{\sqrt{2}b_o}{\sqrt{1 + \sqrt{1 + \sigma_1^2}}} \tag{II-50}$$

which we use to describe how fast a wave travels at each frequency. The phase speed and attenuation are used in Chapter IV to compare the low-intensity theory and experiment.

The first-order radiation boundary condition (Eq. II-40) is

$$\Pi_1(0,\tau) = \mathrm{Im}(e^{j\tau}) + b\,\mathrm{Im}\left(e^{j(2\tau+\phi)}\right) \quad . \tag{II-51}$$

The first order solution of Eq. II-39 is

$$\Pi_1(\chi,\tau) = e^{j(\tau-\Gamma_1\chi)} + b\, e^{j[2(\tau-\Gamma_2\chi)+\phi]} \quad , \tag{II-52}$$

where $\Gamma_2 = \sqrt{1 - j\sigma_1/2}$.

The first order particle velocity function is determined by using Eq. II-52 in Eq. II-38 to obtain

$$U_1 = \frac{P}{\Gamma_1} e^{j(\tau-\Gamma_1\chi)} + \frac{bP}{\Gamma_2} e^{j[2(\tau-\Gamma_2\chi)+\phi]} \quad . \tag{II-53}$$

We stated in Section C that when $\gamma = 1$, the acoustic pressure and density are related by a simple constant b_o^2. In the present case we find that

$$\Pi_1 = \Delta_1 \quad . \tag{II-54}$$

3. Second-Order Solution

Equations II-52 through II-54 are used in Eq. II-44 (set $\gamma = 1$) to obtain

$$\begin{aligned}
\Pi_{2,\tau\tau} - \Pi_{2,\chi\chi} + \sigma_1 \Pi_{2,\tau} = {} & \frac{b(2\Gamma_2 - \Gamma_1^*)[2\eta_1 + j\Gamma_1^2(\Gamma_1^* - \Gamma_2)]}{2\Gamma_1^*\Gamma_2} e^{j[\tau - (2\Gamma_2 - \Gamma_1^*)\chi + \phi]} \\
& + \frac{(-\eta_1 - j4\Gamma_2^2\Gamma_1)}{\Gamma_1} e^{j2(\tau - \Gamma_1\chi)} \\
& - \frac{b(2\Gamma_2 + \Gamma_1)(\eta_1 + j3\Gamma_3^2\Gamma_1)}{\Gamma_1\Gamma_2} e^{j[3\tau - (2\Gamma_2 + \Gamma_1)\chi + \phi]} \\
& - \frac{2b^2(\eta_1 + j16\Gamma_2\Gamma_4^2)}{\Gamma_2^2} e^{j[4(\tau - \Gamma_2\chi) + 2\phi]} \\
& + \frac{(\Gamma_1^* - \Gamma_1)(-\eta_1 + \Gamma_1^*\sigma_1)}{2\Gamma_1\Gamma_1^*} e^{j(\Gamma_1^* - \Gamma_1)\chi} \\
& + \frac{b^2(\Gamma_2^* - \Gamma_2)(-\eta_1 + \Gamma_2^*\sigma_1)}{2\Gamma_2\Gamma_2^*} e^{j2(\Gamma_2^* - \Gamma_2)\chi} \quad .
\end{aligned} \tag{II-55}$$

The last two terms of Eq. II-55 are streaming terms and are ignored in the calculation of an acoustic solution.

The solution of Eq. II-55 is obtained by first writing the left hand side differential operator as

$$L = \frac{\partial^2}{\partial\tau^2} - \frac{\partial^2}{\partial\chi^2} + \sigma_1 \frac{\partial}{\partial\tau} \tag{II-56}$$

and then, by using the theory of differential operators [65], the particular solution is found to be

$$\Pi_{2P} = Q_1 e^{j[\tau-(2\Gamma_2-\Gamma_1^*)\chi+\phi]} + Q_2 e^{j2(\tau-\Gamma_1\chi)} + Q_3 e^{j[3\tau-(2\Gamma_2+\Gamma_1)\chi+\phi]} + Q_4 e^{j[4(\tau-\Gamma_2\chi)+2\phi]} , \tag{II-57}$$

where

$$Q_1 = \frac{b(2\Gamma_2-\Gamma_1^*)[2\eta_1+j\Gamma_1^2(\Gamma_1^*-\Gamma_2)]}{8\Gamma_1^*\Gamma_2(1-\Gamma_1^*\Gamma_2)} ,$$

$$Q_2 = \frac{j\eta_1 - 4\Gamma_2^2\Gamma_1}{2\sigma_1\Gamma_1} ,$$

$$Q_3 = -\frac{b(2\Gamma_2+\Gamma_1)(\eta_1+j3\Gamma_3^2\Gamma_1)}{4\Gamma_1\Gamma_2(1-\Gamma_1\Gamma_2)} ,$$

and

$$Q_4 = \frac{2b^2(j\eta_1-16\Gamma_2\Gamma_4^2)}{2\sigma_1\Gamma_2^2} . \tag{II-58}$$

Since the sum of the particular and homogeneous solutions must satisfy the boundary condition

$$\Pi_2(0,\tau) = 0 \quad , \tag{II-59}$$

then the homogeneous equation has the form

$$\Pi_{2H} = R_1 e^{j(\tau-\Gamma_1\chi+\phi)} + R_2 e^{j(2\tau-2\Gamma_2\chi)} + R_3 e^{j[3(\tau-\Gamma_3\chi)+\phi]}$$

$$+ R_4 e^{j[4(\tau-\Gamma_4\chi)+2\phi]} \quad , \tag{II-60}$$

where the R_i terms are to be determined by using the boundary condition Eq. II-59. The propagation parameters are $\Gamma_3 = \sqrt{1 - j\sigma_1/3}$ and $\Gamma_4 = \sqrt{1 - j\sigma_1/4}$. The form of the propagation parameters is determined by substituting the individual exponentials into the operator L of Eq. II-56 and solving the dispersion relations.

We add the homogeneous and particular solutions, Eqs. II-60 and II-57, and substitute the result into the boundary condition. We find that $-R_i=Q_i$ and and obtain

$$\Pi_2(\chi,\tau) = Q_1\left(e^{-j(2\Gamma_2-\Gamma_1^*)\chi} - e^{-j\Gamma_1\chi}\right)e^{j(\tau+\phi)} + Q_2\left(e^{-j2\Gamma_1\chi} - e^{-j2\Gamma_2\chi}\right)e^{j2\tau}$$

$$+ Q_3\left(e^{-j(2\Gamma_2+\Gamma_1)\chi} - e^{-j3\Gamma_3\chi}\right)e^{j(3\tau+\phi)} + Q_4\left(e^{-j4\Gamma_2\chi} - e^{-j4\Gamma_4\chi}\right)e^{j(4\tau+2\phi)} .$$

(II-61)

To check Eq. II-61 against a similar equation in lossless, isothermal air we used the substitution $P \to 1 - \delta$ and took the limit as $\delta \to 0$. The equations were equal.

Although Eq. II-61 is only of second order, the equation yields information on four harmonic components. Two of the components start at nonzero amplitudes, whereas the other two start at zero amplitude. As we shall see in Chapter IV, this representation of the actual measurement situation is not correct, but, in order to obtain a more realistic representation of experimental results the boundary condition would also have to include the third and higher harmonic components. Although this latter problem is tractable, the mathematics are prohibitive for the relative information that the solution would yield. The solution has not been attempted.

Figure II-4 shows a case of propagation for assumed values of the material properties in Eq. II-61. Computer program PERT4PD was used to generate this plot and is listed in Appendix B. We note several phenomena illustrated on this plot. We see that the intensities of the higher harmonics grow with distance and then decay. The fourth harmonic is not shown because its level is less than 112 dB. The fundamental propagates in a linear fashion. The fundamental propagates in a nonlinear fashion at higher sound levels, for both ϵ and b, and for higher relative nonlinearities η/σ. The nonlinear propagation is exhibited by extra attenuation of the fundamental and more energy being transferred to the harmonic components. When the initial amplitudes are high

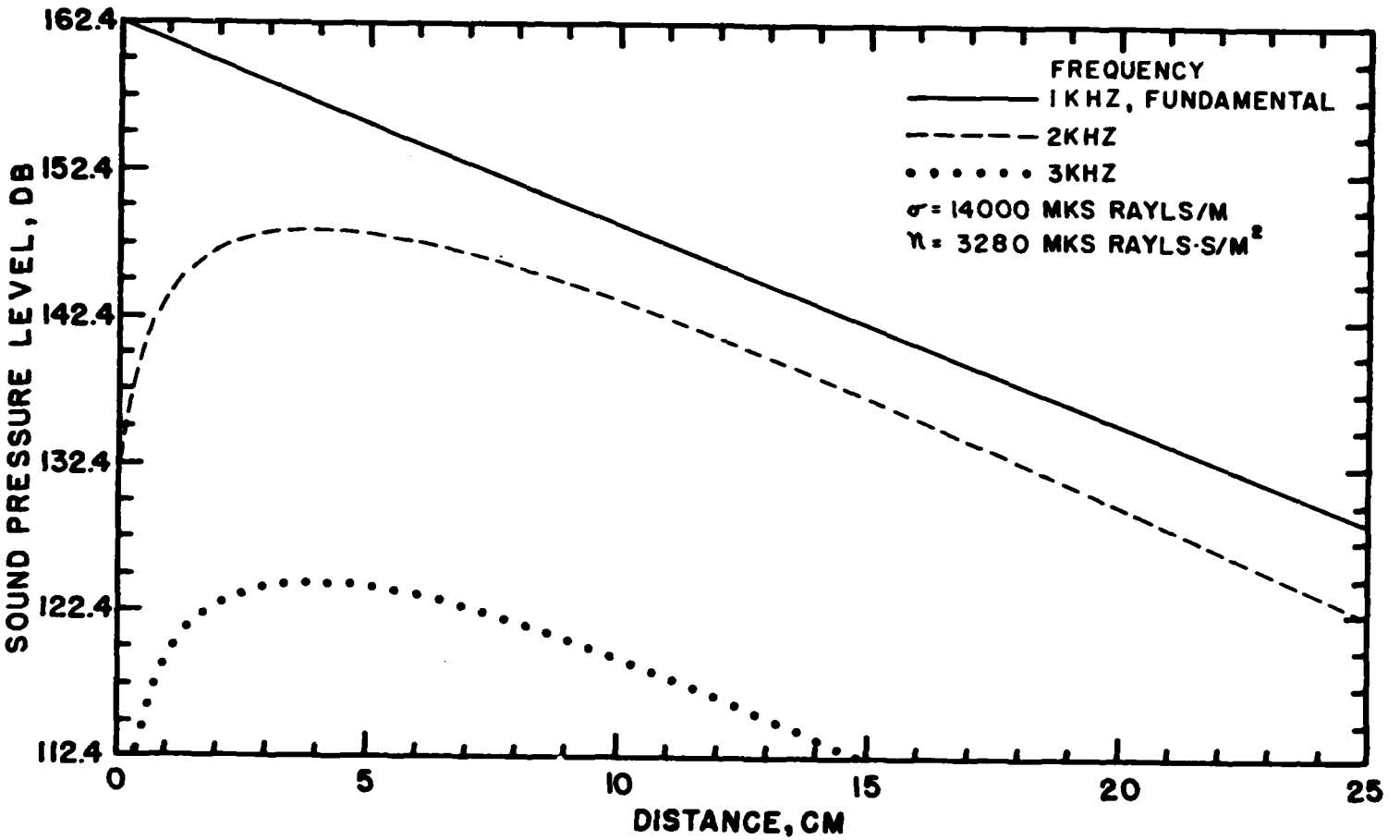

FIGURE II-4
SOUND LEVEL VERSUS DISTANCE FOR THE FIRST FOUR HARMONIC COMPONENTS OF A SECOND HARMONIC DISTORTED SINUSOIDAL WAVE PROPAGATING IN A POROUS MATERIAL.

enough, the second harmonic level exceeds the fundamental level and the model fails. More discussion is presented in Chapter IV, where we find the measured data is not well predicted by the theory.

E. An Approximation to the Impedance and Absorption Properties of Semi-Infinite Nonlinear Porous Materials

As discussed in Chapter I, several investigators [23,32,33, 45,68] have determined relations for the impedance and absorption properties of linear porous materials. Experimentally, the impedance has been found to change with intensity [47,55,64,86]. In this section the dimensionless impedance and absorption equations are found for linearly behaving materials. Because acoustic impedance of porous materials is frequency dependent, the impedance concept is not easily applicable to nonlinear systems. Thus, only an estimation for nonlinear behavior is made for the absorption and impedance.

The acoustic impedance of porous materials is found in the same manner as in Chapter I. For linear behavior the first order solutions U_1 and Π_1, expressed in Eqs. II-53 and II-51 ($b = 0$), are used in calculating the dimensionless impedance

$$Z_1 = \frac{P\Pi_1}{U_1} = \sqrt{1 - j\sigma_1} \quad . \tag{II-62}$$

The resistive (real) part is

$$Re(Z_1) = \frac{1}{\sqrt{2}} \sqrt{1 + \sqrt{1 + \sigma_1^2}} \tag{II-63}$$

and the reactive (imaginary) part is

$$Im(Z_1) = - \frac{1}{\sqrt{2}} \sqrt{-1 + \sqrt{1 + \sigma_1^2}} \quad . \tag{II-64}$$

These functions are the dimensionless counterparts of Eqs. I-8 and I-9.

Once the propagation properties of a high-intensity sound in a fibrous porous material are known, it is advantageous to determine the impedance that an intense incident wave encounters at the material surface. The acoustic resistance that an intense sound encounters is influenced by the material nonlinearity and the amplitude of the sound. If an attempt is made to solve for the ratios Π/U or Π_2/U_2, the results are complicated functions of the different harmonics and their relative amplitudes. Although a solution might be obtained by using the perturbation solutions, it is expected that the result would be far more complicated than the perturbation analysis and not very useful. A simpler approximation is presented here.

The following approximation is good only at the air/surface-interface of a semi-infinite nonlinear porous material. For a sound traveling in the material the perturbation solutions or one of the approximations in Section II-F should be used. To avoid the problem of reflection from the back of the sample, we assume that $\alpha L >> 1$.

We employ a simple substitution in the approximation. In place of the linear dc flow resistivity σ_1, we use the first order relationship for the nonlinear dc flow resisitivty $\sigma_1 + \varepsilon\eta_1/P\sqrt{2}$. This substitution is similar to that used by Ingard [37] for high-intensity impedance of Helmholtz resonators. We use the quantity $\varepsilon/\sqrt{2}$ as an acoustic replacement quantity of the dimensionless dc particle

velocity u_{dc}/b_o. We do not want any time or distance dependency and work only with the appropriate magnitudes. The substitution of this relationship into Eq. II-62 yields the dimensionless nonlinear impedance

$$Z_N = \sqrt{1 - j(\sigma_1 + \varepsilon\eta_1/p\sqrt{2})}, \qquad \text{(II-65)}$$

with the resistive and reactive parts becoming

$$\mathrm{Re}(Z_N) = \frac{1}{\sqrt{2}} \sqrt{1 + \sqrt{1 + (\sigma_1+\varepsilon\eta_1/p\sqrt{2})^2}} \qquad \text{(II-66)}$$

and

$$\mathrm{Im}(Z_N) = \frac{-1}{\sqrt{2}} \sqrt{-1 + \sqrt{1 + (\sigma_1+\varepsilon\eta_1/p\sqrt{2})^2}} \quad . \qquad \text{(II-67)}$$

For a specific material, the above functions may be plotted with respect to the parameters of frequency and acoustic Mach number of the incident sound at the surface. In Fig. II-5 the normal specific acoustic impedance encountered by a 1 kHz wave at the surface of a semi-infinite, fibrous porous material is plotted with respect to the sound pressure level. The magnitudes of both the resistive and reactive parts of the impedance increase with amplitude. These results indicate that both the amplitude and phase change of the reflected wave vary as the amplitude increases. In the analysis review presented in Section I-C-2 we found that the reflection process appears to follow the small signal laws up to about 170 dB. In the test procedure described in Section III-E-2 we find that the results are reliable up to a sound level of about 165 dB. The comparison between the theory and data should be appropriate.

AD-A121 450 HIGH-INTENSITY SOUND IN AIR SATURATED FIBROUS BULK POROUS MATERIALS(U) TEXAS UNIV AT AUSTIN APPLIED RESEARCH LABS H L KUNTZ 03 SEP 82 ARL-TR-82-54 2/3

UNCLASSIFIED N00014-75-C-0847 F/G 11/6 NL

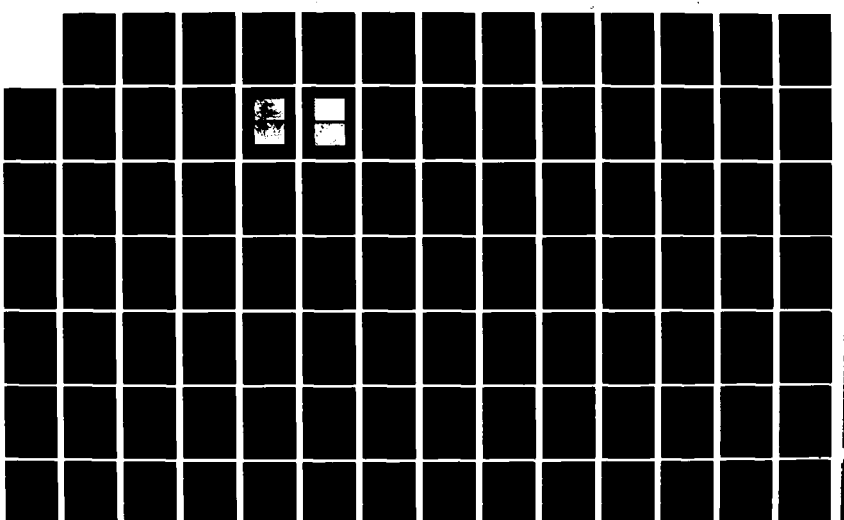

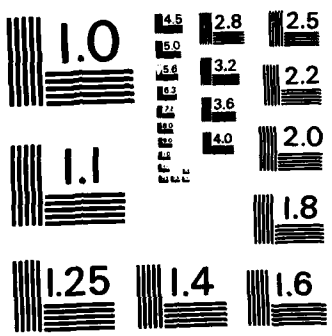

MICROCOPY RESOLUTION TEST CHART
NATIONAL BUREAU OF STANDARDS-1963-A

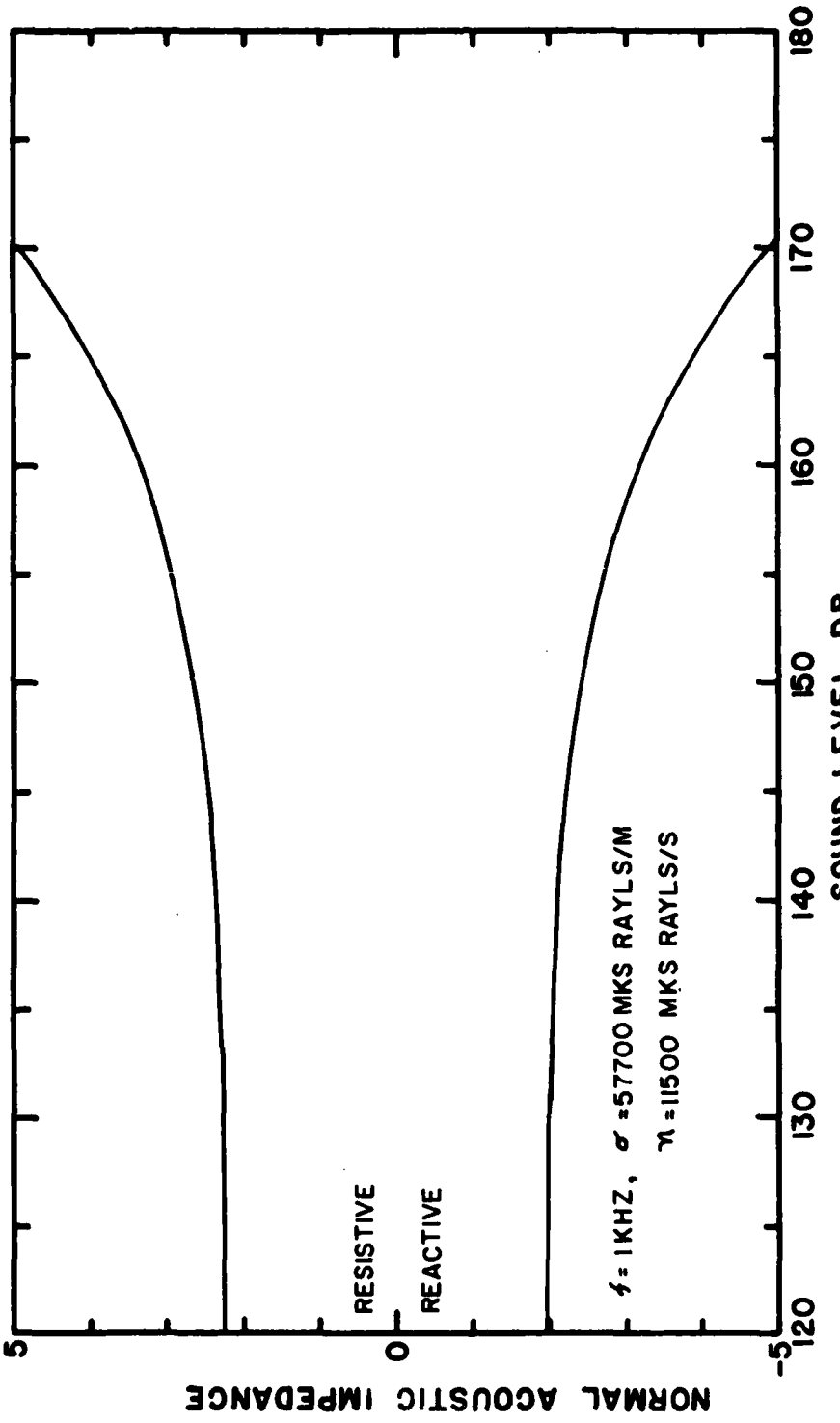

FIGURE II-5
ACOUSTIC IMPEDANCE VERSUS SOUND PRESSURE LEVEL FOR A SEMI-INFINITE POROUS MATERIAL.

The effect of the increased resistance and reactance on the ability of the sound to enter the porous material is examined by studying the absorption coefficient. We can rewrite Eq. I-11 in the nonlinear dimensionless form

$$a_N = 1 - \left|\frac{Z_N - 1}{Z_N + 1}\right|^2 \quad . \tag{II-68}$$

The nonlinear absorption coefficient at 1 kHz versus sound pressure level is plotted in Fig. II-6 for the same material properties as used in Fig. II-5. The absorption coefficient decreases with increases in the sound level. When the resistance increases, the absorption coefficient is expected to decrease. Since the flow resistance increases with sound level, it is harder for the high-intensity sound to enter the material than for the same frequency low-intensity sounds.

The increased impedance has two consequences in the absorption of sound. First, the high-intensity sound cannot enter the absorbing material as easily as low-intensity sound. Second, once the high-intensity sound does enter the material it is more rapidly dissipated than the low-intensity sound. When the level is reduced to low intensities, the sound asymptotically approaches linear propagation. The latter effect is noted in the experimental results (Section IV-B-2) and in the Section II-F approximations.

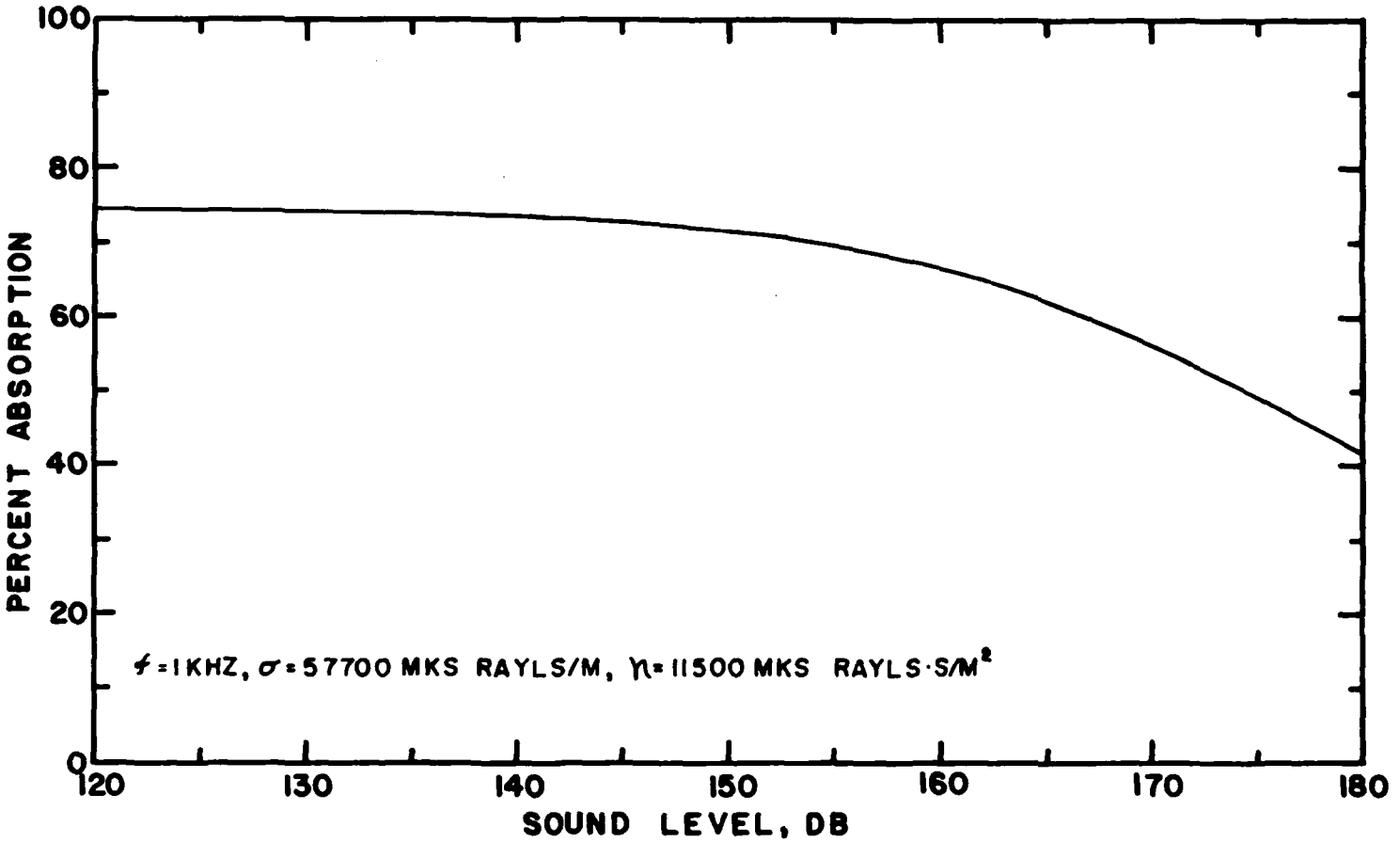

FIGURE II-6
ABSORPTION COEFFICIENT VERSUS SOUND PRESSURE LEVEL
FOR A SEMI-INFINITE POROUS MATERIAL.

F. Approximations to the Attenuation of an Intense Sinusoid Propagating in Nonlinear Porous Materials

In this section we present two models for use in approximating the attenuation of intense sinusoids in porous materials. The linear impedance Z_1 and propagation parameter Γ_1 are intimately related by Eq. II-62. Because of this relation, we can use the approximation of Eq. II-65 to model how the propagation parameter of an initially sinuoisdal wave changes with intensity. We may also analyze the propagation of an initially sinusoidal wave by modeling how energy is lost from the fundamental component as a function of sound level. The mathematics of each model is simple and the models are easy to use. The impedance model is presented first.

1. Impedance Model

We can write the dimensionless propagation parameter as

$$\Gamma_1 = B_1 - jA_1 \quad , \tag{II-69}$$

where the dimensionless attenuation $A_1 = \alpha_1 b_o/\omega$ is given by Eq. II-63 and the dimensionless wave number $B_1 = \beta_1 b_o/\omega$ is given by Eq. II-64. The resulting equations are analogous to Eqs. I-4 and I-5.

Again, the substitution of $\sigma_1 + \varepsilon\eta_1/P\sqrt{2}$ for σ_1 is used to replace the linear equations with

$$\mathrm{Im}(\Gamma_N) = A_N = -\frac{1}{\sqrt{2}}\sqrt{-1+\sqrt{1+(\sigma_1+\varepsilon\eta_1/P\sqrt{2})^2}} \tag{II-70}$$

for the attenuation and

$$\mathrm{Re}(\Gamma_1) = B_N = \frac{1}{\sqrt{2}}\sqrt{1+\sqrt{1+(\sigma_1+\varepsilon\eta_1/P\sqrt{2})^2}} \tag{II-71}$$

for the wave number. The dimensionless phase speed $C_{phN}/b_o = 1/B_N$ is

$$\frac{C_{phN}}{b_o} = \frac{\sqrt{2}}{\sqrt{1 + \sqrt{1 + (\sigma_1 + \epsilon\eta_1/P\sqrt{2})^2}}} \quad . \tag{II-72}$$

We conclude that both the phase speed and attenuation change with intensity. Because of the interaction of the harmonic components, measurement of C_{phN}/b_o is difficult; one cannot differentiate between actual phase speed reduction and harmonic interaction. Of course, the effects of the interaction may be to slow as well as attenuate the fundamental component. In some of the experimental results we measured an apparent slowing of the fundamental, but, because of the limited data, we do not present the results in this study.

In Fig. II-7 the amplitudes of waves propagating in porous materials are plotted versus distance. The solid line indicates the effect of linear attenuation. The dashed line indicates the effect of nonlinear attenuation (Eq. II-70). We have used $\exp[\int A_N d\chi]$ to determine the amplitude attenuation. The attenuation is more rapid where the intensity is highest. The difference in the attenuation is called the excess attenuation. In Chapter IV the approximation, Eq. II-70, is compared to the perturbation solutions and data.

2. Amplitude Attenuation and Saturation Model

Excess attenuation of the fundamental component of an initially sinusoidal wave may also be modeled by a simple rate equation, which includes the decay of the fundamental component due to nonlinear effects as well as the direct decay due to small signal dissipation. We base

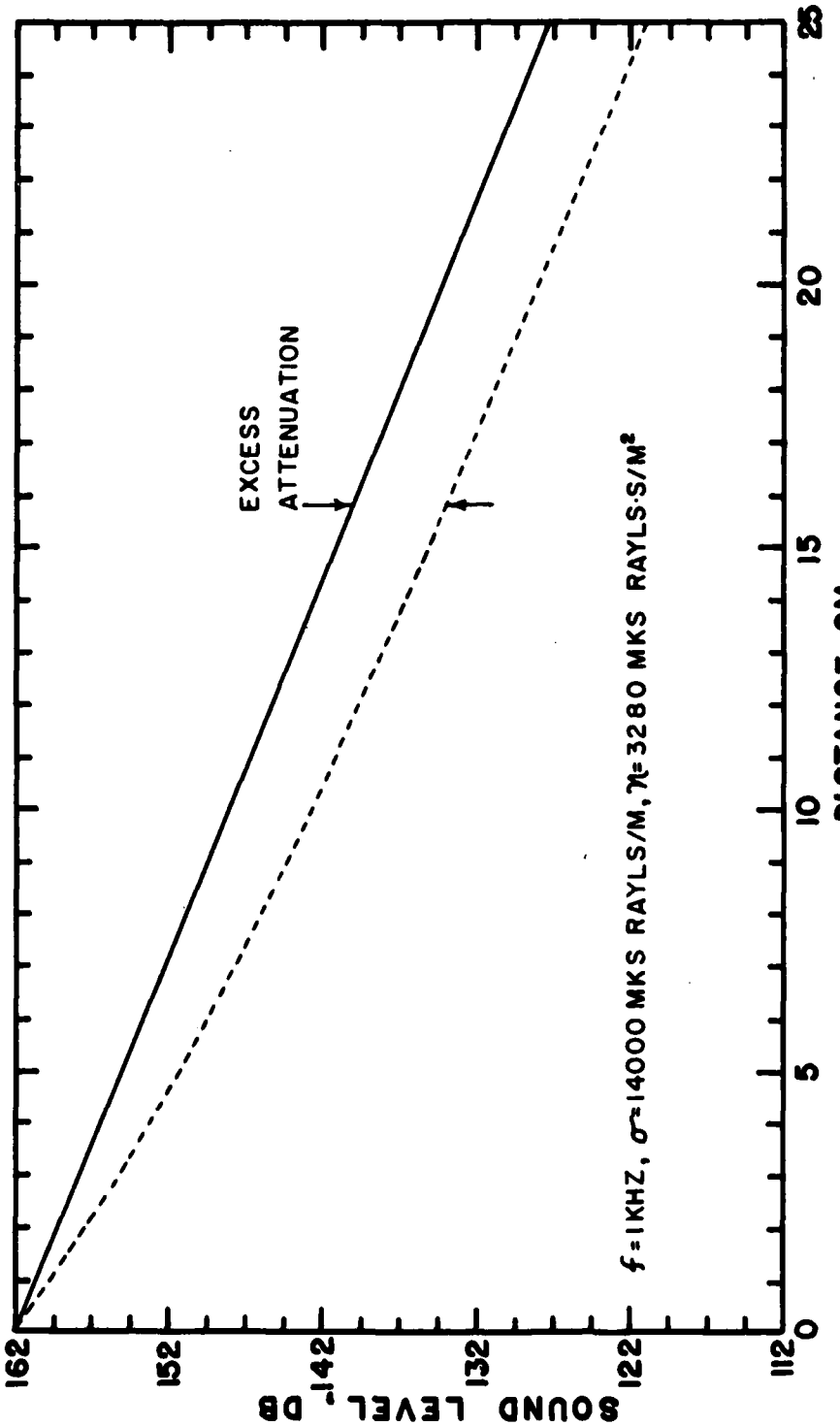

FIGURE II-7
SOUND PRESSURE LEVEL VERSUS DISTANCE FOR AN INTENSE SINUSOID PROPAGATING IN A POROUS MATERIAL.

our model on the concept that, at high intensities, the fundamental loses energy in a consistent manner, regardless of the medium.

In Chapter I we found that the rate of harmonic component generation depends on the amplitude of the original sinusoid and on the thermoviscous attenuation of the fluid medium [16]. The harmonics are generated at the expense of the fundamental. If the rate of harmonic generation is high enough and the attenuation low enough, a shock will form. The presence of the shocks increases dissipation because losses are large at the shocks. Energy is lost by all the harmonics. Thus, we find that the greater the amplitude of the original sinusoid, the quicker the fundamental loses energy.

If we measure the sound level of an intense fundamental component at some remote distance from the source, we will find a nonlinear relation between the source level and remote level. Because the overall decay of the fundamental depends on the source level, the remote sound level depends on the source level, the small signal attenuation, the nonlinearity of the medium, and the distance from the source. A limit in the remote sound level, which is called the saturation level, is a function of the above variables. The excess attenuation, linear region, approach to saturation, and saturation level are all illustrated in the sketch of the amplitude response plot in Fig. II-8. In Chapter IV we present data showing the approach to saturation. We model the saturation effects in the following analysis.

The excess attenuation that the fundamental component of a sinusoidal wave encounters in a porous material may be modeled by

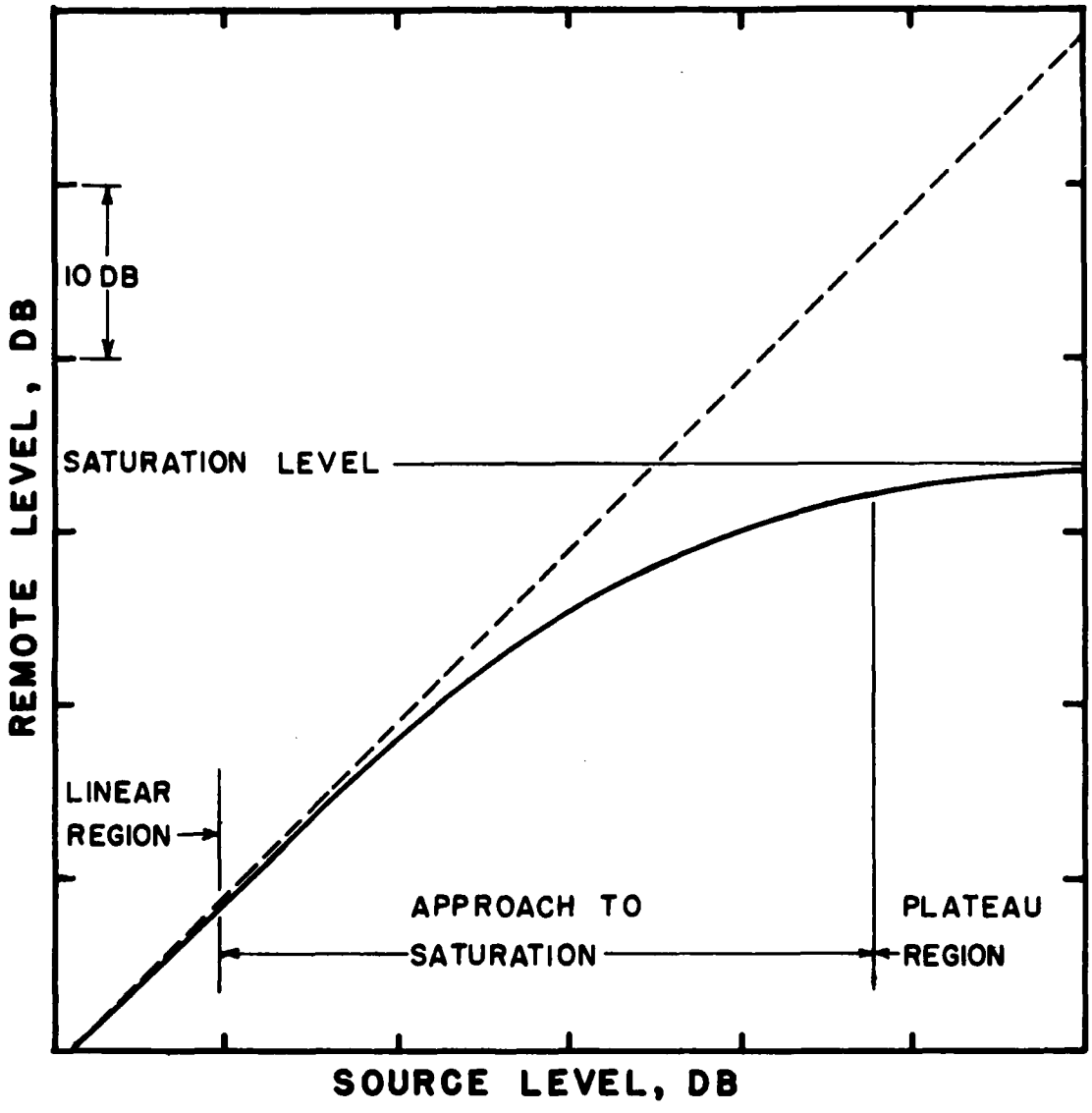

FIGURE II-8
AMPLITUDE RESPONSE CURVE FOR AN INTENSE SINUSOID PROPAGATING IN A POROUS MATERIAL.

considering the two factors causing attenuation of the fundamental component. Others [4,57,76,80,81] have used this method to explain saturation effects in plane waves traveling in an air-filled tube. Ordinary small-signal decay dominates attenuation at low intensities and is described by

$$p_1 = p_o e^{-\alpha x} \quad , \tag{II-73}$$

where p_1 is the pressure amplitude of the fundamental component, p_o is the initial pressure amplitude of the fundamental component, and x is the distance from the source. The decay rate equation associated with Eq. II-73 is

$$\frac{dp_1}{dx} \approx -\alpha p_1 \quad . \tag{II-74}$$

Nonlinear effects dominate the attenuation at high intensities and loss of energy from the fundamental harmonic component depends on intensity. Webster and Blackstock [81] made measurements and confirmed that the pressure amplitude of the fundamental component in the sawtooth region is

$$p_1 = \frac{2p_o}{1+\sigma^*} \quad , \tag{II-75}$$

where $\sigma^* > 3$. Their assumed boundary condition is that the wave starts as a sawtooth. Since $\sigma^* = x/\bar{x}$ and $\sigma^* > 3$ the pressure relation is approximately $p_1 \propto 1/x$ and the decay rate equation associated with Eq. II-75 is

$$\frac{dp_1}{dx} \propto p_1^2 \quad . \tag{II-76}$$

Our measurement results of intense sound propagating in a porous material have shown that excess attenuation exists. We also found that shocks do not form in a porous material. In spite of the lack of shock formation, the approach to saturation appears to be the same as that found in air. We propose that the high-intensity decay rate equation in a porous material is

$$\frac{dp_1}{dx} = -\frac{p_1^2}{T} \quad , \tag{II-77}$$

where T is an unknown coefficient dependent upon the nonlinearity of the medium and the fundamental component frequency. The coefficient T may be defined from either saturation or propagation tests. In Chapter IV we define T in the saturation tests.

Let us assume that the two rates of decay, Eqs. II-74 and II-77, may be added to obtain the overall decay at any pressure p_o. We obtain the relationship

$$\frac{dp_1}{dx} = -\alpha p_1 - \frac{p_1^2}{T} \quad , \tag{II-78}$$

whose solution satisfying the boundary condition $p_1 = p_o$ at $x = 0$ is

$$p_1 = \frac{p_o e^{-\alpha x}}{1 + p_o(1 - e^{-\alpha x})/\alpha T} \quad . \tag{II-79}$$

Equation II-79 is used in Chapter IV to describe both saturation and propagation of intense sinuoidal waves.

Equation II-79 is generally useful. At low source amplitudes $p_o << \alpha T$ Eq. II-79 reduces to Eq. II-73. At high source amplitudes

$p_o >> \alpha T$ and Eq. II-79 may be used to calculate the saturation level. As p_o increases without limit p_1 reaches the saturation pressure and Eq. II-79 becomes independent of p_o. The saturation pressure is

$$p_{1s} = \frac{\alpha T e^{-\alpha x}}{(1 - e^{-\alpha x})} \quad . \tag{II-80}$$

At low attenuations $\alpha \to 0$ Eq. II-79 reduces to $p_1 \to p_o$.

From the above analysis, we conclude that the three variables T, α, and p_o help us define how a sound wave attenuates. In Chapter I we found that the Gol'dberg number $G = \beta' \epsilon k/\alpha$ or $\beta' p_o k/\alpha \rho_o c_o^2$, is used to define the relative effects of attenuation and nonliner distortion. We conclude that, for a porous material, a Gol'dberg type number may be defined from Eq. II-79 as

$$G = \frac{p_o}{\alpha T} \quad . \tag{II-81}$$

We can use Eq. II-81 to describe when nonlinear effects become important to the propagation of intense sounds in a porous material. As $G \to \infty$ nonlinear effects become dominant and as $G \to 0$ attenuation effects dominate. In Chapter IV we determine T and relate T to the relative nonlinearity of the material η/σ and the frequency f.

G. Summary

In this chapter the propagation of sound in and the impedance of porous materials have been modeled. At low intensities the theory presented here agrees with work done by others. At high intensities harmonic components of the fundamental are generated and the attenuation of the fundamental component is increased. The increase in flow resistance at high intensities is found to effectively increase the impedance of the materials. The impedance increase makes it more difficult for a sound to enter and propagate in the material.

In the next chapter, Chapter III, the methods for testing and evaluating porous materials are discussed. In Chapter IV the results of Chapter II are compared to data obtained from the experiments and conclusions about the theoretical methods are discussed.

CHAPTER III

EXPERIMENTAL METHODS

This chapter contains a description of the experimental methods and physical apparatus that were used to determine the properties of the bulk porous materials. The chapter is divided into the following sections:

A. Porosity

B. Material Structures

C. DC Flow Resistivity

D. Acoustic Propagation Parameters

E. Specific Normal Acoustic Impedance

F. Summary

A. Porosity

The porosities of the various materials were determined by using the following procedure. The density of each sample was determined by carefully measuring the sample and weighing it on an analytic balance. The density of the skeleton material was determined from the literature or the manufacturer. The porosity was determined from

$$P = 1 - \frac{m}{DV} \quad ,$$

where m and V are the measured mass and volume, respectively, of the sample and D is the density of the solid material. The porosity ranges of the various materials used in the present study and some densities for the solids of acoustical materials are listed in Table III-1.

TABLE III-1

A LIST OF THE POROSITY RANGES FOR THE SAMPLES USED IN THE PRESENT STUDY AND DENSITIES OF VARIOUS ACOUSTICAL MATERIALS

Material	Density Range D, kg/m^3	Porosity Range P
Kevlar 29 aramid [90] (an aromatic polyamide)	1439 ± 30	0.985-0.809
Polyimides [50]	1439	----
Scottfelt 900-Z [89]	1153 ± 32	0.942-0.853
Polyurethane Plastic [50]	1107 - 1246	0.971
Glass (minimal binder) [50]	2518 - 2601	0.982
Aluminum [50]	2600 - 2900	----
Steel [50]	7400 - 7800	----

Beranek [6] devised an instrument to measure the porosity directly. A device of this type was built for the present study. The device is not as accurate and the measurements are not as repeatable as the weight method described above.

B. Material Structures

The material structures were determined by photographing the materials with a camera-bellows combination. Fiber size and material structure are useful in determining the material properties. Photos of the Kevlar®29 (manufactured by du Pont de Nemours & Co., Wilmington, DE) and the Johns-Manville 1000 (J-M 1000) fiberglass (supplied by Johns-Manville) are shown in Fig. III-1, of the Scottfelt 900-Z-2 (supplied by Scott Paper Co., Foam Division, Chester, PA) and the Blachford Acoustical Foam (BAF) (supplied by H. L. Blachford, Inc., Corona, CA) in Fig. III-2.

We see that the Kevlar 29 fibers are larger (12 μm) than the glass fibers (10 μm). The structural members of the two foams are larger than the Kevlar fibers. The Scottfelt has an effective diameter ≈40 μm (±15 μm) and the BAF effective diameter ranges between 30 and 140 μm (we use 75 μm in later calculations). The BAF has "window panes," which partially close off some of the cells of the foam. The BAF is a partially reticulated foam, whereas the Scottfelt is a fully reticulated foam, i.e., the Scottfelt has no "window panes."

A. BATTED KEVLAR 29

B. JOHNS-MANVILLE 1000 FIBERGLASS

1mm

FIGURE III-1

PHOTOGRAPHS OF BATTED KEVLAR 29 AND

JOHNS-MANVILLE 1000 FIBERGLASS

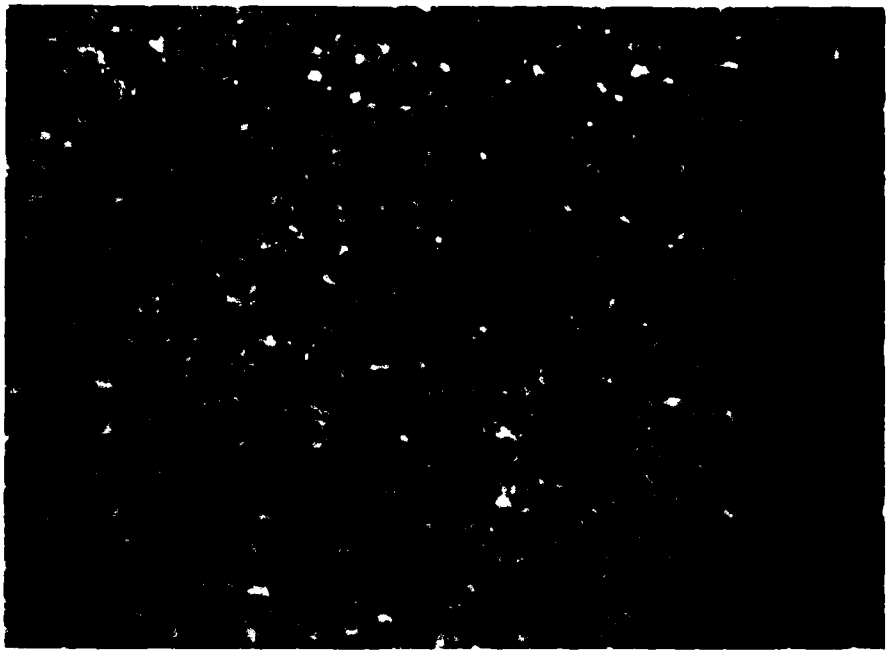

A. SCOTTFELT 900-Z-2

1 mm

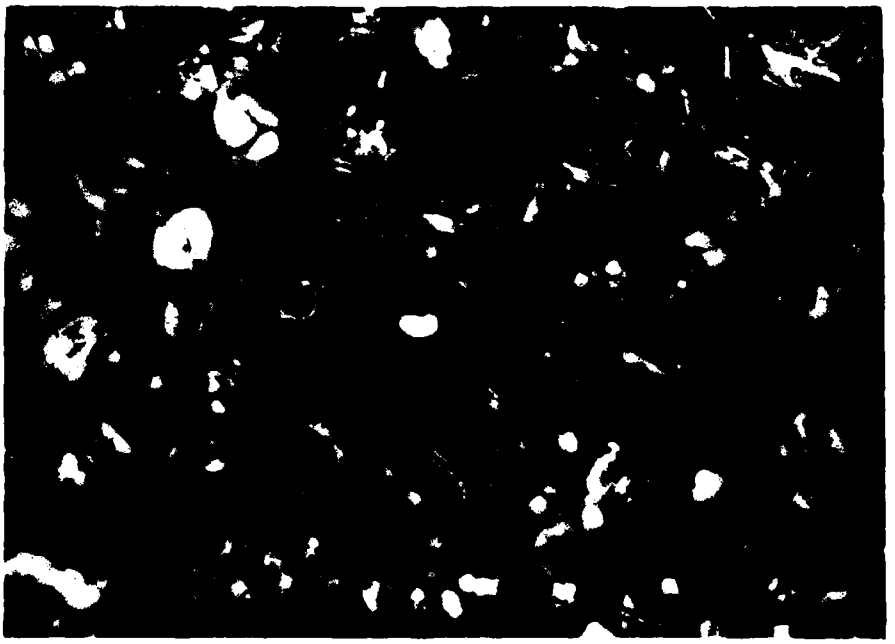

B. BLACHFORD ACOUSTICAL FOAM

FIGURE III-2

PHOTOGRAPHS OF SCOTTFELT 900-Z-2 AND

BLACHFORD ACOUSTICAL FOAM

C. DC Flow Resistivity

In Chapters I and II the dc flow resistivity σ of a porous material was shown to be important in determining the acoustical properties of a porous bulk absorber. In Chapter II, Eqs. II-9 and II-10, we found that the flow resistivity can be measured in dc flow tests. The measurement method is straightforward and follows the ASTM standard [2]. The details of the particular measurement system used here are presented.

A block diagram of the measurement system is shown in Fig. III-3. The porous samples were carefully cut and placed in the tube, which was made of clear Plexiglas. The clear plastic enables the experimenter to accurately measure the material length at any flow rate. The in place length measurement is important because some materials tend to compress with an increase in flow rate. If the compression goes unnoticed, an anomolous measure of the flow resistivity is obtained. Most samples were 7.7 cm in length. The sample was held in place between a fixed screen and a moveable screen. Each screen was made of standard ¼ in. hardware cloth. The sample was located so that its ends were at least 5 cm from the intake and exhaust ports in the tube end pieces. There was then a fairly even flow across the surface of the sample. Great care was taken to avoid flanking, that is, flow around the outside of the sample. If flanking was noticed, it was stopped by inserting thin plastic sheets between the tube wall and the material. Corrections for the presence of the plastic sheets were then made in calculating the flow resistivity.

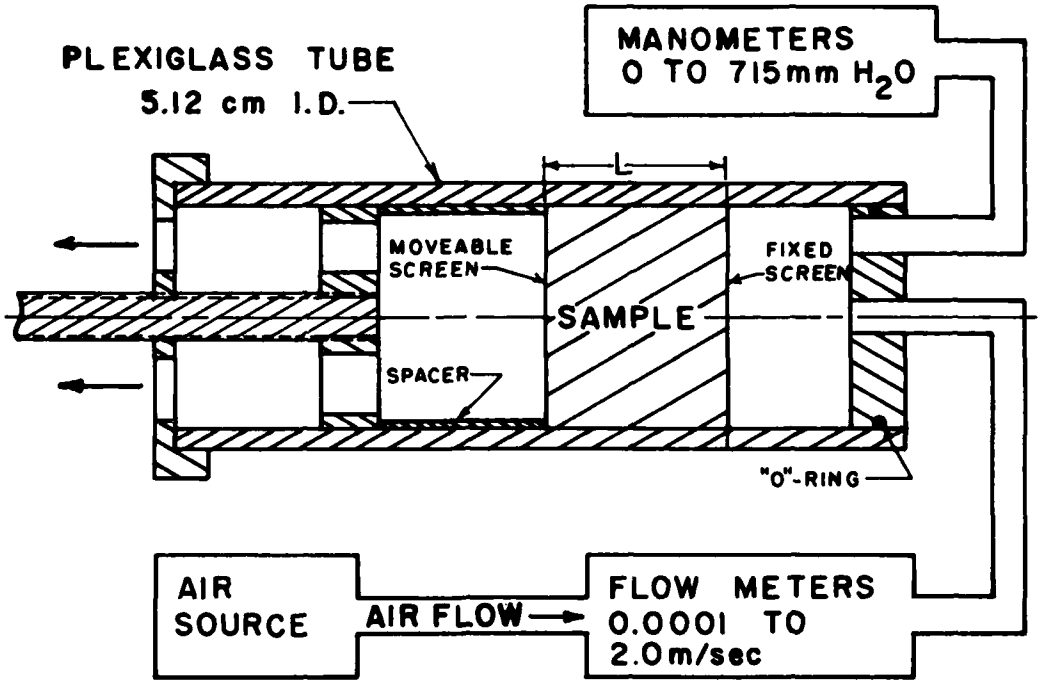

BLOCK DIAGRAM OF THE DC FLOW RESISTIVITY MEASUREMENT SYSTEM.

AIR FLOW METERS	VOLUME FLOW RATES (SCF/HR)
DWYER RMA-1	0.05 - 0.5
DWYER RMA-3	0.2 - 2.0
DWYER RMB-50	1.0 - 10
GILMONT B312	5 - 70
DWYER RMB-55	40 - 400

MANOMETERS

DWYER 1 INCH GAUGE

WEHLING 3 INCH GAUGE

UTUBE 15 INCH

FIGURE III-3
BLOCK DIAGRAM OF THE DC FLOW RESISTIVITY MEASUREMENT SYSTEM AND A LIST OF DEVICES USED.

Five flow meters were used to measure the velocity of the flow. The meter types and ranges are listed on Fig. III-3. The meter ranges overlapped and the total range of particle velocity measurement was from $7 \cdot 10^{-4}$ m/s to 1.6 m/s. Flow rate measurements at the lower end of each flowmeter range tended to be in error by up to ±12%. In the least squares fit of the data this error was minimized because of the many measurements taken and because of the data overlap.

Three manometers were used to measure the pressure drop across the sample. The manometer types and ranges are listed in Fig. III-3. The range of pressure measurement was from 5 Pa ($5 \cdot 10^{-5}$ atm) to 7700 Pa (0.076 atm).

D. Propagation Parameters

First, attenuation α (nepers/meter) and phase β (radians/meter) were measured in a square duct at low sound intensity for the various porous materials used in this study. From the phase measurements the phase speed was calculated. A simple two microphone method was used. Several different types of low-intensity sound signals were used and gave comparable results. The system and measurements are discussed in subsection 1 below. The high amplitude sound testing was done with the same experimental system, but only pulsed sinusoids were used as signals. These measurements are discussed in subsection 2 below.

1. Propagation at Low Intensities

Measurements of the small-signal propagation parameters were made with the material to be tested in a traveling wave tube. A block diagram of the propagation parameter measurement system is shown in Fig. III-4. See Appendix B for detailed drawings of the system. The Brüel and Kjaer type 4136 microphones (¼ in. diameter) were placed in holes in the tube wall. The microphones were recessed ($\simeq$ 4 mm) from the material surface. The remote microphone was vibration isolated (see Appendix B). Vibration isolation for the source microphone was found to be unnecessary. Measurements were taken at several microphone separations d (see Fig. III-4). Unused microphone holes were plugged and sealed. The material length was such that reflections from the far end of the material were unimportant [$\alpha(L-d) >> 1$]. The passband of the James B. Lansing 375-H (aluminum diaphragm) acoustic driver was

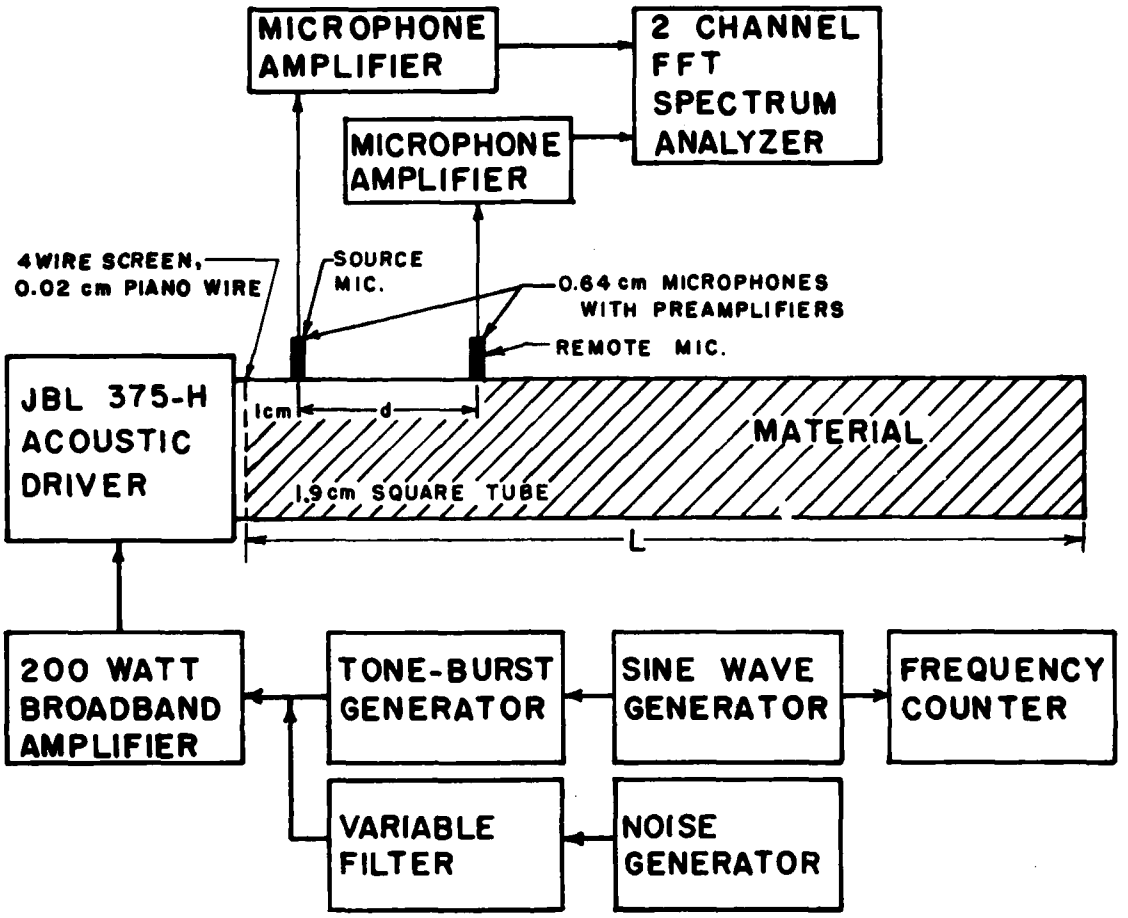

MICROPHONE HOLE SPACINGS:
d = 1, 2, 3, 4, 5, 8, 11, 15, 20, 25, 30, 35, and 40 cm.
WIRE SCREEN LOCATED 9 cm FROM THE DIAPHRAGM.

FIGURE III-4
BLOCK DIAGRAM OF THE TRAVELING WAVE TUBE SYSTEM USED IN THE PROPAGATION PARAMETER AND SATURATION TESTS.

approximately 0.25-8 kHz. The upper limit of the useful frequency range of each tube is the first cross mode cut-on frequency in the material. The cut-on frequency depends on the material and is between 5 and 9 kHz.

The propagation parameters α and β were measured by using several excitation signals, broadband noise, narrowband noise, sine sweep, pure tone, and tone bursts (the tone bursts are described in the next subsection). In each case the fast Fourier transform (FFT) spectrum analyzer was used to display the waveforms, spectra, and transfer function. The different excitation signals gave equivalent results and the transfer function of the broadband noise signal between the microphones was used to determine most of the small signal propagation parameters.

2. Propagation and Saturation at High Intensities

The experimental setup in the high-amplitude sound propagation testing was the same as described in Section B-1. Because of the limited steady-state power handling capabilities of the driver ($\approx$ 25 W), the high-amplitude sounds could only be achieved by using unfiltered pulsed sinusoids. The maximum pressure amplitude was limited by the power output of the amplifier (200 W at 70 Vrms). It was felt that the drivers would be capable of handling this power as long as the duty cycle was very short [64]. It turned out that one driver failed after several thousand pulses and a second started to generate unwanted harmonics after several thousand pulses. In each case the voice coil separated from the diaphragm. In the first case the coil distorted, rubbed the magnet, and shorted out. The sound pressure levels of the fundamental component obtained were up to 173 dB at 1 kHz,

170 dB at 2 kHz, and 172 dB at 3 kHz. These values were obtained by driving the amplifier up to its clipping limit (100 V peak amplitude). The pulse length was 0.004 to 0.005 seconds, and at least five pulses were averaged by the Fourier transform analyzer. The second harmonic distortion of the microphone system is ≈2.5% at 173 dB SPL, i.e., the second harmonic component introduced by the microphone system is 141 dB [20]. Above 170 dB the measured second harmonic distortion of the waveforms ranged from 7-25% at the source microphone.

Two types of tests were made. The change of the amplitude of the harmonic components with distance was measured. During the same tests the distance was fixed and the change of the amplitude of the harmonic components with increase in the source level was measured. At each frequency the sound levels were started at 120 dB and increased in 5 or 10 dB steps until the maximum level was obtained. The latter study shows the approach to saturation of a wave traveling in the material. The phase change with amplitude between the components was also measured. The test results indicate how sounds propagate in porous materials with respect to distance, frequency, amplitude, and material attenuation and nonlinearity. An interesting point is made here about the waveforms: Even at very high intensities very little distortion of the waveform was seen; most waveforms were sinusoids or slightly distorted sinusoids. This slight distortion may be inferred from the spectrum measurements presented in Chapter IV.

E. Specific Normal Acoustic Impedance

Specific normal acoustic impedance was measured by using a standard standing wave impedance tube for the low-intensity tests [1] and single cycle sine wave tone bursts for the high-intensity tests [47]. The low-intensity tests are discussed first.

1. Impedance at Low Intensities

Specific normal acoustic impedance at low sound amplitudes was measured with two standing wave tube systems, one for low frequencies and one for high frequencies. The block diagram of the basic measurement system is shown in Fig. III-5. The low-frequency (0.1-1.3 kHz) tube had been constructed years earlier and is described in Ref. 71. The high-frequency (0.8-3.9 kHz) tube was designed for this project. Construction drawings for it are included in Appendix B.

The test method follows ANSI/ASTM C384-77[1]. The equipment was calibrated by using a tight-fitting aluminum plug (5 cm long) in the high-frequency tube and a thick steel end-cap, sealed around the edges, at the end of the low-frequency tube. In each case the termination was assumed to be of infinite impedance and the distance between the microphone and the termination was acoustically measured at each test frequency. The calibration results were used to correct for the environmental effects (such as tube wall attenuation, effective microphone position, etc.) in calculating the material impedance. In the high-frequency tube the probe position can be located to within ±0.1 mm and test results are very repeatable. In the low-frequency tube the microphone location can be determined to within ±4 mm and the error affected the measurement accuracy.

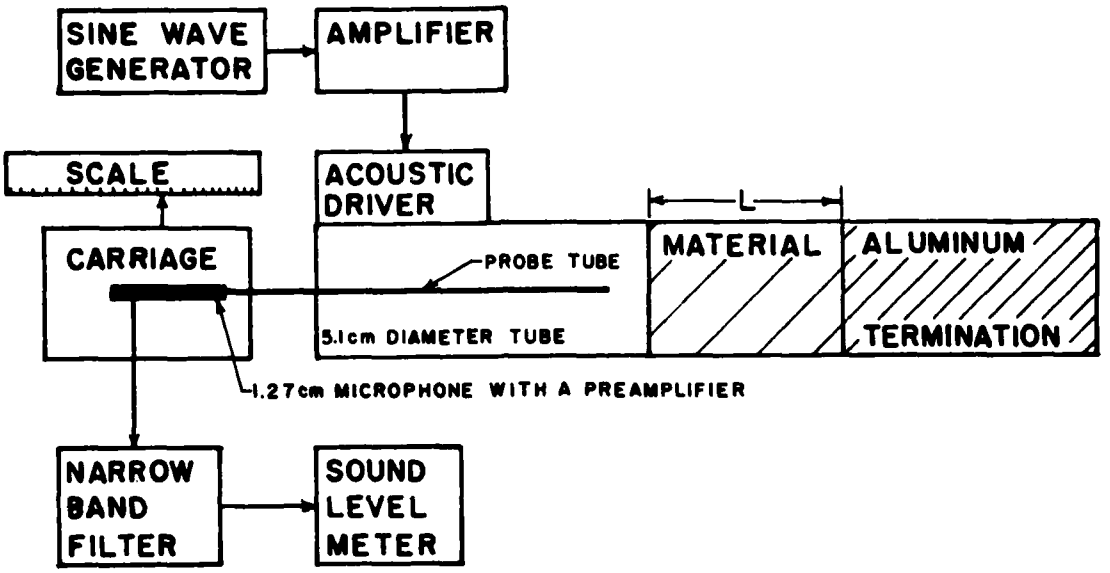

FIGURE III-5
BLOCK DIAGRAM OF THE STANDING WAVE IMPEDANCE TUBE SYSTEM USED IN THE MEASUREMENT OF THE IMPEDANCE OF FINITE THICKNESS MATERIALS.

Materials of various types and thicknesses were measured in each tube, but the most common thickness was approximately 7.7 cm. (For checking the reliability of the single-cycle pulse measurement method, described next, a 30.7 cm thick sample was used in the high-frequency tube.)

2. Impedance at High Intensities

The single cycle tone burst test used here is a simple and, apparently, unique method for measuring the impedance of bulk acoustic materials at high intensities. There are several reasons for using a tone burst to measure the high-intensity impedance. We have already discussed several reasons in Section I-C-2.

As sound intensity increases in a standing wave tube nonlinear effects become evident. Distortion and shock formation cause the method to fail because the waveshape and amplitude change as the wave travels toward the sample and again after reflection. The properties of intense standing waves are much harder to predict than those of intense traveling waves. If the sample behaves nonlinearly, additional wave distortion is introduced at the material surface and separation of the nonlinear effects becomes extremely difficult.

We can limit the noticeable nonlinear effects on the traveling wave by using a tone burst. As we shorten the tone burst less travel distance is necessary to resolve the incident and reflected waves at the microphone. As the amplitude increases, the shock formation distance is reduced, according to $\bar{x} = 1/\beta' \epsilon k$, and the waveform distorts at a faster rate [16]. When $\bar{x} < x$, where x is the travel

distance, a shock is formed in the calibration signal and the measurement method is no longer reliable.

The assumption on which the test method is based is that, as long as a shock is not formed, the attenuation of a wave as it travels down the tube and is reflected from the termination will proceed in an almost linear fashion [16]. The calibration tests at the various amplitudes and frequencies can be used to cancel out any small excess attenuation encountered by the fundamental in the production of the higher harmonic components.

A block diagram of the measurement system is shown in Fig. III-6. The mirophone was placed to minimize the travel distance of a 1 kHz single cycle tone burst. The useful frequency range is 1 kHz (set by tube length) to 4 kHz (set by cross-modes). The sound level limits are dependent on tube length and frequency. When $\bar{x} = x = 96.4$ cm, the sound level upper limits are, for 1 kHz, 167 dB and, for 4 kHz, 155 dB.

The polarity of the signal is such that a 165 dB, 1 kHz single cycle sine wave, shown in Fig. III-7.A, is produced. The frequency spectrum of the signal is shown in the right column. In Fig. III-7.B an ideal single cycle sine wave and its spectrum are shown. By comparing the waveforms in Figs. III-7.A and III-7.B, we find that the actual signal is asymmetric and contains an extra "tail." The "tail" is formed by high frequency cross-modes that are generated in the tube and travel at different phase speeds than the tone burst. Both the asymmetry and "tail" affect the frequency spectrum by adding more low-frequency and high-frequency energy. The high-frequency lobes

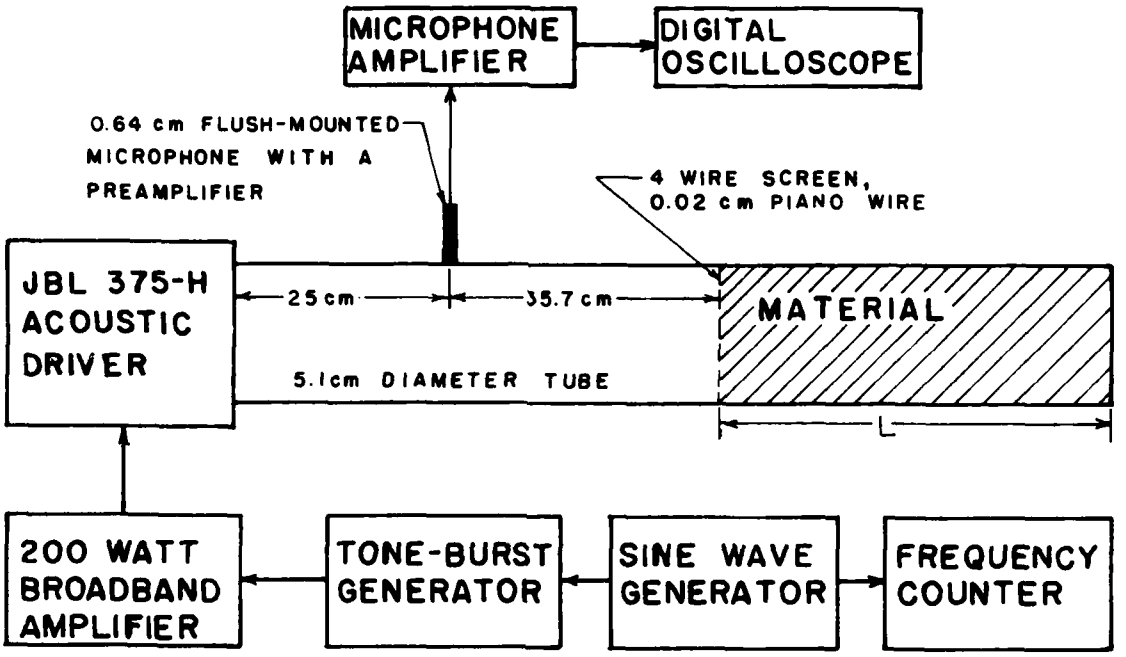

FIGURE III-6
BLOCK DIAGRAM OF THE TRAVELING WAVE IMPEDANCE TUBE SYSTEM USED IN THE LOW- AND HIGH-INTENSITY SOUND IMPEDANCE TESTS.

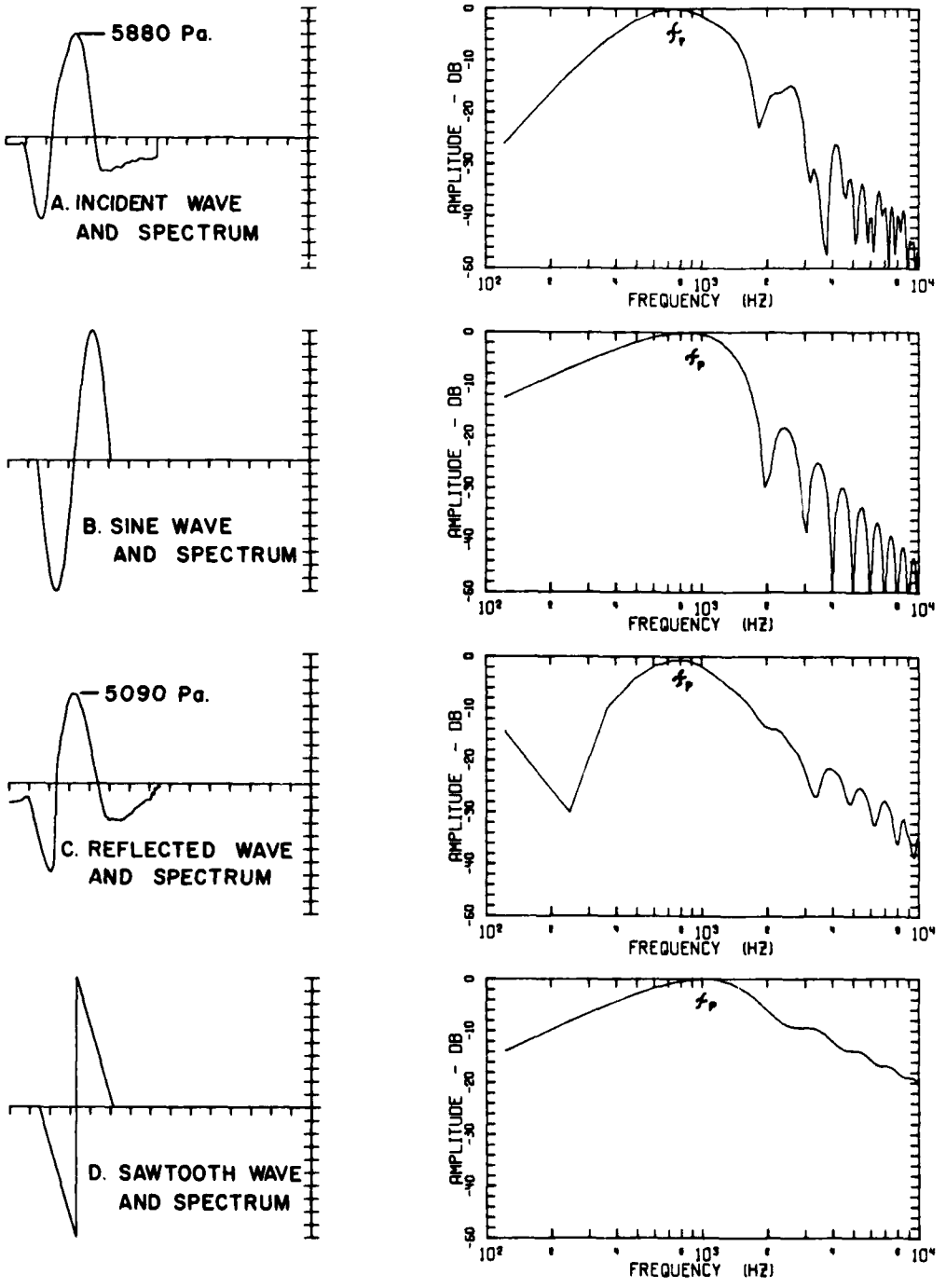

FIGURE III-7
IDEAL AND MEASURED WAVEFORMS AND SPECTRA OF A SINGLE CYCLE SINE WAVE AND OF A SINGLE CYCLE SAWTOOTH WAVE.

of the actual signal are not as uniform as for the spectrum of the ideal wave. In addition, the peak frequency is approximately 100 Hz lower than for the spectrum of the ideal wave. If the analysis is done in the frequency domain, then this extra energy can cause severe problems which could lead to erroneous analysis. We restrict our analysis to measuring the peak-to-peak amplitudes of the waves and the time delay.

The waveform polarity was chosen such that, as the wave travels, a shock forms at the center. If the wave is symmetric, all three axis intersection points will travel at the adiabatic sound speed c_o and the frequency spectrum peak will not shift. The waveforms are asymmetric and after a shock forms the relative time delay is uncertain. If the waveform polarity was reversed, shocks would form on each end of the wave and the frequency spectrum would shift as a function of amplitude.

In Fig. III-7.C the incident wave of Fig. III-7.A is shown after it was reflected off an aluminum termination. The waveform has almost formed a shock. The associated frequency spectrum shows that energy has been shifted to the higher frequencies. The wave is on its way to forming a single cycle sawtooth waveform. In Fig. III-7.D an ideal single cycle sawtooth waveform and spectrum are shown. We see that the spectrum in Fig. III-7.C shows that the reflected wave is partway between the ideal waves shown in Figs. III-7.B and III-7.D.

For higher frequency tone bursts the spectra are influenced more and more by the "tail." The resulting frequency spectra tend to "smear" and a localized frequency peak is not definable. If the "tail"

is cut off, the peak is more localized, but other high frequency components are introduced by the cutting operation.

In this testing program we measured (1) the time delay between the incident and reflected wave-center zero crossings and (2) the change in peak-to-peak amplitude. The ANSI/ASTM C384-77 test method [1] was modified to deal with traveling waves. The amplitude change was used to determine the material absorption coefficient and the delay time was used to determine the phase shift. The impedance was calculated from a combination of the amplitude change and the phase shift. The system was calibrated by replacing the material with a tight-fitting aluminum plug and by assuming that the measurement results indicate an infinite impedance. In the experiment, shock formation caused excess attenuation of the traveling wave. Past the shock formation distance calibration canceled some of the excess attenuation, but not all of it. In our case, asymmetry of the waveform (the positive pressure magnitude is greater than the negative pressure magnitude) caused the shock to propagate faster than the speed of sound and the associated phase shift could not be computed past $\bar{x}$. This waveform asymmetry is caused by inertia of the driver diaphragm.

The advantages of this measurement method over other measurement methods [59,64] are that the travel distance is short and the tone burst does not lengthen as it travels [16]. In addition, as the shock forms, the tone burst spectrum changes only a moderate amount. This spectrum change is illustrated in Fig. III-7 for both the ideal and measured signals [18]. Finally, the material needs only to be long

enough that a wave reflected from the material termination does not interfere with the wave reflected from the material surface.

The disadvantages of this measurement method are that it is amplitude limited and the waveform tends to be asymmetric. In addition, the spectrum is not that of a pure tone, but narrowband (see Fig. III-7, where, ideally, the -3 dB bandwidth is 0.74 f_p and -6 dB bandwidth 1.1 f_p, where f_p is the nominal frequency peak in the spectrum).

F. Summary

The various measurement systems and methods for the determination of porous material properties have been described. The topics covered have been on determination of porosity, material structures, dc flow resistivity, propagation parameters, and impedance.

In Chapter IV the measured material properties are compared to theoretical results from Chapters I and II. The dc flow resistivity results are found to depend on the porosity and particle velocity in the expected manner. The material structure has definite effects on the acoustic measurement results. The low-intensity and high-intensity results are illustrative of the topics discussed in the previous chapters

CHAPTER IV

EXPERIMENTAL RESULTS

In this chapter data from experiments are compared to results of the theory developed in Chapters I and II. The objectives of this chapter are to illustrate the acoustical properties of porous materials with changing sound level and to determine how accurately the experimental results can be predicted by using the theoretical models. A variety of materials was used in the various tests and, where reasonable, representative results from the tests for each material are presented. Generalizations are made for various materials and limitations of the theories are discussed.

In Section A we present measured and predicted results and discuss (1) the linear and nonlinear dc flow resistivity coefficients, (2) the applicability of the previously derived dependence of flow resistivity on porosity, and (3) the applicability of the modified Reynolds number in predicting nonlinearity threshold. The results of Section A are used in the calculations of Sections B and C.

In Section B we present measured and predicted results and discuss (1) the small signal attenuation and phase speed, (2) excess attenuation and the approach to saturation, and (3) high-intensity propagation.

In Section C we present measured and predicted results and discuss (1) the small signal impedance for finite and semi-infinite porous materials, and (2) the impedance change of semi-infinite materials with sound intensity.

In Section D we summarize the results of this chapter.

A. DC Flow Resistivity

The physical measurement apparatus and method used to determine the dc flow resistivity of porous materials is described in Section III-A. After first presenting the flow resistivity data and determining the nonlinearity, we then discuss how well the empirical models fit the data.

1. Flow Resistivity Determination

Flow resistivity data were taken in a particle velocity range of $2 \cdot 10^{-4}$-2 m/s. From a least squares fit of the data the coefficients σ and η were calculated; see Eq. II-10.

In Fig. IV-1 the measured dc flow resistivities for five porosities of Kevlar® 29 are plotted versus dc particle velocity. Each sample was 7.7 cm in length. For the three highest porosities, at particle velocities above 1 m/s, the data have been corrected for the small length compression that occurred. The compression had no measureable effect on the porosity, but noticeably affected the resistivity because the resistivity is inversely proportional to the material length. This material exhibits linear flow resistivity for most of the test velocity range. As discussed in Chapter I, all porous materials are expected to exhibit nonlinear behavior for particle velocities above some threshold value. The Kevlar 29 fiber diameter is 12 μm and we use Eq. I-27 to calculate the nonlinearity threshold ($R_m = 1$) to occur at 0.099 m/s for $p = 0.980$ and at 0.40 m/s for $p = 0.918$. The theoretical thresholds are indicated by the vertical bars on the figures. In comparing the predicted threshold particle

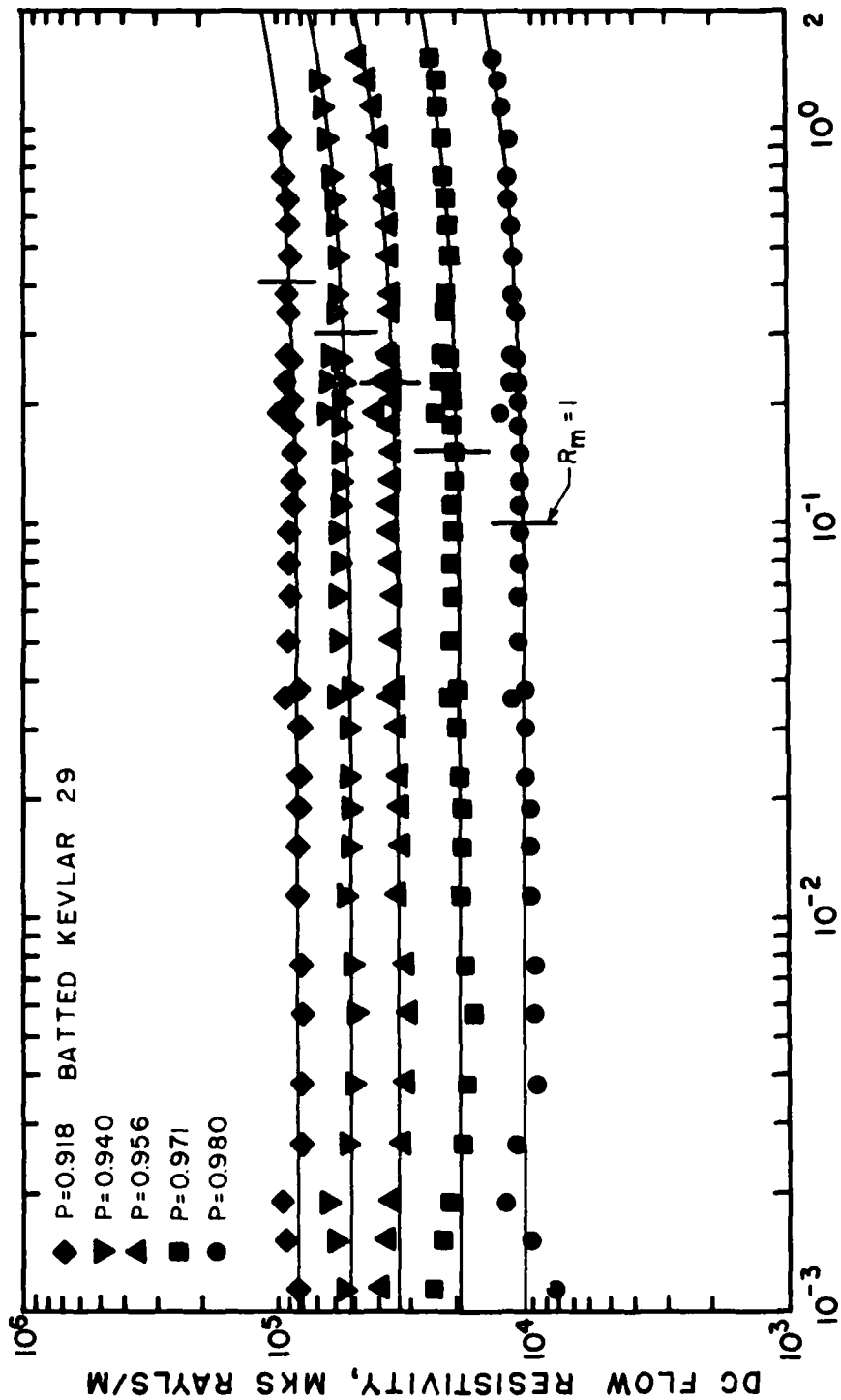

FIGURE IV-1
MEASURED DC FLOW RESISTIVITY VERSUS PARTICLE VELOCITY
FOR FIVE POROSITIES OF BATTED KEVLAR 29.

velocities with the points at which the curves actually start to turn up we see that the nonlinearity threshold is not precisely predicted by the modified Reynolds number at the lower porosities. The measured deviation from linear behavior is 2% for $P = 0.980$ at 0.099 m/s and 7% for $P = 0.918$ at 0.40 m/s. Though slightly inconsistent, the predicted and measured thresholds are in general agreement.

In Fig. IV-2 the measured dc flow resistivites for three different Scottfelt samples are plotted versus dc particle velocity. Each sample was approximately 7.7 cm in length. These materials did not compress with increase in particle velocity. Scottfelt exhibits linear flow resistivity behavior over as wide a particle velocity region as Kevlar. Even though the Scottfelt is not fibrous, we assume the effective "fiber" diameter of the foam material to be 40 μm (Fig. III-2). We calculate the nonlinear threshold to occur at 0.086 m/s (3% deviation) for 900-Z-2 Scottfelt ($P = 0.942$) to 0.218 m/s (7% deviation) for 900-Z-6 Scottfelt ($P = 0.852$). As with the Kevlar the estimate based on $R_m \approx 1$ is reasonably good.

In Fig. IV-3 the measured flow resistivities for two pieces of Blachford Acoustical Foam (BAF), Johns-Manville 1000 (J-M 1000) fiberglass, and Globe-Albany (G-A) needled and felted Kevlar 29 are plotted versus dc particle velocity. The two fibrous materials, Kevlar 29 and fiberglass, are linear over most of the particle velocity range. The BAF exhibits nonlinear behavior at a relatively low particle velocity. Although the two BAF samples were taken from areas within a half meter of each other in the same 7.6 cm thick sheet,

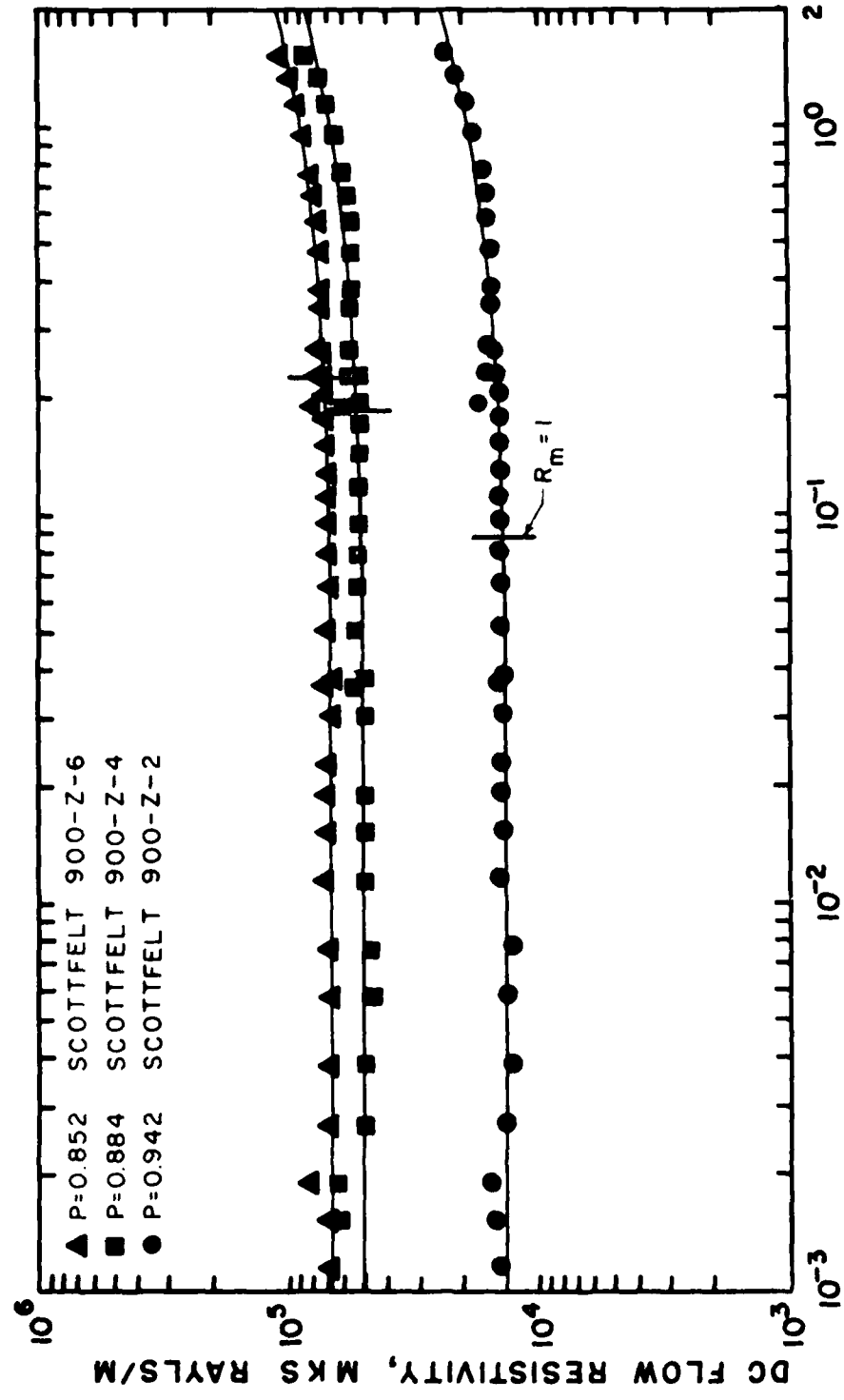

FIGURE IV-2
MEASURED DC FLOW RESISTIVITY VERSUS PARTICLE VELOCITY
FOR THREE POROSITIES OF SCOTTFELT.

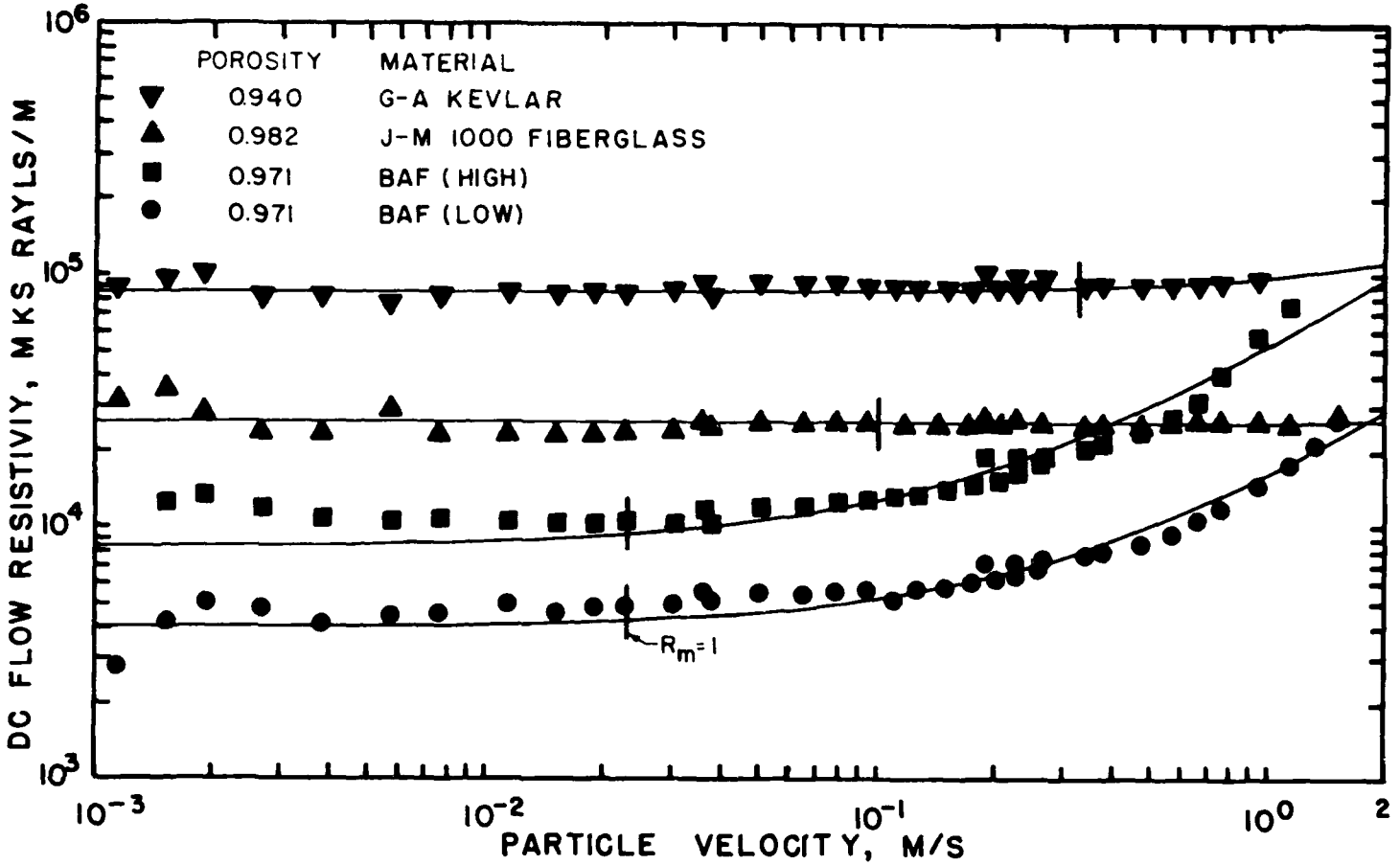

FIGURE IV-3
MEASURED DC FLOW RESISTIVITY VERSUS PARTICLE VELOCITY FOR GLOBE-ALBANY KEVLAR 29, JOHNS-MANVILLE 1000 FIBERGLASS, AND BLACHFORD ACOUSTICAL FOAM.

the flow resistivities of the two samples were different by a factor of 2-4. This result illustrates that, for foams, variations that are not discernable can drastically influence the flow resistivity properties. In turn, the acoustical properties may also be expected to vary drastically. The porosities of each of the many BAF samples tested were measured to be 0.971 ±0.001. The small porosity range and large flow resistivity range indicate that structural factors are important. The fiberglass fiber diameters are approximately 10 μm, the G-A Kevlar 29 fiber diameters are approximately 11 μm, and the foam "fiber" diameters range from 31 μm through 140 μm, (75 μm was used in the calculations). The calculated nonlinearity thresholds based on $R_m = 1$ are for the J-M 1000 fiberglass 0.11 m/s (0.1% deviation), for the G-A Kevlar 0.32 m/s (5% deviation), and for the BAF 0.023 m/s (Low 7% and High 12.5% deviations).

In addition to the large "fiber" size, the low threshold of nonlinearity found in the BAF may also be partially explained by the material structure. The BAF is a partially reticulated material, meaning that some of the spaces between the structural members have thin membrane window panes. The window panes obstruct the flow and make the flow turbulent at a lower particle velocity than the average fiber size 75 μm indicates. The measured nonlinearity threshold is still reasonably close to the predicted value. The windows cover less than 25% of the foam openings. The threshold is therefore lowered only a relatively small amount. A material with a higher percentage of closed windows would be expected to have both a lower nonlinearity

threshold and a higher flow resistivity. This statement is supported by the fact that the fully reticulated Scottfelt has a high nonlinearity threshold and is of the same structure as the BAF but without window panes.

The dc flow resistivity data presented here shows that most materials behave nonlinearly and illustrates the relative dc nonlinearities of the various materials. The least squares data fit is a good descriptor of both the linear and nonlinear regions of the flow resistivity. For most of the materials, Carman's analysis of the location of the threshold of nonlinearity is reasonable in the porosity region $0.8 < P < 1.0$. From the previous measurement results, a general rule of thumb would be that Carman's modified Reynolds number predicts the nonlinearity threshold of fully reticulated materials to be in a region of between 2% and 7% of the flow resistivity deviation from linear. Table IV-1 lists a summary of the linear and nonlinear dc flow resistivity coefficients and the relative nonlinearities of the materials used in this study.

2. Linear Flow Resistivity Prediction

Hersh and Walker [33,34] presented two equations for use in predicting the linear flow resistivity of fibrous porous materials; see Eqs. I-12 and I-17. One equation can be used for calculating flow resistivity for flow axially along the fibers (the axial condition was not realized in our measurements). Both equations can be used for calculating flow resistivity for flow normal to the fibers. Each equation has an empirical constant so that different material types

TABLE IV-1

LINEAR AND NONLINEAR DC FLOW RESISTIVITY COEFFICIENTS

AND RELATIVE NONLINEARITIES OF BULK POROUS MATERIALS

Material, Porosity P	Linear DC Flow Resistivity Coefficient σ, MKS Rayls/m	Nonlinear DC Flow Resistivity Coefficient η, MKS Rayls/sec	Relative Nonlinearity η/σ
Batted Kevlar			
0.980	10800.	2370.	0.219
0.971	19100.	3860.	0.202
0.956	33700.	7930.	0.235
0.940	51200.	11400.	0.223
0.918	83600.	14300.	0.172
Scottfelt			
0.942	13400.	5350.	0.399
0.884	49200.	16500.	0.335
0.852	66500.	21500.	0.323
G-A Kevlar			
0.940	83000.	12000.	0.145
J-M 1000 Fiberglass			
0.982	25500.	220.	0.0086
BAF			
0.970	6390.	27000.	4.23
0.971	3900.	12000.	3.08
0.972	8260.	43600.	5.28

may be dealt with. The two curves have been fit to measured data for batted Kevlar 29, as shown in Fig. IV-4. The solid curve is for Eq. I-12 and the dashed curve for Eq. I-17. The constants were chosen for a best Chi-squared fit to the five data points. Both curves fit the data points very well in the region of interest. For batted Kevlar 29 Hersh and Walker found that $g = 0.059$ fit their low frequency acoustic equation [33]; here we find $g = 0.061$. Hersh and Walker found $V_n = 0.44$ [34]; here, $V_n = 0.445$. In the first case the small difference in values arises from the fact that Hersh and Walker's single data point was fit to an approximate acoustic equation and not to dc flow resistivity data. In the second case the agreement is excellent and supports Davies' [24] analysis which was done with a variety of materials. In Fig. IV-5 the measured dc linear flow resistivities for several samples of each of the other materials are plotted versus the porosity. The two curves, generated from Eq. I-12 (solid line) and Eq. I-17 (dashed line), show the best Chi-squared fits to the Scottfelt data; the fits yield $g = 0.0166$ and $V_n = 1.39$. The single data points for the other materials yield $g = 0.029$, and $V_n = 0.923$ for the J-M fiberglass and $g = 0.043$, and $V_n = 0.605$ for the G-A Kevlar.

The values of g and V_n are not the same for all materials because of the vast differences in the material structures. The foams are, by no means, fibrous, the fiberglass fibers tend to bunch together (see Fig. III-1) and the G-A Kevlar does not have long, parallel strands normal to the flow. These structural effects all influence

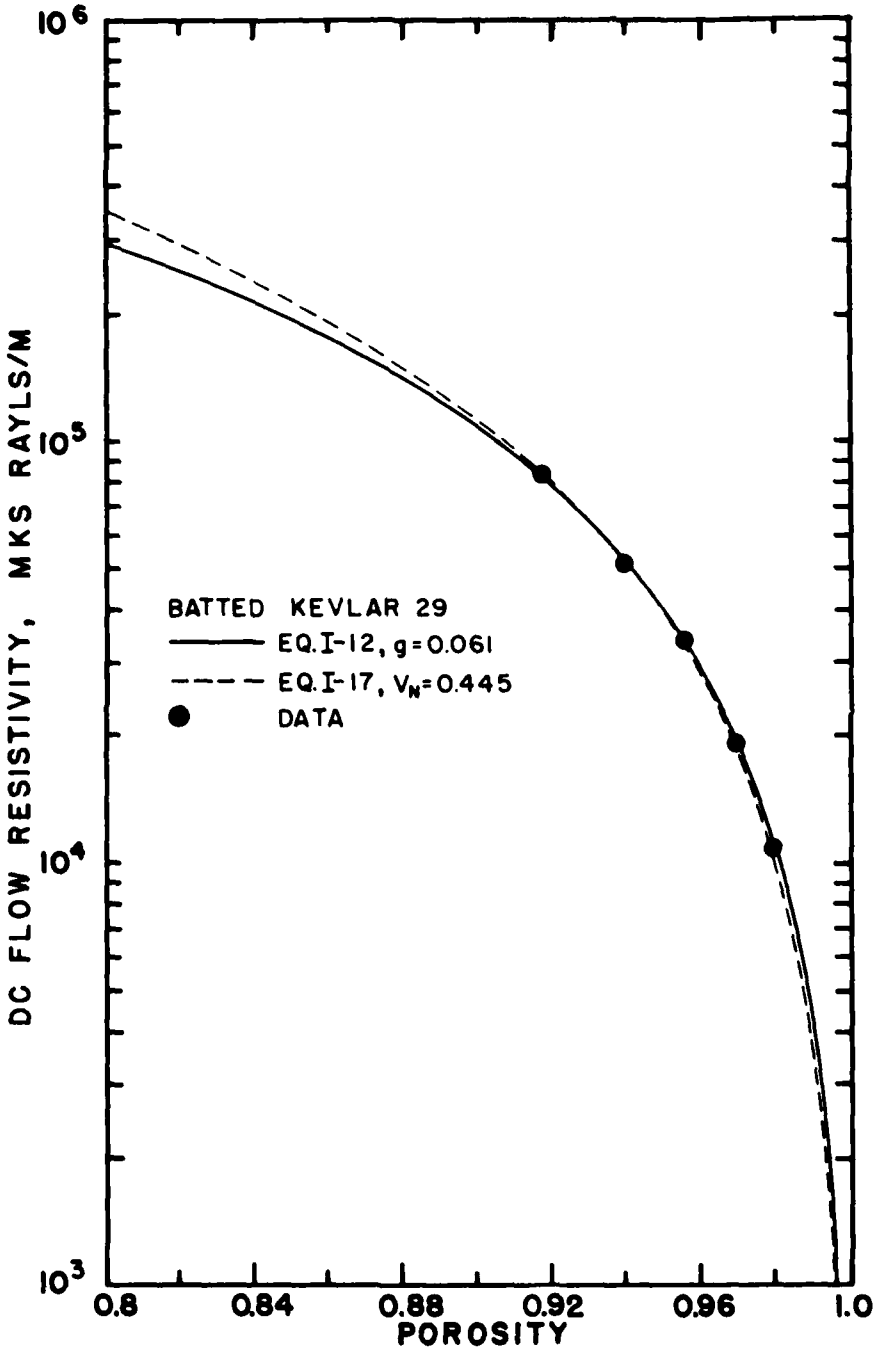

FIGURE IV-4
MEASURED DC FLOW RESISTIVITY VERSUS POROSITY FOR FIVE POROSITIES OF BATTED KEVLAR 29.

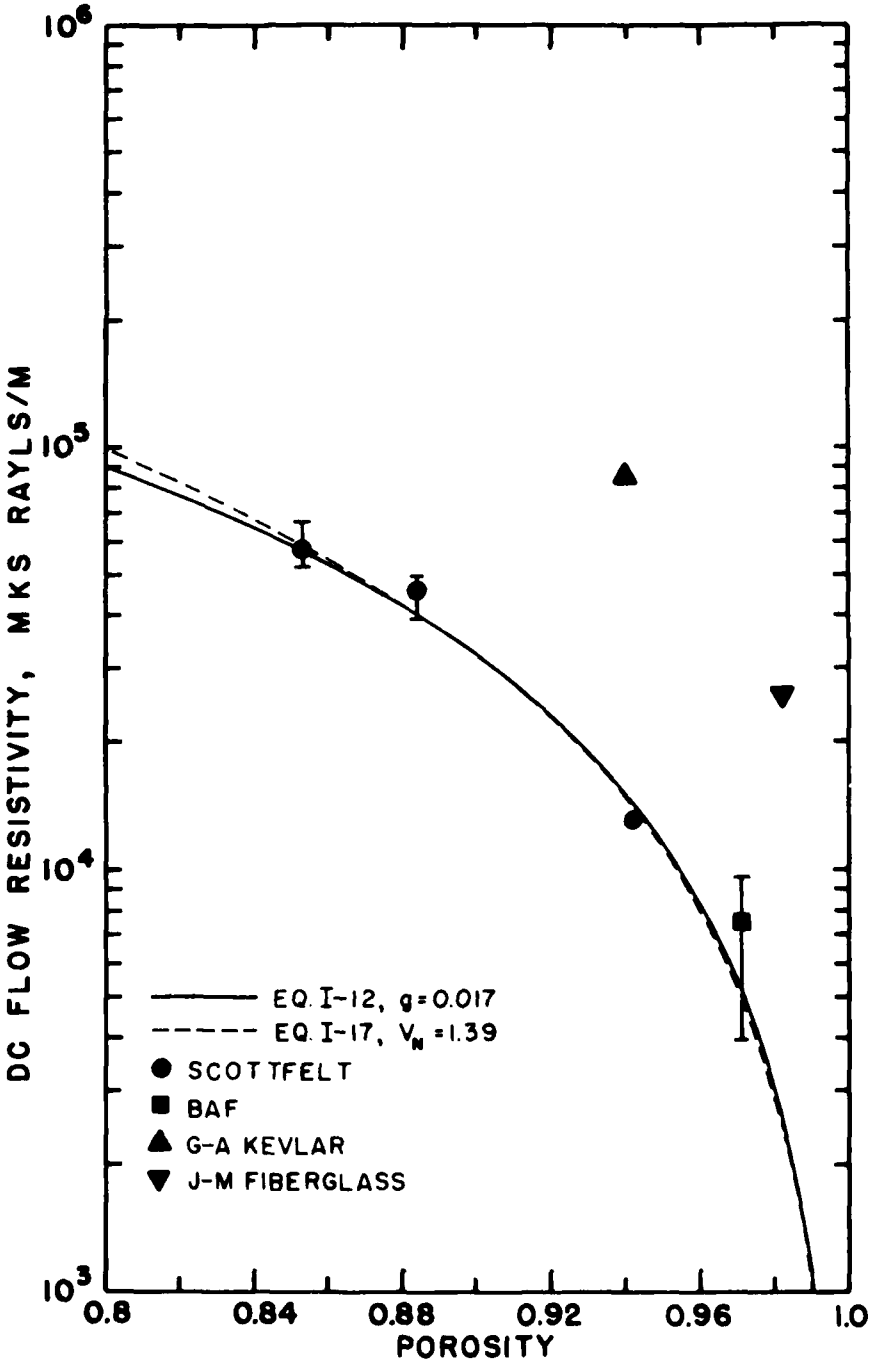

FIGURE IV-5
MEASURED DC FLOW RESISTIVITY VERSUS POROSITY FOR GLOBE-ALBANY KEVLAR 29, JOHNS-MANVILLE 1000 FIBERGLASS, BLACHFORD ACOUSTICAL FOAM, AND THREE POROSITIES OF SCOTTFELT.

the way the flow is impeded by the material. Each material type must therefore be measured separately to determine both g and V_n.

In this section it has been shown that, in the region $0.8 < P < 1.0$, once a dc flow resistivity, fiber diameter, and porosity have been determined, the change of the dc flow resistivity with porosity can be correlated to either Eq. I-12 or I-17. In the next section both measured and predicted dc flow resistivity values are used to calculate the small signal propagation of sound through the porous materials.

B. Propagation

The results of three sets of measurements, and comparison with theoretical predictions, are presented in this section. Subsection 1 is about low-intensity propagation, Subsection 2 excess attenuation and the approach to saturation, and Subsection 3 high-intensity propagation.

Measurements were made on two materials, batted Kevlar 29 and BAF. The Kevlar is of greatest interest because of its high nonlinearity threshold and the large range of porosities to which it can be compressed. The BAF is of interest because of its different structure and low nonlinearity threshold.

1. Propagation at Low Intensities

Measurements of low-intensity propagation were made in a material filled plane wave guide, as described in Section III-D. In general, broadband noise in the range 0.1-10 kHz was used to determine the propagation parameters α and β. The phase β was then used to calculate the phase speed c_{PH}. Measurements made with 1, 2, and 3 kHz tone bursts corroberated the noise measurements.

A highly magnified picture of batted Kevlar 29 is shown in Fig. III-2. The fibers are very small ($\approx$12 μm) and the material is very porous. The porosity range used in the propagation tests, $0.985 \geq P \geq 0.809$, was large enough to enable us to test the theory over a wide range.

In Fig. IV-6 the predicted and measured attenuation of sound in batted Kevlar 29 ($P = 0.980$, 0.956, 0.916, 0.875, and 0.809) is plotted versus frequency. The horizontal bars show the range of the measured data points. Where no horizontal bars are drawn, either the data points

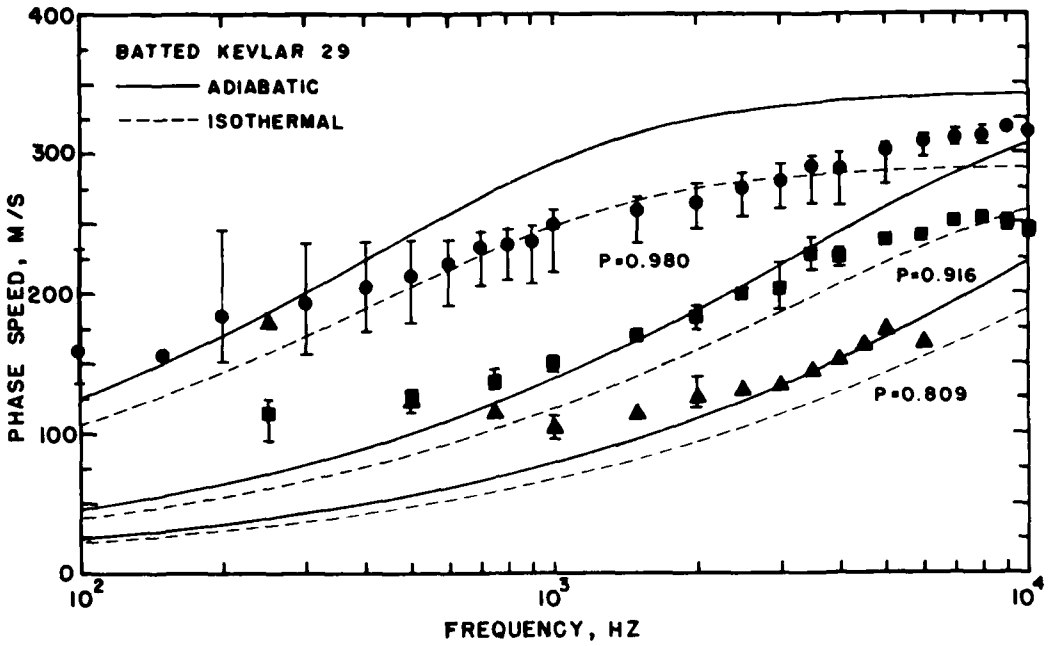

A. P = 0.980, 0.916, AND 0.809

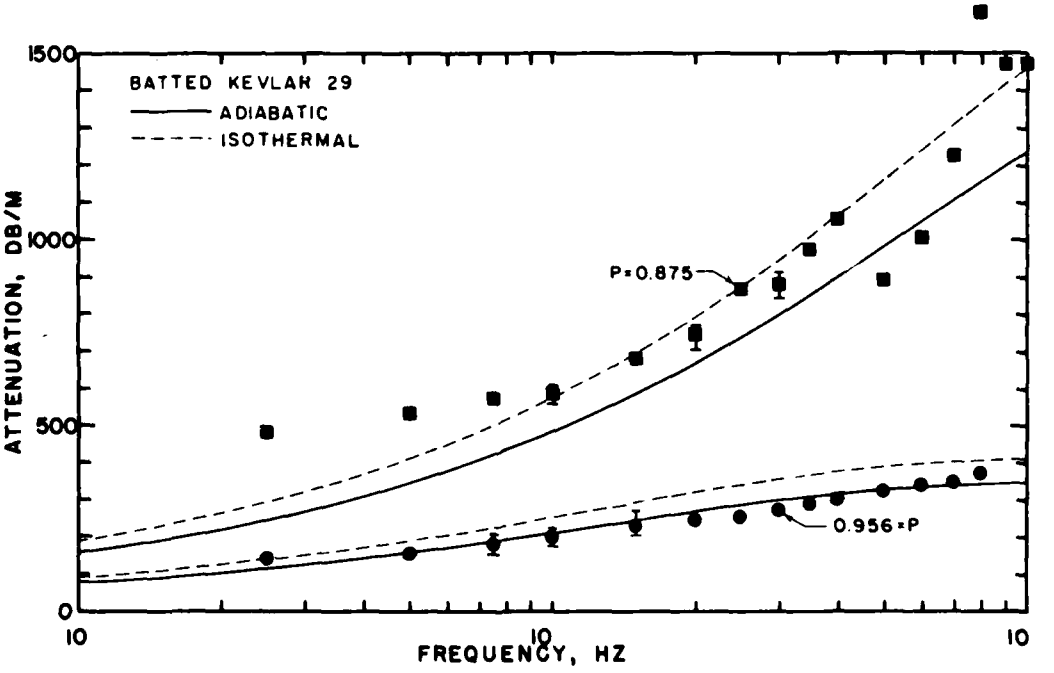

B. P = 0.956 AND 0.875

FIGURE IV-6
MEASURED AND PREDICTED ATTENUATION VERSUS FREQUENCY FOR SOUND PROPAGATING IN FIVE POROSITIES OF BATTED KEVLAR 29.

coincide, or only one data point was measured. The symbols indicate the average value of up to seven measurements at various microphone separations. The scatter in the measured values is due to inhomogeneity of the material. Since several microphone separation distances were used, the results therefore depended on the material homogeneity between the two microphones. The results of material inhomogeneity are seen later in the amplitude versus distance plots.

In the theory we assumed the isothermal sound speed. In Appendix A this assumption is shown to be inexact. In Fig. IV-6 the solid line indicates the theoretical attenuation when the adiabatic sound speed is used in Eq. I-4. The dashed line indicates the isothermal sound speed case. Since dc flow resistivity measurements were made for only five porosities ($P \geq 0.914$), Eq. I-12 ($g=0.061$) was used to calculate the unmeasured resistivities ($P = 0.916$, 0.875, and 0.809).

At each porosity there are frequency ranges where the data and predictions agree and other ranges where they diverge. The divergence of the data above 2 kHz at porosities 0.980 and 0.916 is of unknown origin but was confirmed by measurements at several microphone positions. At the low porosities, $P<0.916$, there is a leveling off of the attenuation at low frequencies. We cannot explain this low porosity, low frequency attenuation. Other researchers [33,34,49] limited their measurements of batted Kevlar 29 to $P>0.9$ and did not observe this phenomena.

From the arguments in Appendix A, the attenuation at the lowest porosity, $P = 0.809$ is expected to be very close to the isothermal (dashed) line. The data in Fig. IV-6.A show otherwise. One possible

explanation is that the flow resistivity σ is overestimated by Eq. I-12 in this porosity range. We shall return to prediction of the effective acoustic flow resistivity later in this section.

In Fig. IV-7 the predicted and measured phase speed of sound in batted Kevlar 29 ($P = 0.980$, 0.956, 0.916, 0.875, and 0.809) is plotted versus frequency. The dashed lines were calculated by using Eq. IV-6. The solid line were calculated by using Eq. I-6 with the replacement of b_o (isothermal sound speed) with c_o (adiabatic sound speed). The separation between the lines indicates the limitations of heat transfer effects on the phase speed. Although the range bars appear to indicate greater error in Fig. IV-6 than in Fig. IV-7, the largest error, in each case, is approximately ±20%.

We now discuss some of the limitations of these propagation measurement results. As the porosity is reduced the high frequency attenuation increases drastically, the coherence between the source and remote microphone signals is reduced, and the veracity of the data becomes questionable. The error starts in both the phase speed and attenuation data for $P = 0.875$ and $f > 3$ kHz. For $P = 0.809$ we have not included the $f > 4$ kHz data, because the low coherence and the large oscillations in the data lead to meaningless results.

As in the low frequency attenuation results, the low frequency phase speed results deviate from predictions at low porosities. In the low frequency case, the coherence between the signals is not reduced as much as at high frequencies. The data deviations in Figs. IV-6 and IV-7 appear to be contradictory. The attenuation increase indicates

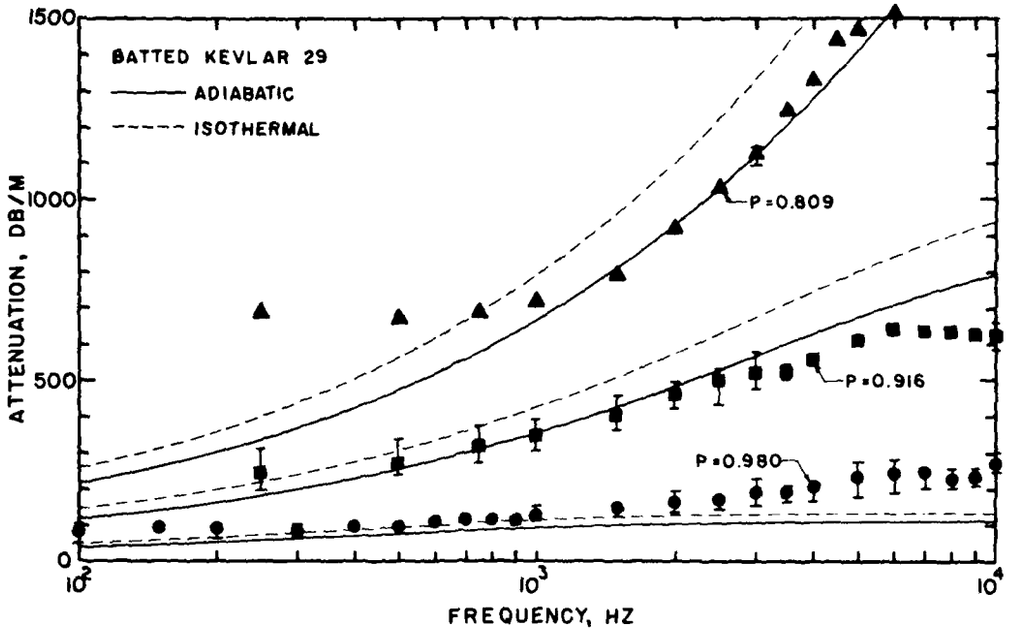

A. P = 0.980, 0.916, AND 0.809

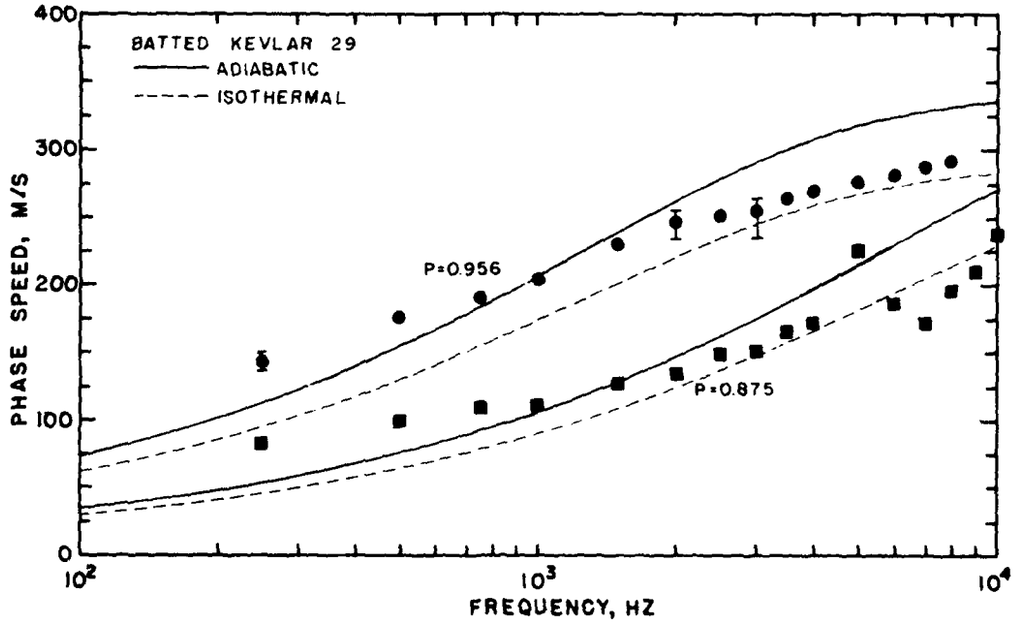

B. P = 0.956 AND 0.875

FIGURE IV-7
MEASURED AND PREDICTED PHASE SPEED VERSUS FREQUENCY
FOR SOUND PROPAGATING IN FIVE POROSITIES OF BATTED KEVLAR 29.

that the phase speed should be slower, not faster than the theory predicts. The phase speed data cannot be explained by a flanking path, because then the attenuation would be less than theory predicts. The low frequency, low porosity deviations from theory may be caused by a failure in the theory or in the measurement procedure. The deviation in question has not been resolved here. The propagation test results presented in Subsections 2 and 3 are at 1 kHz or above; the low frequency deviations do not influence other results in this study.

In Fig. IV-8 the relative sound pressure levels of three low intensity tone bursts of 1, 2, and 3 kHz are plotted versus microphone separation distance. The material is batted Kevlar 29, of porosities 0.980 and 0.809. The straight lines are computed by the average measured attenuation values (indicated by the symbols in Fig. IV-6). Up to a distance of 10 cm the Fig. IV-8 data confirm the data in Fig. IV-6 and show the materials to be homogeneous. At 20 cm the attenuation appears to be less than implied by Fig. IV-6. This reduced attenuation could be caused by one or more mechanisms, material inhomogeneity, tube wall vibrations, or a flanking path between the material and the tube wall. Although several attempts (microphone vibration isolation and material repacking) were made to solve this problem, the solutions were unsuccessful. Nonuniform material packing is the most likely cause to the deviation.

The other material tested was the Blachford Acoustical Foam (BAF). The foam was cut into a long strip of square cross section and pulled into the tube. The predicted and measured attenuations plotted

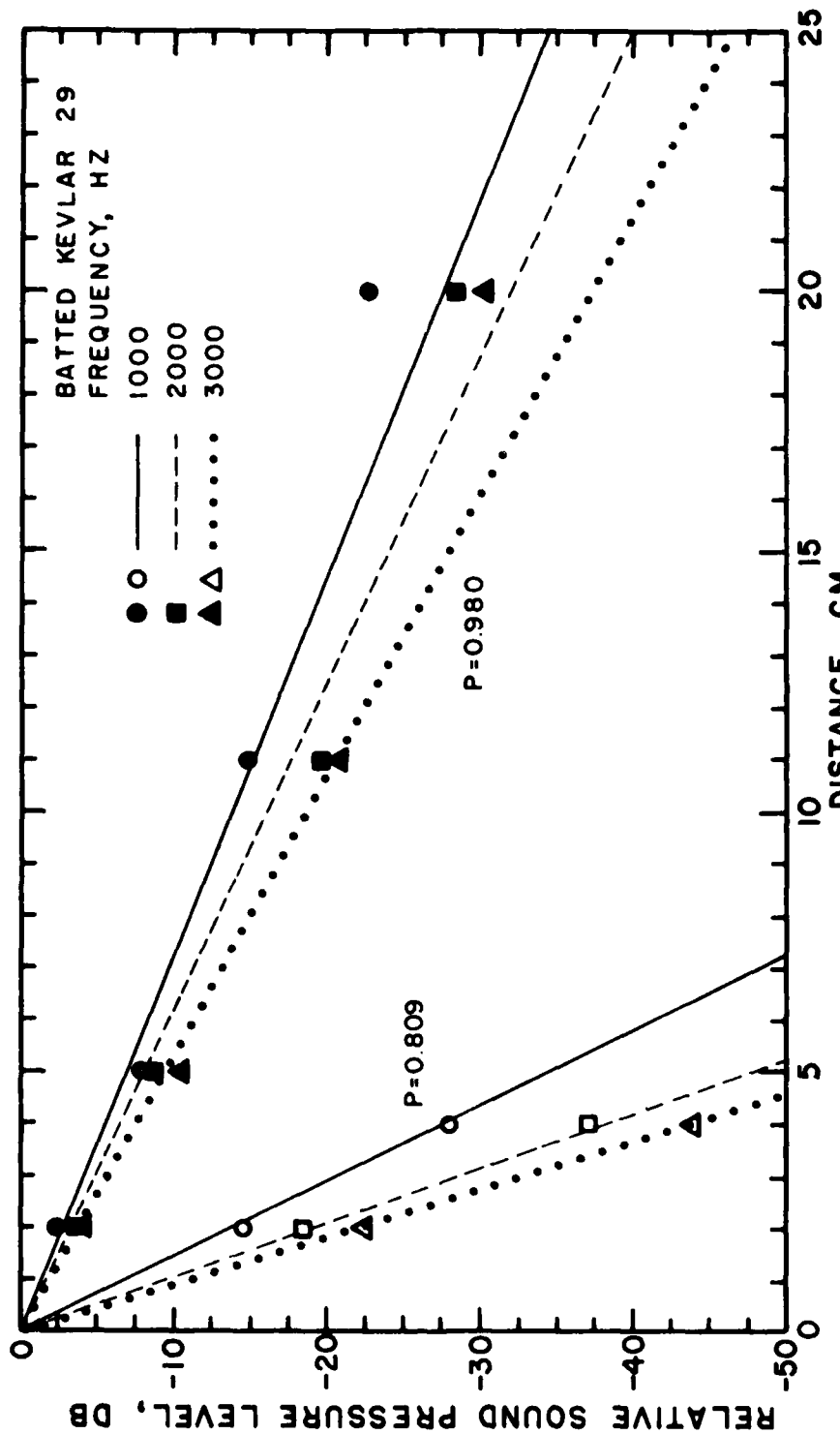

FIGURE IV-8
SMALL SIGNAL SOUND LEVELS VERSUS DISTANCE FOR THREE SINUSOIDAL WAVES PROPAGATING IN TWO POROSITIES OF BATTED KEVLAR 29.

in Fig. IV-9 versus frequency show good agreement up to about 4 kHz. The same high frequency attenuation rise was seen in Fig. IV-6 for the porosity 0.980. In Fig. IV-9 the data rises to a peak and the introduction of a cross-mode propagating in the material may be causing this extra attenuation.

The predicted and measured phase speeds plotted in Fig. IV-10 show little agreement. The predicted phase speed is 40-70% too high at frequencies above 1 kHz. This material is a partially reticulated foam. The structure that dc flow encounters is much different than that which ac flow encounters, and, for partially reticulated foam materials, the dc flow resistance model is inadequate for calculating β or C_{PH}. Zwikker and Kosten [88] discuss some of the effects a partially reticulated foam will have on both dc and acoustic flow. Another theory, such as Zarek's [82], Beranek's [8], or Zwikker and Kosten's [88], might predict the propagation properties of a partially reticulated foam with more accuracy than the present model. Unfortunately, in each of the cited theories, both the flexibility and the structure factor of the material must be determined, and these two factors may have different meaning at high-intensities. Taking these variables into account would also make the perturbation solution of Chapter II even more complicated. Thus, a partially reticulated foam is found to be an inapplicable case for use of the dc flow resistance theory. Because the relative nonlinearity of this material is so large, the material is used throughout the rest of this chapter as a comparator to the relatively linear materials.

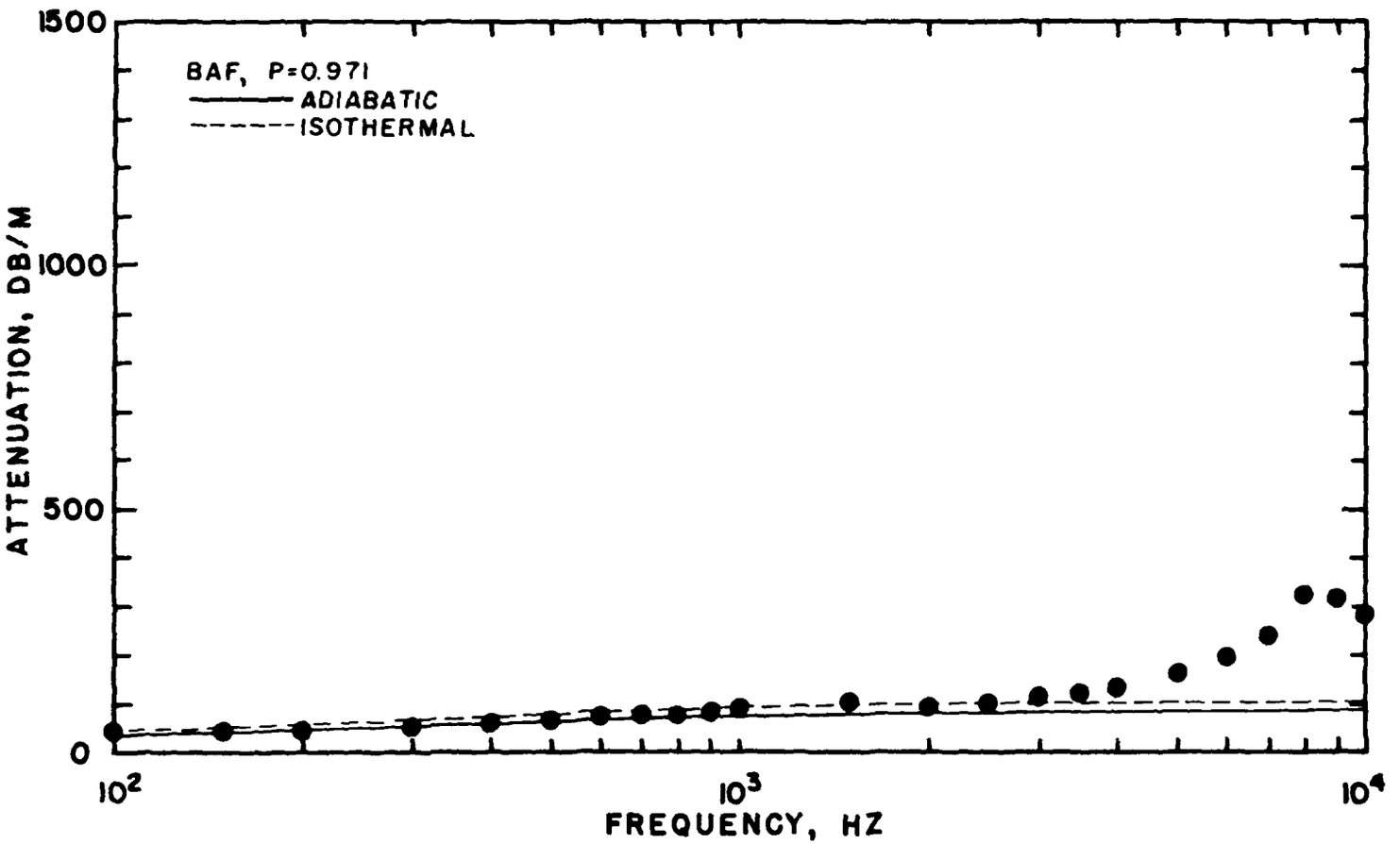

FIGURE IV-9
MEASURED AND PREDICTED ATTENUATION VERSUS FREQUENCY
FOR SOUND PROPAGATING IN BLACHFORD ACOUSTICAL FOAM.

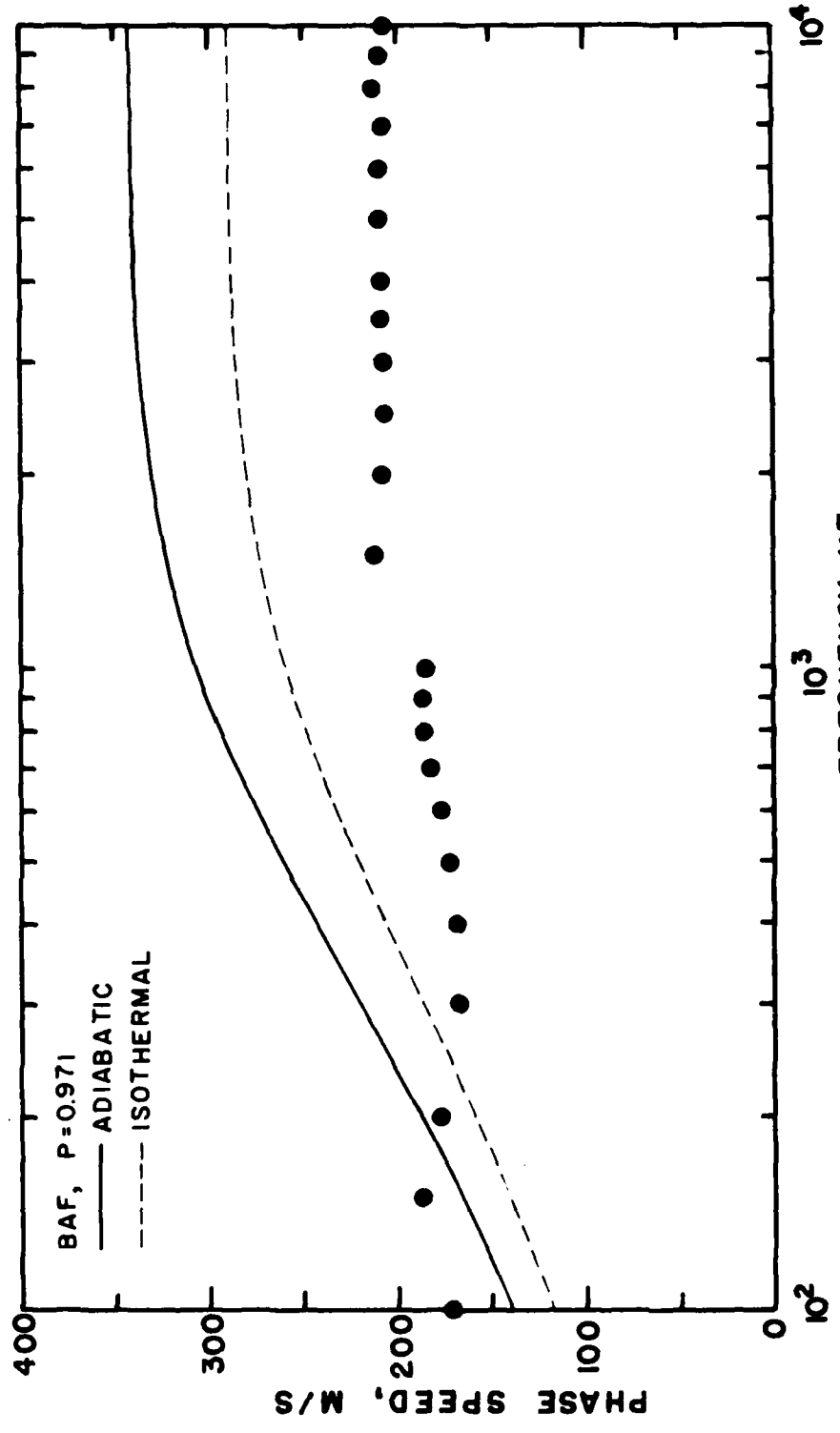

FIGURE IV-10
MEASURED AND PREDICTED PHASE SPEED VERSUS FREQUENCY FOR SOUND PROPAGATING IN BLACHFORD ACOUSTICAL FOAM.

As with the batted Kevlar 29, we want to determine how homogeneous the BAF is. In Fig. IV-11 the relative sound pressure levels of 1, 2, and 3 kHz low-intensity tone bursts in BAF are plotted versus microphone separation distance. In this material there is some deviation from the average attenuation, but it is not as large as found in the Kevlar material.

In some frequency regions the measured attenuation and phase speed values diverge from the predicted values. If the basic model is valid, that is, if the attenuation is due to the material flow resistivity, agreement between theory and experiment may be obtained by using an acoustic flow resistivity. We measure the acoustic flow resistivity by using the attenuation data and Eq. I-4 to compute σ. The values of σ are calculated by using the average of the calculations from the Fig. IV-6 attenuation results at 1, 2, and 3 kHz. The average values (●) and standard deviations are plotted versus porosity in Fig. IV-12. Equation I-12 was used to generate the curve in the figure. The constant, $g = 0.079$, was chosen for a best Chi-squared fit to the data. For Kevlar flow resistivity values not measured, Eq. I-12 was used to calculate σ in the remainder of this study.

We made the above calculations for the BAF acoustic flow resistivity at 1, 2, and 3 kHz and found no change between the average dc flow resistivity value and the specific BAF sample used in the propagation tests (see Fig. IV-9).

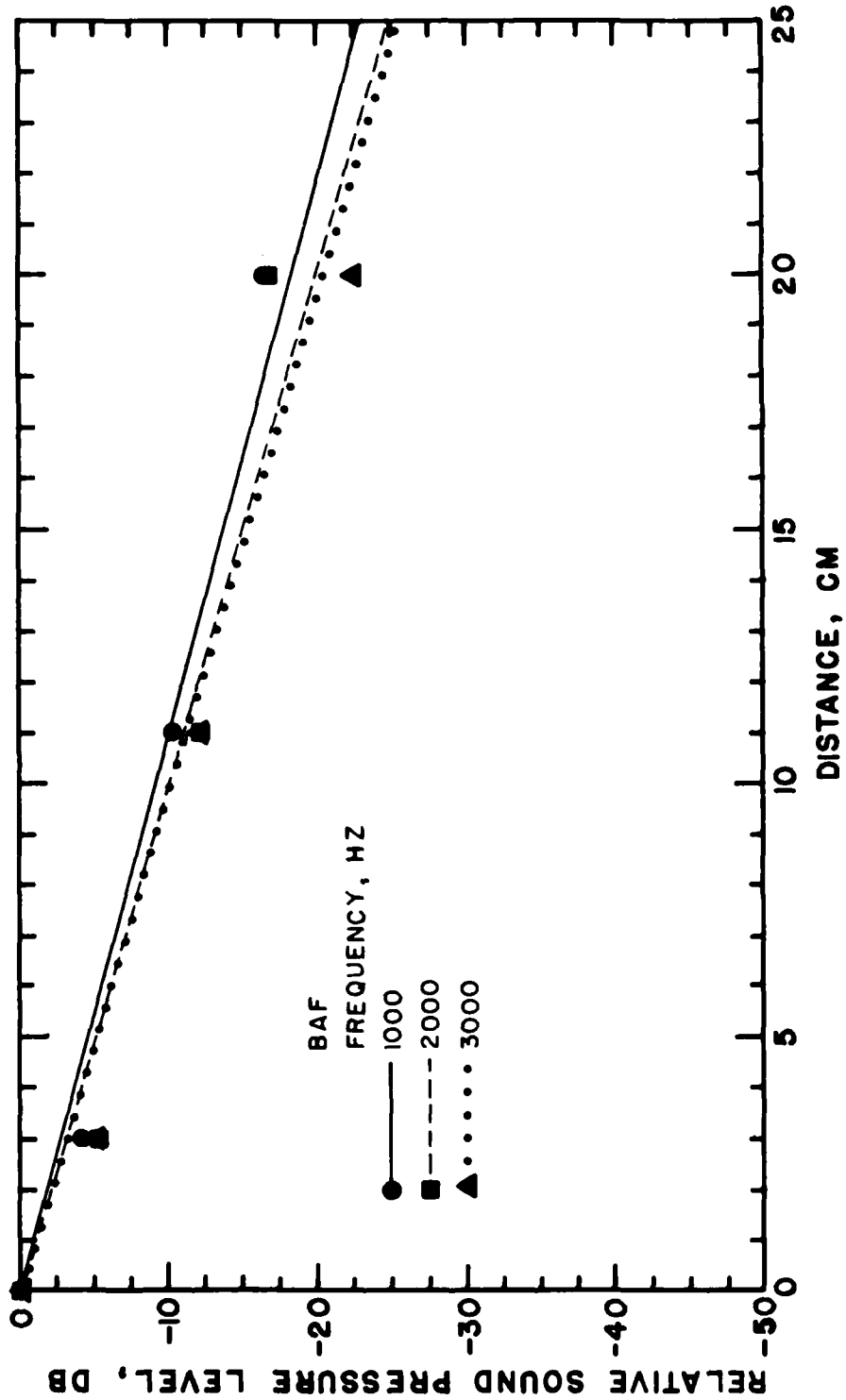

FIGURE IV-11
SMALL SIGNAL SOUND LEVELS VERSUS DISTANCE FOR THREE SINUSOIDAL WAVES PROPAGATING IN BLACHFORD ACOUSTICAL FOAM.

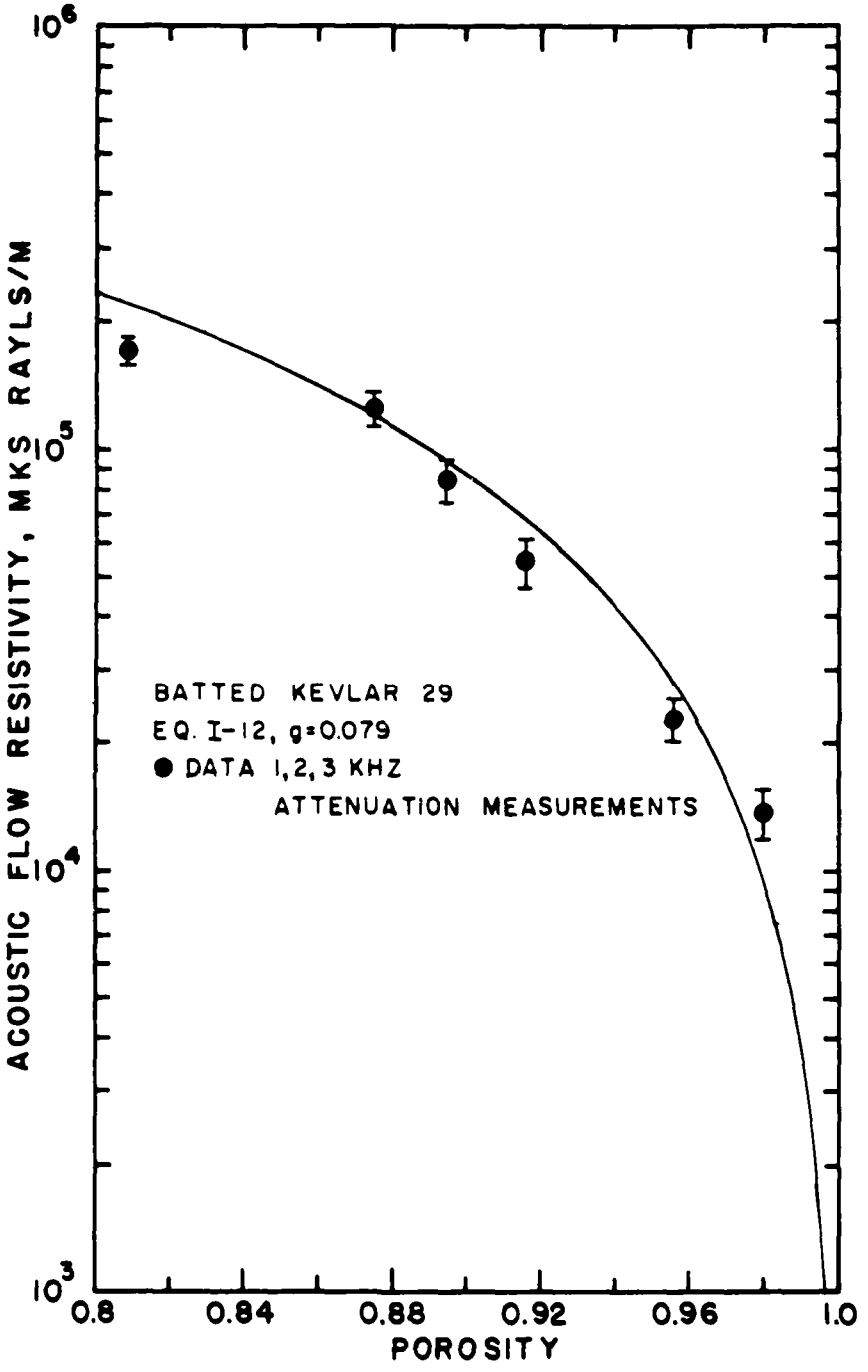

FIGURE IV-12
ACOUSTIC FLOW RESISTIVITY VERSUS POROSITY FOR VALUES OF FLOW RESISTIVITY USED IN THE FOLLOWING PREDICTIONS OF THE ACOUSTICAL PROPERTIES OF BATTED KEVLAR 29.

2. Excess Attenuation and Saturation

In Section I-C-1 both excess attenuation and saturation have been shown to occur in both water [76] and air [80,81] for initially sinusoidal waves. In Section II-F-2 a model was developed for use in describing excess attenuation and saturation. In this section we present data on saturation and determine values for the nonlinearity parameter T. The test method was described in Section III-D-2.

In fitting Eq. II-77 to the saturation data, we set the value of α so that Eq. II-77 predicts a data point in the linear region and then set T so that Eq. II-77 predicts the highest level data point. Saturation data was taken at a variety of porosities (0.980, 0.956, 0.916, 0.895, 0.875, and 0.809), frequencies (1, 2, and 3 kHz) and microphone separation distances (1-20 cm). For $P < 0.916$ the results were not useable because of noise levels at the remote microphone. For $P \geq 0.916$ and several microphone separation distances the value of T was found to be constant with porosity changes. Approximate values of T at frequencies of 1, 2, and 3 kHz are listed for two materials in Table IV-2. A 1 kHz value of T for the BAF could not be determined from the experimental data because, for a 1 kHz wave in BAF, T appears to be dependent on sound level. This dependence is discussed more in Subsection 3. Given these values of T, Eq. II-77 fits almost all the data to within ± 0.5 dB. The excellent fit is illustrated in Fig. IV-13, which shows the approach to saturation of three separate fundamentals for batted Kevlar 29 ($P = 0.980$). In each case, deviation from linear behavior begins to occur in the range of 140-150 dB source level.

TABLE IV-2

EXPERIMENTALLY DETERMINED VALUES OF THE NONLINEARITY

PARAMETER T FOR BATTED KEVLAR 29 AND BLACHFORD ACOUSTICAL FOAM

MATERIAL	T, 1 kHz	T, 2 kHz	T, 3 kHz
Batted Kevlar 29	388	248	228
Blachford Acoustical Foam (BAF)	X X	83.6	73.2

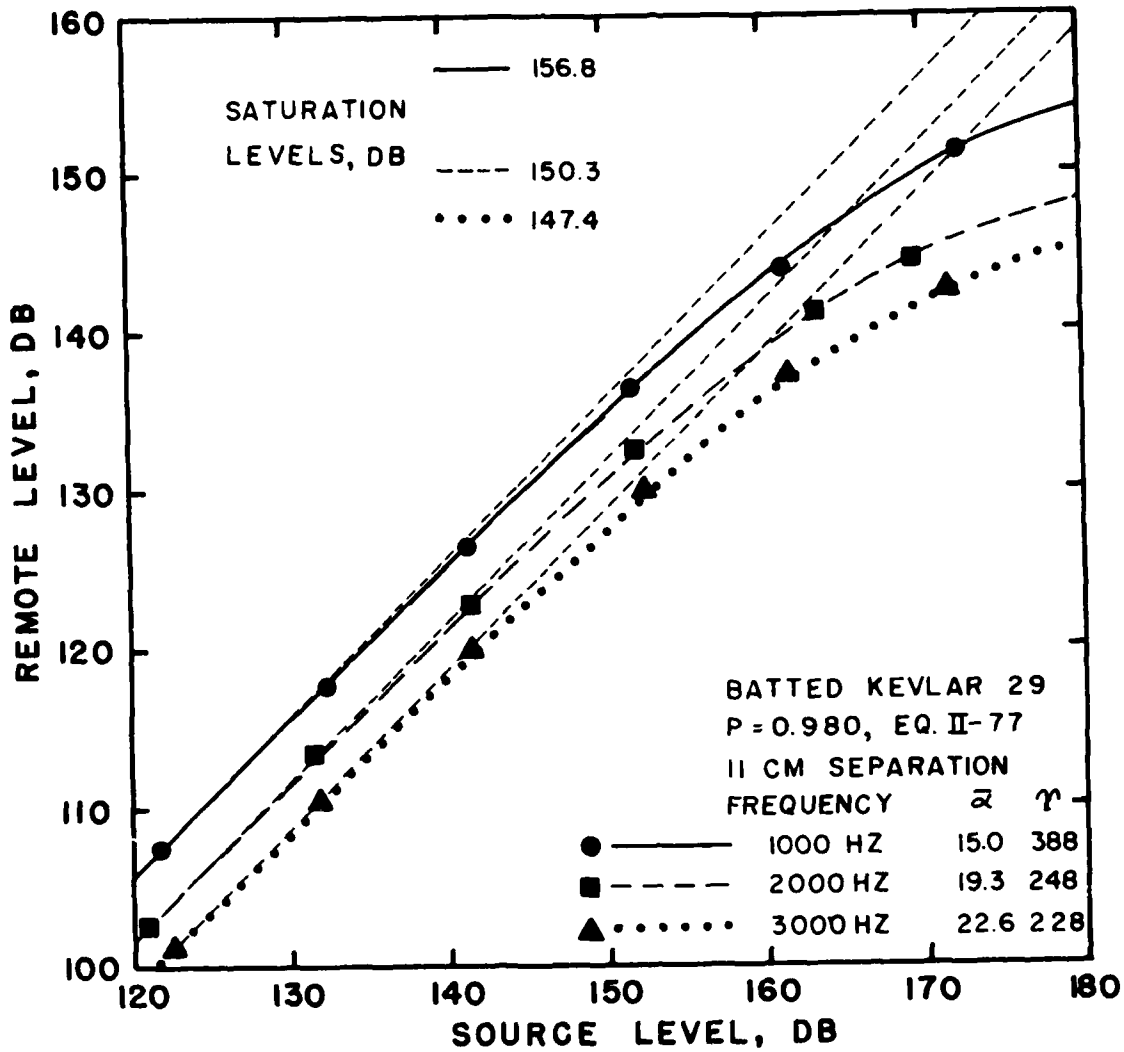

FIGURE IV-13
AMPLITUDE RESPONSE CURVES FOR THREE INDIVIDUALLY PROPAGATING SOUNDS (1, 2, and 3 kHz FUNDAMENTAL COMPONENTS) IN BATTED KEVLAR (P = 0.980).

The corresponding particle velocity amplitude range 0.7-2.0 m/s is the same range at which the dc flow resistivity begins to deviate from linear behavior.

In the dc flow resistivity tests the BAF had the lowest nonlinearity threshold. On the basis of the results for batted Kevlar, one would expect BAF to have a correspondingly low threshold for extra attenuation. The expectation is fulfilled as Fig. IV-14, which gives data for two fundamental frequency components, shows. The deviation from linear behavior is much larger than for the Kevlar. The deviation starts at about 120 dB, or about 0.07 m/s in particle velocity amplitude. This amplitude also marks the onset of nonlinearity in the dc flow resistivity tests.

These experiments demonstrate that the value of T depends on two factors, the dc nonlinearity of the material and the frequency of the propagating sound. In Subsection 3 we will find that, up to 172 dB, shocks do not form in initially sinusoidal waves propagating in bulk porous materials. Although shocks do not form, the equation governing the furdamental component amplitude attenuation is of the same form as for when shocks form in air. In both cases the attenuation is governed by an equation of the form of Eq. II-78.

The plot in Fig. IV-15 indicates that the apparent functional relation for T is inversely proportional to $(f)^{0.5}$ and $(\eta/\sigma)^{0.4}$. We find that an approximate relation is

$$T = 6400(f)^{-0.5}\left(\frac{\sigma}{\eta}\right)^{0.4} \quad . \qquad \text{(IV-1)}$$

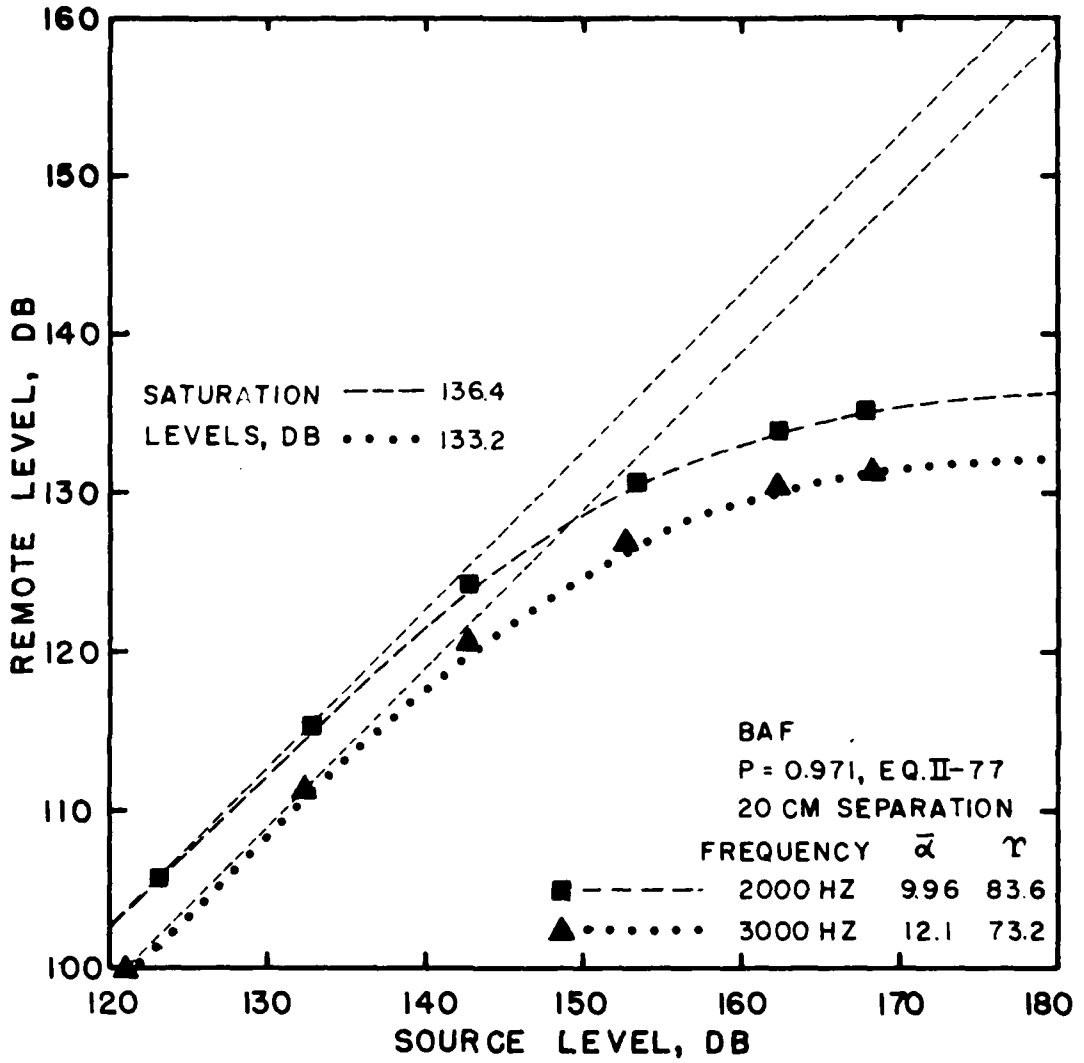

FIGURE IV-14
AMPLITUDE RESPONSE CURVES FOR TWO INDIVIDUALLY PROPAGATING (SOUNDS 2 AND 3 kHz FUNDAMENTAL COMPONENTS) IN BLACHFORD ACOUSTICAL FOAM.

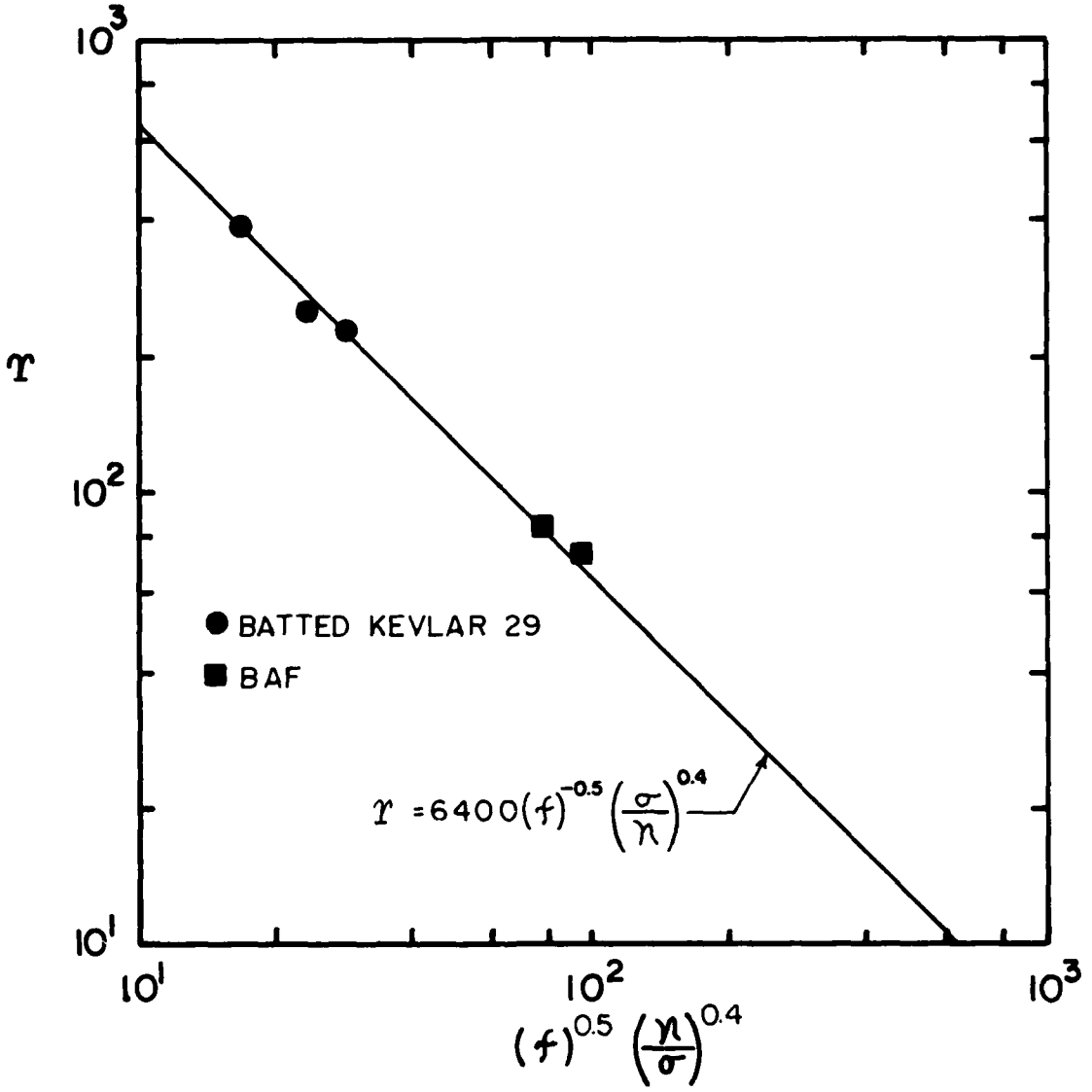

FIGURE IV-15
EMPIRICAL PARAMETER Υ VERSUS FREQUENCY $f^{0.5}$ AND RELATIVE NONLINEARITY $(\eta/\sigma)^{0.4}$.

An exact relation would be ill defined by these few tests and more extensive tests are called for before a good empirical relationship can be defined.

Equation II-77 and the values of Υ are used in the next part of this section to predict propagation of the fundamental component at high intensities.

3. Propagation at High Intensities

In this section we present comparisons of measured and predicted propagation for intense sound in porous materials. The propagation explored in this section is in both BAF and batted Kevlar 29. Tone bursts of 1, 2, and 3 kHz were used to determine the material properties. The test method was described in Section III-D-2. Although propagation measurements were made on many porosities of batted Kevlar, only two representative data sets are presented here and compared to the theories. We find that when the perturbation solution is compared to the data, the solution does not adequately describe the propagation of intense waves in a porous material and reasons for this discrepancy are discussed. In addition, the impedance and saturation models are compared to the data. These models show the excess attenuation of the fundamental, but do not address the problem of harmonic component generation.

Propagation measurements were made with batted Kevlar 29 at a variety of porosities (0.980, 0.956, 0.916, 0.895, 0.875, and 0.809). The results show general trends, which we illustrate here by presenting 1 kHz results at only two porosities (0.980 and 0.809). The extra

attenuation showed that the Kevlar 29 behaves linearly for sounds below 140 dB. The predicted and measured sound levels of an intense (162.4 dB)1 kHz tone burst propagating through Kevlar 29 ($P = 0.980$) are shown in Fig. IV-16. The predictions are made from a combination of Eqs. II-52 and II-61 in Eq. II-35a (Program PERT4PD). Although the first four harmonics are accounted for in this solution, only three appear in the figure. The 4 kHz component level is less than 112 dB. The prediction does not show the excess attenuation that is found in the measured data; the computed fundamental component behaves as a small signal. The first two harmonic components are accounted for at the source microphone (0 cm). The presence of the third harmonic component is not accounted for at the source microphone. The data points have been corrected for inhomogeneous material effects. The corrections are given by the differences found between data points and theory in Fig. IV-7.

The data for the measured harmonic components do not follow the theoretical curves. The 1 kHz component attenuates in a nonlinear fashion. The initial attenuation is larger than linear. The attenuation approaches the linear value as the sound level decreases. The 2 and 3 kHz components are also attenuated in a nonlinear fashion. The 2 kHz component has a rapid initial attenuation which is reduced with distance. The 3 kHz component increases in level at the 2 and 5 cm positions, but is suddenly attenuated between 5 and 11 cm. These results indicate interaction between the components which is unexplained by the theory. The discrepancies may be caused by one or more

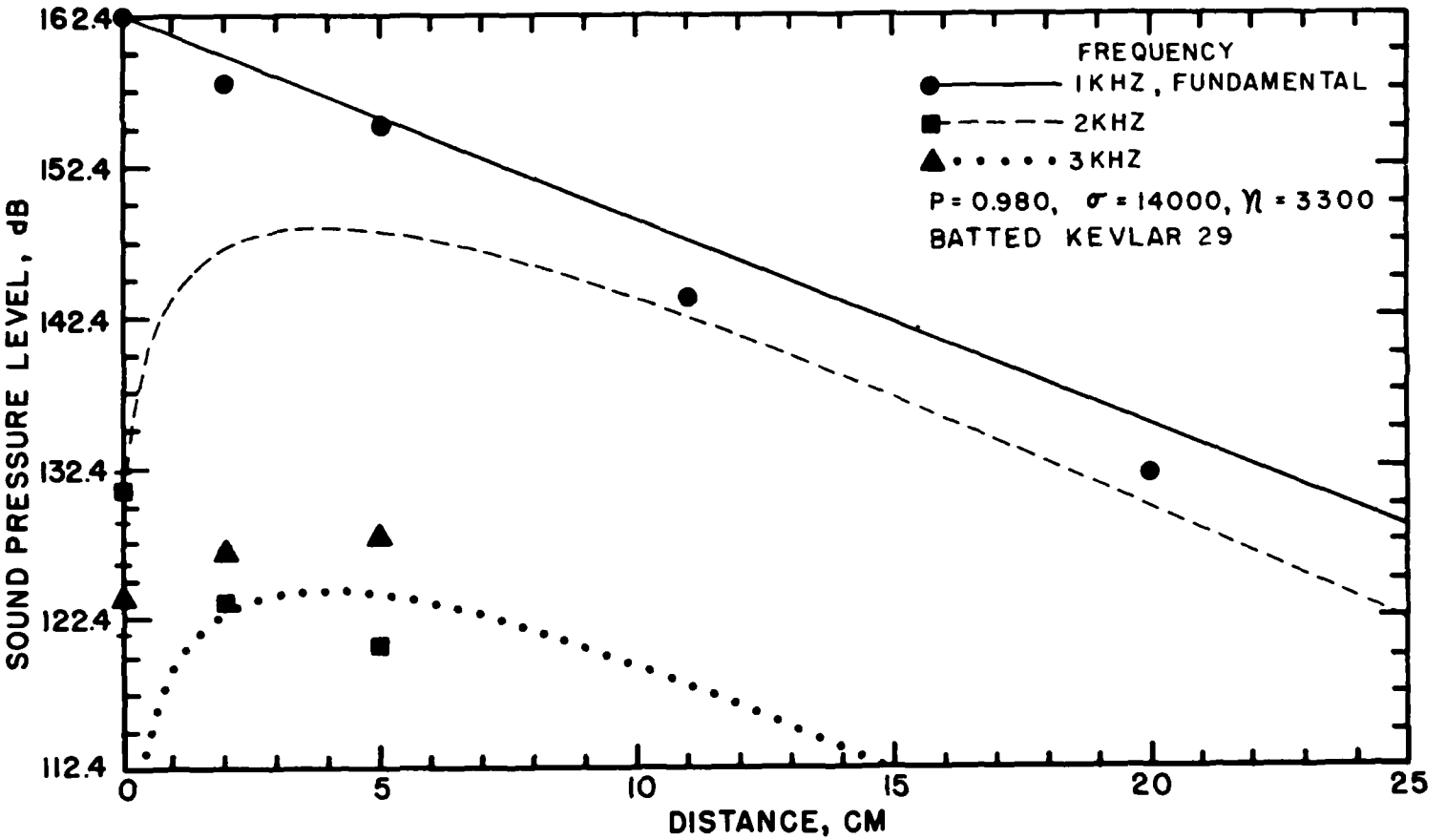

FIGURE IV-16
MEASURED AND PREDICTED (PERT4PD) HARMONIC COMPONENTS SOUND LEVELS VERSUS DISTANCE FOR AN INTENSE 1 kHz SOUND (162.4 dB) PROPAGATING IN BATTED KEVLAR 29 (P = 0.980).

factors. First, the presence and relative phases of the higher frequency harmonic components may influence the lower frequency components more than expected. Second, the perturbation may have to be performed to higher orders to show enough excess attenuation. Third, the definition of nonlinear behavior may be ill defined by simply using the dc flow resistivity test results; a better definition may be needed. Finally, perturbation may be inappropriate for determining the propagation of very intense sound in a porous material. We found in Section IV-B-1 that for small signals the perturbation theory and measurement results were in agreement. Until harmonic generation by and excess attenuation of the fundamental is encountered, the perturbation theory works well in predicting the attenuation (below about 140 dB).

We now consider how well the perturbation theory predicts the attenuation of sound for materials of low porosities. In Table IV-1 we found that the relative nonlinearity of the material η/σ is independent of the porosity. The resistivity and attenuation are dependent on the porosity. At low porosities $G \to 0$ (Eq. II-81) and the nonlinearity is overshadowed by the large attenuation. In Fig. IV-17 the perturbation solution and data are presented for batted Kevlar 29 $P = 0.809$. Here there is very little excess attenuation; theory and experiment agree. The 2 kHz component shows linear attenuation between the two data points. A small rise is found in the predicted 2 kHz level. The discrepancy between data and theory here may be caused by lack of initial phase information. Changing the phase in the computer program changed the generation and attenuation of the 2 kHz component. The phase in

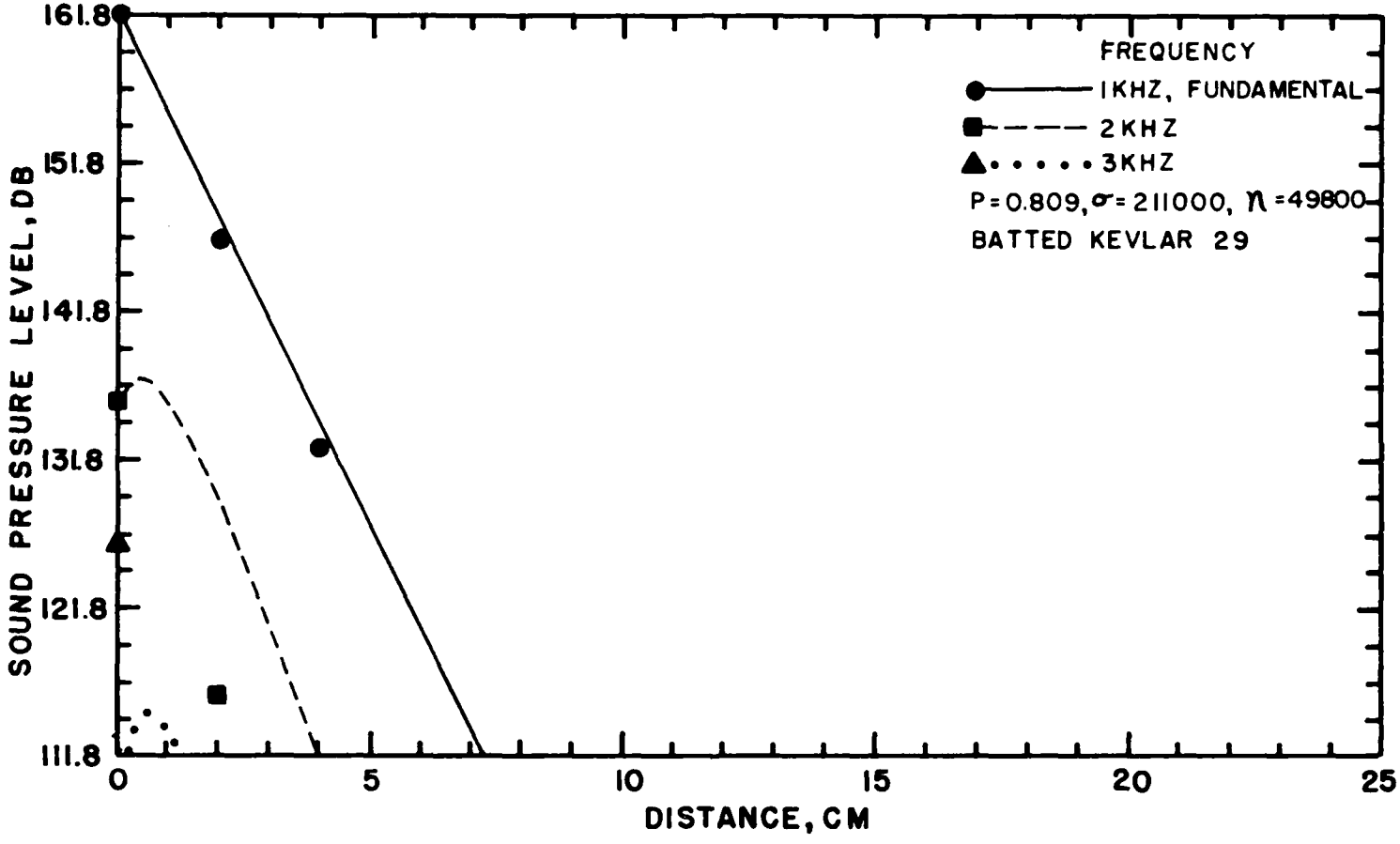

FIGURE IV-17
MEASURED AND PREDICTED (PERT4PD) HARMONIC COMPONENT SOUND LEVELS VERSUS DISTANCE FOR INTENSE 1 kHz SOUND (161.8 dB) PROPAGATING IN BATTED KEVLAR 29 (P = 0.809.).

Fig. IV-17 was set to zero. For porosities between the two examples, we found a transition from some excess attenuation at high porosities to little excess attenuation at low porosities.

We now use test results to verify the two attenuation models presented in Section II-F. We use the values of the nonlinearity parameter T from Section IV-B-2 and the values of the relative nonlinearity η/σ from Section IV-A-1. The acoustically determined flow resistivity values are taken from Section IV-B-1. We first consider the 1 kHz Kevlar data and then the 1 kHz BAF data. We find that the measurements and predictions agree for the Kevlar, but there are some discrepancies for the BAF.

In Fig. IV-18 the measured and predicted attenuations of a 1 kHz, 162.4 dB, wave are plotted versus distance. This is the same data as used in Fig. IV-16. The solid line indicates the small-signal attenuation. The dashed line is a plot of Eq. II-77, the excess attenuation model and the dotted line is a plot of the result of using Eq. II-70, the impedance model. The excess attenuation model fits the data the best. The impedance model predicts too much excess attenuation, a fact that indicates that, for the impedance approximation the values of η/σ derived in Section IV-A-1 are too large for the approximation. The need to reduce the values of η/σ is confirmed by the other comparisons of data with theory, including those of impedance. Since the predictions based on Eq. II-79 show good agreement with the

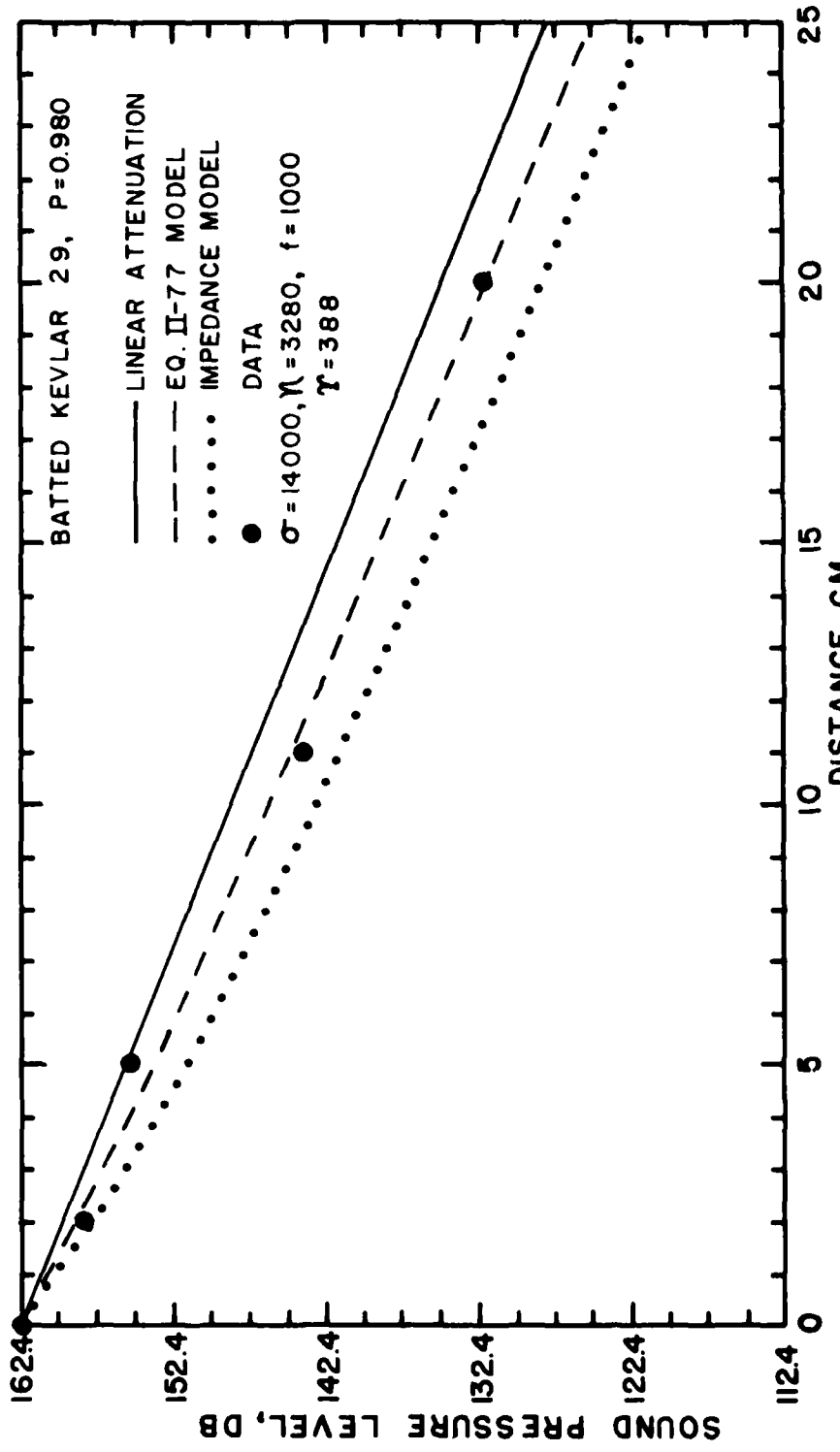

FIGURE IV-18
MEASURED AND PREDICTED FUNDAMENTAL COMPONENT SOUND LEVELS VERSUS DISTANCE FOR AN INTENSE 1 kHz SOUND (162.4 dB) PROPAGATING BATTED KEVLAR 29 (P = 0.980).

data, Eq. II-79 will be used in the remainder of this section. Estimates for the reduction of η/σ are made in Section IV-C.

In Fig. IV-19 we continue with the very porous batted Kevlar 29 ($P = 0.980$) and increase the sound level at the source microphone to 172.3 dB, again for a fundamental freuqency of 1 kHz. The conclusions are the same: predictions based on the use of Eq. II-79 are in excellent agreement with the data over the region measured.

A similar measurement in low porosity ($P = 0.809$) batted Kevlar 29 is shown in Fig. IV-20. In this case the material nonlinearity is not as important as the linear attenuation. Even so, the agreement between data and predictions based on Eq. II-79 continues to be excellent. Moreover, the earlier conclusion that T for a given material is independent of porosity is now seen to hold for porosities as low as $P = 0.809$.

The same sort of tests were done with BAF. It will be recalled that a 1 kHz value for T could not be determined from the saturation measurements, even though the 2 and 3 kHz values could be determined. From Eq. II-79 we estimate $T = 115$. In the BAF tests for 162.1 dB presented in Fig. IV-21, we find $T_1 = 115$ to be a good estimate. In Fig. IV-22 the initial sound level is 173.1 dB. We find that the model and data do not agree as well. The estimate for the BAF value $T = 115$ appears to be low. If T is increased to fit the two cases shown here, the results are $T = 143$ for Fig. IV-21 and $T = 200$ for Fig. IV-22. In other words, T seems to have an amplitude dependence that was not seen for Kevlar 29. The dependence on amplitude may be

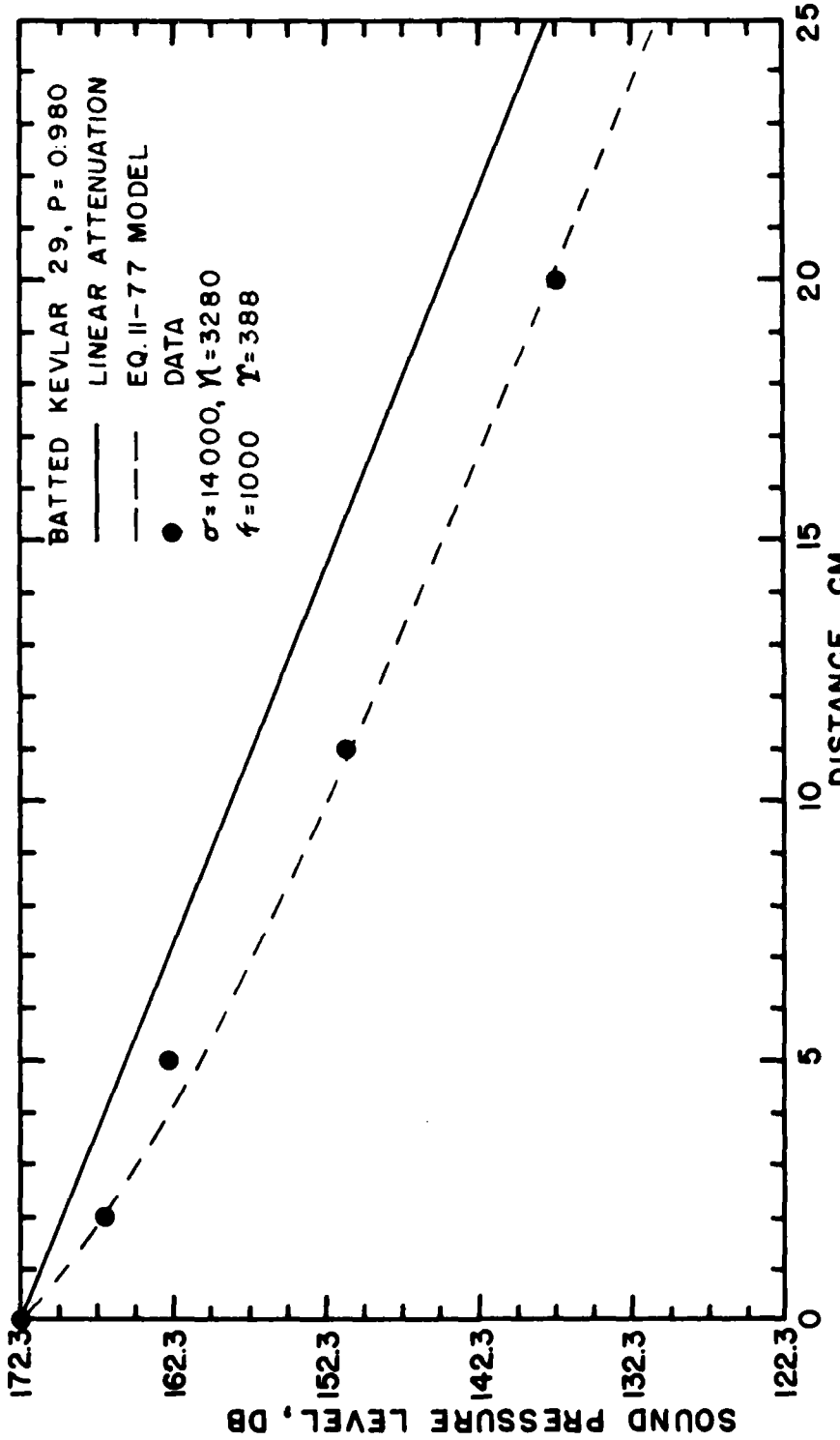

FIGURE IV-19
MEASURED AND PREDICTED FUNDAMENTAL COMPONENT SOUND LEVELS VERSUS DISTANCE FOR AN INTENSE 1 kHz SOUND (172.3 dB) PROPAGATING IN BATTED KEVLAR 29 (P = 0.980).

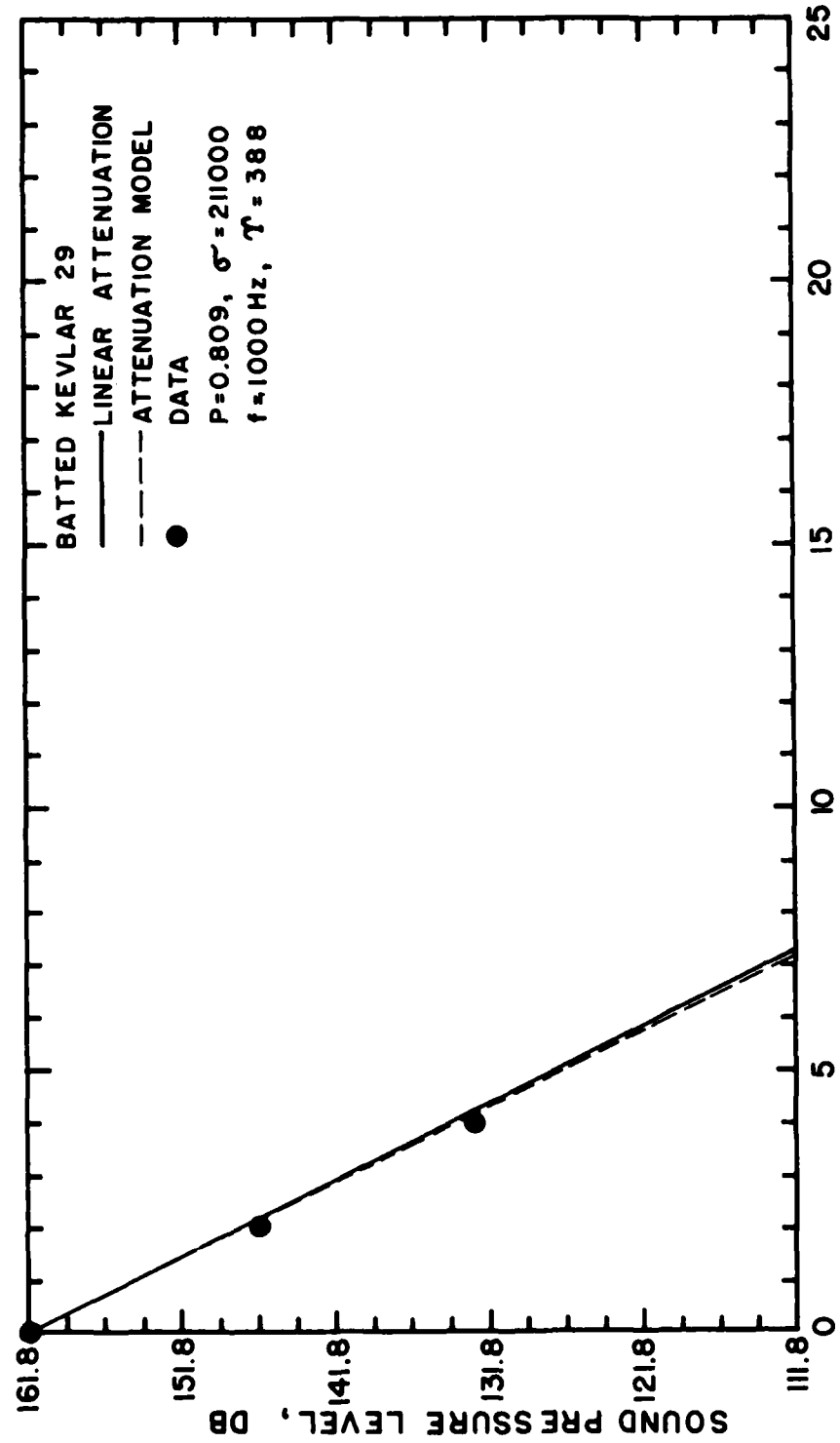

FIGURE IV-20
MEASURED AND PREDICTED FUNDAMENTAL COMPONENT SOUND LEVELS VERSUS DISTANCE FOR AN INTENSE 1 kHz SOUND (161.8 dB) PROPAGATING IN BATTED KEVLAR 29 (P = 0.809).

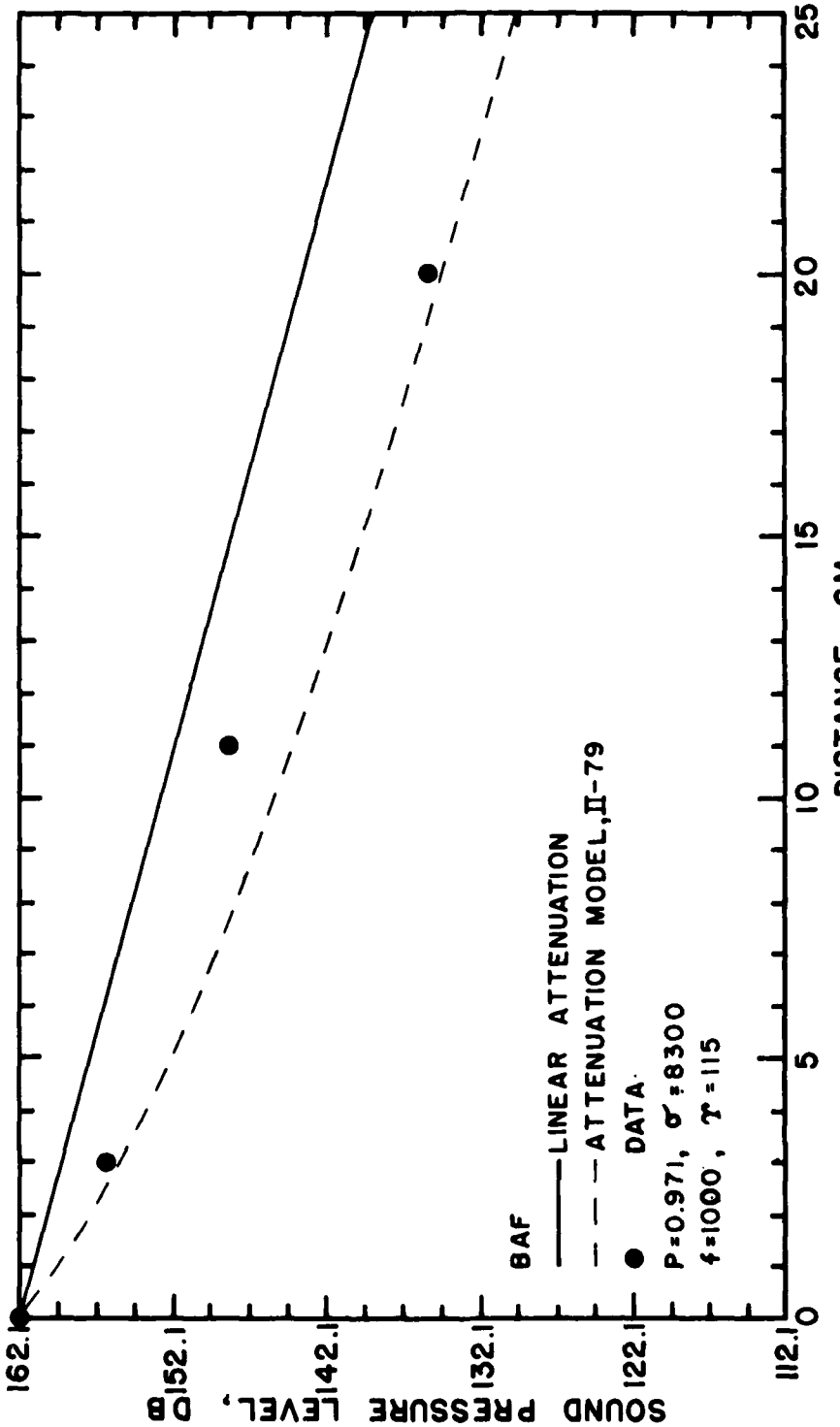

FIGURE IV-21
MEASURED AND PREDICTED FUNDAMENTAL COMPONENT SOUND LEVELS VERSUS DISTANCE FOR AN INTENSE 1 kHz SOUND (162.1 dB) PROPAGATING IN BLACHFORD ACOUSTICAL FOAM.

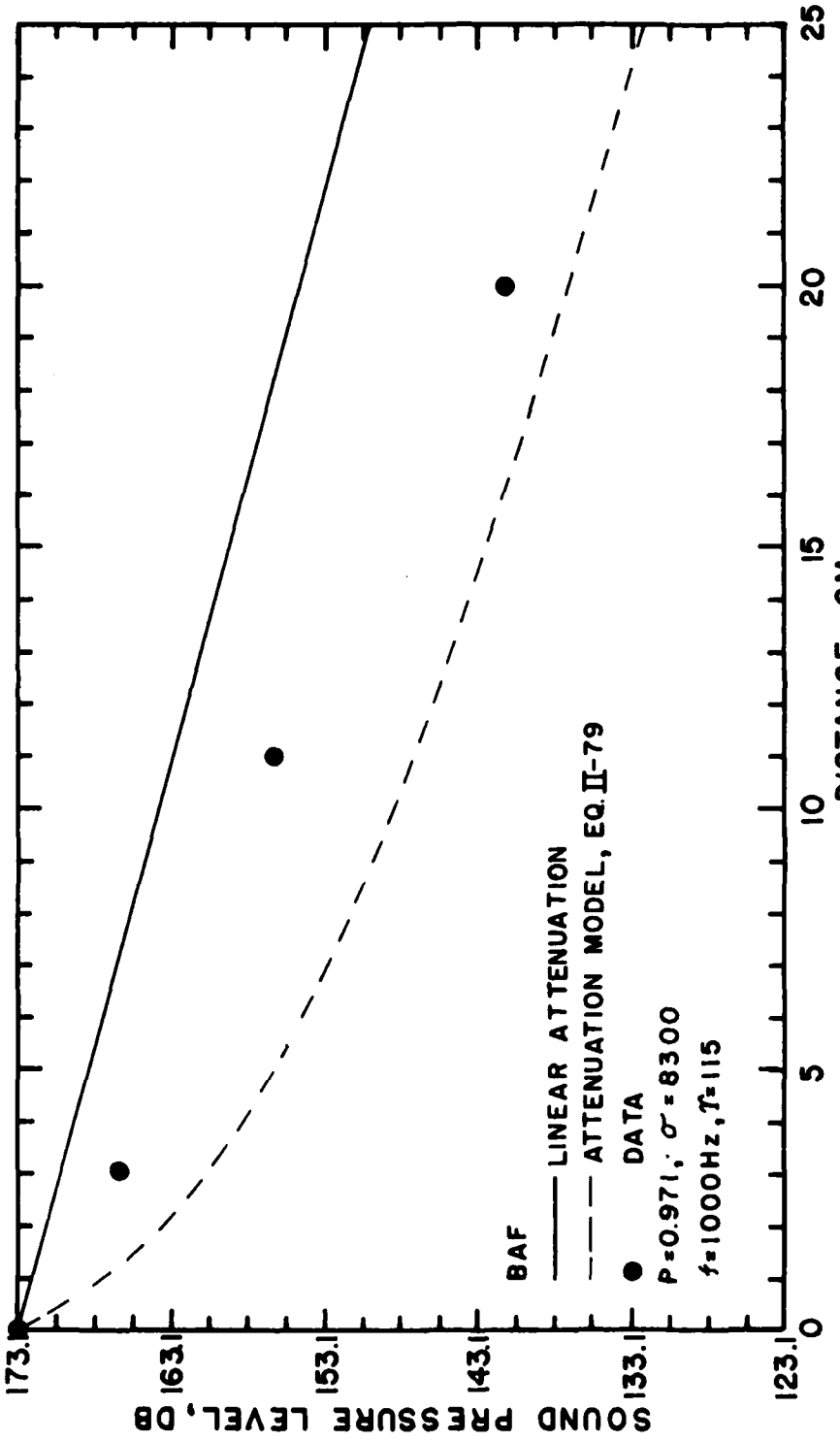

FIGURE IV-22
MEASURED AND PREDICTED FUNDAMENTAL COMPONENT SOUND LEVELS
VERSUS DISTANCE FOR AN INTENSE 1 kHz SOUND (173.1 dB) PROPAGATING
IN BLACHFORD ACOUSTICAL FOAM.

caused by the complicated material structure which influences the acoustic flow in a different manner as the intensity increases. For the 2 and 3 kHz tests amplitude dependence of T was not encountered.

We have seen here that, although the second-order perturbation solution does not work for intense sound propagation in a porous material, we have two empirical models that do work. Future work in theoretically defining the parameters T and η/σ would be an important step in being able to predict the propagation of intense sound in porous materials.

In Section IV-C the acoustic impedance theory and data are compared. Acoustic values for η/σ are found for use in the impedance relations.

C. Specific Normal Acoustic Impedance

The acoustic impedance measurement systems used in this section are described in Section III-E. The measurement systems consist of two low-intensity sound standing wave tubes and one high-intensity sound traveling wave tube. Measurements were done in these tubes for a wide range of frequencies, materials, and sound levels. All the results cannot reasonably be reported here. Tabel IV-3 lists the range of measurements made on the various materials. Low-frequency standing wave tube measurements were not made on the batted Kevlar 29 because of our inability to hold the material in place at various porosities and keep the material flush with the tube walls. The low-intensity measurements are presented and discussed first, then the high-intensity measurements.

1. Impedance at Low Intensities

Most porous materials are of finite length and the measured impedance is affected by the material impedance and the sample length. The impedance data presented here were obtained from both the standing and traveling wave tubes. In the standing wave tube the sample lengths were of the order of 7.6 cm. In the traveling wave tube the sample was long enough to qualify as semi-infinite ($\alpha L >> 1$). We use the traveling wave tube to measure the characteristic impedance of the material. The test results from the traveling wave tube are presented first. The flow resistivity values used in the calculations are taken from both the dc flow resistivities, described in Section A of this chapter, and the acoustically determined flow resistivities, described

TABLE IV-3

TABULATION OF MEASUREMENTS MADE IN THE THREE IMPEDANCE TUBES ON THE VARIOUS MATERIALS

MATERIAL	BATTED KEVLAR 29											
POROSITY	0.985	0.980	0.971	0.970	0.958	0.956	0.940	0.930	0.918	0.915	0.895	0.875
TRAVELING WAVE IMPEDANCE TUBE -(FREQUENCY, kHz) -(SOUND LEVEL, dB)	1-4 119-164	-	1-4 121-167	-	1-4 120-167	-	-	1-4 121-167	-	1-4 121-166	1-4 121-164	1-4 121-165
LOW FREQUENCY STANDING WAVE IMPEDANCE TUBE -(FREQUENCY, kHz)	-	-	-	-	-	-	-	-	-	-	-	-
HIGH FREQUENCY STANDING WAVE IMPEDANCE TUBE -(FREQUENCY, kHz)	-	0.8-3.5	-	0.8-3.5	-	0.8-3.5	0.8-3.5	-	0.8-3.5	-	-	-

MATERIAL	JOHNS-MANVILLE 1000 FIBERGLASS	GLOBE-ALBANY KEVLAR	SCOTTFELT 900-Z-2	SCOTTFELT 900-Z-4	SCOTTFELT 900-Z-6	BLACHFORD ACOUSTICAL FOAM
POROSITY	0.982	0.940	0.942	0.884	0.85.	0.971
TRAVELING WAVE IMPEDANCE TUBE -(FREQUENCY, kHz) OUND LEVEL, dB)	-	1-4 120-165	1-4 120-165	1-4 120-165	-	1-4 120-165
LOW-FREQUENCY STANDING WAVE IMPEDANCE TUBE -(FREQUENCY, kHz)	0.1-1.3	-	-	-	-	0.1-1.3
HIGH-FREQUENCY STANDING WAVE IMPEDANCE TUBE -(FREQUENCY, kHz)	0.8-3.5	0.8-3.5	0.8-3.5	0.8-3.5	0.8-3.5	0.8-3.5

in Section B of this chapter. The characteristic impedance data illustrate how well the low-intensity sound model predicts the impedance for a semi-infinite material. The measurements are combined with the theory of Chapters I and II to yield a prediction for the impedance of the finite materials.

For a finite length porous material backed by an infinite impedance a simple relation [88] was found. This relation, given by Eq. I-10, links the propagation parameters α and β, the semi-infinite material impedance, and the finite length material impedance $W(L)$ together. Equation I-10 can be rewritten in terms of the dimensionless variable Γ_1 as

$$Z_1(L) = \Gamma_1 \coth\left(\frac{j\omega\Gamma_1 L}{c}\right) \quad . \tag{IV-2}$$

We note that, when $\alpha L >> 1$, $Z_1 \simeq \Gamma_1$. As noted in Chapter I, the measurement of the small signal impedance of a semi-infinite material is equivalent to measuring the propagation parameters.

In Fig. IV-23 the predicted (Eq. II-62) and measured (traveling wave impedance tube) impedance of batted Kevlar 29 ($P = 0.985$, 0.956, 0.914, and 0.875) are plotted versus frequency. For the higher porosities the data and theory are in good agreement. At $P = 0.875$, however, as in the attenuation and phase speed tests, the predicted values are larger than the measured values. The acoustically measured resistivity values are used in the calculations. If the dc flow resistivity values are used, the predicted curves for the impedance are higher than the curves in Fig. IV-23. At the higher porosities ($P > 0.875$) the small discrepancies

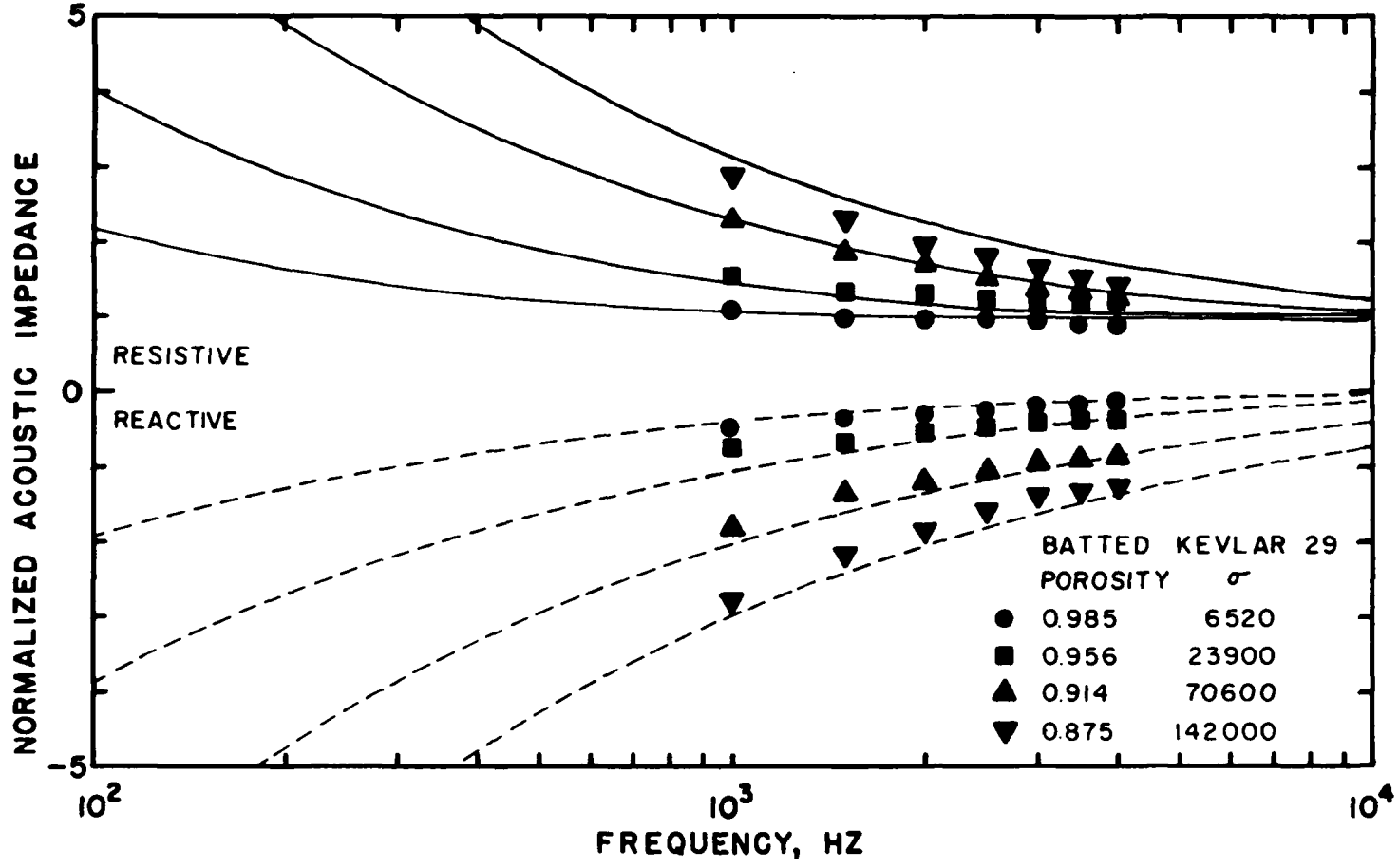

FIGURE IV-23
MEASURED AND PREDICTED IMPEDANCE VERSUS FREQUENCY FOR FOUR POROSITIES OF SEMI-INFINITE BATTED KEVLAR 29.

between the measured and predicted values can be accounted for by the small inaccuracy in measuring the phase (time delay) in the tests.

Samples of 7.7 cm thick batted Kevlar 29 were measured in the standing wave tube. The data are compared with predictions based on Eq. IV-2 (acoustic resistivity values) in Fig. IV-24 for porosities 0.980 and 0.918. Except for the $P = 0.918$ resistance data, the agreement is seen to be good. When the dc flow resistivity values are used in the predictions, the differences are barely discernable from the curves in Fig. IV-24. It would appear that for $\alpha L < 1$, that the differences between how the flow resistivites are determined becomes unimportant and either flow resistivity may be used in the calculations.

We stated that when $\alpha L > 1$, the standing and traveling wave impedance tube measurements should yield similar results. A comparison of Figs. IV-23 and IV-24 indicates that the test results should be similar for $P = 0.918$, 0.914, where $\alpha L > 1$ and dissimilar for $P = 0.980$, 0.985, where $\alpha L < 1$. The theoretical curves indicate the above statement to be fairly reliable. The data for $P = 0.985$, 0.980 disagree in the manner indicated by the theory. The reactance data for $P = 0.918$, 0.914 agree, but the resistance data disagree. The resistances ($P = 0.918$, 0.914) measured in the standing wave tube are between 15 and 35% higher than both the theory and the resistances measured in the traveling wave tube. As we shall see, the disagreement in the measured resistances for $P = 0.918$ and 0.914 appears to be more in this specific data than in the procedure, i.e., we find more consistant agreement in other results.

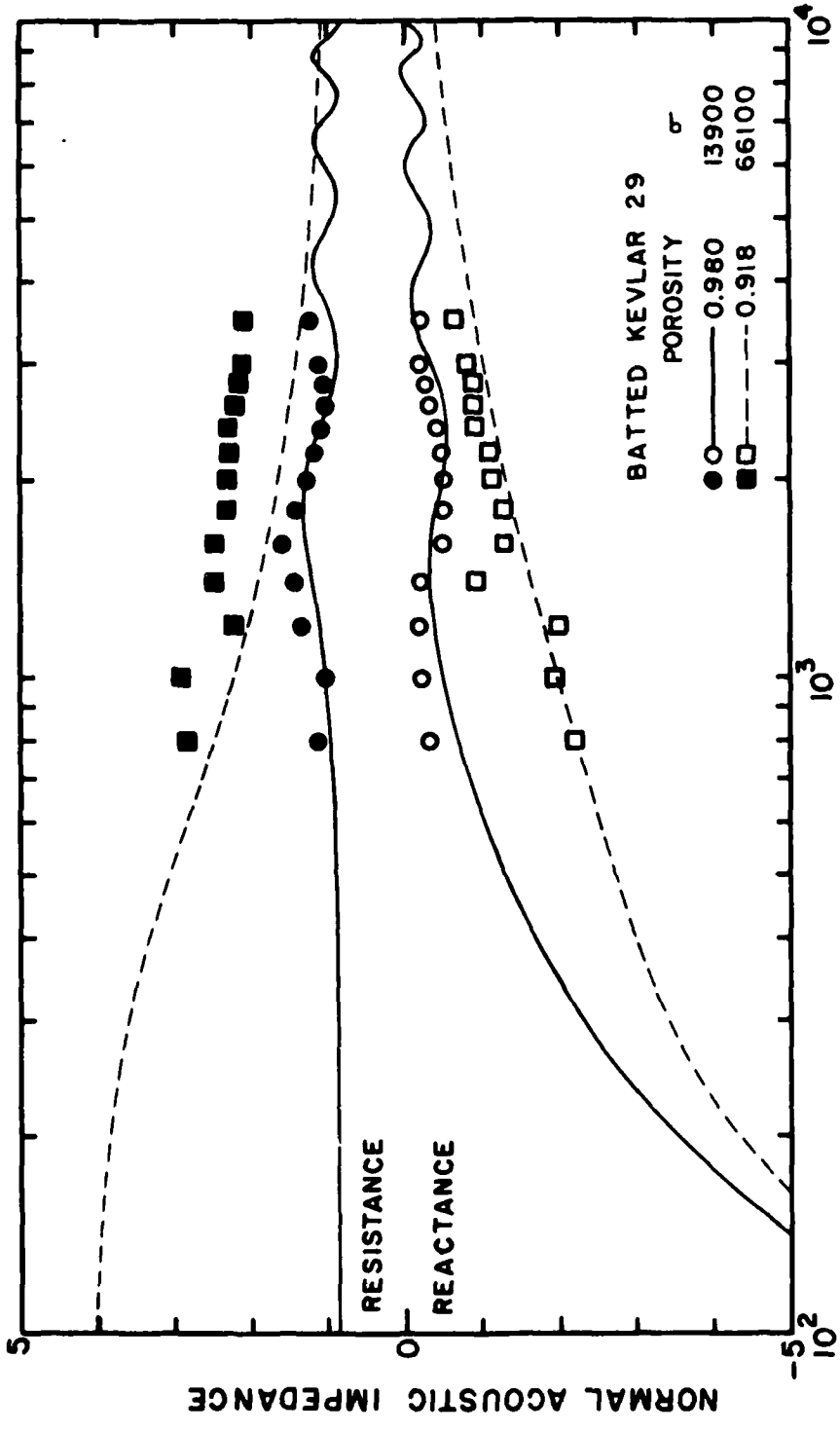

FIGURE IV-24
MEASURED AND PREDICTED IMPEDANCES VERSUS FREQUENCY FOR TWO POROSITIES OF 7.7 cm THICK BATTED KEVLAR 29.

In Fig. IV-25 the predicted and measured impedances of needled and felted Kevlar 29 ($P = 0.940$) for semi-infinite and 6.2 cm samples are plotted versus frequency. No propagation tests were made on this material; the dc flow resistivity was used in the predictions. The two sets of high-frequency data are in good agreement. The agreement between theory and data is good at high frequencies but not at low frequencies. The discrepancy at low frequency is attributed to uncertainty in locating the impedance tube microphone, a problem discussed in Chapter III.

In Fig. IV-26 the impedance of a 6.2 cm thick sample of Johns-Manville 1000 fiberglass ($P = 0.982$) is plotted versus frequency. The agreement between theory (dc flow resistivity) and data is excellent, significant deviation occurs at only the lowest frequencies.

The next material is Scottfelt 900-Z-2 ($P = 0.942$). The predicted (dc flow resistivity) and measured impedances of the Scottfelt for semi-infinite and 7.5 cm samples are plotted versus frequency in Fig. IV-27. The measured resistances are between 0 and 50% higher than predicted. The measured reactances are in good agreement with the predictions. In both cases the measured results are in excellent agreement. The agreement between theory and experiment for other Scottfelt samples is similar. The dc flow resistivity was used in the theoretical predictions. Although agreement between theory and data is not quite as good as for the fibrous materials, it is still fairly good. We therefore conclude that the behavior of the fully reticulated foam is similar to that of a fibrous material. One reason

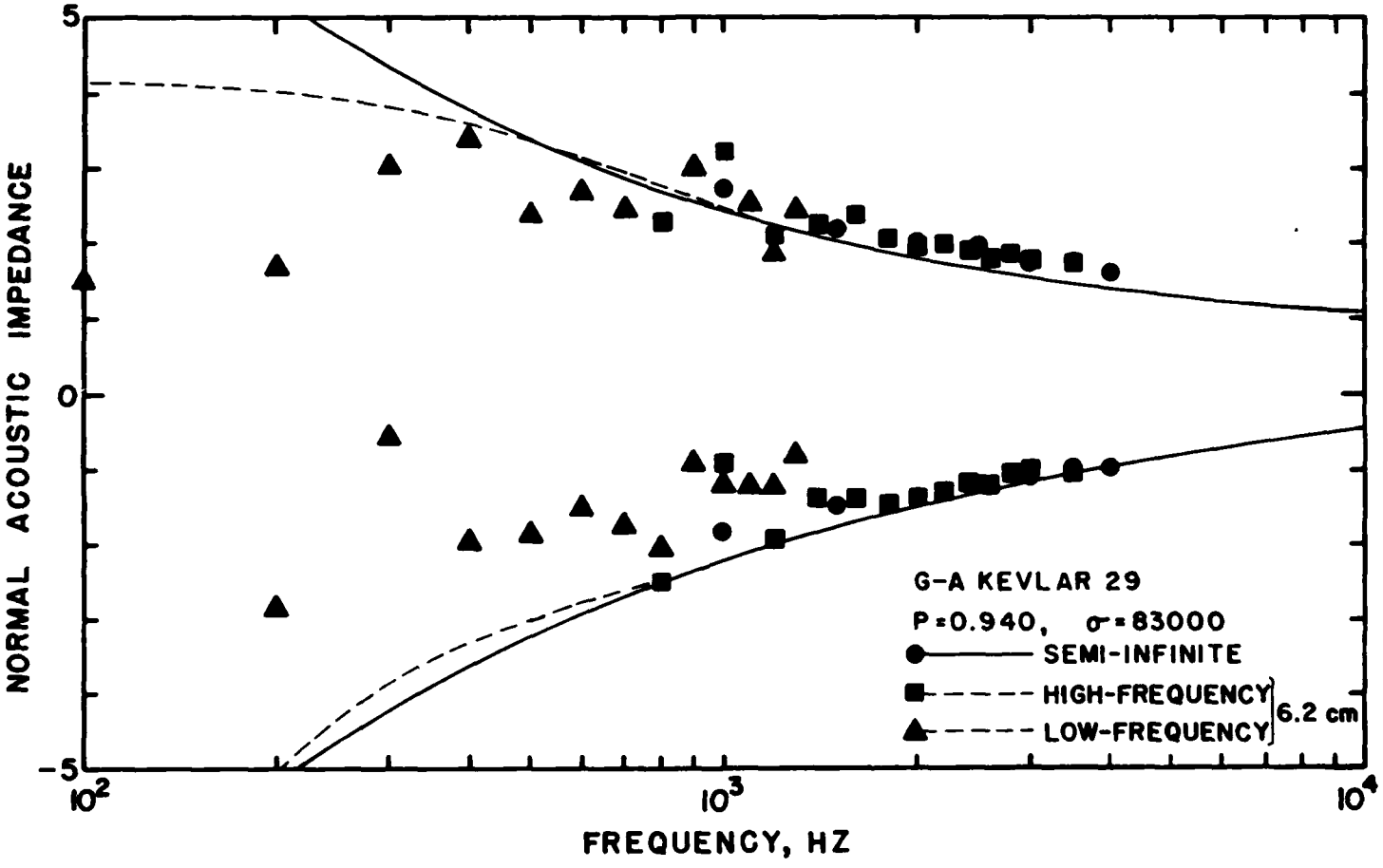

FIGURE IV-25
MEASURED AND PREDICTED IMPEDANCES VERSUS FREQUENCY FOR
6.2 cm THICK AND SEMI-INFINITE GLOBE-ALBANY KEVLAR 29.

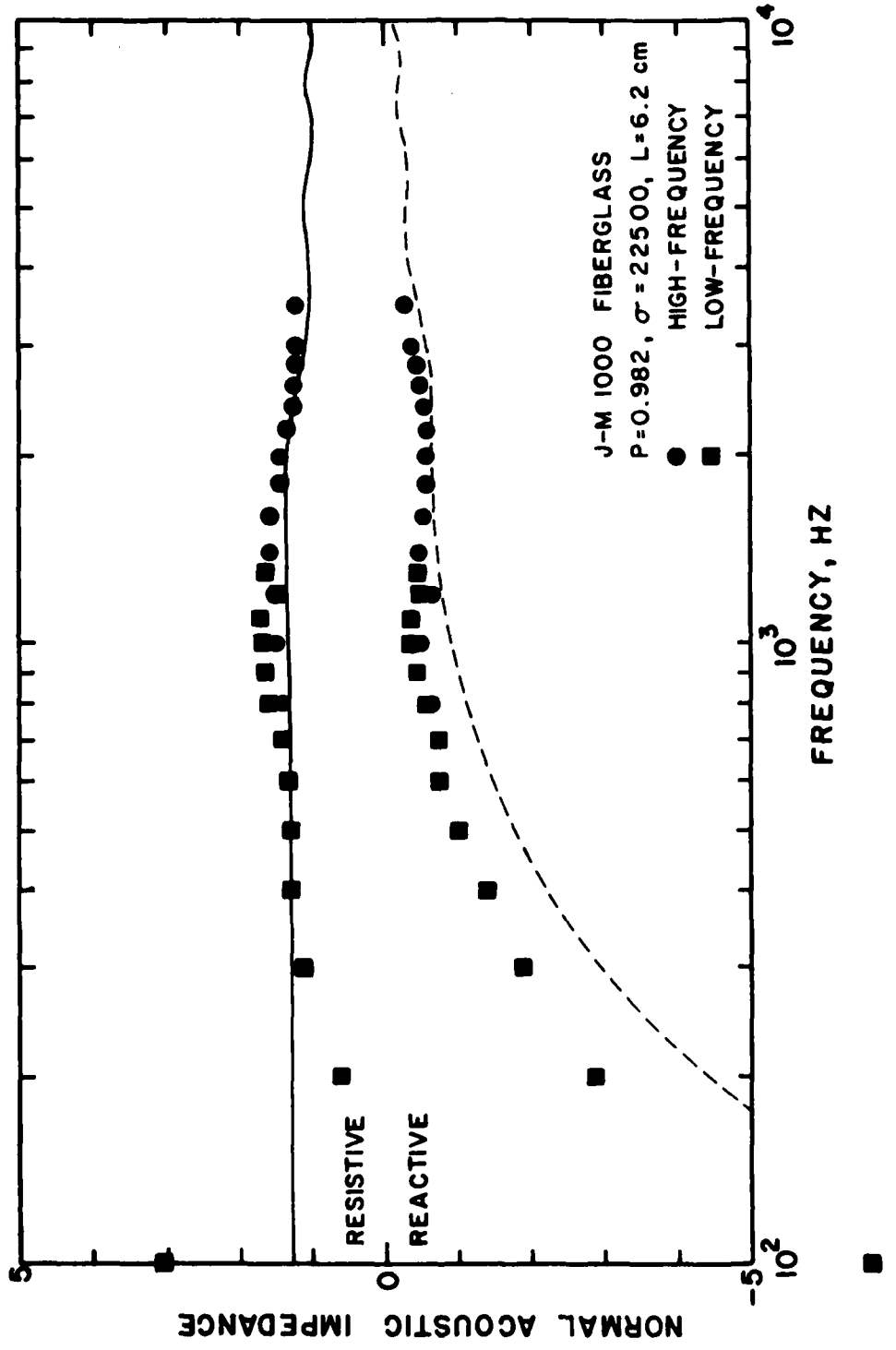

FIGURE IV-26
MEASURED AND PREDICTED IMPEDANCES VERSUS FREQUENCY FOR
6.2 cm THICK JOHNS-MANVILLE 1000 FIBERGLASS.

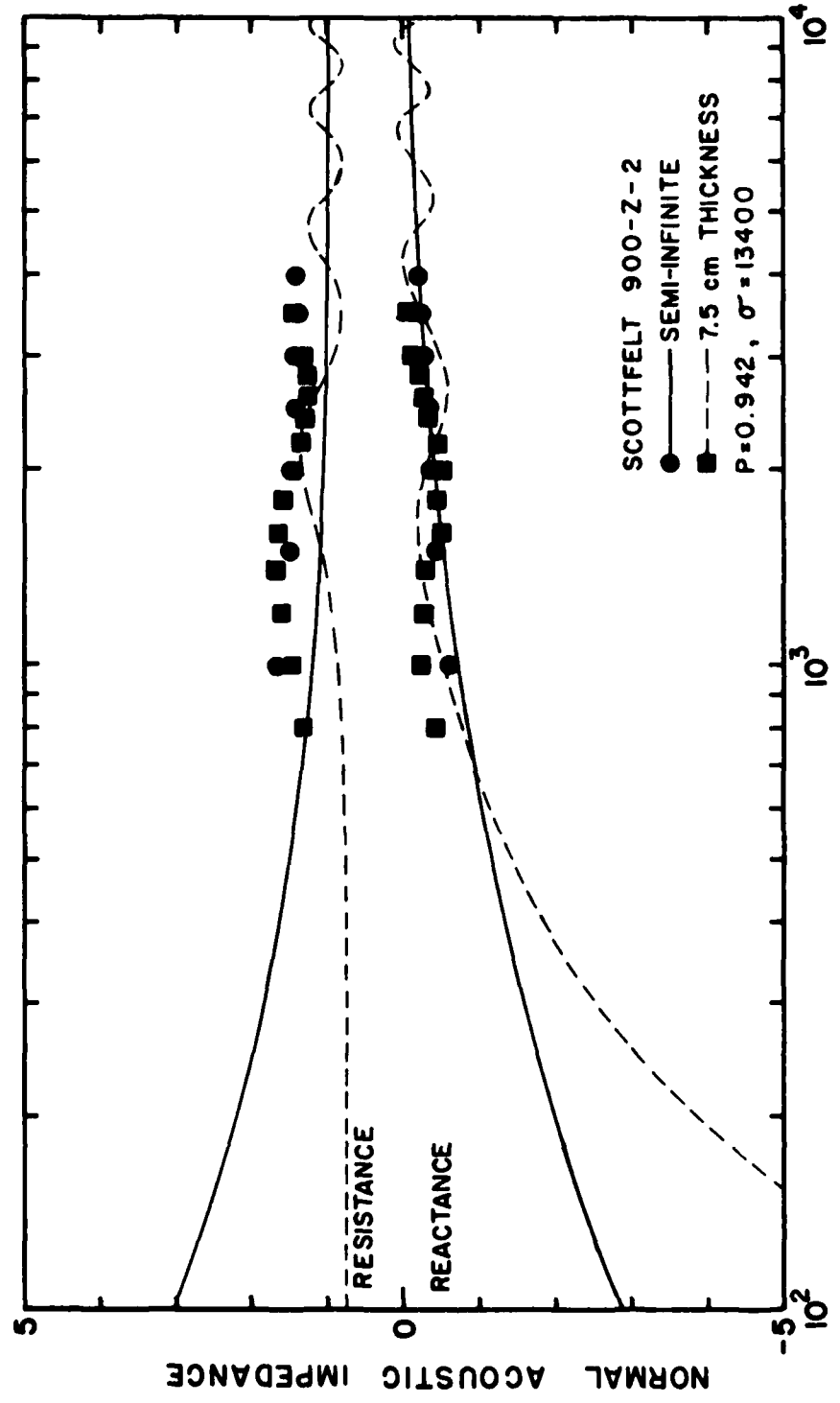

FIGURE IV-27
MEASURED AND PREDICTED IMPEDANCES VERSUS FREQUENCY FOR
7.5 cm THICK AND SEMI-INFINITE SCOTTFELT 900-Z-2.

this material was not used in the propagation parameter tests is that many pieces were not uniform in porosity throughout their thickness. The pieces were, in many cases, less porous at the surface than in the center. Although the samples chosen for this test were apparently uniform, invisible nonuniformity may have been one of the causes of the higher measured than predicted acoustic resistance.

In Fig. IV-28 the predicted and measured impedances of BAF ($P = 0.971$) for semi-infinite and 7.6 cm samples are plotted versus frequency. As expected from the propagation test results, the agreement between the theory and data is not good. The disagreement is much greater than for Scottfelt, but the trends are similar: The resistive part is much higher than predicted, whereas the reactive part is close to the predicted curve.

By comparing the data and theoretical results in Figs. IV-23 through IV-28, we find that fibrous and fully reticulated foam materials have similar acoustical properties and may be treated as rigid materials in the small signal case. On the other hand, the partially reticulated foam (BAF) has a measured acoustic resistance that is inexplicably high. As noted in Section IV-E above, one of the more general theories (see Chapter I) may provide a better explanation of the behavior of a partially reticulated foam.

2. Impedance at High Intensities

Proceeding with the ongoing quest for the definition of a useful nonlinearity parameter for bulk porous materials leads to the ad hoc nonlinear impedance model presented in Section II-E. The model consists of substituting the nonlinear dc flow resistivity

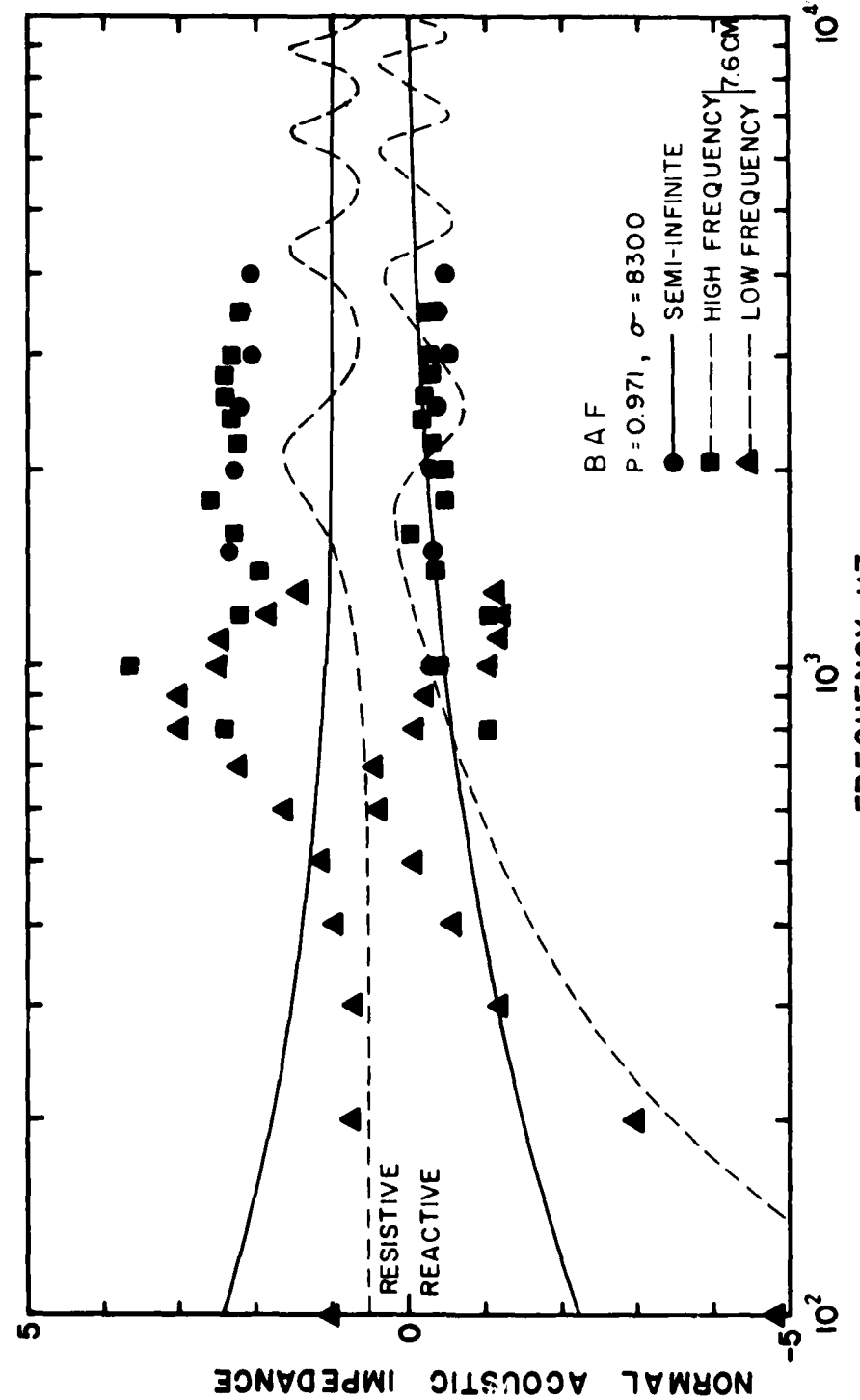

FIGURE IV-28
MEASURED AND PREDICTED IMPEDANCES VERSUS FREQUENCY FOR 7.6 cm THICK AND SEMI-INFINITE BLACHFORD ACOUSTICAL FOAM.

$\sigma_1 + \varepsilon\eta_1/P\sqrt{2}$ for the linear flow resistivity σ_1 in the definition of Γ_1. High-intensity measurements were not made in the standing wave tubes and only the test results for semi-infinite materials are presented. The materials are the same as those reported in part 1.

In making many comparisons between the measured and predicted nonlinear impedance behavior, we find that use of the dc flow resistivity in the theoretical calculations leads to an incorrect prediction of the material nonlinearity. (In the cases where acoustic resistivity values were used in the predictions, the same ratio of η/σ as found in Table IV-1 was employed to calculate η.) For the following comparisons the values of η are fit to the data.

In Fig. IV-29 the impedance at 1 kHz of several porosities ($P = 0.985$, 0.958, and 0.895) is plotted versus sound pressure level. The relative nonlinearities used in this figure are $\eta/\sigma = 0.24$, 0.12, and 0.06, whereas in Table IV-1 we found $\eta/\sigma \approx 0.2$. As with the excess attenuation parameter Γ and its relationship to the attenuation α, we find that the importance of the nonlinearity apparently decreases with increased attenuation.

Neither the resistive nor reactive parts of the impedance vary in magnitude to any great extent. In each of the three cases the measured reactive part appears to be slightly more linear in behavior than the resistive part. This behavior is found to exist at all porosities and frequencies in this material. The asymmetric behavior is illustrated in Fig. IV-30 where the frequency dependence of the

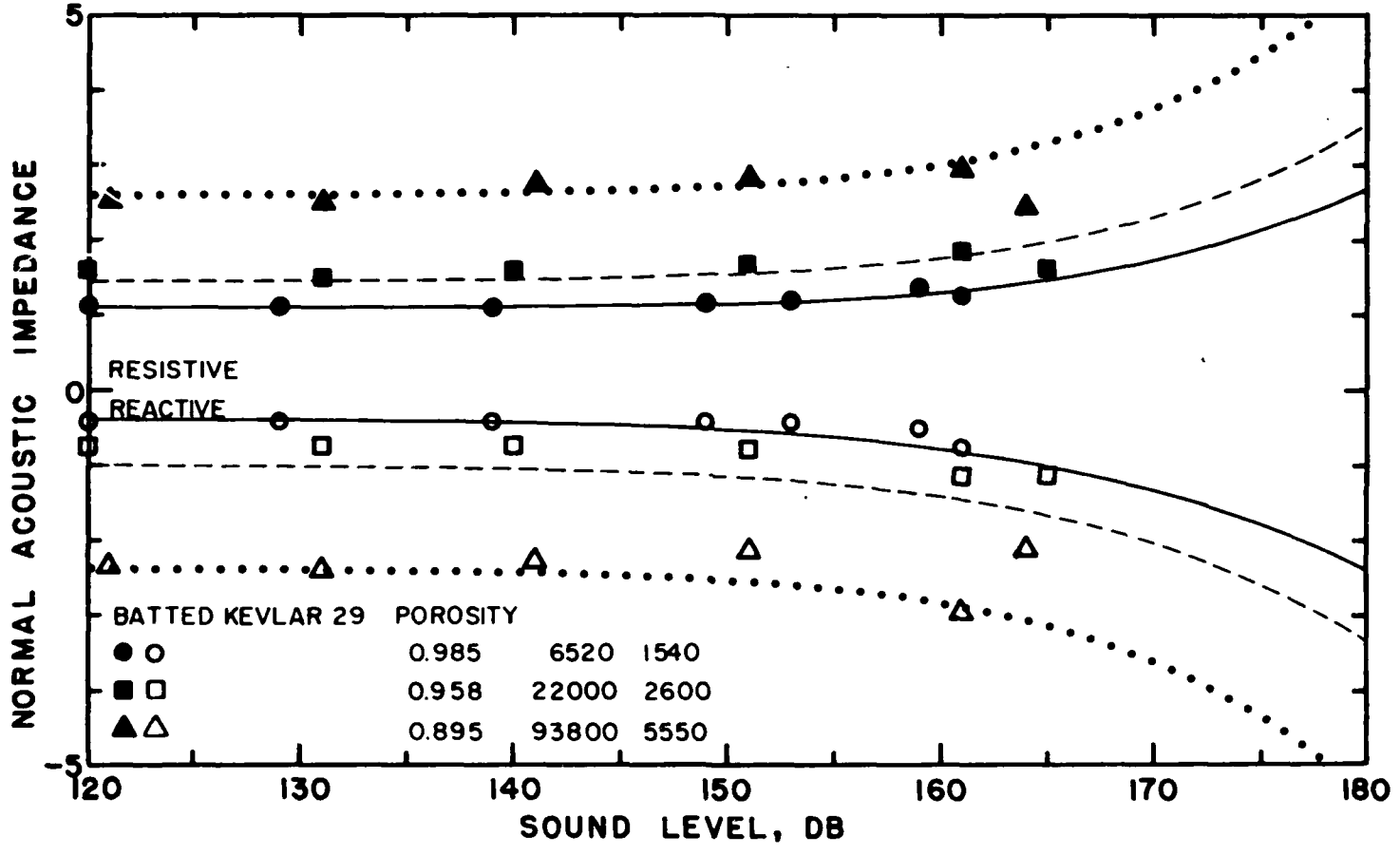

FIGURE IV-29
MEASURED AND PREDICTED IMPEDANCES AT 1 kHz VERSUS SOUND PRESSURE LEVEL FOR THREE POROSITIES OF SEMI-INFINITE BATTED KEVLAR 29.

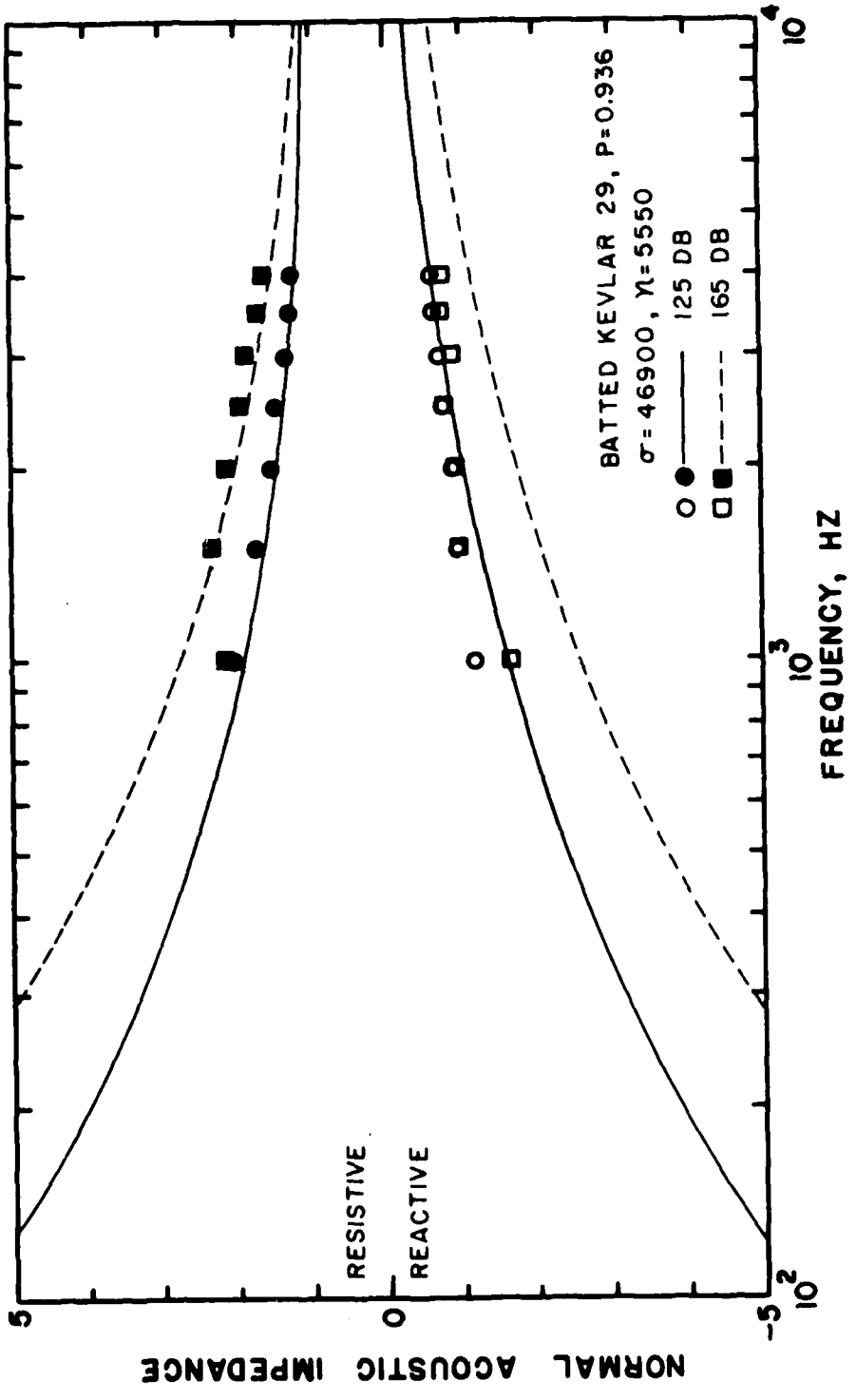

FIGURE IV-30
MEASURED AND PREDICTED IMPEDANCES AT TWO SOUND LEVELS VERSUS FREQUENCY FOR SEMI-INFINITE BATTED KEVLAR 29 (P = 0.936).

AD-A121 450 HIGH-INTENSITY SOUND IN AIR SATURATED FIBROUS BULK POROUS MATERIALS(U) TEXAS UNIV AT AUSTIN APPLIED RESEARCH LABS H L KUNTZ 03 SEP 82 ARL-TR-82-54 3/3

UNCLASSIFIED N00014-75-C-0847 F/G 11/6 NL

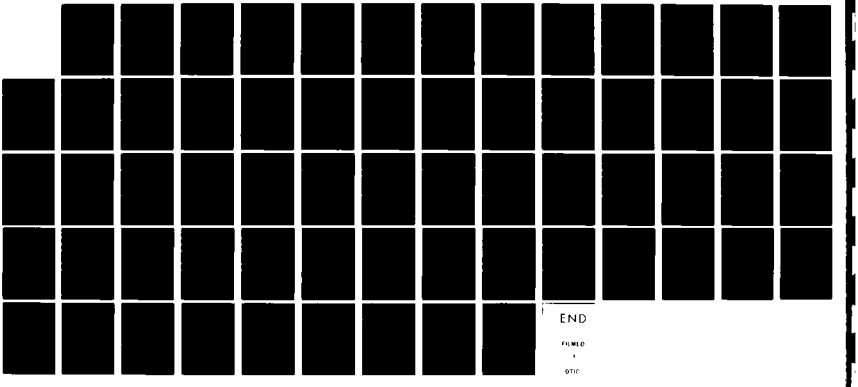

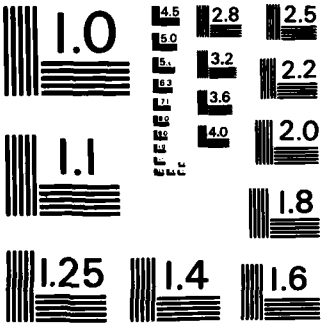

MICROCOPY RESOLUTION TEST CHART
NATIONAL BUREAU OF STANDARDS-1963-A

batted Kevlar ($P = 0.936$, $\eta/\sigma = 0.12$) impedance is plotted at two sound levels. The resistive part of the impedance is accurately predicted for all frequencies at both low and high intensities. On the other hand, the reactive part is well predicted at low intensity, but not at high intensity. Constancy in the reactive part of the impedance might be caused by fiber motion or by near independence of the reactance on particle velocity.

In Fig. IV-31 the predicted and measured 1 kHz impedances of the needled and felted (G-A) Kevlar 29 ($P = 0.940$) and the Scottfelt ($P = 0.942$) are plotted versus sound pressure level. The porosities of the materials in this figure are similar to the material in Fig. IV-30, but the material structures are quite different. The relative nonlinearities fit to the data are $\eta/\sigma = 0.08$ for the G-A Kevlar and $\eta/\sigma = 0.44$ for the Scottfelt.

The last material considered is the BAF. The dc flow resistivity tests indicated that this material has very nonlinear behavior. This fact is supported in the plot of the 1 kHz impedance versus sound level in Fig. IV-32. The relative nonlinearity $\eta/\sigma = 1.2$ has been fit to the data. The relative nonlinearity is much less than that listed in Table IV-1 ($\eta/\sigma \approx 4$). As opposed to the predictions for the other materials, the trends of <u>both</u> the resistive and reactive parts of the impedance are predicted by the nonlinear impedance equations. Except for the last data point, the resistive part is slightly more nonlinear than the reactive. A conclusion we draw from this figure is that the impedance model predicts changing reactance for all materials. In the cases of fibrous or fully reticulated

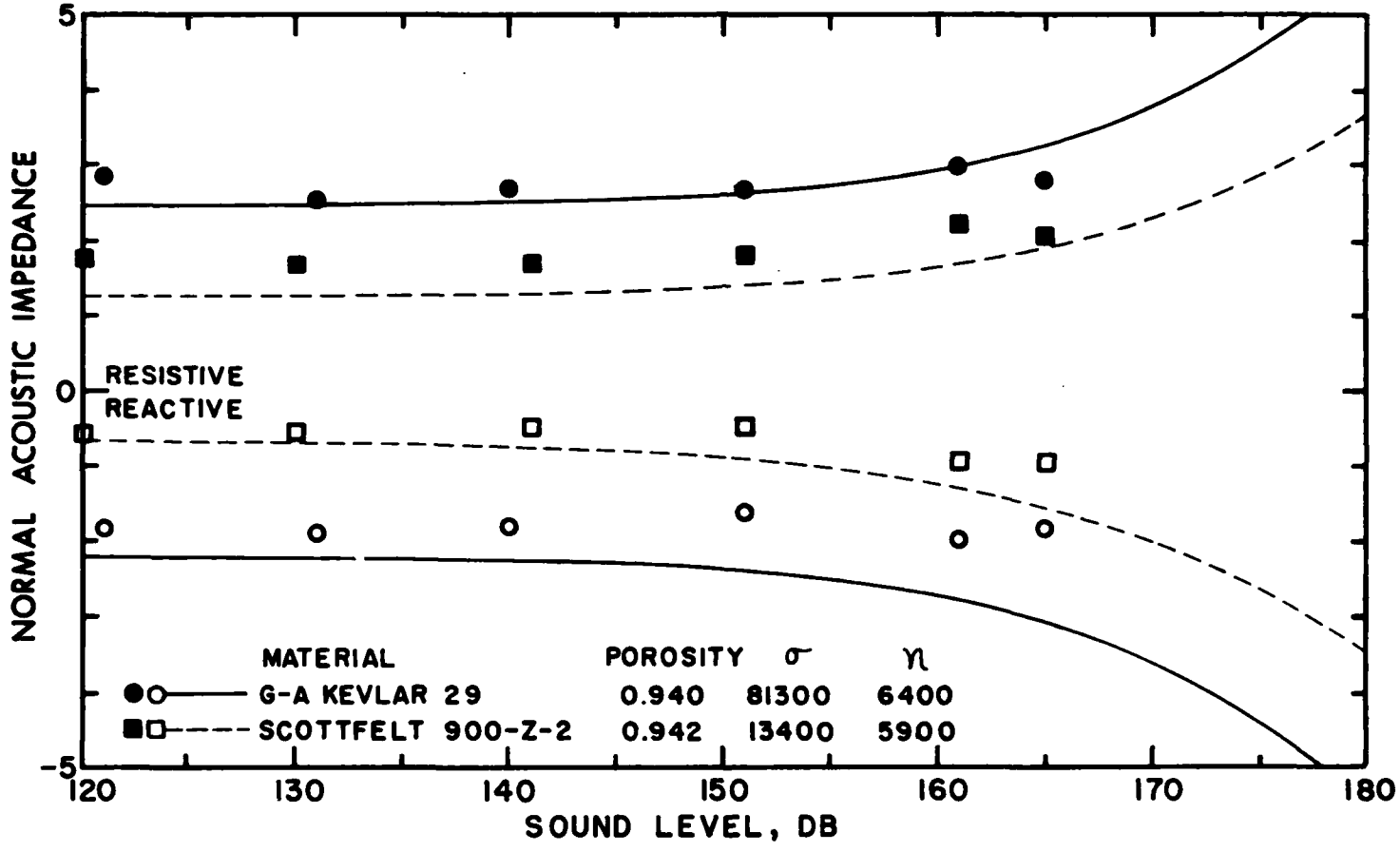

FIGURE IV-31
MEASURED AND PREDICTED IMPEDANCES AT 1 kHz VERUS SOUND PRESSURE LEVEL FOR GLOBE-ALBANY KEVLAR 29 AND SCOTTFELT 900-Z-2.

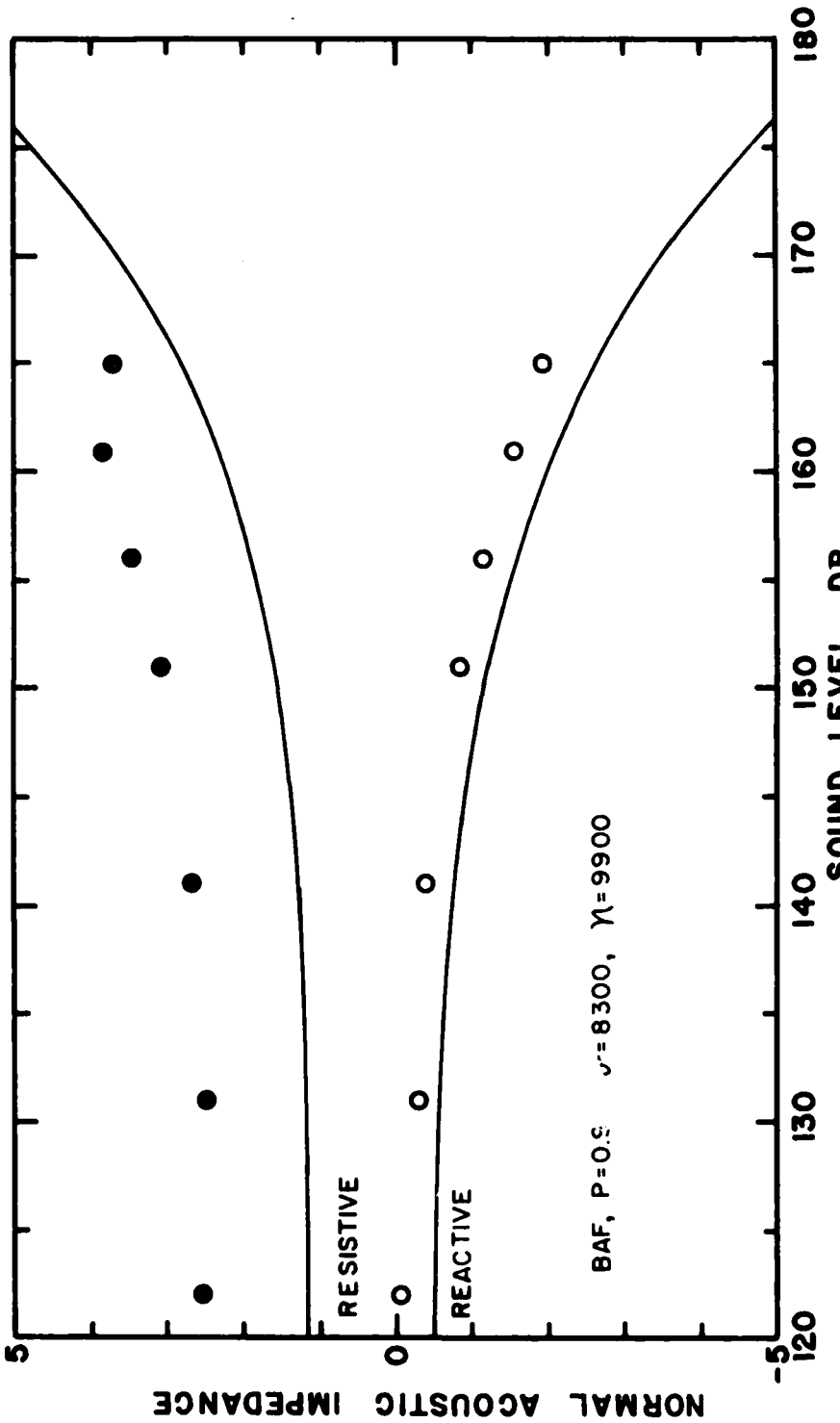

FIGURE IV-32
MEASURED AND PREDICTED IMPEDANCES AT 1 kHz VERSUS SOUND PRESSURE LEVEL FOR SEMI-INFINITE BLACHFORD ACOUSTICAL FOAM.

foam materials the threshold of nonlinear reactive behavior may be higher than anticipated by this model.

In Fig. IV-33 the frequency dependence of BAF at two sound levels is shown. We again see that the behavior is quite different from the batted Kevlar (Fig. IV-30) and that while the reactive part is accurately predicted at both sound levels, the resistive part is not.

In this ad hoc model, as opposed to the other high intensity sound models presented, the nonlinear effects are apparently dependent on the porosity (and, in turn, the attenuation). The nonlinearity decreases in importance as the porosity decreases, but this has not been accounted for in the model. A specific relationship between porosity and relative nonlinearity has not been drawn because the relationship appears to differ with the material.

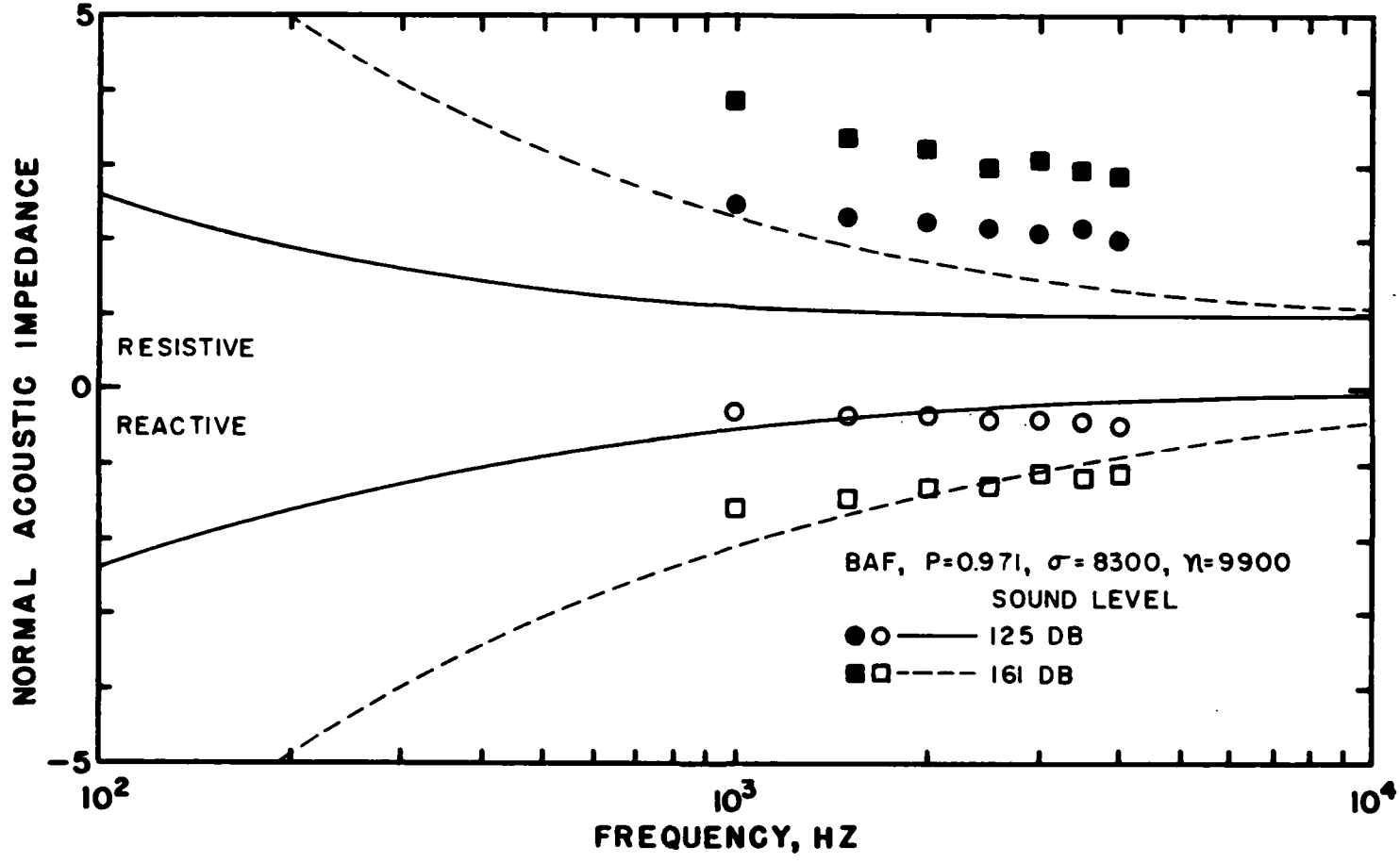

FIGURE IV-33
MEASURED AND PREDICTED IMPEDANCES AT TWO SOUND PRESSURE LEVELS VERSUS FREQUENCY FOR SEMI-INFINITE BLACHFORD ACOUSTICAL FOAM.

D. Summary

In this chapter the theoretical predictions have been compared with data from experiments for flow resistivity, propagation parameters, saturation effects, and specific normal acoustic impedance. Where possible, analysis has been presented with respect to frequency, sound pressure level, porosity, and material type. The agreement and disagreement between the data and theory have been discussed. The major points of the analysis are summarized in this section.

Two conclusions from the dc flow resistivity measurements (Section A) are drawn. First, each material exhibits nonlinear behavior at some threshold particle velocity. The onset of nonlinearity appears to be related to the material structure. For most fibrous materials and fully reticulated foams the modified Reynolds number can be used to estimate the nonlinearity threshold. Second, the dc linear flow resistivity was found to be a function of the porosity and the material structure. The exact relationship is unknown, but two previously derived functions [33,34] Eqs. I-12 and I-17 fit the data for two materials very well. Although only single porosities of some materials were measured, the functions should be good descriptors of the porosity-flow resistivity relationship.

The propagation measurements (Section B) yield important information about the definition of acoustic material nonlinearity. Analysis of the small-signal measurements (Part 1) showed that use of the dc flow resistivity data leads to a small, systematic error in the prediction of the acoustic propagation parameters of the porous materials. In the case of the batted Kevlar 29 material, the empirical

constant g in Eq. I-12 was changed to reflect a more realistic value for the material properties. No changes were made in the empirical constants of the other materials.

In Part 2 saturation effects in bulk porous materials were studied. It was determined that, although shocks never form, at high intensities the energy loss by the fundamental and the approach to saturation are governed by the same mathematical relationship in Eq. II-76 as when shocks do form in waves propagating in fluids. A Gol'dberg-type number is found in Eq. II-79. From comparison with data we define values for a porous material nonlinearity parameter T which is part of the Gol'dberg-type number. The nonlinearity parameter was found to depend on frequency and relative nonlinearity (material type), but, at least for batted Kevlar 29, not on porosity. High-intensity propagation measurements were reported in Part 3 and compared with the results of the perturbation solution of the conservation equations. At low intensities the propagation of the sinusoidal waves was found to be affected by material inhomogeneities. At high intensities the inhomogeneities affected the results and could be corrected for. At the higher porosities of Kevlar 29 the second-order perturbation solution results were found to diverge from the measured data. The theory predicted too much harmonic generation and not enough excess attenuation of the fundamental. As the porosity was decreased the theory was found to agree with the data at higher sound levels. The energy lost by the fundamental to excess attenuation was, apparently, not all shifted to the higher harmonics, as it is in fluids. It appears that

shocks do not form in the porous material because the nonlinearity is a turbulence related phenomena and the transference of energy out of the fundamental may be done on a broadband as well as a pure tone basis. There is no experimental basis for this statement, but it is offered as a possible explanation to where the energy goes.

Section C (impedance measurements) contains important information for the definition of the material impedance and support information on the propagation parameters. In Part 1 the low intensity theoretical and measured impedance for semi-infinite and finite materials were found to agree. Since the propagation parameters and the impedance of semi-infinite materials are directly related to each other, the agreement between data and theory supports the calculations and measurements for the propagation parameters.

In Part 2 the ad hoc impedance model was compared to the impedances of several materials at different frequencies and sound levels. The definition of the material nonlinearity through the use of this model acts in opposition to the dc flow resistivity model as well as the saturation model. The nonlinearity defined by the nonlinear impedance model is independent of frequency, but depends upon the porosity (attenuation) of the material. This result is not surprising because there is no actual theoretical basis for combining second order effects in a first order impedance equation. As a rough approximation, the approach works.

CHAPTER V

SUMMARY AND CONCLUSIONS

The propagation of intense sound in bulk porous materials has been studied both theoretically and experimentally. In the theoretical analysis, rigid material structure has been assumed and the viscous loss has been defined by the measured dc flow resistivity. In the linear analysis region these analytical assumptions have been successfully used by others [23,32,33,34,45] to explain their data. We have also experimentally verified the theory here.

A brief, small signal analysis of oscillatory heat transfer effects in fibrous porous materials is presented in Appendix A. Heat transfer effects modify the compressibility of the gas and, thus, the reference sound speed. The resultant reference sound speed is a function of fiber size, porosity, and frequency. Because the heat conductivity and heat capacity of porous materials are much larger than that of the air, the type of material used does not affect the analysis. The heat transfer analysis results are not used directly in the analysis presented in the main body of this study because the effects are small relative to the viscous effects. The heat transfer effect limits (isothermal and adiabatic sound speeds) are used to indicate the range of modifications to the viscous theory.

Standard nonlinear acoustic theory has been used as a basis for understanding the nonlinear effects on intense sound propagating in porous materials. Unfortunately, nonlinear acoustic theory of fluids

is not directly applicable to intense sound propagation in a porous material because of the high attenuation and severe dispersion found in these materials. For sounds propagating in fluids, viscous attenuation and dispersion effects are usually ignored in the pre-shock region. In bulk porous materials the attenuation and dispersion are so large that shocks never form. Despite the lack of shock formation, some of the effects of shock formation on the fundamental component, excess attenuation and saturation, are found to occur as if shocks had actually formed.

The experimentally determined approach to saturation is useful in describing how much of the acoustic energy of intense sound is propagated, or not propagated, in the porous material. The modeling of saturation effects was based on knowledge of how the energy is lost from the fundamental in the sawtooth region of an intense wave in a fluid [76,80,81]. For the high intensity energy loss an empirical parameter T has been defined and found to depend upon frequency f and the relative nonlinearity η/σ of the material. Because of the limited data, the exact relationship $T(f,\eta/\sigma)$ is unknown, but we defined an approximation. It is possible that T is a function of porosity. The excess attenuation and saturation experiments might be used to define the acoustical nonlinearity of the material. Possibly, a relationship between the saturation defined acoustic nonlinearity and the dc flow resistivity nonlinearity could be determined. There is probably a definable function between the two nonlinearities for fibrous materials or fully reticulated foams, but it may not be reasonable to

expect such a function for partially reticulated foams. In most cases we find that the fit of the excess attenuation model to the data to be excellent.

The perturbation solution of the conservation equations was derived in an attempt to explain excess attenuation of the fundamental and harmonic component generation in the measurement results. The model does not work well at high intensities, porosities, and nonlinearities. As the porosity is lowered the agreement between prediction and measurement results is improved.

Success of the excess attenuation model and failure of the perturbation theory have led us to re-examine how the excess attenuation energy is lost from the fundamental component. It appears that the fundamental component energy is lost not only to the harmonic components, but, because the nonlinearity is a turbulence process, to broadband random noise. This broadband noise level can be as much as 60-70 dB down from the fundamental component level, thus making it difficult to measure and not noticeable.

Impedance measurements and predictions for many materials have been presented to illustrate that the theory is applicable to most finite and semi-infinite materials at low intensities. These results are also presented in support of the propagation parameter measurements, since when $\alpha L >> 1$, $Z_1 \rightarrow \Gamma_1$ and the same results are obtained for each measurement.

A new experimental technique was developed for use in measuring the impedance of semi-infinite porous materials at high intensities.

The technique has some advantages over techniques developed by others. The system is simple to make and use and measurements may be made up to sound levels of 167 dB. As with some other measurement techniques, shock formation limits the sound level to which this method is applicable.

High-intensity sound measurements were done to evaluate how well an ad hoc model predicts the effect of sound level on impedance of a semi-infinite material. For the ad hoc model to be useful, the relative nonlinearity of the material has to be reduced with reduced porosity in order to predict the measured values. Because of the simplicity of the saturation and impedance models, relationships between the three experimentally determined nonlinearities would be useful in acoustical analysis. The determination of these relationships appears to be a fruitful area for future research.

The nonlinear effects described in this study are only applicable to materials exposed to very intense sound fields; even the most nonlinearly behaving materials do not exhibit nonlinear behavior below 120 dB. The most important area for use of these results is to bulk material use in the sound reduction of jet engine noise. Materials such as Kevlar 29 have recently been used inside the Helmholtz resonators that act to absorb sound before it is radiated out the engine intake. The additional treatment is, apparently, successful in reducing the radiated noise [92]. There may be a combination of effects caused by the porous material that offsets the

nonlinear behavior of the resonators and increases their effectiveness relative to resonators without porous materials. For example, the porous material impedance changes may offset the resonator impedance changes with sound level. Or, saturation effects may increase the sound absorption of a sound once it has entered the resonator, not letting as much sound out as without the porous material.

This study has been successful in describing how sinusoidal (or almost sinusoidal) waves interact with a bulk porous material. The results of the study should also be useful in laying the groundwork for future studies in this area. Important topics for future research would be (1) an investigation of the relationships between the acoustic nonlinearities as defined in the various theories and experiments in this study and (2) an investigation of the interaction of the acoustic field and a resonator filled with a fibrous material.

APPENDIX A

A Theoretical Description of Oscillatory Heat Transfer Effects on the Propagation of Sound in a Fibrous Porous Material

In this appendix a mathematical model of heat transfer effects on sound propagation in air saturated fibrous material is derived. The resulting model is good for low-intensity sounds propagating in the air of the porous material. The conductive heat transfer properties of both the air and the fibers are accounted for. In the final analysis, the specific heat transfer properties of the fibers are found to have a minimal effect on the sound propagation and may be neglected. The heat transfer primarily affects the sound speed. Its influence on the attenuation is small relative to that of viscosity and is ignored.

The derivation that follows is for cylindrical fibers, and cylindrical coordinates are used. The heat transfer is assumed to be due to conduction only, i.e., convective heat transfer and acoustic streaming (mixing) at high intensities are not accounted for. A primary effect of convection and streaming would be to raise the heat transfer rate and thus increase the tendency of the propagation to be isothermal.

Two steps are used in determining the oscillatory heat transfer in fibrous porous materials. First, the general problem of oscillatory heat transfer between the medium and the cylindrical fiber is determined. Two different boundary conditions at the fiber surface are considered, and the effects of each on the sound propagation are discussed. Second, the relation describing the effect of the heat transfer

on the phase speed is derived. This relation is used in Eq. I-6 for comparison to the phase speed of Kevlar 29 ($P = 0.980$).

I. Oscillatory Heat Transfer in Cylindrical Coordinates

In this section the oscillatory heat transfer between a single fiber and the infinite material in which it is immersed is considered. The general heat transfer equation is presented and solved for two sets of boundary conditions. The two solutions are compared.

A. Equation and General Solution

The governing equation for radial heat conduction in cylindrical coordinates is [22]

$$\left(\frac{\partial^2 T}{\partial r^2} + \frac{1}{r}\frac{\partial T}{\partial r}\right) - \frac{1}{\alpha_T}\frac{\partial T}{\partial t} = \Lambda \quad , \tag{A-1}$$

where $\alpha_T = \kappa/\rho C$ is the thermal diffusivity, ρ is the density, C is the specific heat, κ is the thermal conductivity, r is the radial distance from the fiber center, T is the temperature, t is the time, and Λ is an arbitrary driving function. The driving function Λ may be a function of the coordinate system and time. The relation $\kappa\Lambda$ is the rate of heat production per unit volume [22].

If the driving function Λ is sinusoidal in time, i.e.,

$$\Lambda = \Lambda_o e^{j\omega t} \quad , \tag{A-2}$$

then the steady state solution of Eq. A-1 is [22,52,61]

$$T(r,t) = \left[BJ_o\left(\xi r j^{3/2}\right) + DK_o\left(\xi r j^{1/2}\right) - \frac{\Lambda_o}{j\omega}\right] e^{j\omega t} + T_o \quad , \tag{A-3}$$

where J_o is the Bessel function of the first kind of order zero, K_o is the modified Bessel function of the second kind of order zero, T_o is the reference (ambient) temperature, and $\xi = \sqrt{\omega/\alpha_T}$. In this presentation we assume that Λ_o is constant in the region of interest, either internal or external to the fiber. Bessel functions with imaginary arguments can be written in terms of Kelvin functions with real arguments. The relations are [22,52,61]

$$J_\nu\left(zj^{3/2}\right) = \text{ber}_\nu z + j\ \text{bei}_\nu z \tag{A-4}$$

and

$$K_\nu\left(zj^{1/2}\right) = j^\nu\left(\text{ker}_\nu z + j\ \text{kei}_\nu z\right) \quad . \tag{A-5}$$

Alternately, the Kelvin functions can be written in polar form as

$$M_\nu(z)e^{j\theta_\nu(z)} = \sqrt{\text{ber}_\nu^2 z + \text{bei}_\nu^2 z}\ \left(\cos\theta_\nu(z) + j\ \sin\theta_\nu(z)\right) \tag{A-6a}$$

and

$$N_\nu(z)e^{j\phi_\nu(z)} = \sqrt{\text{ker}_\nu^2 z + \text{kei}_\nu^2 z}\ \left(\cos\phi_\nu(z) + j\ \sin\phi_\nu(z)\right) \quad , \tag{A-6b}$$

where

$$\theta_\nu(z) = \arctan\frac{\text{bei}_\nu z}{\text{ber}_\nu z} \tag{A-7a}$$

and

$$\phi_\nu(z) = \arctan \frac{\text{kei}_\nu z}{\text{ker}_\nu z} \quad . \tag{A-7b}$$

The equations above are valid in most regions of the coordinate system. The $K_\nu\left(zj^{\frac{1}{2}}\right)$ term becomes infinite at z=0 and the $J_\nu\left(zj^{3/2}\right)$ term becomes infinite at z=∞. In what follows, the subscript I denotes the region internal to the fiber and the subscript E the surrounding material. The constants B and D are determined by the boundary conditions, which are discussed next.

Table A-1 is a listing of the thermal properties of various materials. Several of these values are used in following examples.

B. Boundary Conditions

Two sets of boundary conditions at the fiber surface are considered here. In one case the fiber surface is assumed to be isothermal, in the other case non-isothermal. But first, general boundary conditions, that is, conditions at r=0 and ∞ must be stated.

1. General

The boundary condition at the fiber center is that the temperature is finite, or

$$\left.\frac{\partial T_E(r,t)}{\partial r}\right|_{r=0} = 0 \quad . \tag{A-8}$$

The boundary condition at an infinite distance from the fiber is

TABLE A-1

THERMAL PROPERTIES OF SEVERAL MATERIALS

MATERIAL	κ THERMAL CONDUCTIVITY W/m°K	ρ DENSITY kg/m^3	C_p SPECIFIC HEAT J/kg°K	α_T THERMAL DIFFUSIVITY m^2/s	ξa f=1000 Hz $a=6\cdot10^{-6}$ m
COPPER [50]	390	8900	385	$1.1\cdot10^{-4}$	0.045
STEEL [50]	45	7700	450	$1.3\cdot10^{-5}$	0.13
AIR (300°K) [28]	0.026	1.2	1006	$7.5\cdot10^{-9}$	0.10
GLASS [50]	2.5	2600	775	$1.2\cdot10^{-6}$	0.42
KEVLAR [50]	0.7	1445	1200	$4.0\cdot10^{-7}$	0.75
NYLON [50]	0.2	1100	1700	$1.1\cdot10^{-7}$	1.5
TEFLON [50]	0.24	2200	1050	$1.0\cdot10^{-7}$	1.5
POLYURETHANE [50]	0.3	1150	1000	$2.6\cdot10^{-7}$	0.93

$$\left.\frac{\partial T_E(r,t)}{\partial r}\right|_{r=\infty} = 0 \quad . \tag{A-9}$$

2. Isothermal Surface

The mathematical analysis is simplest if the surface temperature is constant, i.e., isothermal,

$$T(a,t) = T_o \quad , \tag{A-10}$$

where a is the fiber radius and T_o is the reference (ambient) temperature. In this case the external and internal temperature fields are decoupled. As will be seen, this condition closely approximates the actual surface boundary condition of the fiber in air. The isothermal boundary condition is justified when the fiber has a much greater heat capacity and thermal diffusivity than the surrounding medium.

3. Oscillating Surface Temperature

The mathermatical analysis is still simple in this case; we have just shifted the heat source from a volume to a surface. We set

$$\Lambda_o = 0 \tag{A-11}$$

and

$$T(r,t)\big|_{r=a} = \Lambda_a e^{j\omega t} \quad , \tag{A-12}$$

where Λ_a is defined only at the fiber surface. The internal and external temperature fields are decoupled. This case closely approximates the temperature oscillations of a fiber in a medium. For more general conditions the exact boundary conditions must be used. They are discussed next.

4. Non-Isothermal Surface

In the situation where both the fiber and surrounding medium specific heats and thermal diffusivities are similar, the isothermal surface condition cannot be assumed. The heat flux and the temperature at the fiber surface must be equal at all times. The mathematical definition as to what occurs at the fiber surface is defined by [22,38]

$$\kappa_I \left.\frac{\partial T_I(r,t)}{\partial r}\right|_{r=a} = \kappa_E \left.\frac{\partial T_E(r,t)}{\partial r}\right|_{r=a} \qquad \text{(A-13)}$$

and

$$T_I(a,t) = T_E(a,t) \quad . \qquad \text{(A-14)}$$

With these two sets of boundary conditions any simple heat conduction problem with a cylinder in a different infinite medium can be solved. Next the above solution and boundary conditions are applied to the problem at hand.

C. Internal Heat Transfer

Heat transfer within the fiber with an oscillating surface temperature, Eq. A-12, is described first. In this case only the

boundary conditions at the center and surface are needed to solve Eq. A-3 (Λ_o=0). The exact solution is

$$T_I(r,t) = \frac{\Lambda_o}{j\omega} \frac{J_o\left(\xi_I r j^{3/2}\right)}{J_o\left(\xi_I a j^{3/2}\right)} e^{j\omega t} + T_o \quad . \qquad \text{(A-15)}$$

Gröber [31] derived relations similar to Eq. A-15 for convective heat transfer to a cylinder. The paper has many theoretical examples and is quite complete.

We set T_o=0 and plot the normalized magnitude of Eq. A-15 $(T_I-T_o)/\kappa\Lambda_a$ versus distance for various values of ξa in Fig. A-1. If we define the thermal boundary layer thickness as $\delta=\sqrt{2\alpha_T/\omega}$, we find that $\xi=\sqrt{2}/\delta$. The internal thermal boundary layer is illustrated by the region near the surface which changes its temperature, and, as $\xi_I a$ becomes larger, the relative boundary layer thickness becomes smaller, indicating that heat transfer is less important when $\xi_I a > 10$. The internal thermal boundary layer of the fiber is significant only when the frequency is low, the fiber diameter is small, and/or the thermal diffusivity is large ($\xi_I a < 10$).

D. External Heat Transfer

Heat transfer outside the fiber with an isothermal surface, Eq. A-12, is described next. In this case only the boundary conditions at the fiber surface and infinity are needed to solve Eq. (A-3). The exact solution is

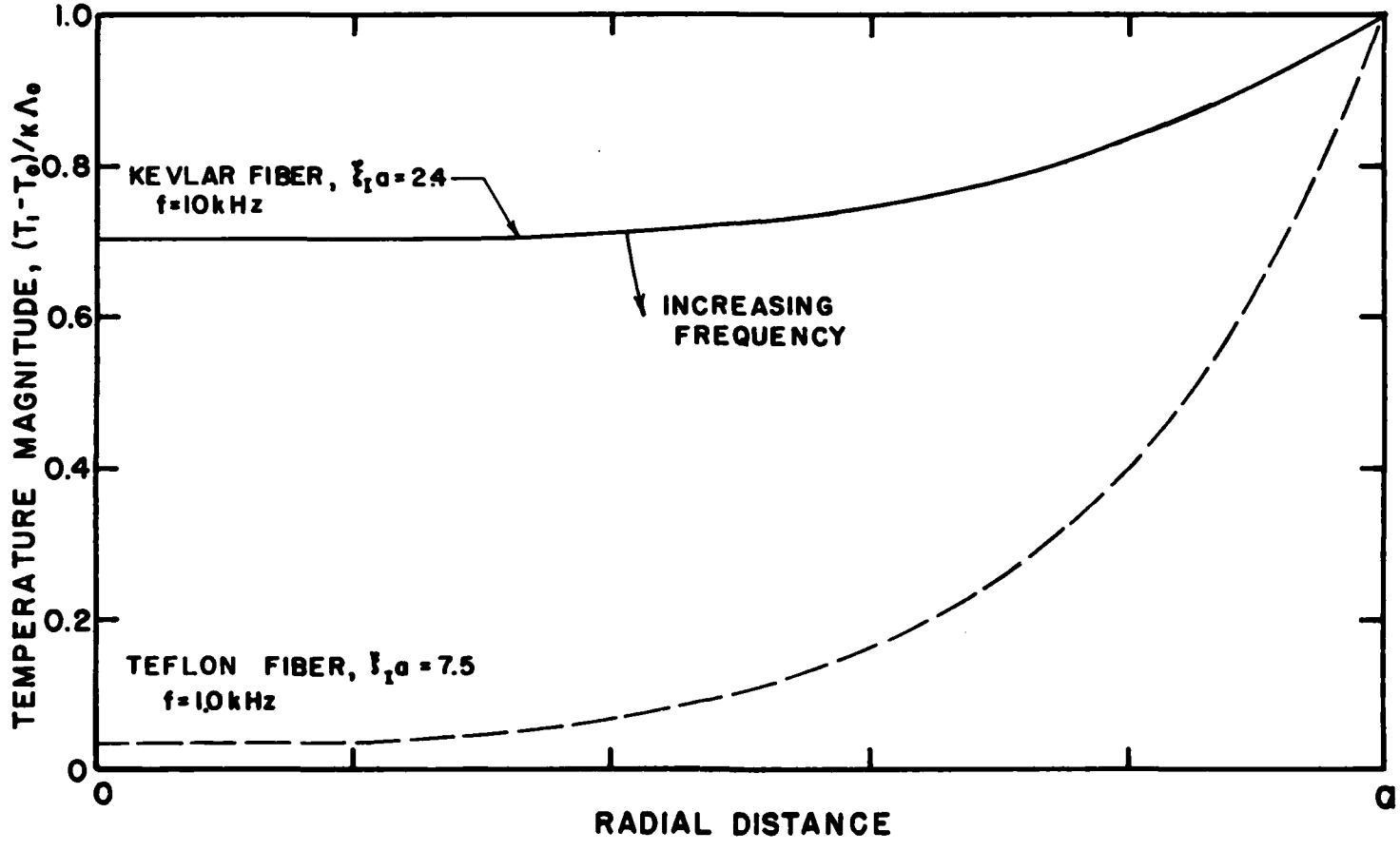

FIGURE A-1
NORMALIZED MAGNITUDE OF THE INTERNAL, OSCILLATORY TEMPERATURE VERSUS RADIAL DISTANCE FOR A FIBER WITH AN ISOTHERMAL SURFACE.

$$T_E(r,t) = \frac{\Lambda_o}{j\omega}\left[-1 + \frac{K_o\left(\xi_E r j^{1/2}\right)}{K_o\left(\xi_E a j^{1/2}\right)}\right] e^{j\omega t} + T_o \quad . \qquad \text{(A-16)}$$

We set T_o=0 and plot the normalized magnitude of Eq. A-16 $(T_E - T_o)/\kappa\Lambda_o$ versus distance, for various values of $\xi_E a$, in Fig. A-2. The external thermal boundary layer is illustrated here. As shown in part C, when $\xi_E a$ increases the relative boundary layer thickness decreases. The boundary layer thickness is important only when $\xi_E a < 1.0$.

E. Coupled Heat Transfer

This case is not so simple because the internal and external fields are coupled. The result is two coupled equations which define the total thermal field.

Inside the fiber the solution is

$$T_I(r,t) = \frac{j\Lambda_o \xi_E \kappa_E K_o'\left(\xi_E a j^{1/2}\right) J_o\left(\xi_I r j^{3/2}\right)}{\omega E} e^{j\omega t} + T_o \qquad \text{(A-17)}$$

and outside the fiber the solution is

$$T_E(r,t) = \frac{\Lambda_o}{\omega}\left[j + \frac{\xi_I \kappa_I J_o'\left(\xi_I a j^{3/2}\right) K_o\left(\xi_E r j^{1/2}\right)}{E}\right] e^{j\omega t} + T_o \quad , \qquad \text{(A-18)}$$

where

$$E = \xi_E \kappa_E K_o'\left(\xi_E a j^{1/2}\right) J_o\left(\xi_I a j^{3/2}\right) + j\xi_I \kappa_I J_o'\left(\xi_I a j^{3/2}\right) K_o\left(\xi_E a j^{1/2}\right) \qquad \text{(A-19)}$$

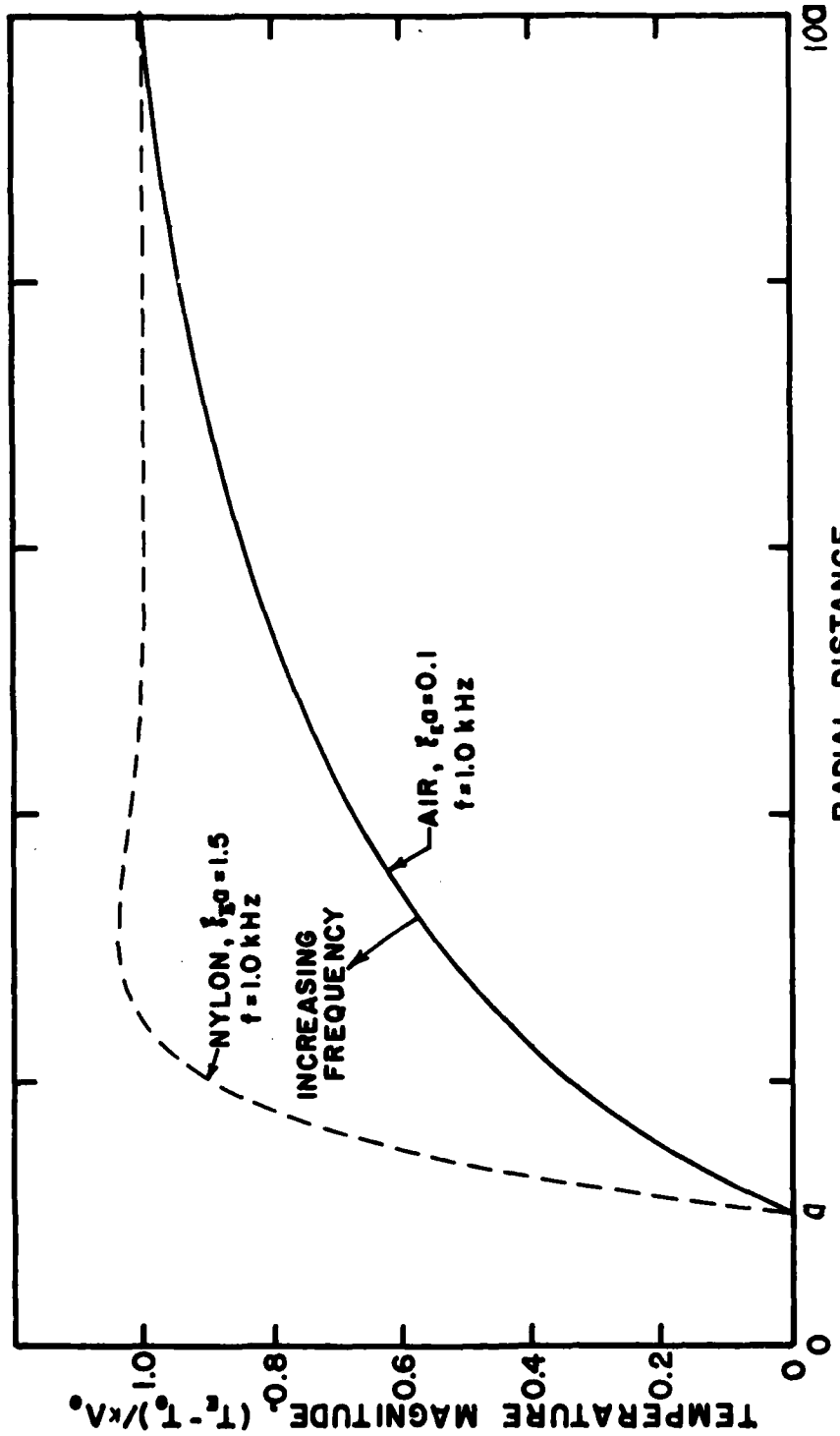

FIGURE A-2
NORMALIZED MAGNITUDE OF THE EXTERNAL, OSCILLATORY TEMPERATURE VERSUS RADIAL DISTANCE FOR A HEAT-CONDUCTING MEDIUM CONTAINING A SINGLE ISOTHERMAL FIBER.

and the primes denote derivatives with respect to the function argument.

A plot of these equations versus distance, for several values of $\xi_I a$ and $\xi_E a$, is shown in Fig. A-3. This plot shows that the isothermal surface boundary conditions are adequate for our purposes. The dotted curve is for a Kevlar fiber in air and a 0.1 kHz temperature oscillation. As the frequency increases, the boundary layer becomes smaller and the fiber-air system becomes more isothermal, as shown by the solid curve. The dashed curve indicates what the temperature oscillations would be for two materials of similar properties (a Teflon fiber in nylon).

In this section the oscillatory heat transfer in and around a cylinder has been studied. For the purposes of our study it has been shown that the fiber material is inconsequential to the formation of the thermal boundary layer in air and the isothermal surface boundary condition can be used in the analysis in part II of this appendix.

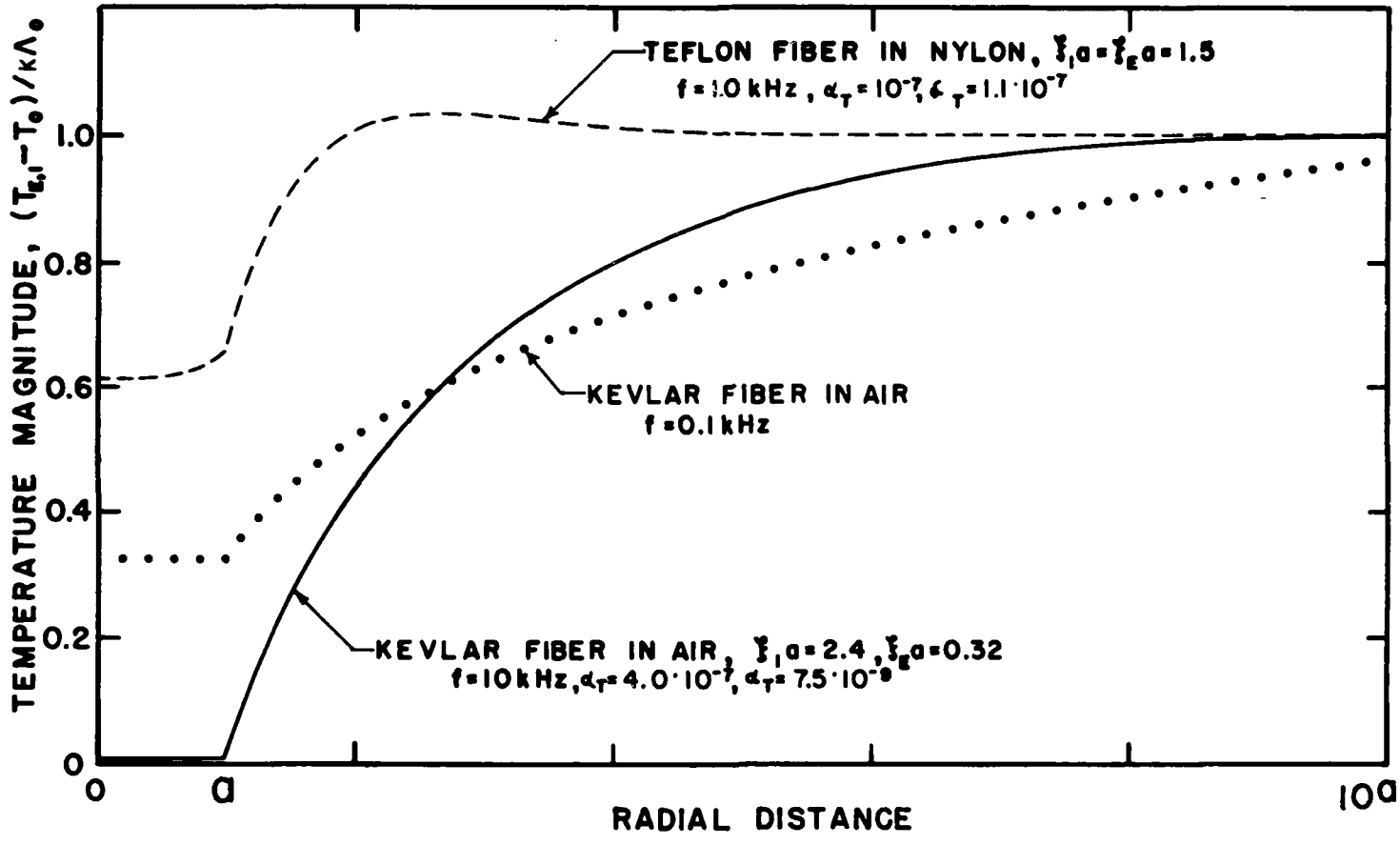

FIGURE A-3
NORMALIZED MAGNITUDE OF THE OSCILLATORY TEMPERATURE VERSUS RADIAL DISTANCE FOR A SINGLE FIBER IN A HEAT-CONDUCTING MEDIUM.

II. Oscillatory Heat Transfer Effects in an Air Saturated, Fibrous Porous Material

In the previous analysis the only consideration was the heat transfer to and from a single fiber in an infinite medium. In this section the conservation of energy equation, which turns out to have the form of Eq. A-1, is used to study the heat transfer to and from a single fiber when the temperature oscillation is caused by an acoustic wave for which $\lambda >> a$. The results are used to determine the heat transfer effects on the phase speed and attenuation in a porous material. The approach in this section is modeled after an analysis by Pfreim [63] and restated by Devin [26] on heat transfer effects in oscillating gas bubbles in water.

In the following, the energy equation is derived and solved, the sound speed is determined, and then the effects of viscosity and heat transfer are simply added and a complete small signal solution obtained.

A. Energy Equation

The process to be described must obey the first law of thermodynamics, the conservation of energy

$$\frac{dE}{dt} = \frac{dQ}{dt} + \frac{dW}{dt} \quad , \tag{A-20}$$

where dE/dt is the rate of increase in the internal energy of the gas per unit volume, dQ/dt is the rate of heat transferred to the gas per unit volume, and dW/dt is the rate of work done on the gas per unit volume. Since the fluid considered here is a perfect gas, the rate of increase of energy per unit volume is

$$\frac{dE}{dt} = \rho C_v \frac{dT}{dt} \quad , \tag{A-21}$$

where C_v is the specific heat at constant volume. Our analysis is for small signals and we can set $\rho = \rho_o$, where ρ_o is the ambient density, and use partial derivatives in Eq. A-21 and the following. The rate of heat transferred to the gas per unit volume (in cylindrical coordinates) is

$$\frac{\partial Q}{\partial t} = \kappa\left[\frac{\partial^2 T}{\partial r^2} + \frac{1}{r}\frac{\partial T}{\partial r}\right] \quad . \tag{A-22}$$

The rate of work done on the gas per unit volume is

$$\frac{\partial W}{\partial t} = \frac{P}{\rho}\frac{\partial \rho}{\partial t} \quad , \tag{A-23}$$

where P is the total pressure. The only overt differences between the above equations and the equations in Devin's analysis [26] are that Devin was concerned with spherical coordinates and viewed everything on a per unit mass basis. Equations A-21, A-22, and A-23 are used in Eq. A-20 to yield the energy equation

$$\rho_o C_v \frac{\partial T}{\partial t} = \kappa\left[\frac{\partial^2 T}{\partial r^2} + \frac{1}{r}\frac{\partial T}{\partial r}\right] + \frac{P}{\rho}\frac{\partial \rho}{\partial t} \quad . \tag{A-24}$$

We need to replace the density term with a pressure. The gas is assumed to be ideal and

$$P = \rho(C_p - C_v)T \quad , \tag{A-25}$$

where C_p is the specific heat at constant pressure. If a time

derivative of Eq. A-25 is taken and Eq. A-25 substituted into the derivative, the result is

$$\frac{P}{\rho}\frac{d\rho}{dt} = \frac{dP}{dt} - \rho(C_p - C_v)\frac{dT}{dt} \quad . \tag{A-26}$$

Substitute Eq. A-26 into Eq. A-24, eliminate like terms, and write the equation as

$$\kappa \frac{\partial^2 T}{\partial r^2} + \frac{1}{r}\frac{\partial T}{\partial r} - \frac{1}{\alpha_T}\frac{\partial T}{\partial t} = -\frac{1}{\kappa}\frac{\partial P}{\partial t} \quad . \tag{A-27}$$

Equation A-27 is a general equation applicable to a small signal acoustic wave in the gas whenever $\lambda >> a$. Equation A-27 is equivalent to Eq. A-1, with

$$\Lambda = -(\partial P/\partial t)/\kappa \quad . \tag{A-28}$$

The analysis can probably be performed for waves other than sinusoids, but, for the analysis here, sinusoids are the only waves considered.

B. General Solution

The solution of Eq. A-27 is accomplished by assuming that the acoustic wave is a sinusoid such that

$$P = P_o + p\,e^{j\omega t} \quad , \tag{A-29}$$

where P_o is the ambient pressure, p is the magnitude of the acoustic pressure, and $\lambda >> a$. Since $\lambda >> a$ and this is a boundary layer problem, there is no pressure gradient in the vicinity of the fiber; in other words the acoustic pressure p is assumed to have no dependence on the radial distance r. Equation A-27 becomes

$$\frac{\partial^2 T}{\partial r^2} + \frac{1}{r}\frac{\partial T}{\partial r} - \frac{1}{\alpha_T}\frac{\partial T}{\partial t} = -\frac{j\omega p}{\kappa} e^{j\omega t} \quad . \tag{A-30}$$

If we assume that the fiber temperature remains constant, then Eq. A-16 is used to obtain the solution of Eq. A-30. The solution is

$$T(r,t) = T_o + \frac{\xi^2 p}{\rho_o C_p}\left[1 - \frac{K_o(\xi r j^{\frac{1}{2}})}{K_o(\xi a j^{\frac{1}{2}})}\right] e^{j\omega t} \quad . \tag{A-31}$$

This solution is used in the next section to calculate the heat transfer effects on the sound speed in a fibrous porous material.

C. Heat Transfer Effects on the Phase Speed

Now that the radial dependence of the temperature is known, the small signal phase speed may be calculated. Since we have losses caused by heat transfer effects, the phase speed is neither adiabatic nor isothermal. The phase speed is written as

$$c_T^2 \approx \frac{dp}{d\rho} \quad . \tag{A-32}$$

The limitation that the compressions be isentropic has been removed because the compressions are no longer lossless. From Eq. A-32 the phase speed can only be calculated if a relation between the pressure and density can be found. In order to do this the heat transfer effects are integrated from the fiber surface out to some reference distance. The specific reference distance is determined later in this appendix. The volume integration is performed in cylindrical coordinates.

In cylindrical coordinates the specific volume per unit mass and per unit length of any shell is cylindrical

$$\frac{1}{\rho_o} = 2\pi r dr \tag{A-33}$$

and infinitesimal changes in pressure and temperature are written, respectively, as

$$dP = pe^{j\omega t} \tag{A-34}$$

and

$$dT = \theta(r)e^{j\omega t} \quad . \tag{A-35}$$

The relation of the thermodynamic states between any two shells is

$$\frac{P}{\rho} = \frac{P_o}{\rho_o T_o} T \quad . \tag{A-36}$$

The above equations are now combined to determine a differential form of Eq. A-31. Differentiate Eq. A-36 and substitute Eqs. A-33 through A-35 and Eq. A-31 into the differential of Eq. A-36 to obtain

$$d\left(\frac{1}{\rho}\right) = -\frac{2\pi r p e^{j\omega t}}{\gamma P_o}\left\{1 + (\gamma-1)\left[1 - \frac{K_o(\xi r j^{\frac{1}{2}})}{K_o(\xi a j^{\frac{1}{2}})}\right]\right\} dr \quad . \tag{A-37}$$

Integration of Eq. A-37 is accomplished by noting that [52]

$$\begin{aligned}\int_o^x xK_o(xj^{\frac{1}{2}})dx &= -\frac{x}{j^{\frac{1}{2}}}K_1(xj^{\frac{1}{2}}) \\ &= -xj^{\frac{1}{2}}(kei_1 x + j\ kei_1 x) \\ &= x(kei'x + j\ kei'x) \quad .\end{aligned} \tag{A-38}$$

The upper limit of integration in r is taken as arbitrary and the exact value is determined later. After integrating over the volume around

the fiber and some algebra the resulting equation is

$$\frac{\rho_o}{\rho} = \frac{P_o - P}{\gamma P_o}\left[1 - \frac{2(\gamma-1)j^{-\frac{1}{2}}[rK_1(\xi r j^{\frac{1}{2}}) - aK_1(\xi a j^{\frac{1}{2}})]}{\xi(r^2 - a^2)\, K_o(\xi a j^{\frac{1}{2}})}\right] \quad . \text{(A-39)}$$

The last step is to take the derivative of this equation and solve for $dP/d\rho$. This result yields

$$c_T^2 = \frac{\gamma P_o}{\rho_o}\left[1 - \frac{2(\gamma-1)j^{-\frac{1}{2}}[rK_1(\xi r j^{\frac{1}{2}}) - aK_1(\xi a j^{\frac{1}{2}})]}{\xi(r^2 - a^2)K_o(\xi a j^{\frac{1}{2}})}\right]^{-1} \quad . \text{(A-40)}$$

Although desirable, the transform to the time domain could not be accomplished. Thus, this equation, in its present form, is only good for single frequencies.

It is important to determine whether the function has the proper values in the limits of fiber packing. If the fibers are spaced infinitely far apart, then $r \to \infty$ and

$$c_T^2 = \frac{\gamma P_o}{\rho_o} \quad , \qquad \text{(A-41)}$$

which is the square of the adiabatic sound speed.

In the limit in which the fibers are packed as close together as possible, $r \to a$, and the equation becomes

$$c_T^2 = \frac{P_o}{\rho_o} \quad , \qquad \text{(A-42)}$$

which is the square of the isothermal sound speed.

In a porous material the fibers are packed in a spacing well between these two extremes. The relative fiber packing is used to

determine the upper limit of integration. Assume that the fibers are evenly spaced and parallel, as shown in Fig. A-4. The dotted lines indicate the radius at which the thermal boundary layers intersect. The small spaces labeled M indicate the area missed by the integration (19%), but this area has little effect on the calculated phase speed as Eq. A-45 is a slowly varying function.

For two cases, $P = 0.918$, the magnitude of the sound speed is plotted versus frequency in Fig. A-5. Since the largest phase angle of Eq. A-45 is less than 2°, the phase angle is ignored in further calculations. The magnitude change of the sound speed is found to be a very slowly varying function of both porosity and frequency. Increase of the thermal diffusivity will cause the phase speed to approach isothermal. This effect is the same as lowering the frequency, since $\xi = \sqrt{\omega/\alpha_T}$. For a constant porosity, reduction of the fiber size causes the fibers to be more tightly packed, as shown in Fig. A-4 ($r \propto a$). Increased packing density causes a lower phase speed.

It is now important to compare the heat transfer effects to the viscous effects in the same porous material. This is the topic of the next section.

D. Thermoviscous Effects on the Phase Speed

In this section the heat transfer and viscosity effects in a porous material are combined. Since only low-intensity sound is being considered in this appendix, a simple replacement of b_o by Eq. A-40 in

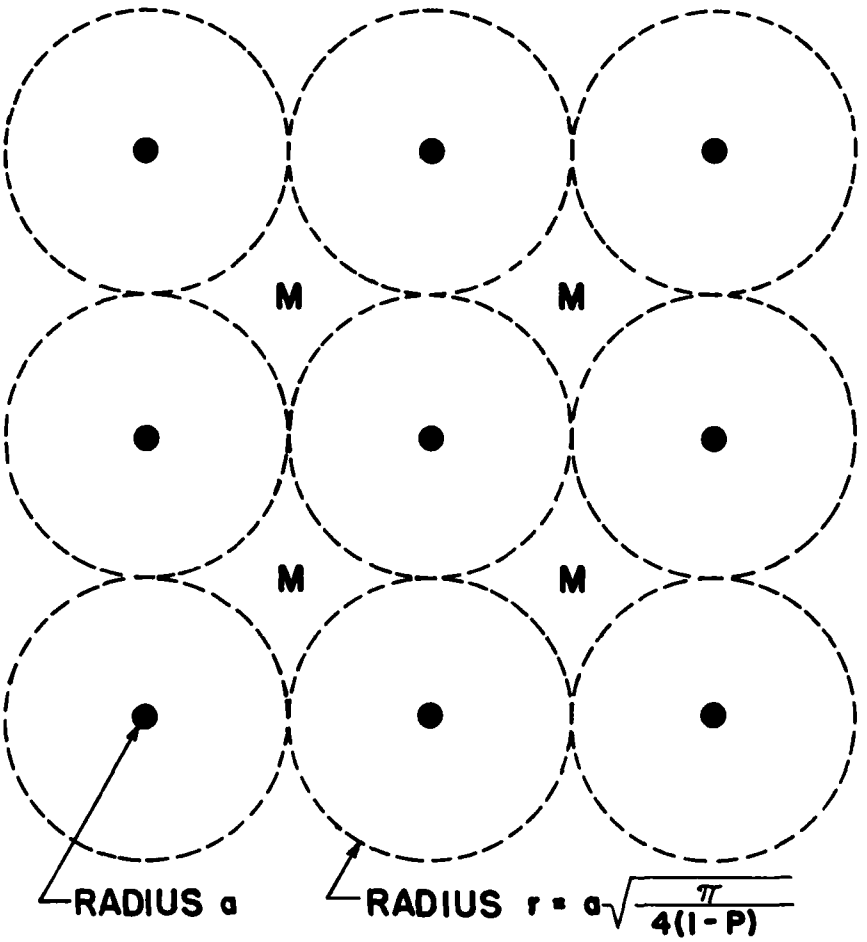

FIGURE A-4
SKETCH OF THE FIBER ARRANGEMENT IN AN IDEAL POROUS MATERIAL.

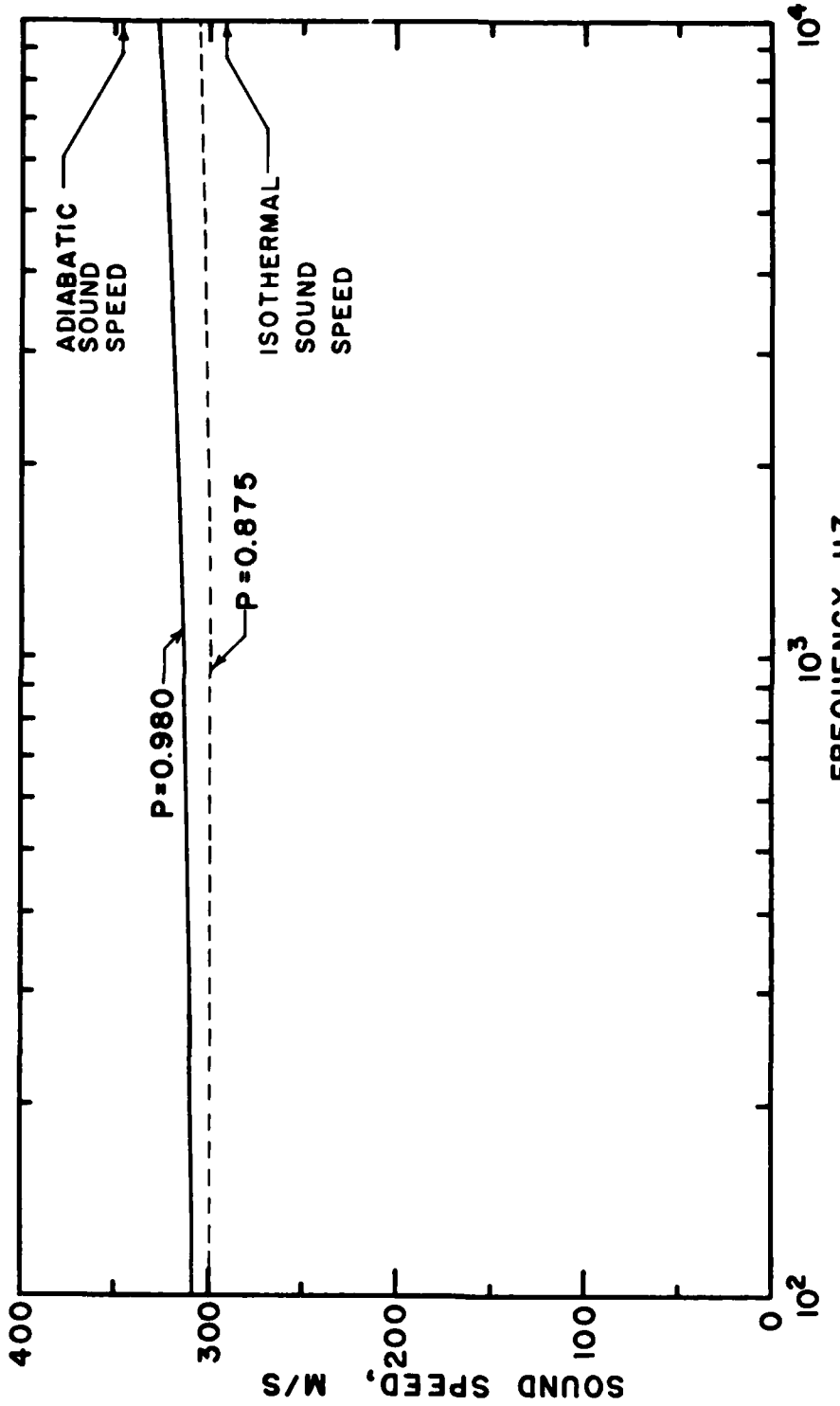

FIGURE A-5
MAGNITUDE OF THE SOUND PSEED VERSUS FREQUENCY FOR TWO POROSITIES OF A FIBROUS POROUS MATERIAL.

Eq. I-16 is assumed to be valid. The result of the above substitution plotted versus frequency in Fig. A-6.

In Fig. A-6 the thermoviscous phase speed predictions and data for Kevlar 29 (ρ = 0.980) are plotted versus frequency. This combination works fairly well for the full frequency range.

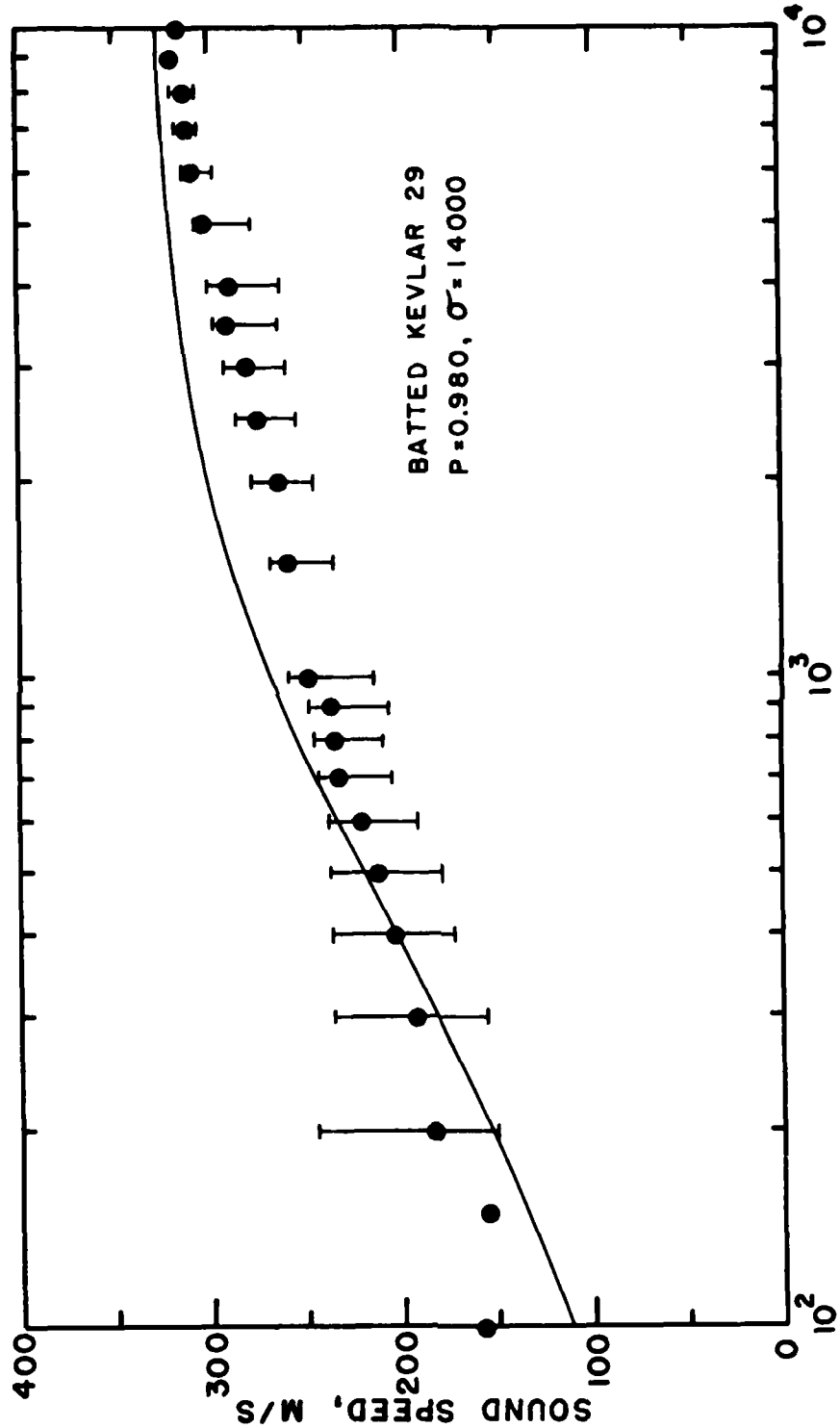

FIGURE A-6
MEASURED AND PREDICTED THERMO-VISCOUS PHASE SPEED VERSUS FREQUENCY FOR BATTED KEVLAR 29 (P = 0.980).

III. Summary and Conclusions

In this appendix the oscillatory heat transfer effects in fibrous porous materials have been determined. The results have been combined with viscous effects and used to predict phase speed in a fibrous porous material. In the analysis, the fiber type was found to have minimal effect on the heat transfer boundary layer in air surrounding the fibers and an isothermal boundary condition is used in predicting the soundspeed.

As anticipated, the heat transfer effects on the sound speed are bounded by the isothermal and the adiabatic sound speeds. These limits encompass a change of about 18% from the adiabatic sound speed.

Because of the complication of using Eq. A-45 in the body of this dissertation, the limiting cases of the isothermal and adiabatic sound speeds are used in the low-intensity sound predictions. When intense sounds propagate through a porous material the acoustic particle velocity and displacement become large. The large particle displacement causes the heat transfer to be convective, rather than conductive, and causes acoustic streaming which mixes the fluid. Both of these effects shift the curves in Fig. A-5 so that, for a given frequency ω, the fluid compressions are more isothermal and the sound speed is slower. In addition, the isothermal sound speed is used in the high-intensity sound predictions because of the increased heat transfer and gas mixing caused by the high particle velocities.

APPENDIX B

DRAWINGS

Construction drawings of two devices built for the experiments in this study are presented in this appendix. Figures B-1 through B-3 show the construction drawings for the standing wave tube. Figure B-4 shows the construction drawing for the traveling wave tube.

In Fig. B-1-A the impedance tube, the sample holder, and the aluminum plug are drawn. In Fig. B-1-B the driver/probe tube adaptor for the impedance tube is drawn. In Fig. B-2 the impedance tube support/carriage track is drawn. In Fig. B-3 the microphone carriage and microphone holder are drawn.

In Fig. B-4 the traveling wave tube and its accessories are drawn.

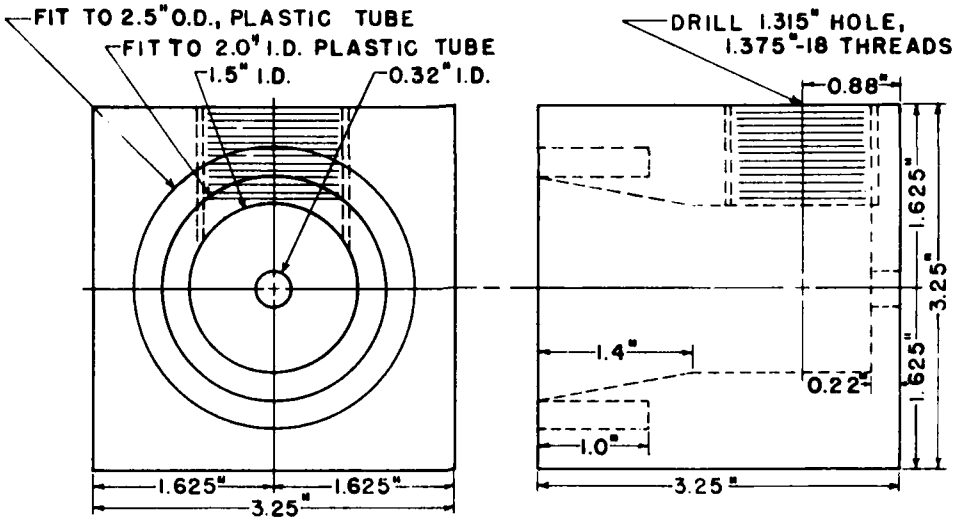

ALUMINUM ADAPTOR, DRIVER AND PROBE TUBE FOR IMPEDANCE TUBE

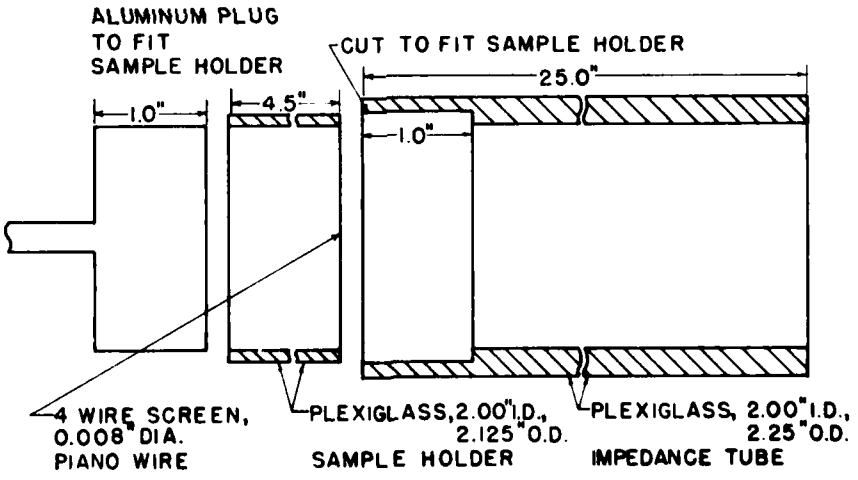

FIGURE B-1
DRAWINGS OF THE ACOUSTIC DRIVER AND PROBE TUBE ADAPTOR, IMPEDANCE TUBE, AND ALUMINUM TERMINATION FOR THE STANDING WAVE TUBE.

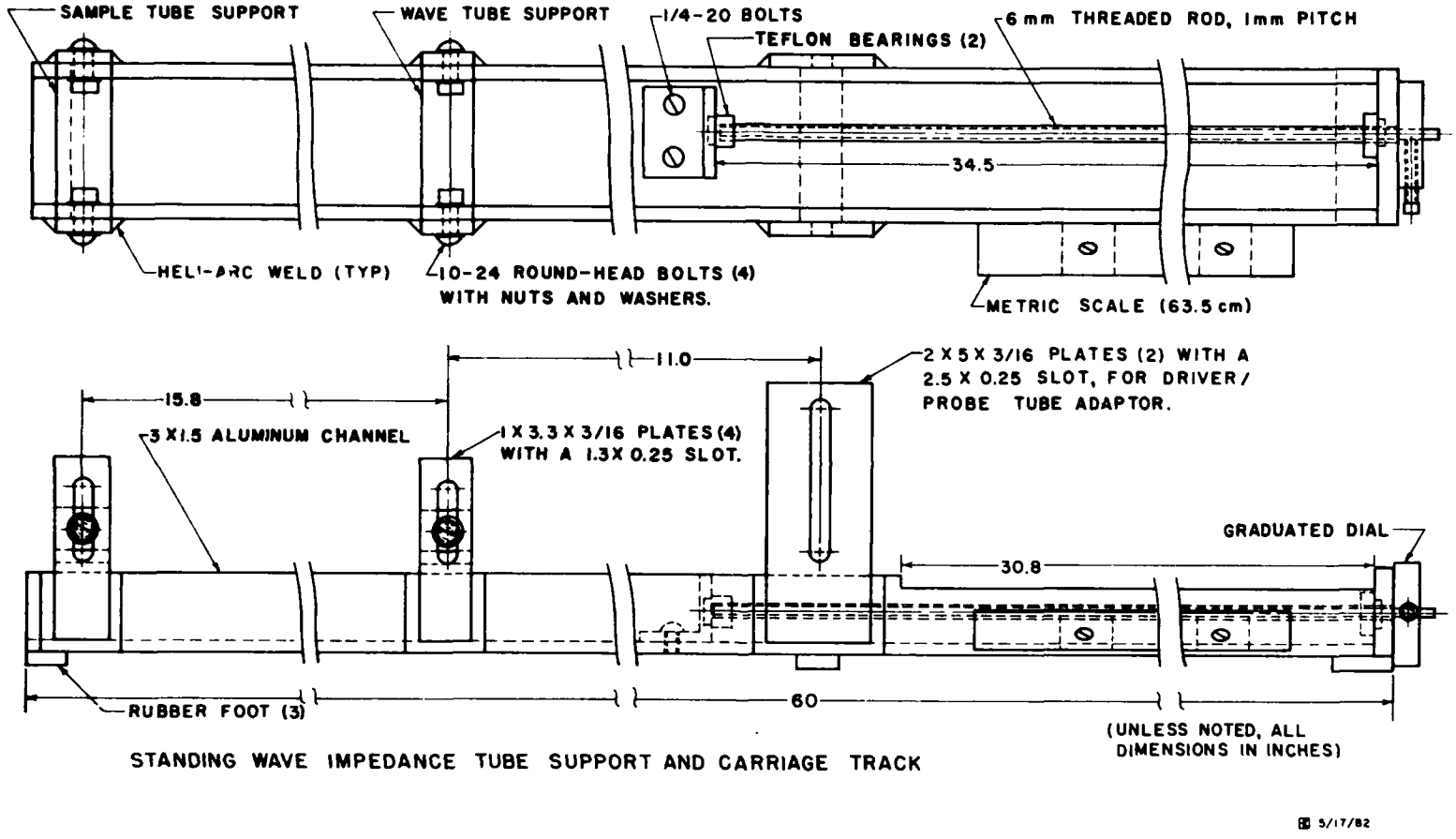

STANDING WAVE IMPEDANCE TUBE SUPPORT AND CARRIAGE TRACK

FIGURE B-2
DRAWING OF THE TRACK AND TUBE HOLDER FOR THE STANDING WAVE TUBE.

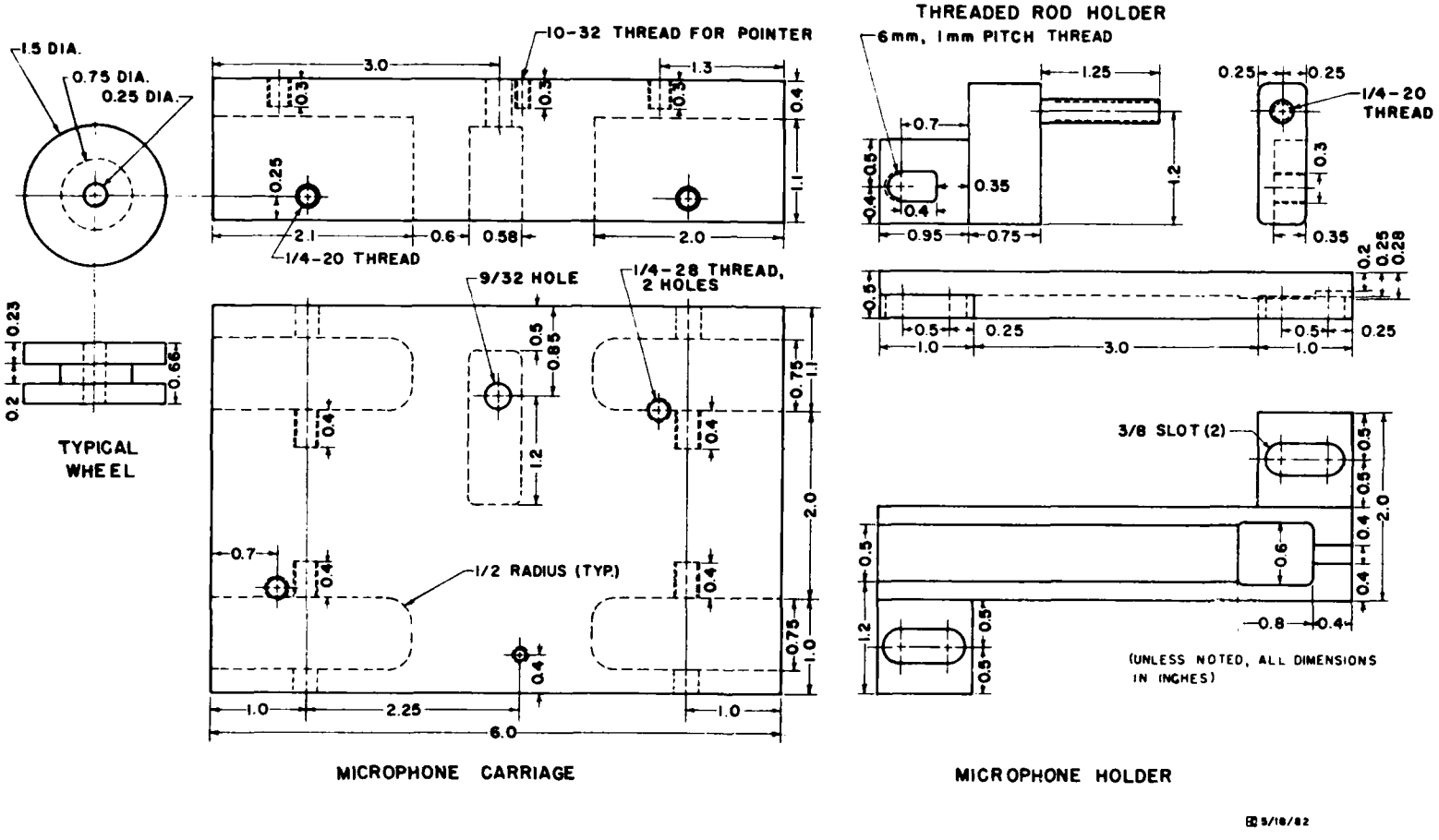

FIGURE B-3
DRAWING OF THE MICROPHONE CARRIAGE AND MICROPHONE HOLDER FOR THE STANDING WAVE TUBE.

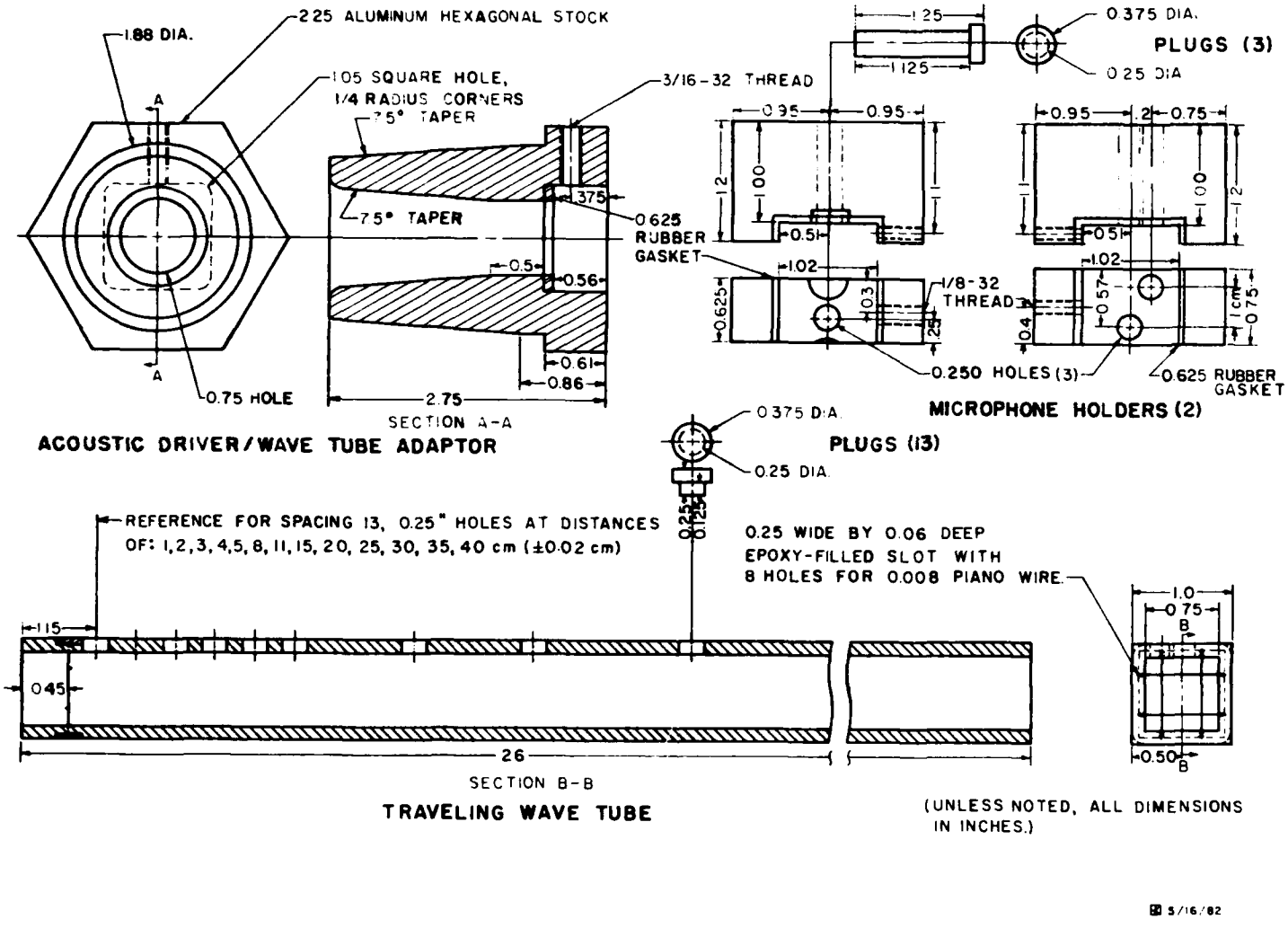

FIGURE B-4
DRAWINGS OF THE WAVE TUBE, ACOUSTIC DRIVER ADAPTOR, AND ACCESSORIES FOR THE TRAVELING WAVE TUBE.

APPENDIX C

COMPUTER PROGRAMS

Two of the programs used in this study are listed here. A short description is given for each program.

PERT4PD

This interactive program is used to calculate the propagation of an initial wave consisting of a fundamental and a second harmonic component of arbitrary amplitudes and relative phase in a porous material. The program calculates and plots the sound levels of the four harmonic components with distance (0-25 cm). The information needed to use the program is the frequency f, linear flow resistivity $\sigma/415$, nonlinear flow resistivity $\eta/415$, fundamental component sound level, porosity P, second harmonic component sound level, and relative phase ϕ.

PHSPED

This interactive program is used to calculate the heat transfer effects on the phase speed of sound in a porous material. The program calculates and plots the magnitude and phase angle of the phase speed versus frequency. The information needed to use the program is the thermal conductivity, density, and specific heat of the fibrous material, the fiber radius, and the half spacing between the fibers.

```
      PROGRAM PERT4PD(INPUT,OUTPUT,DATPTS,PLOT,TAPE5=PLOT)
C
C     HLK (PAD) 6-1-82
C     THIS PROGRAM IS USED TO CALCULATE THE AMPLITUDES OF THE FIRST
C     FOUR HARMONIC COMPONENTS, WITH RESPECT TO DISTANCE, FOR AN
C     ACOUSTIC WAVE TRAVELING IN A BULK POROUS MATERIAL.
C     THE BOUNDARY CONDITION CONSISTS OF AN ARBITRARY COMBINATION
C     OF THE FIRST AND SECOND HARMONICS.  DATA FOR THE FIRST FOUR HARMONIC
C     COMPONENTS ARE  PLOTTED.  THE IMAGINARY PART OF THE PROPAGATED WAVE
C     AMPLITUDES ARE PLOTTED.
C
      INTEGER LABX(1),LABY1(1),LABY2(1),MAT(2)
      REAL P1P0(1601),X(1601),P2P0(1601)
      REAL P1P02(1601),P3P0(1601),P4P0(1601)
      REAL XD(21),FND(21),SND(21),TRD(21),FRTH(21)
      COMPLEX Q1,Q2,Q3,Q4,U21,U22,U23,U24,V1,V2
      COMPLEX GAMMA1,GAMMA2,J,GAMA1C,GAMA2C,GAMMA3,GAMMA4
C
C     SPECIFICATION OF CONSTANTS FOR PROGRAM.
C
      AXLEN=8.5
      AYLEN=5.0
      J=CMPLX(0.,1.)
      C=292.
      RHO0=1.21
      PI=0.0
      LDAT=6LDATPTS
C
    5 CONTINUE
C
C  DATA ENTRY
C
      PRINT*,'INPUT NO. POINTS/INCH TO PLOT (180 MAX.), IOPT ='
      READ*,NPINCH,IOPT
C
C     PROGRAM INPUT TERMINATION.
C
      IF(NPINCH.EQ.0) STOP
C
C     DATA VV = # OF DATA LINES, PLOT 'TITLE',POROSITY: DECIMAL, SIGMA: LINEAR
C     COEFFICIENT OF RESISTIVITY PER RHO0*C, ETA: NONLINEAR COEFFICIENT OF
C     RESISTIVITY PER RHO0*C, FREQUENCY: HERTZ, B: RELATIVE
C     AMPLITUDE OF THE SECOND HARMONIC COMPONENT WITH RESPECT
C     TO THE FUNDAMENTAL, PSI: RELATIVE PHASE BETWEEN THE
C     FUNDAMENTAL AND SECOND HARMONIC COMPONENTS.
C
      READ(LDAT,*)ND,MAT(1),MAT(2),P,F
      IF(ND.EQ.0) GO TO 500
C
      OMEGA=6.283185*F
C
      PRINT*,'SIGMA, ETA, PSI='
      READ*,SIGMA,ETA,PSI
C
      DO 150 JD=1,ND
      READ(LDAT,*) XD(JD),FND(JD),SND(JD),TRD(JD),FRTH(JD)
      IF(JD.GT.1) GO TO 17
      EPS=10**((FND(1)-191.2)/20.)
      B=10**((SND(1)-FND(1))/20.)
      ZERO=FND(1)
   17 FND(JD)=-ZERO+FND(JD)
```

```
      SND(JD)=-ZERO*SND(JD)
      TRD(JD)=-ZERO*TRD(JD)
      FRTH(JD)=-ZERO*FRTH(JD)
      IF(SND(JD).LT.-50.0) SND(JD)=10.0
      IF(TRD(JD).LT.-50.0) TRD(JD)=10.0
      IF(FRTH(JD).LT.-50.0) FRTH(JD)=10.0
  150 CONTINUE
C
      SIGMA1=415.*SIGMA/(RHO0*OMEGA)
      ETA1=415.*ETA*C/(RHO0*OMEGA)
      GAMMA1=CSQRT(1.-J*SIGMA1)
      GAMMA2=CSQRT(1.-J*SIGMA1/2.)
      GAMA1C=CSQRT(1.+J*SIGMA1)
      GAMA2C=CSQRT(1.+J*SIGMA1/2.)
      GAMMA3=CSQRT(1.-J*SIGMA1/3.)
      GAMMA4=CSQRT(1.-J*SIGMA1/4.)
      NP=NPINCH*AXLEN
      DELTAX=25.0*OMEGA/(NP*100.*C)
      SVAL=-10.*AYLEN
      PSI=0.01745*PSI
C
C     COMPUTATION OF THE FIRST FOUR HARMONIC COMPONENT AMPITUDES,
C     WITH RESPECT TO DISTANCE, FOR AN ACOUSTIC WAVE TRAVELLING
C     IN A RULK POROUS MATERIAL.
C
      DO 10 JL=1,NP
      X(JL)=DELTAX*JL
      IF (IOPT.EQ.1) GO TO 15
      IF (IOPT.EQ.0) P1P0(JL)=20.*ALOG10(CABS(CEXP(-J*GAMMA1*X(JL))))
      IF (IOPT.EQ.0 .AND. P1P0(JL).LT.SVAL) P1P0(JL)=SVAL
   15 V1=8*(2.*GAMMA2-GAMA1C)
      V2=2.*ETA1-J*(GAMMA1**2)*(GAMMA2+GAMA1C)
      V1=V1*V2
      V2=8.*GAMA1C*GAMMA2*(1.-GAMA1C*GAMMA2)
      Q1=V1/V2
      V1=J*ETA1-J*2.*(SIGMA1+J*2.)*GAMMA1
      Q2=V1/(2.*SIGMA1*GAMMA1)
      V1=ETA1+J*GAMMA1*(3.-J*SIGMA1)
      V2=4.*GAMMA2*GAMMA1*(1.-GAMMA1*GAMMA2)
      Q3=8*(2.*GAMMA2+GAMMA1)*V1/V2
      V1=(8**2)*(2.*(GAMMA2**2)*SIGMA1)
      V2=J*ETA1-J*4.*GAMMA2*(SIGMA1+J*4.)
      Q4=V1*V2
      V1=CEXP(J*(-GAMMA1*X(JL)+PSI))
      V2=CEXP(J*(-(2.*GAMMA2-GAMA1C)*X(JL)+PSI))
      U21=(V2-V1)
      V1=CEXP(J*2.*(-GAMMA2*X(JL)))
      V2=CEXP(J*2.*(-GAMMA1*X(JL)))
      U22=(V2-V1)
      V1=CEXP(J*(3.*(-GAMMA3*X(JL))+PSI))
      V2=CEXP(J*(-(2.*GAMMA2+GAMMA1)*X(JL)+PSI))
      U23=(V2-V1)
      V1=CEXP(J*(4.*(-GAMMA4*X(JL))+2.*PSI))
      V2=CEXP(J*(4.*(-GAMMA2*X(JL))+2.*PSI))
      U24=(V2-V1)
      V1=CEXP(-J*GAMMA1*X(JL))
      V1=V1+EPS*Q1*U21
      V2=8*CEXP(-J*(2.*GAMMA2*X(JL)+PSI))
      P1P02(JL)=20.*ALOG10(CABS((V1)))
      P2P0(JL)=20.*ALOG10(CABS((V2+EPS*Q2*U22)))
      P3P0(JL)=20.*ALOG10(CABS((EPS*Q3*U23)))
      P4P0(JL)=20.*ALOG10(CABS((EPS*Q4*U24)))
```

```
      IF (P1P02(JL).LT.SVAL) P1P02(JL)=SVAL
      IF (P2P0(JL).LT.SVAL) P2P0(JL)=SVAL
      IF (P3P0(JL).LT.SVAL) P3P0(JL)=SVAL
      IF (P4P0(JL).LT.SVAL) P4P0(JL)=SVAL
   10 CONTINUE
C
      DO 30 JN=1,NP
      X(JN)=X(JN)*100.*C/OMEGA
   30 CONTINUE
C
C**** PLOT THE VALUES.
C
      LABX(1)='X, CM'
      LABY1(1)='LOG(U1/U0)'
      LABY2(1)='LOG(UI/U0)'
      XORG=1.0
      YORG=2.0
      DX=25.0/AXLEN
      DY=10.
C
C     BRANCHING FOR PLOTTING CHOICES.
C     PLOT U1/U0
C
      IF (IOPT.EQ.1) GOTO 20
C
      CALL PLTLFN(4LPLOT)
      CALL PLTDIM(11.0,8.5,1,4.0)
      CALL PLTORG(XORG,YORG)
C  DRAW AXES
      CALL PLTAXIS(0.0,0.0,AXLEN,0.0,0.0,25.0,1.0,LABX,-6,5,-.1,-.1)
      CALL PLTAXIS(0.0,0.0,AYLEN,90.,-50.,0.0,2.5,LABY1,10,5,-.1,-.1)
      CALL PLTAXIS(0.0,AYLEN,AXLEN,0.0,0.0,25.0,1.0,LABX,-6,0,.1,.1)
      CALL PLTAXIS(AXLEN,0.0,AYLEN,90.0,-50.,0.0,2.5,LABY1,10,0.,.1,.1)
C
C  PLOT THE DATA.
C
      CALL PLTDATA(X,P1P0,NP,0,0,0.,DX,-50.0,DY,.08,2)
      CALL PLTLINE(4.25,-1.2,-0.14)
      WRITE(5,100) P,F,SIGMA
      CALL PLTEND(11.0,8.5)
   20 CONTINUE
C
C
C  PLOT UIU0.
      CALL PLTLFN(4LPLOT)
      CALL PLTDIM(11.0,8.5,1,4.0)
      CALL PLTORG(XORG,YORG)
C  DRAW AXES
      CALL PLTAXIS(0.0,0.0,AXLEN,0.0,0.0,25.0,1.0,LABX,-6,5,-.1,-.1)
      CALL PLTAXIS(0.0,0.0,AYLEN,90.,-50.,0.0,2.5,LABY2,10,5,-.1,-.1)
      CALL PLTAXIS(0.0,AYLEN,AXLEN,0.0,0.0,25.0,1.0,LABX,-6,0,.1,.1)
      CALL PLTAXIS(AXLEN,0.0,AYLEN,90.0,-50.,0.0,2.5,LABY2,10,0.,.1,.1)
```

```
C
      CALL PLTDATA(X,P1P02,NP,0,0,0,DX,-50.0,DY,.08,2)
      CALL PLTDATA(X,P2P0,NP,0,0,0,DX,-50.0,DY,.08,9)
      CALL PLTDATA(X,P3P0,NP,0,0,0,DX,-50.0,DY,.08,4)
      CALL PLTDATA(X,P4P0,NP,0,0,0,DX,-50.0,DY,.08,8)
      CALL PLTDATA(XD,FND,ND,-1,2.0,.DX,-50.0,DY,0.16,3)
      CALL PLTDATA(XD,SND,ND,-1,5.0,.DX,-50.0,DY,0.16,3)
      IF(TRD(1).GT.10.0) GO TO 65
      CALL PLTDATA(XD,TRD,ND,-1,9.0,.DX,-50.0,DY,0.16,3)
   65 IF(FRTH(1).GT.0.0) GO TO 75
      CALL PLTDATA(XD,FRTH,ND,-1,11.0,.DX,-50.0,DY,0.16,3)
   75 CALL PLTLINE(4.25,-0.9,-0.14)
      WRITE(5,200) P,F,ZERO
      CALL PLTLINE(4.25,-1.3,-0.14)
      WRITE(5,300) SIGMA,ETA
      CALL PLTLINE(4.25,-1.8,-0.14)
      WRITE(5,400) B,PSI
      CALL PLTEND(11.0,8.5)
C
C     PLOT LABELING FOR INPUT PARAMETERS.
C
  100 FORMAT('P = ',F9.3,'  F = ',F9.3,'  SIGMA = ',F9.3)
  200 FORMAT('P = ',F9.3,'  F = ',F9.3,'  SPL = ',F9.3)
  300 FORMAT('SIGMA = ',F9.3,'  ETA = ',F9.3)
  400 FORMAT('B = ',F9.3,'  PSI = ',F9.3)
      GOTO 5
C
  500 PRINT*,MAT(1),MAT(2),' SAVE PLOTS'
C
      END
```

```
      PROGRAM PHSPED (INPUT,OUTPUT,PLOT,OUT,TAPE2=OUT,TAPE5=PLOT)
      COMPLEX C2S,C2S1,C2SD,V,V1,V2,V3
      INTEGER LABX(2),LABY(2),LABY2(2)
      REAL C2SM(1701),LOGF(1701),PHASE(1701),F,RER,ALP,DLF,KERA,KEIA,
     *     KERDA,KEIDA,KERDR,KEIDR,KI,PI,CPI
C
C  INITIALIZE VARIABLES
      GAMMA=1.402
      ALPHAF=2.216E-5
      REP1=SQRT(2.*3.1415927/ALPHAE)
      AEP1=REP1
C
    5 PRINT*,'ENTER KI, PI, CPI'
      READ*,KI,PI,CPI
      IF(PI.EQ.0.0)STOP
      PRINT*,'ENTER FIBER RADIUS, RADIUS, NO PLOTTER STEPS'
      READ*,A,R,N
C
      REP=REP1*R
      AEP=AEP1*A
      DLF=2./N
      ALPHAI=KI/PI/CPI
      AIP=SQRT(2.*3.1415927/ALPHAI)*A
      VSR=SQRT(31.0711/(KI*PI*CP1))
      M=N+1
C
C  COMPUTE PHASE SPEED.
      DO 10 J=1,M
      LOGF(J)=2.+(J-1)*DLF
      F=10.**(LOGF(J))
      RE=REP*SQRT(F)
      AE=AEP*SQRT(F)
      AI=AIP*SQRT(F)
      CALL MMKELO(AE,BER,BEI,KERA,KEIA,IER)
      CALL MMKELD(AE,BER,BEI,KERDA,KEIDA,IER)
      CALL MMKELD(RE,BER,BEI,KERDR,KEIDR,IER)
      CALL MMKELO(AI,BERA,BEIA,XKER,XKEI,IER)
      CALL MMKELD(AI,BERDA,BEIDA,XKER,XKEI,IER)
      X1=RE*KEIDR-AE*KEIDA
      X2=AE*KERDA-RE*KERDR
      C2S1=CMPLX(X1,X2)
      C2SD=CMPLX(KERA,KEIA)
      V1=CMPLX(KERDA,KEIDA)
      V2=CMPLX(BERA,BEIA)
      V3=CMPLX(BERDA,BEIDA)
      V=VSR*V1*V2/V3-C2SD
      C2S=343./CSQRT(1.-2*(GAMMA-1.)*C2S1/((RE*RE-AE*AE)*V))
      C2SM(J)=CABS(C2S)
      PHASE(J)=ATAN2(AIMAG(C2S),REAL(C2S))*180./3.1415927
   10 CONTINUE
C
C  PRINT OUT VALUES.
      WRITE(2,150)
      DO 20 J=1,M
      F=10.**LOGF(J)
      WRITE(2,*)F,C2SM(J),PHASE(J)
   20 CONTINUE
  150 FORMAT('1')
```

```
C  PLOT MAGNITUDE AND PHASE VS. FREQUENCY.
      DATA LABX/≠FREQUENCY,≠,≠ HERTZ≠/,LABY/≠NORM PHASE≠,≠ SPEED≠/
      DATA LABY2/≠PHASE ANGL≠,≠E≠/
      XORG=1.0
      YORG=2.0
      AXLEN=8.5
      AYLEN=5.0
      DX=2./AXLEN
      DY=400./AYLEN
      DY2=20./AYLEN
C
      CALL PLTLFN(4LPLOT)
      CALL PLTDIM(11.0,8.5,1,4.0)
      CALL PLTORG(XORG,YORG)
C  DRAW AXES.
      CALL LOGAXIS(0.0,0.0,AXLEN,0.0,100.,10000.,LABX,-16,-.1)
      CALL PLTAXIS(0.0,0.0,AYLEN,90.0,0.0,400.,50.,LABY,16,2,-.1,-.1)
      CALL LOGAXIS(0.0,AYLEN,AXLEN,0.0,100.,10000.,LABX,0,-.1)
      CALL PLTAXIS(AXLEN,0.0,AYLEN,90.0,0.0,1.0,.1,LABY,0,0,.1,.1)
C
      CALL PLTDATA(LOGF,C2SM,M,0.0,2.,DX,0,DY,0.)
      CALL PLTLINE(2.0,-1.2,,14)
      WRITE(5,100)A,R
      CALL PLTEND(11.0,8.5)
C
C PLOT PHASE ANGLE.
      CALL PLTLFN(4LPLOT)
      CALL PLTDIM(11.0,8.5,1,4.0)
      CALL PLTORG(XORG,YORG)
C  DRAW AXES.
      CALL LOGAXIS(0.0,0.0,AXLEN,0.0,10.,10000.,LABX,-16,-.1)
      CALL PLTAXIS(0.0,0.0,AYLEN,90.0,-10.,10.,1.,LABY2,11,2,-.1,-.1)
      CALL LOGAXIS(0.0,AYLEN,AXLEN,0.0,10.,10000.,LABX,0,-.1)
      CALL PLTAXIS(AXLEN,0.0,AYLEN,90.0,-10.,10.,1.,LABY2,0,0,.1,.1)
C
      CALL PLTDATA(LOGF,PHASE,M,0.0,1.,DX,-10.,DY2,0.0)
      CALL PLTEND(11.0,8.5)
C
C
      GOTO 5
C
  100 FORMAT(≠A=≠,E9.3,10X,≠R=≠,E9.3)
      END
```

REFERENCES

1. ANSI/ASTM C384-77, "Standard test method for impedance and absorption of acoustical materials by the impedance tube method," American National Standards Institute, New York, NY.

2. ASTM C522-73, "Standard test method for airflow resistance of acoustical materials," American Society for the Testing of Materials. American National Standards Institute, New York, NY.

3. K. Attenborough and L. A. Walker, "Scattering theory for sound absorption in fibrous media," J. Acoust. Soc. Am., 49, 1331-1338 (1971).

4. J. F. Bartram, "A useful analytical model for the parametric acoustic array," J. Acoust. Soc. Am., 52, 1042-1044 (1972).

5. G. K. Batchelor, An Introduction to Fluid Dynamics, (Cambridge University Press, London, 1967).

6. L. L. Beranek, "Acoustic impedance of porous materials," J. Acoust. Soc. Am., 13, 248-260 (1942).

7. L. L. Beranek, "Acoustic impedance of commercial materials and the performance of rectangular rooms with one treated surface," J. Acoust. Soc. Am., 12, 14-23 (1940).

8. L. L. Beranek, "Acoustical properties of homogeneous, isotropic rigid tiles and flexible blankets," J. Acoust. Soc. Am., 19, 556-568 (1947).

9. R. T. Beyer, "Parameter of nonlinearity in fluids," J. Acoust. Soc. Am., 32, 719-721 (1960).

10. R. T. Beyer, Nonlinear Acoustics, Naval Sea Systems Command (Department of the Navy, 1974).

11. D. A. Bies, "Acoustical Properties of Porous Materials," Chapter 10, Noise and Vibration Control, L. L. Beranek, Ed., (McGraw-Hill, Inc., New York, 1971).

12. D. A. Bies and C. H. Hansen, "Flow resistance information for acoustical design," Applied Acoustics, 13, 357-391 (1980).

13. M. A. Biot, "Generalized theory of acoustic propagation in porous dissipative media," J. Acoust. Soc. Am. 34, 1254-1264 (1962).

14. L. Bjørnø, "Finite-amplitude wave propagation through water saturated marine sediments," Acustica, 38, 195-200 (1977).

15. D. T. Blackstock, "Propagation and reflection of plane sound waves of finite amplitude in gases," Technical Memorandum No. 43, Acoustics Research Laboratory, Department of Engineering Sciences and Applied Physics, Harvard University, Cambridge, Massachusetts (1960).

16. D. T. Blackstock, "Connection between the Fay and Fubini solutions for plane sound waves of finite amplitude," J. Acoust. Soc. Am. 39, 1029-1026 (1966).

17. D. T. Blackstock, "Generalized Burgers equation for plane waves," Presented to the International Symposium in Nonlinear Acoustics, England (1981).

18. R. N. Bracewell, The Fourier Transform and its Applications, 2nd ed. (McGraw-Hill, Inc., New York, 1978).

19. R. L. Brown and R. H. Bolt, "The measurement of flow resistance of porous acoustic materials," J. Acoust. Soc. Am. 13, 337-344 (1942).

20. Brüel & Kjaer, Inc., Condenser Microphone and Microphone Preamplifiers, Theory and Application Handbook, (Denmark 1977).

21. P. C. Carman, Flow of Gases Through Porous Media, (Academic Press, New York, 1956).

22. H. S. Carslaw and J. C. Jaeger, Conduction of Heat in Solids, 2nd ed., (Oxford at the Clarendon Press, D. R. Hillman and Sons, Ltd., 1959).

23. L. Cremer, "Theorie de Schallabsorption in porösen Wänder," Elektrische Nachriechten-Technik, 10, 242-251 (1933) (Theory of Sound Absorption in Porous Walls).

24. C. N. Davies, "The separation of airborne dust and particles," Proc. Inst. Mech. Engrs. (London), B1, 185-19º (1952).

25. M. E. Delany and E. N. Bazley, "Acoustical characteristics of fibrous absorbent materials," National Physical Laboratory, Aerodynamics Division, NPL Aero Report AC 37, (1969).

26. C. Devin, Jr., "Survey of thermal, radiation, and viscous damping of pulsating air bubbles in water," J. Acoust. Soc. Am. 31, 1654-1667, (1959).

27. D. S. Dosonjd, "Interaction of grids with traveling shock waves," NACA, Technical Note 3680, (1956) (corrected copy).

28. D. Ensminger, Ultrasonics. The Low- and High-Intensity Applications, (Marcel Dekker, Inc., New York, 1973).

29. W. B. Fulks, R. B. Guenther, and E. L. Roetman, "Equations of motion and continuity for fluid flow in a porous medium," Acta Mechanics, 12, 121-129 (1971).

30. A. Gemant, "Die Bedingungen für den günstigsten Schallschlucker," Elektrische Nachrichten-Technik, 10, 446-450 (1933) (The Conditions for the Ideal Sound Absorber).

31. H. Gröber, "Temperatureverlauf und Wärmeströmungen in Periodisch Erwärmten Körpern," Forschungsarbeiten auf dem Gebrite des Ingenieurwesens, #300, 3-13 (1928) (Temperature Variation and Heat Flow in Periodically Heated Bodies).

32. J. Harmans, "Messung von Schallschluckstoffen und deren Verwendung zur Dämpfung von Rohren," Akustische Zeitschrift, 5, 215-231 (1940) (Measurements on Sound Absorbing Material and its Application to the Damping of Rooms).

33. A. S. Hersh and B. Walker, "Acoustic behavior of a fibrous bulk material," Presented at the AIAA 5th Aeroacoustics Conference, Seattle, WA, Paper #79-0599 (1979).

34. A. S. Hersh and B. Walker, "Acoustic behavior of fibrous bulk materials," Presented at the AIAA 6th Aeroacoustic Conference, Hartford, Conn., Paper #80-0986 (1980).

35. A. S. Hersh and B. Walker, "Shock tube investigation of the nonlinear behavior of fibrous sound absorbing bulk materials," Presented at the AIAA 7th Aeroacoustics Conference, Palo Alto, CA. (1981).

36. J. M. Hovem, "The nonlinearity parameter of saturated marine sediments," Applied Research Laboratories, The University of Texas at Austin Technical Paper 79-17 (ARL-TP-79-17).

37. U. Ingard, "Nonlinear attenuation of sound in a duct," J. Acoust. Soc. Am. 43, 167-168 (1968).

38. M. Jakob, Heat Transfer, Volume I, (John Wiley and Sons, Inc., New York, 1949).

39. Y. Kawasima, "Sound propagation in a fibre block as a composite medium," Acustica, 10, 208-217 (1960).

40. W. Keck and R. T. Beyer, "Frequency spectrum of finite amplitude ultrasonic waves in liquids," Phys. Fluids 3, 346-352 (1960).

41. G. Kirchhoff, "Über den Einfluss der Wärmeleitung in einem Gase auf die Schallbewegung," Annalen der Physik und Chemie (Poggendorff's Annalen), 134, 177-193 (1868) (Concerning the influence of heat conduction in a gas on sound propagation).

42. V. N. Kozhin, "Radiation and scattering of sound by a cylinder in a viscous medium," Sov. Phys.-Acoust. 16, 223-227 (1970).

43. V. N. Kozhin, "Scattering and absorption of a plane sound wave by a cylinder of arbitrary radius in a viscous medium," Sov. Phys.-Acoust. 16, 335-339 (1971).

44. V. N. Kozhin, "Sound propagation in a viscous medium containing cylindrical filaments," Sov. Phys.-Acoust. 16, 462-466 (1971).

45. V. Kühl and E. Meyer, "Untersuchungen über die Winkel-und Frequenzabhängigkeit der Schallschluckung von porösen Stoffen," Akademie der Wissenachaptern, Berlin, Mathematisch-Naturwissen-

schaftliche Klasse, Sitzungsberichte der Physikalische-Mathesmatisch Klasse., 26, 416-435 (1932) (Investigation of the Angular-and Frequency-Dependence of the Sound Absorption of Porous Materials).

46. H. L. Kuntz, D. T. Blackstock, and N. D. Perreira, "High-intensity sound propagation in bulk porous materials," presented at the 101st Meeting of the Acoustical Society of America, Ottawa, Canada, 1981.

47. H. L. Kuntz, D. T. Blackstock, and N. D. Perreira, "Reflection and absorption of high-intensity sound at the surface of bulk porous materials," presented at NOISE-CON 81, Raleigh, North Carolina, 1981, NOISE-CON 81 Proceedings.

48. V. J. Kurze and C. H. Allen, "Influence of flow and high sound level on the attenuation in a lined duct," J. Acoust. Soc. Am. 49, 1643-1653 (1971).

49. R. F. Lambert, "Acoustical properties of highly porous fibrous materials," NASA Technical Memorandum 80135, Langley Research Center (1977).

50. 1978 Materials Selector, Materials Engineering 86, Penton/IPC Reinhold Publishing Co., Cleveland, Ohio (1977).

51. J. H. Masliyah, "Viscous flow across banks of circular and elliptical cylinders: momentum and heat transfer," The Canadian Journal of Chemical Engineering 51, 550-555 (1973).

52. N. W. McLachlan, Bessel Functions for Engineers (Oxford University Press, 1934).

53. F. P. Mechel, "Eine Modelltheorie zum Faserabsorber Teil I: Reguläre Faseranordnung," Acustica, 36 53-64 (1976/77) (A Model Theory for the Fibrous Absorber, Part I: Regular Fiber Arrangements).

54. F. P. Mechel, "Eine Modelltheorie Faserabsorber Teil II: Absorbermodel aus Elementarzellen und numerische Ergebnisse," Acustica, 36, 65-89 (1976/77) (A Model Theory for the Fibrous Absorber Part II: A Model Consisting of Elementary Cells and the Numerical Results).

55. T. H. Melling, "The acoustic impedance of perforates at medium and high sound pressure levels, J. Sound Vib. 29, 1-65 (1973).

56. T. H. Melling, "An impedance tube for precision measurement of acoustic impedance and insertion loss at high sound pressure levels," J. Sound Vib. 28, 23-54 (1973).

57. H. M. Merklinger, "Fundamental-frequency component of a finite-amplitude plane wave," J. Acoust. Soc. Am., 54, 1760-1761 (1973).

58. T. Nakamura, A. Nakamura, and R. Takeuchi, "Absorption mechanism of porous material of a sound pulse," Acustica, 44, 1-9 (1980).

59. T. Nakamura, A. Nakamura, and R. Takeuchi, "Measurement of nonlinear reflection of N-wave at the open end of a circular pipe," Acustica 44, 323-329 (1980).

60. R. H. Nichols, Jr., "Flow-resistance characteristics of fibrous acoustical materials," J. Acoust. Soc. Am. 19, 866-871 (1947).

61. L. N. Nosova, Tables of Thompson Functions and their First Derivatives, Translated from the Russian by Prasenjit Bosu, (Pergamon Press, New York, 1961) (Detailed function tables between 0 and 100 argument).

62. F. M. Pestorius, "Propagation of acoustic noise of finite amplitude," Ph.D. Dissertation, The University of Texas, Austin, Applied Research Laboratories, Technical Report, ARL-TR-73-23, AD778868 (1973).

63. H. Pfriem, "Zur thermischer Dämpfung in kugelsymmetrisch schwingenden Gasblasen," Akustische Zeitschrift, 5, 101-212 (1940) (On the thermal damping in spherically symmetric oscillating gas bubbles).

64. J. G. Powell and J. J. Van Houten, "A tone-burst technique of sound-absorption measurement," J. Acoust. Soc. Am. 48, 1299-1303 (1970).

65. E. Raineville and Bedient, Elementary Differential Equations, 4th ed., (The Macmillan Company, New York, 1969).

66. Lord Rayleigh, J. W. S., "On porous bodies in relation tc sound," Philosophical Magazine, XVI, 181-186 (1883). [Scientific Papers, I, 103, pp. 220-225].

67. Lord Rayleigh, J. W. S., Theory of Sound, Vol. II, 2nd ed., (The Macmillan Company, New York, 1945).

68. M. Rettinger, "On the theory of sound absorption of porous materials," J. Acoust. Soc. Am. 6, 188-191 (1935).

69. M. Rettinger, "The theory of sound absorption of porous materials, flexible and nonflexible," J. Acoust. Soc. Am. 8, 53-59 (1936).

70. E. L. Roetman and R. P. Kochlar, "Reflection of acoustical waves at porous surfaces," J. Acoust. Soc. Am. 59, 1057-1064 (1976).

71. J. A. Rudolph, "A device for the measurement of acoustic radiation impedance in air," (Masters Thesis), The University of Texas at Austin, June (1969).

72. C. J. T. Sewell, "The extinction of sound in a viscous atmosphere by small obstacles of cylindrical and spherical form," Philosophical Transactions of the Royal Society, Series A, 210, 239-270 (1910).

73. R. A. Scott, "The absorption of sound in a homogeneous porous medium," 1946 Proceedings of the Physical Society, 58, 165-183.

74. R. A. Scott, "The propagation of sound between walls of porous material," 1946 Proceedings of the physical society, 58, 358-368.

75. Scott Paper Company, "Acoustical properties of Scott Industrial foam and Scottfelt," Report #1 (Chester, PA).

76. J. A. Shooter, T. G. Muir, and D. T. Blackstock, "Acoustic saturation of spherical waves in water," J. Acoust. Soc. Am., 55, 54-62 (1974).

77. D. J. Sides, K. Attenborough, and K. A. Mulholland, "Application of a generalized acoustic propagation theory to fibrous absorbents," J. Sound Vib., 19, 49-64 (1971).

78. R. R. Sullivan, "Specific surface measurements on compact bundles of parallel fibers," J. Appl. Phys. 13, 725-730 (1942).

79. K. O. Tong, C. J. Knight, and B. N. Srivastava, "Interaction of weak shock waves with screens and honeycombs," AIAA Journal, 18, Article #79-0210R, 1298-1305 (1980).

80. D. A. Webster, "Saturation of plane acoustic waves and notes on the propagation of finite-amplitude spherical waves," Applied Research Laboratories Report, ARL-TR-77-4, AD/A 035694,AFOSR-TR-77-0063 (Master's Thesis) (1977).

81. D. A. Webster and D. T. Blackstock, "Finite-amplitude saturation of plane sound waves in air," J. Acoust. Soc. Am. 62, 518-523 (1977).

82. J. H. B. Zarek, "Sound absorption in flexible porous materials," J. Sound Vib. 61, 205-234 (1978).

83. W. E. Zorumski and T. L. Parrott, "Nonlinear acoustic theory for thin porous sheets," NASA SP-189, 17-27 (1968).

84. W. E. Zorumski, "Acoustic scattering by a porous elliptic cylinder with nonlinear resistance," Ph.D. Thesis, Virginia Polytechnic Institute, (1970).

85. W. E. Zorumski, "Computation methods for nonlinear acoustic absorbers," Presented at the 79th Meeting of the ASA, Atlantic City, NJ (1970).

86. W. E. Zorumski and T. L. Parrott, "Nonlinear acoustic theory for rigid porous materials," NASA TN-6196, 1971.

87. W. E. Zorumski, "Acoustic scattering and absorption by a rigid porous elliptic cylindrical shell, "NASA Technical Note, NASA TND-6340, August 1971.

88. E. Zwikker and C. W. Kosten, Sound Absorbing Materials, (Elsevier Publishing Company, Inc., New York, 1949).

89. Scott Paper Company, Chester, PA.

90. du Pont de Nemours, Baltimore, MD.

91. E. J. Rice, personal communication.

DISTRIBUTION LIST

Copy No.

NASA Lewis Research Center
21000 Brookpark Road
Cleveland, OH 44135
1 - 3 Attn: E. J. Rice, Mail Stop 54-3
4 K. J. Baumeister, Mail Stop 54-3
5 J. A. Saggio, Mail Stop 500-302
6 Report Control Office, Mail Stop 5-5
7 - 8 Library Mail Stop 60-3

NASA Scientific and Technical Information Facility
P. O. Box 8757
Baltimore/Washington International Airport, MD 21240
9 - 34 Attn: Accessioning Department

ASAPL-DO
Wright-Patterson Air Force Base, OH 45433
35 Attn: E. E. Bailey

Commanding Officer
Office of Naval Research
Arlington, VA 22217
36 Attn: L. Hargrove (Code 412)

37 - 49 Defense Technical Information Center
Cameron Station
Alexandria, VA 22314

NASA Langley Research Center
Acoustics and Noise Reduction Division
Hampton, VA 23365
50 - 52 Attn: W. E. Zorumski, Mail Stop 461
J. M. Seiner, Mail Stop 460
W. L. Willshire, Mail Stop 460

Matematisk Institutt
Allegaten
53-55
5014 Bergen - U
NORWAY
53 Attn: S. Tjøtta
J. Tjøtta

Department of Physics
The University of Texas at Austin
Austin, TX 78712
54 - 55 Attn: W. Nolle
T. Griffy

Department of Electrical Engineering
The University of Texas at Austin
Austin, TX 78712
56 Attn: E. L. Hixson

H. L. Blachford, Inc.
463 N. Smith Ave.
P. O. Box 1059
Corona, CA 91720
57 Attn: G. L. Marlotte

Scott Paper Company
Scott Foam Division
1500 E. Second Street
Chester, PA 19013
58 Attn: M. A. Hebner

Globe-Albany Industrial Fabrics
Auburn, ME 04210
59 Attn: E. Trask

Copy No.

ARTEC Consultants, Inc.
245 Seventh Avenue
Eighth Floor
New York, NY 10001
60 Attn: R. D. Essert

Department of Aerospace Engineering and Engineering
The University of Texas at Austin
Austin, TX 78712
61 - 62 Attn: A. Bedford
C. H. Yew

Department of Mechanical Engineering
The University of Texas at Austin
Austin, TX 78712
63 - 64 Attn: R. L. Panton
N. D. Perreira

Electrical Engineering Department
University of Minnesota
Minneapolis, MN 55455
65 Attn: R. F. Lambert

Group d'Etude et de Recherche de Detection Sous-Marines
Le Brusc
B.C.A.N. Toulon
FRANCE
66 Attn: B. G. Lucas

Norwegian Institute of Technology
Electronics Research Laboratory
N-7034 Trondheim - NTH
NORWAY
67 Attn: J. Hovem

Hersh Acoustical Engineering
9545 Cozycraft Ave.
Chatworth, CA 91311
68 Attn: A. S. Hersh

Getty Oil Company
Exploration and Production Research Center
P. O. Box 70070
Houston, TX 772150070
69 Attn: S. Rutherford

Hoover Keith and Bruce Inc.
9730 Town Park
Houston, TX 77036
70 Attn: H. L. Kuntz

71 J. W. Hadden
2400 Westover Road
Austin, TX 78703

72 D. C. Wooten
912 Alder Place
Newport Beach, CA 92660

Georgia Institute of Technology
School of Mechanical Engineering
Atlanta, GA 30332
73 Attn: A. D. Pierce

Kalamazoo College
Department of Physics
Kalamazoo, MI 49007
74 Attn: W. M. Wright

DISTRIBUTION LIST (Cont'd.)

Copy No.	
75	H. O. Berktay School of Physics University of Bath Claverton Down Bath BA2 7AY ENGLAND
76	Technical University of Denmark Fluid Mechanics Department Building 404 DK-2800 Lyngby DENMARK Attn: L. Bjørnø
77 - 78	Institute of Sound Vibration Research The University Southampton SO9 5NH ENGLAND Attn: Dr. C. L. Morfey Professor P. E. Doak
79	David R. Kleeman Lockheed Missiles and Space Co. P. O. Box 504 Sunnyvale, CA 94086
80	Louis C. Sutherland Wyle Labs 128 Maryland St. El Segundo, CA 90245
81	Henry E. Bass Department of Physics and Astronomy University of Mississippi University, MS 38677
82	Mark Theobald 177 Lexington Street Bellmont, MA 02178
83 - 88	ARL:UT Groups
89	David T. Blackstock, ARL:UT
90	Yves Berthelot, ARL:UT
91	Charles R. Culbertson, ARL:UT
92	William C. Dickson, ARL:UT
93	James M. Estes, ARL:UT
94	Karl C. Focke, ARL:UT
95	Terry L. Foreman, ARL:UT
96	Harlan G. Frey, ARL:UT
97	Mark F. Hamilton, ARL:UT
98	Loyd D. Hampton, ARL:UT
99	Claude W. Horton, ARL:UT
100	John M. Huckabay, ARL:UT
101	Chester M. McKinney, ARL:UT

Copy No.	
102	E. Eugene Mikeska, ARL:UT
103	Stephen K. Mitchell, ARL:UT
104	T. G. Muir, ARL:UT
105	David A. Nelson, ARL:UT
106	Lori B. Orenstein, ARL:UT
107	Clark S. Penrod, ARL:UT
108	Jack A. Shooter, ARL:UT
109	James A. TenCate, ARL:UT
110	Paul J. Vidmar, ARL:UT
111	Reuben H. Wallace, ARL:UT
112	Suk Wang Yoon, ARL:UT
113	Library, ARL:UT
114 - 150	Reserve, ARL:UT